

Polymer Precursor-Derived Carbon

ACS SYMPOSIUM SERIES **1173**

Polymer Precursor-Derived Carbon

Amit K. Naskar, Editor
Oak Ridge National Laboratory
Oak Ridge, Tennessee

Wesley P. Hoffman, Editor
Air Force Research Laboratory
Edwards AFB, California

Sponsored by the
ACS Division of Polymer Chemistry, Inc.



American Chemical Society, Washington, DC

Distributed in print by Oxford University Press



Library of Congress Cataloging-in-Publication Data

Polymer precursor-derived carbon / Amit K. Naskar, editor, Oak Ridge National Laboratory, Oak Ridge, Tennessee, Wesley P. Hoffman, editor, Air Force Research Laboratory, Edwards AFB, California ; sponsored by the ACS Division of Polymer Chemistry, Inc.

pages cm. -- (ACS symposium series ; 1173)

Includes bibliographical references and index.

ISBN 978-0-8412-2966-2 (alk. paper)

1. Carbon composites. 2. Carbon. 3. Polymers. I. Naskar, Amit K., editor. II. Hoffman, Wesley P., editor. III. American Chemical Society. Division of Polymer Chemistry.

QD181.C1P58 2014

546'.681--dc 3

2014037321

The paper used in this publication meets the minimum requirements of American National Standard for Information Sciences—Permanence of Paper for Printed Library Materials, ANSI Z39.48n1984.

Copyright © 2014 American Chemical Society

Distributed in print by Oxford University Press

All Rights Reserved. Reprographic copying beyond that permitted by Sections 107 or 108 of the U.S. Copyright Act is allowed for internal use only, provided that a per-chapter fee of \$40.25 plus \$0.75 per page is paid to the Copyright Clearance Center, Inc., 222 Rosewood Drive, Danvers, MA 01923, USA. Republication or reproduction for sale of pages in this book is permitted only under license from ACS. Direct these and other permission requests to ACS Copyright Office, Publications Division, 1155 16th Street, N.W., Washington, DC 20036.

The citation of trade names and/or names of manufacturers in this publication is not to be construed as an endorsement or as approval by ACS of the commercial products or services referenced herein; nor should the mere reference herein to any drawing, specification, chemical process, or other data be regarded as a license or as a conveyance of any right or permission to the holder, reader, or any other person or corporation, to manufacture, reproduce, use, or sell any patented invention or copyrighted work that may in any way be related thereto. Registered names, trademarks, etc., used in this publication, even without specific indication thereof, are not to be considered unprotected by law.

PRINTED IN THE UNITED STATES OF AMERICA

Foreword

The ACS Symposium Series was first published in 1974 to provide a mechanism for publishing symposia quickly in book form. The purpose of the series is to publish timely, comprehensive books developed from the ACS sponsored symposia based on current scientific research. Occasionally, books are developed from symposia sponsored by other organizations when the topic is of keen interest to the chemistry audience.

Before agreeing to publish a book, the proposed table of contents is reviewed for appropriate and comprehensive coverage and for interest to the audience. Some papers may be excluded to better focus the book; others may be added to provide comprehensiveness. When appropriate, overview or introductory chapters are added. Drafts of chapters are peer-reviewed prior to final acceptance or rejection, and manuscripts are prepared in camera-ready format.

As a rule, only original research papers and original review papers are included in the volumes. Verbatim reproductions of previous published papers are not accepted.

ACS Books Department

Preface

Carbon is essential to life on Earth, and it forms complex molecules with oxygen, hydrogen, and nitrogen that are ubiquitous in the biosphere. Elemental carbon has been valued for thousands of years for its use in processing metal ores. The variety of carbon allotropes as well as the vast variety of carbon's architectures, and forms is made possible by its ability to form sp , sp^2 , and sp^3 electronic orbitals through hybridization. These various architectures and forms can encompass a very broad spectrum of properties, which, in turn enable a myriad of applications. Traditional methods for synthesizing carbon-based materials include catalytic vapor growth, hydrothermal processing of colloids, chemical vapor deposition, as well as pyrolysis of precursors, such as fibers, bulk monoliths, fuels, and fuel derivatives. Some of these methods follow a combinatorial optimization approach, which does not necessarily enable the desired control of carbon architecture. The science of controlling carbon structure with predefined geometries and controlled levels of long-range order from atypical char-forming precursors has yet to be established.

Over the last two decades there have been significant improvements in synthesis routes of carbon materials, analytical tools for characterization, and in the properties of carbon materials. Monolithic or continuous matrix carbon products are commercially produced from polymeric and pitch carbon precursors. Specialty carbon materials are used for energy applications and reduction in carbon emission, membrane separation, energy storage, catalysis, solar utilization, electronics, and sensing. New generation higher-performance structural carbon fibers have the potential to enhance vehicle efficiency and reduce greenhouse gas emission when used as composite lightweight structures.

This book, *Polymer Precursor-Derived Carbon*, is based on an international symposium organized by the editors, along with Professor Dennis W. Smith Jr. of UT-Dallas, and held at the 2013 national ACS meeting in New Orleans, Louisiana. Many exciting new findings were reported in the symposium, which was attended by researchers from academia, industry, and government research laboratories.

The editors would like to thank the authors for their timely contributions to this endeavor, for without their cooperation this undertaking would not have succeeded. The editors would also like to thank POLY Division of the American Chemical Society and Oak Ridge National Laboratory for sponsoring the symposium. A very special thank you goes to Professor Dennis Smith, who has worked in this field for years, conceived the idea for this symposium, spearheaded its organization, and worked tirelessly toward its success.

We are also grateful to the publishing editor and editorial office of the American Chemical Society for their efforts and professionalism in publishing this book.

Amit K. Naskar

Senior R&D Staff & Carbon and Composites Group Leader
Materials Science and Technology Division
Oak Ridge National Laboratory
Oak Ridge, Tennessee 37931-6053
naskarak@ornl.gov (e-mail)

Wesley P. Hoffman

Principal Scientist and Group Leader
Air Force Research Laboratory
AFRL/RQRC
10 E. Saturn Blvd.
Edwards AFB, California 93524-7680
wesley.hoffman.1@us.af.mil (e-mail)

Dedication

In memory of Professor James E. McGrath,
who inspired us to organize this endeavor.

Editors' Biographies

Amit K. Naskar

Dr. Amit K. Naskar is a senior R&D staff member and leader of the Carbon and Composites group of the Materials Science and Technology Division at Oak Ridge National Laboratory in Oak Ridge, Tennessee. He has developed technologies for the conversion of polyolefin into structural carbon materials, lignin-based carbon precursors and polymers for composites, and tailored carbon morphology for energy storage applications. He has more than 15 years of research experience in carbon, polymeric fibers, rubbers, plastics, and composite materials.

Wesley P. Hoffman

Dr. Wesley P. Hoffman is a Principal Scientist and the Group Lead of the High Temperature Components Group at the Air Force Research Laboratory in Edwards California, whose focus is rocket propulsion. He has been working in the field of carbon research, principally in the areas of carbon-carbon composites and surface characterization, for over 40 years both at the Air Force Research Laboratory and the Institut de Science des Matériaux de Mulhouse in Mulhouse, France. After serving in various capacities, he served three terms as Chairman of the Executive Committee of the American Carbon Society.

Chapter 1

Self-Assembly of Polyaromatic Precursors for 1D and 2D Carbon Structures

**Katrin Wunderlich,¹ Armin Gölhäuser,²
Markus Klapper,^{*,1} and Klaus Müllen^{*,1}**

**¹Max Planck Institute for Polymer Research,
Ackermannweg 10, 55128 Mainz, Germany**

²Faculty of Physics, University of Bielefeld, 33615 Bielefeld, Germany

***E-mail: klapper@mpip-mainz.mpg.de**

***E-mail: muellen@mpip-mainz.mpg.de**

Self-assembly of amphiphiles is used as a tool for structuring carbonaceous materials in one and two dimensions. The dynamics of low-molecular weight amphiphiles are combined with the stability of their high-molecular weight analogues in order to control the self-assembly of these molecules. Two concepts for structuring carbon by self-assembly are presented. In the first, hexaphenylbenzene-polyethylene glycol (HPB-PEG) derivatives lead to fiber-like structures in aqueous solution. The water content in the hydrogel fibers of HPB-PEG derivatives can be controlled by the substitution pattern of the amphiphile and by the length of the PEG chains. The fiber formation is verified by light scattering and TEM. In the second concept, homogeneous porous carbon membranes are obtained after electron irradiation and pyrolysis of a thiol-substituted HPB. In both concepts, amphiphilicity, geometry and size of the molecules are decisive parameters for the formation of defined structures.

Introduction

Synthesis of carbonaceous materials is becoming more and more important in materials science. Most prominent examples of the obtained materials are fullerenes (1), carbon nanotubes (CNTs) (2) and carbon fibers. Fullerenes and CNTs are fabricated by chemical vapor deposition (CVD) (3), laser ablation (4) or arc discharge (5). Carbon fibers can be produced by spinning of poly(acrylonitrile) or other carbon sources and pyrolysis (6). Another well-known allotrope of carbon is graphene. Graphene is a monolayer of graphite. Segments of graphene can be prepared as graphene nanoribbons (GNRs). They are produced by electron beam lithography, opening of CNTs (7) or synthetically starting from small aromatic molecules (8–11). They can be used in field-effect transistors due to their finite band gap (12).

In most cases, pyrolysis of precursors or CVD yield carbonaceous materials with defect structures or multilayers. For more defined materials, we propose self-assembly processes which are known from nature (cf. protein folding, DNA, cell membranes, tobacco mosaic virus) (13) as a useful tool for structuring carbonaceous materials on the nanometer scale. In particular, we suggest the formation of well-defined aggregates of precursor molecules for the formation of carbon rich materials is possible. Self-assembly is defined as the formation of discrete architectures from building blocks that can range in size from atoms and molecules up to macroscopic units (14). Despite the great deal of progress made over the last several years, understanding the parameters and predicting the properties of self-assembly remain fundamental problems. The driving force for self-assembly is microphase separation of hydrophilic and hydrophobic blocks in ordered structures (15). The structures can be controlled by intramolecular and intermolecular interactions such as hydrogen bonds, π - π stacking and van der Waals forces.

A prerequisite for the use of self-assembly for carbonaceous materials is the understanding of the process and the parameters for the aggregation. In order to tune the structures by self-assembly, there must be a balance between the stability and the thermodynamic control. Small amphiphiles like sodium dodecyl sulfate or lutensols with high critical micelle concentration (cmc) ($\text{cmc} > 10^{-2} \text{ mol l}^{-1}$) form small aggregates (micelles) in an equilibrium while amphiphilic block copolymers with a high-molecular weight ($\text{cmc} < 10^{-7} \text{ mol l}^{-1}$) lead to kinetically arrested non-equilibrated structures (16–18). By preparing amphiphiles with intermediate molecular weights, the potential advantages of low-molecular weight (dynamics) and high-molecular weight copolymers (stability) can be combined and investigated. The self-assembly of these structures with respect to the different size of the polar groups and the shape of the molecules is explored (Figure 1).

Until now, self-assembly of functionalized aromatics has dealt with linear rigid aromatics (e.g. tetra-*p*-phenylene, oligo(phenylene vinylene)) (19). In contrast to literature, we have chosen amphiphiles with a bulkier headgroup to study the influence of the shape of the hydrophobic and hydrophilic part of the self-assembly. We focus on the propeller-like hexaphenylbenzene (HPB) because the corresponding dehydrogenated disk-like hexa-*peri*-hexabenzocoronene

(HBC) as hydrophobic building block (Figure 2) is already known for forming extended columns in solution due to the strong π - π stacking between the extended polyaromatic units. Therefore, a thermodynamic control of the self-assembly process cannot be guaranteed (20).

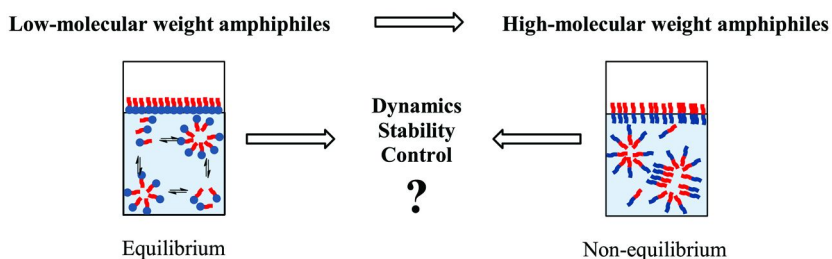


Figure 1. Schematic representation of low-molecular weight amphiphiles (left) and of high-molecular weight analogues (right).

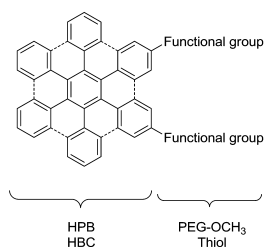


Figure 2. Schematic structural formula of the molecules whose self-assembly is presented in this work.

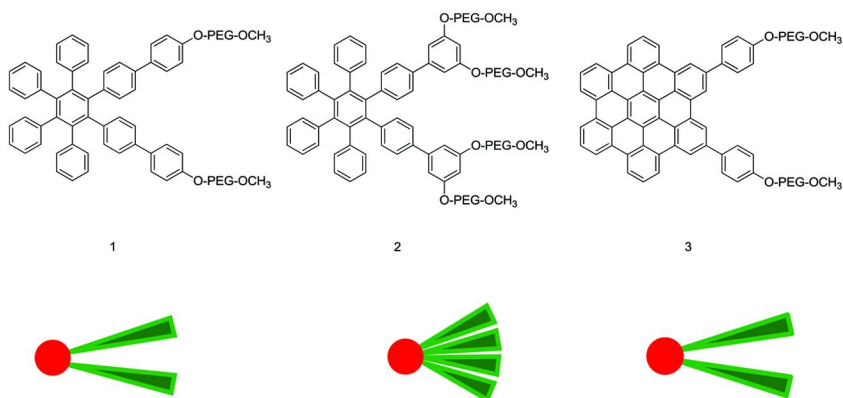


Figure 3. Molecular structure of Molecule 1 - 3 and a schematic representation of the aspect ratio. (see color insert)

The main focus of this work is on the fiber formation in one dimension and on membranes in two dimensions based on these amphiphiles. In the first concept, HPB is decorated with two and four PEG chains (Figure 3). It will be shown that depending on the molecular structure, the self-assembly can be adjusted. We are able to demonstrate that HPB-PEG derivatives form either micelles or lamellar structures. Sheet-like structures are achieved by surface deposition of dithiol functionalised HPB on gold. Subsequent crosslinking by electron beam followed by pyrolysis yields nanomembranes.

Fibers of HPB/HBC with PEG Chains – 1D

In fiber formation processes, either physical methods such as extrusion (21), microfluidic processes (22), electrospinning (23) or spontaneous self-organization (24) are used. We investigate the self-assembly of aromatics with PEG chains for fiber formation. It is expected that supramolecular structures are formed by the amphiphilicity. Self-assembly of aromatics with PEG chains have been described in many cases in literature (25). However, a dense packing inside the core and the shell is always assumed and the role of water has been ignored. In order to better understand the kinetics of the self-assembly and water's possible role in these processes, we make a comparison of amphiphilic, aromatic propeller-like molecules and planar, rigid molecules. Therefore, the self-assembly of HPB-PEG derivatives is compared with the more rigid HBC-PEG derivative (3) (Figure 4).

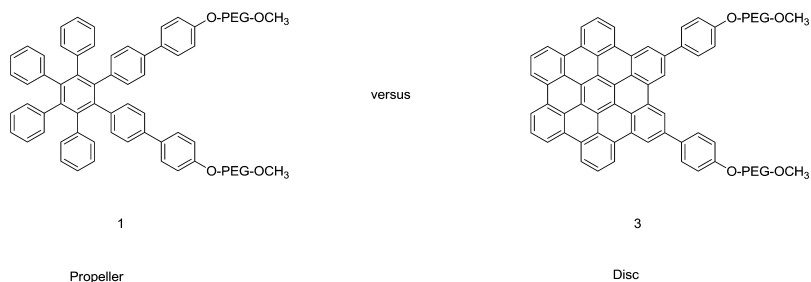


Figure 4. Molecular structure of HPB with two PEG chains (1) and HBC with two PEG chains (3).

Self-Assembly of HPB-PEG Derivatives

Two HPB derivatives 1 and 2 were designed (Figure 5) in order to study the influence of the amphiphility and the shape on the self-assembly process. Molecule 1 has two long PEG chains ($M_n = 750 \text{ g mol}^{-1}$) whereas molecule 2 has four short PEG chains ($M_n = 380 \text{ g mol}^{-1}$). In both molecules the weight percentage of PEG is the same but the number of attached chains and the length of the PEG chain is different, which results in an alteration of the overall shape of the molecule (Figure 5).

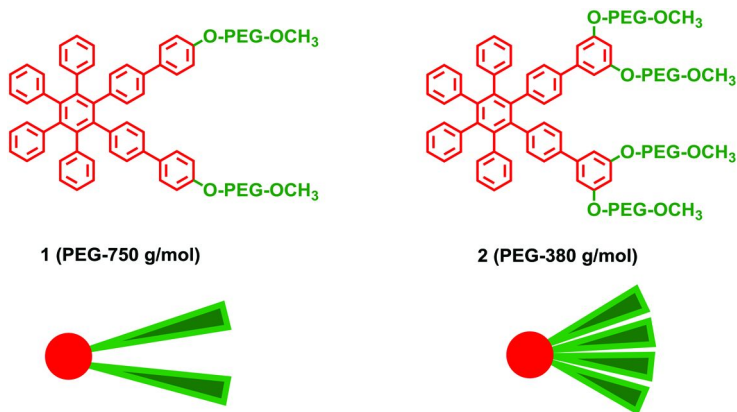


Figure 5. Molecular structure of the HPB-PEG derivatives **1** and **2**. (see color insert)

For the synthesis of HPB with two PEG chains (**1**), a Diels-Alder reaction with subsequent carbon monoxide extrusion of 1,2-bis(4-bromophenyl)ethyne (**7**) and 2,3,4,5-tetraphenylcyclopenta-2,4-dienone (**8**) was performed leading to 4,4''-dibromo-3',4',5',6'-tetraphenyl-1,1':2',1''-terphenyl (**9**) (Figure 6). Then 4,4''-dimethoxy-3',4',5',6'-tetraphenyl-1,1':4',1''':2',1''':4'',1''''-quinquephenyl (**10**) was prepared by palladium-catalyzed Suzuki coupling reaction with 4,4''-dibromo-3',4',5',6'-tetraphenyl-1,1':2',1''-terphenyl (**9**) and 4-methoxyphenyl boronic acid. The following deprotection of the methoxyphenyl groups and etherification of HPB containing two hydroxyphenyl groups (**11**) with α -methoxy- ω -bromo-PEG (PEG: $M_n = 750 \text{ g mol}^{-1}$) gave **1**; while **2** was synthesized under similar conditions, however, using the (3,5-dimethoxyphenyl)boronic acid and a shorter α -methoxy- ω -bromo-PEG derivative (**26**).

Self-assembly was studied by cryo-TEM and light scattering. Cryo-TEM micrographs revealed worm-like structures formed by **1** (37 g l^{-1} in water) with diameters of approximately 4 nm and lengths up to 400 nm. Spherical shapes formed by the amphiphiles with four short PEG chains (**2**) with only a few worm-like structures were observed. The average diameter of these spheres was $\sim 4 \text{ nm}$. This difference can be explained by the shape of the molecule. While in the more linear case (**1**) a fibrous structure was detected, spherical micelles of **2** were obtained due to steric reasons caused by the bulky hydrophilic part (**15**). This structural effect is also observed in surface pressure – area (π -A isotherms) using a Langmuir-Blodgett trough at a constant temperature. During these measurements, the surface pressure is measured as a function of the available area for each molecule in a floating monolayer. The collapse of the monolayer is characterized by the formation of three-dimensional aggregates as well as by the loss of molecules diving into the subphase. The area per molecule which the amphiphile occupies at the collapse point is called the collapse area A_c . The collapse area of molecule **1** is $170 \text{ \AA}^2/\text{molecule}$ whereas the collapse area of molecule **2** with $1740 \text{ \AA}^2/\text{molecule}$ (**27**). For comparison, the collapse area of a small amphiphile such as SDS is 40 to $70 \text{ \AA}^2/\text{molecule}$. With these results it is obvious that the head group HPB has limited influence on the surface

area/molecule; however the number of PEG chains proves decisive. The more PEG chains the higher the surface area/molecule.

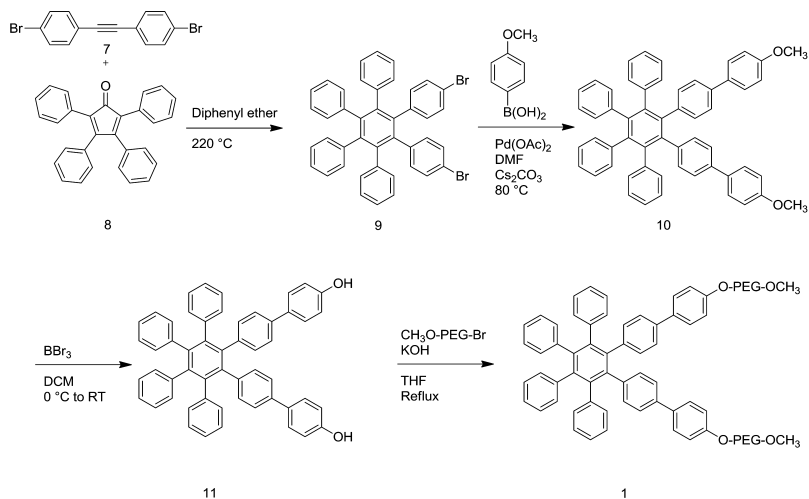


Figure 6. Synthesis of the HPB-PEG derivative 1.

In addition to cryo-TEM investigations, light scattering experiments were performed to determine the aggregate characteristics in solution. This initially proved challenging as standard dynamic light scattering (DLS) techniques were unable to provide useful information on the length and diameter of the anisotropic aggregates, polarized and depolarized dynamic light scattering utilizing the spatiotemporal resolution of the phonon correlation spectroscopy were applied. For this reason, more advanced techniques were necessary. Therefore polarized and depolarized dynamic light scattering utilizing the spatiotemporal resolution of the phonon correlation spectroscopy are applied. With these measurements, we demonstrate the static and dynamic properties of the mesoscale sized self-assemblies can be elucidated. The overlap concentration c^* above which interactions between the molecules in aqueous solutions becomes very low (Figure 7). To avoid these interactions, very dilute solutions ($< 3 \times 10^{-2} \text{ g l}^{-1}$) were measured.

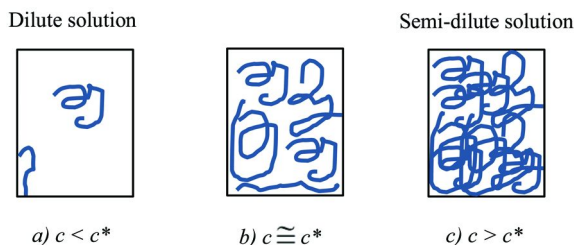


Figure 7. Schematic representation of a dilute aqueous solution (a), a solution with the overlap concentration c^* (b), and a semi-dilute solution (c).

These measurements revealed that **1** forms worm-like structures with a length of 2.25 μm and a diameter of 30 nm. Surprisingly, the length of the aggregates of molecule **2** increased up to 6.00 μm . Remarkably, the diameter is unaffected. In both cases a 30 nm thickness of the fibers formed by **1** and **2** was detected (Table I).

Table I. Structural parameters for the self-assembled structures of **1 and **2** in very dilute aqueous solution obtained from dynamic and static experiment. Data are from reference (26).**

	<i>1</i>	<i>2</i>
Length [μcm]	2.25	6.00
Diameter [nm]	30	30
M_w [g mol ⁻¹]	1.3×10^8	1.8×10^9
Molecules in an aggregate	60.000	780.000
Molecules in one “layer”	16	78
Density [g·cm ⁻³]	0.2	0.7

By comparing the molecular weight and the length of the fibers, we were able to calculate the number of molecules in an aggregate or in one “layer”. The distance between two “layers” was assumed as the distance between two HPBs. This distance is reported in literature as 0,67 nm (28). With 16 (**1**) and 78 molecules (**2**) in one layer, we assume that bundles of hydrogel fibers in very dilute aqueous solution are formed (Figure 8). In a fiber, the hydrophilic part protects the hydrophobic part from water. The fiber formation of the HPB-PEG derivatives can be compared with Percec’s tobacco mosaic virus model (29). The assumption of the formation of bundles of fibers was also confirmed by cryo-TEM micrographs (see enlarged micrograph in Figure 8). However, the concentration of **1** in the cryo-TEM studies was much higher than in the light scattering experiments. The density of the aggregates of **1** was much lower than the density of **2**. This corresponds to a difference in the water uptake of the fibers.

From these results we assume that the water amount in the hydrogel fibers does not depend on the number of hydrophilic groups but on the length of the PEG chains and the shape of the precursor molecules. Molecule **2** with the shorter PEG chains formed longer self-assembled structures containing less water than the fibers formed by the longer PEG chains. The denser packing of the four PEG chains in **2** is assumed to hamper the water uptake, while **1** having only two PEG chains can more easily swell in an aqueous phase.

The formation of fibers by self-assembly is surprising, as typically hydrogel fibers are formed by chemical methods and require further processing and postmodification such as a chemical crosslinking. For example, extruded fibers of poly(vinyl alcohol) and poly(acrylic acid) can be converted to bundles of hydrogel fibers after a crosslinking by ester formation upon heating (30, 31). Furthermore, molecular self-assembly, i.e. formation of discrete architectures from molecules via intermolecular forces, is used to make hydrogel fibers (32). Such a process is

very common in nature. Therefore, our process can be considered as an analogue to a biological fiber formation process. Remarkably, the water content of the fibers can be adjusted by the substitution pattern and the length of the PEG chains in the amphiphile.

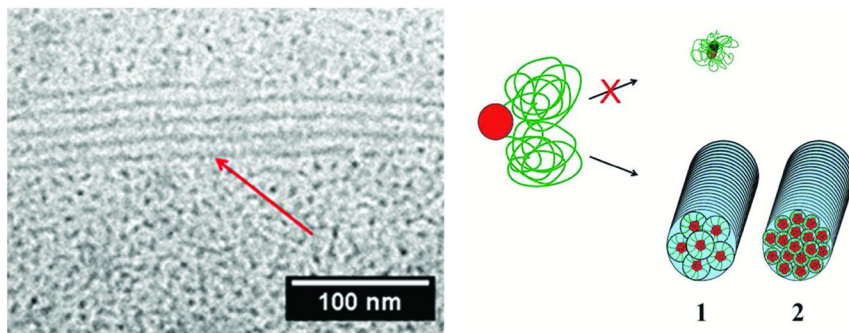


Figure 8. Cryo-TEM micrograph of bundles of fibers of molecule **1** (37 g l^{-1}) in water (left). Schematic representation of the proposed self-assembled equilibrium structures of **1** and **2** (right). (see color insert)

Self-Assembly of HBC-PEG Derivatives

To evaluate the kinetics of the fiber formation process, we also synthesized HBC with PEG chains (**3**) (Figure 10). As we assume that the HBC-PEG compound will probably behave similar to a high-molecular weight amphiphiles which means that stable micelles are formed and the control of the aggregates is not possible (see Figure 1 on the right). In particular, molecule **3** has the same percentage of PEG as molecule **1** and **2**. In comparison to **1** and **2**, this time the hydrophobic part was changed. A planar, rigid hydrophobic part was used in contrast to the propeller-like HPB in **1** and **2**. We expect due to the rigidity of the HBC in **3** that the aggregates are in a non-equilibrium.

HBC bearing two triethylene glycol chains on one side and two dodecyl chains on the other side was already reported in literature by *Aida et al.* (33) (Figure 9).

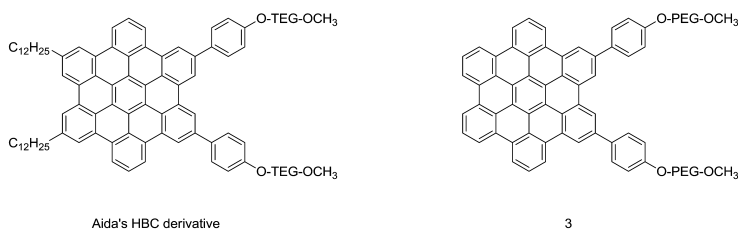


Figure 9. Molecular structure of Aida's HBC derivative and the HBC-PEG derivative (**3**).

While Aida's amphiphile self-assembled into graphitic nanotubes in THF/water solution. Herein, the self-assembly of HPB/HBC-PEG derivatives with longer PEG chains is used in order to get defined structures e.g. spherical micelles or lamellar structures.

For the synthesis of HBC with two PEG chains (**3**), 4-(4,4,5,5-tetramethyl-1,3,2-dioxaborolan-2-yl)phenol (**12**) was first subjected to etherification with α -methoxy- ω -bromo-PEG ($M_n(\text{PEG})=750 \text{ gmol}^{-1}$). Oxidative cyclodehydrogenation of 4,4''-dibromo-3',4',5',6'-tetraphenyl-1,1':2',1''-terphenyl (**9**) led to 2,5-dibromohexabenzob[bc,ef,hi,kl,no,qr]-coronene (**14**). Then a palladium-catalysed Suzuki coupling of the **13** and 2,5-dibromohexabenzob[bc,ef,hi,kl,no,qr]-coronene (**14**) gave HBC with two PEG chains (**3**) (Figure 10). The synthesis of **3** will be published.

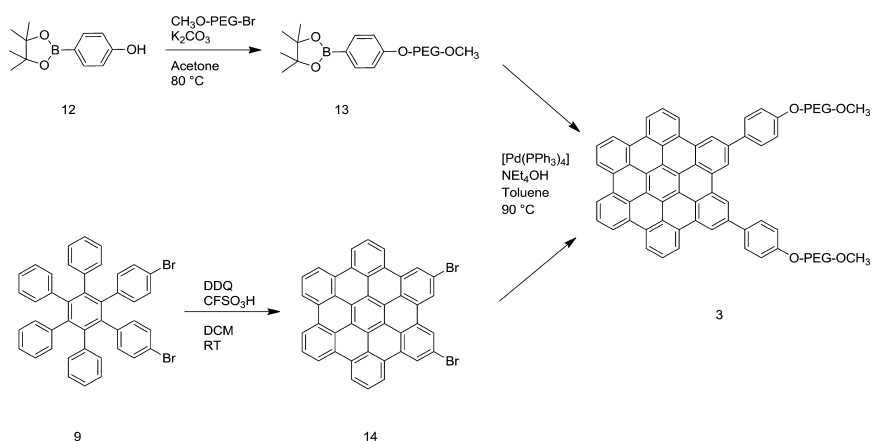


Figure 10. Synthesis of the HBC-PEG compound **3**.

Cryo-TEM micrographs of **3** reveal fiber-like structures (Figure 11). The length of the fibers reaches several hundred nanometers. Notably, the individual fibers show a “necklace” structure. The 1.0 nm segment periodicity is almost identical throughout all structures and corresponds well to the HBC. The possible schematic representation demonstrates how the molecules arrange in aqueous solution. Such rare structures are suggested to occur due to kinetic trapping. Kinetically trapped wormlike structures from block copolymers have also recently been observed (34, 35).

Upon comparing both systems, we conclude that the fiber formation, in our case is controlled by the strength of the different molecular interactions (hydrogen bonds, van der Waals forces) similar to nature. These interactions have to be carefully tuned to allow a thermodynamic control which we showed by the comparison between amphiphiles containing HPB and HBC as hydrophobic building blocks. The main difference is that nature achieves such extended hydrogel fibers by the self-assembly of large polymers such as polysaccharides or polypeptides, while we focus on “small” two-dimensional amphiphiles which form large fibers.

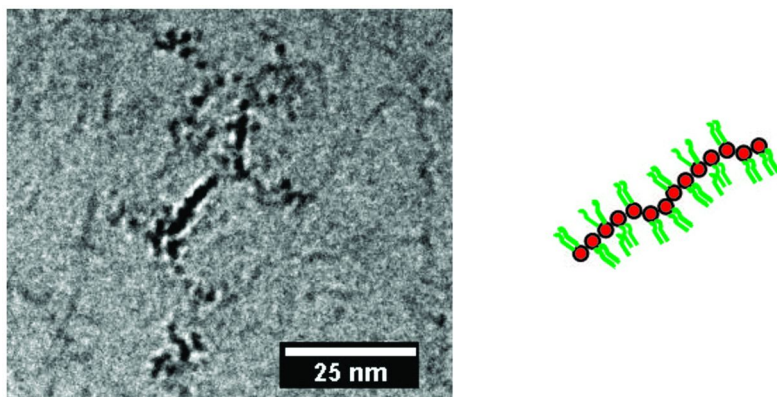


Figure 11. Cryo-TEM micrograph of the HBC-PEG compound (3) in aqueous solution (15 g l⁻¹) (left). A schematic representation of the self-assembly of HBC-PEG compound is depicted (right).

Carbon Membranes with Thiol-Substituted HPBs – 2D

After demonstrating how HPB- and HBC-PEG derivatives form one-dimensional fibers in solution we extended the self-assembly concept to the formation of two-dimensional structures. Nanomembranes can be fabricated by diverse methods. One popular example is the layer-by-layer technique. In this method, an electrically charged surface is sequentially dipped into solutions of positively and negatively charged polyelectrolytes and polymeric membranes with thicknesses from 15 nm to 100 nm are obtained (36). Thinner membranes can be prepared by exfoliation of single sheets out of a layered material, e.g. graphene can be fabricated out of graphite by this method (37). However, with this method graphene cannot be prepared on a large scale. Another method for fabrication of graphene is CVD (3).

A fabrication route for ultrathin (0.6 - 2.0 nm) carbon nanomembranes (CNMs) with large lateral dimensions (few cm²), based on a “top-down” approach, was developed by *Gözlhäufer et al.* (38, 39). These membranes can be used as transparent electronic coatings, filters and sensors.

The primary building units of the carbon nanomembranes (CNMs) are aromatics, self-organized on a metal or semiconducting substrate. Structural characterization was performed by x-ray photoelectron spectroscopy (XPS), low-energy electron diffraction (LEED) and phase-modulated reflection-absorption spectroscopy (PM-IRRAS). A low-energy electron exposure (100 eV, dose: 60 mC/cm²) induces lateral cross-linking of the aligned phenyl rings within the self-assembled monolayers (SAM) and results in the formation of a uniform and stable monomolecular film. *In situ* characterization of the cross-linked (irradiated) samples by XPS revealed the chemical composition. Furthermore, this polymer structure sustains the release from the underlying substrate by the PMMA approach, developed in Gözlhäufer’s group, and the subsequent transfer to various types of soft, solid or perforated supports. The

structural integrity and morphology of the cross-linked samples was imaged by helium ion microscope. These ultrathin films were annealed (1200 K) to form nanocrystalline graphene sheets which were characterized by AC-HRTEM. This finding opens a novel molecular route towards the direct large-scale synthesis of carbon nanomembranes with tunable thickness on different functional substrates (Figure 12) (40). The formation of CNMs with [1,1'-biphenyl]-4-thiol as primary building unit by electron irradiation and pyrolysis has not been understood completely (41). In this process, it is assumed that the electrons are taken up by the aromatics, leading to anions. Subsequent hydrogen abstraction of the opposing aromatic results in the formation of an aryl/aryl bond.

Transformation toward graphene is confirmed by the appearance of the characteristic G-peak in the Raman spectrum and onset of electrical conductivity. The sheet resistivity is $\sim 100 - 500 \text{ k}\Omega/\text{sq}$. The pyrolysed carbon nanomembrane can be used for many applications e.g. transparent flexible window electrode as substitute for indium-tin oxide in solar cells (42). Furthermore, these membranes can be applied as filter for gas separation. The advantage is that gases or liquids typically pass probably much faster through the porous layers due to the lower thickness than in conventional filters (43, 44).

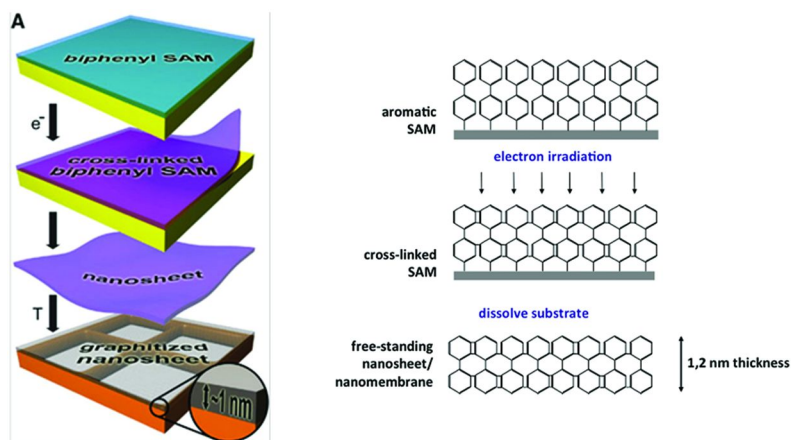
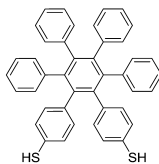


Figure 12. Schematic representation of nanomembrane formation by electron irradiation and pyrolysis. Reproduced with permission from reference (40). Copyright 2011, Wiley. (see color insert)

Besides the [1,1'-biphenyl]-4-thiol, we applied similar protocols to a variety of other polyaromatic molecule. Three different types of molecules were investigated: nonfused oligophenyl derivatives with a linear molecular backbone (biphenyl, *para*-triphenylene), condensed polycyclic precursors (naphthalene, anthracene) and bulky molecules (hexaphenylbenzene, hexa-*peri*-hexabenzocoronene).

HPB substituted with two thiols is the workhorse for the preparation of carbon nanomembranes (Figure 13). HPB substituted with two thioesters was synthesized by reacting the aryl halide 4,4''-dibromo-3',4',5',6'-tetraphenyl-1,1':2',1''-terphenyl (9) with *n*-butyllithium (*n*-BuLi), followed by addition of

sulfur, and trapping with acetyl chloride. Subsequent deprotection with NH_4OH led to 3',4',5',6'-tetraphenyl-[1,1':2',1''-terphenyl]-4,4''-dithiol (**4**). The synthesis of **4** has been published (43).



4

Figure 13. Molecular structure of 3',4',5',6'-tetraphenyl-[1,1':2',1''-terphenyl]-4,4''-dithiol (**4**).

Molecule **4** shows very homogeneous CNMs after electron irradiation by helium-ion microscopy (Figure 14).

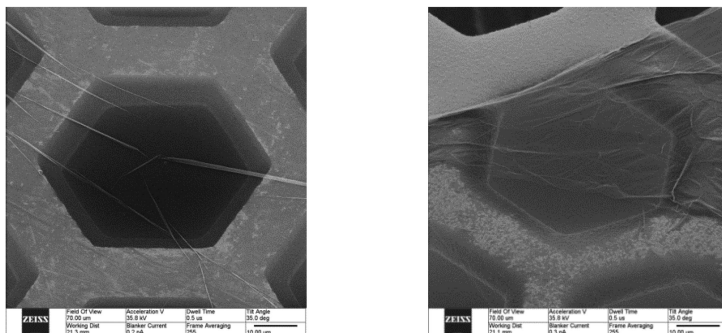


Figure 14. Helium ion microscopy (HIM) images of freestanding CNMs with pore sizes of 3 nm formed from molecule **4** on a TEM grid after electron irradiation.

AC-HRTEM micrographs revealed very thin CNMs (0.8 nm) after pyrolysis (Figure 15). Most of the sheet area consisted of single-layer graphene (~50%, blue) with the clearly recognizable hexagonal arrangement of carbon atoms; randomly oriented graphene nanocrystallites were connected with each other via the typical heptagon-pentagon grain boundaries (see inset: Figure 15).

A small fraction of the sheet (~20%, yellow-green) consisted of graphene double-layer. Grey and pink areas corresponded to the disordered carbon and nanopores, respectively. These porous membranes are promising materials for filtration. The thickness, conductivity, chemical functionalization, and appearance of nanopores can be adjusted depending on the molecule. The resistivity correlates with the thickness of the pyrolysed nanomembrane, with lower resistivity for the thicker sheets (43).

By varying the structure of the molecular constituents of the SAMs, we expect that the atomic constitution and the doping atom amount of the nanomembrane can be altered. We fabricated N-doped carbon based precursors by employing heterocyclic non-condensed aromatic systems (Figure 16).

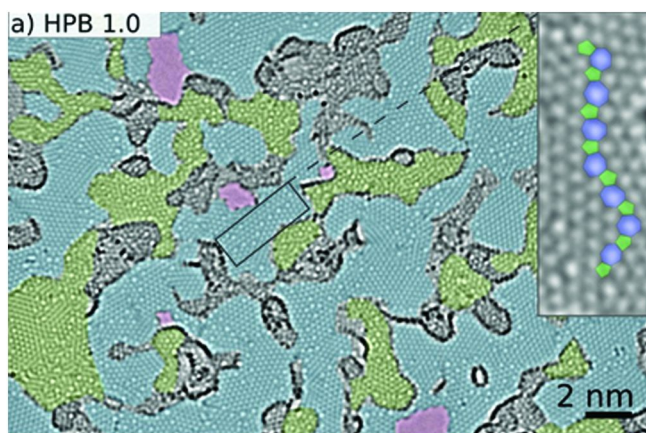


Figure 15. Aberration corrected high-resolution transmission electron microscope (AC-HRTEM) micrographs at 80 kV of pyrolysed carbon membranes. Reproduced with permission from reference (43). Copyright 2013, ACS publications. (see color insert)

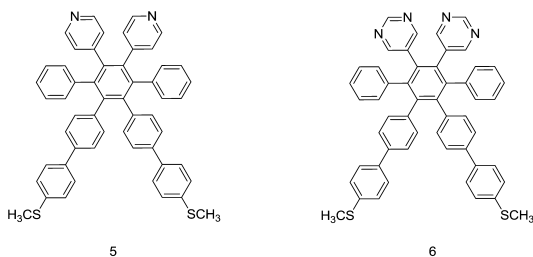


Figure 16. Chemical structure for nitrogen doped HPB **5** and **6**.

Diels-Alder reaction with subsequent carbon monoxide extrusion of 1,2-di(pyridin-4-yl)ethyne (**15**) and 3,4-bis(4-bromophenyl)-2,5-diphenylcyclopenta-2,4-dienone (**16**) led to 4,4'-(5',6'-bis(4-bromophenyl)-[1,1':4',1''-terphenyl]-2',3'-diyl)dipyridine (**17**). **5** was prepared by palladium-catalyzed Suzuki coupling reaction with 4,4'-(5',6'-bis(4-bromophenyl)-[1,1':4',1''-terphenyl]-2',3'-diyl)dipyridine (**17**) and (4-(methylthio)phenyl)boronic acid. **6** was synthesized under similar conditions, however using the 1,2-di(pyrimidin-5-yl)ethyne instead of 1,2-di(pyridin-4-yl)ethyne (**15**).

We will use these precursors for the formation of nitrogen doped carbon membranes including preparation of SAMs on gold surface, electron irradiation and pyrolysis. Due to the pronounced electrochemical activity, good electrical conductivity, thermal stability and low cost heteroatom-doped carbon materials exhibit, these materials can become attractive as metal free electrodes in fuel cells and lithium-ion batteries (45). Such an approach might be able to replace the nowadays in electrodes used metals like palladium and platinum by unlimited available materials (Figure 17).

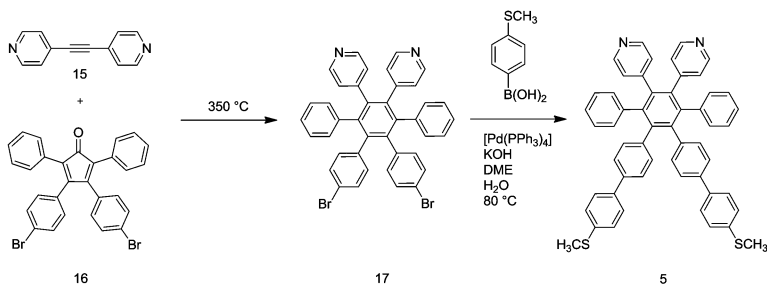


Figure 17. Synthesis of the nitrogen doped HPB 5.

Conclusion

A prerequisite for the use of a self-assembly process for carbonaceous materials is the understanding of self-assembly and the parameters for the aggregation. For tuning the self-assembly, there must be a balance of the stability and the thermodynamic control. The self-assembly of HPBs containing PEG chains or thiols was studied in solution and on surfaces. HPB with two/ four PEG chains (**1** - **2**) in water self-assembled into fibers in which the HPB stacked. Notably, the water content in the hydrogel fibers does not depend on the number of hydrophilic groups but on the length of the PEG chains and the shape of the precursor molecules. Molecule **2** with the shorter PEG chains formed longer self-assembled structures containing less water than the fibers formed by the longer PEG chains. We assume that the denser packing of the four PEG chains in **2** hampers the water uptake, while **1** has only two PEG arms that can easily swell in an aqueous phase. In contrast to the propeller-like HPB-PEG derivatives, the rigid, planar HBC-PEG derivative **3** forms a necklace structures. These structures were suggested to occur due to kinetic trapping.

A “top-down” approach for preparing homogeneous carbon membranes was developed. In this approach the aromatics on gold were crosslinked by electron irradiation and pyrolysis. Thus, homogeneous carbon nanomembranes with thicknesses of less than 0.8 nm were obtained. The thickness, conductivity, chemical functionalization, and appearance of nanopores can be adjusted dependent on the molecule and the resistivity correlates with the thickness of the pyrolysed nanomembrane, with lower resistivity for the thicker sheets.

In both concepts, geometry and size of the molecules are decisive parameters for the formation of defined structures. This interdisciplinary area between synthetic organic chemistry and physical chemistry leads to interesting new aspects in the area of fiber formation and membrane fabrication. Furthermore, the present work contributes to the understanding of the self-assembly at the nanoscale and at the macroscale.

References

1. Kroto, H. W.; Heath, J. R.; Brien, S. C. O.; Curl, R. F.; Smalley, R. E. *Nature* **1985**, *318*, 162–163.
2. Iijima, S. *Nature* **1991**, *354*, 56–58.
3. Jose-Yacamán, M.; Miki-Yoshida, M.; Rendon, L.; Santiesteban, J. G. *Appl. Phys. Lett.* **1993**, *62*, 657–659.
4. Thess, A.; Lee, R.; Nikolaev, P.; Dai, H.; Petit, P.; Robert, J.; Xu, C.; Lee, Y. H.; Kim, S. G.; Rinzler, A. G.; Colbert, D. T.; Scuseria, G. E.; Tomanek, D.; Fischer, J. E.; Smalley, R. E. *Science* **1996**, *273*, 483–487.
5. Bethune, D. S.; Kiang, C. H.; de Vries, M. S.; Gorman, G.; Savoy, R.; Vazquez, J.; Beyers, R. *Nature* **1993**, *363*, 605–607.
6. Frank, E.; Hermanutz, F.; Buchmeiser, M. R. *Macromol. Mater. Eng.* **2012**, *297*, 493–501.
7. Kosynkin, D. V.; Higginbotham, A. L.; Sinitskii, A.; Lomeda, J. R.; Dimiev, A.; Price, B. K.; Tour, J. M. *Nature* **2009**, *458*, 872–876.
8. Cai, J.; Ruffieux, P.; Jaafar, R.; Bieri, M.; Braun, T.; Blankenburg, S.; Mouth, M.; Seitsonen, A. P.; Saelh, M.; Feng, X.; Müllen, K.; Fasel, R. *Nature* **2010**, *466*, 470–473.
9. Fogel, Y.; Zhi, L.; Rouhanipour, A.; Andrienko, D.; Räder, H.; Müllen, K. *Macromolecules* **2009**, *42*, 6878–6884.
10. Wu, J.; Gherghel, L.; Watson, M.; Li, J.; Wang, Z.; Simpson, C.; Kolb, U.; Müllen, K. *Macromolecules* **2003**, *36*, 7082–7089.
11. Yang, X.; Dou, X.; Rouhanipour, A.; Zhi, L.; Räder, H.; Müllen, K. *J. Am. Chem. Soc.* **2008**, *130*, 4216–4217.
12. Xie, L.; Jiao, L.; Dai, H. *J. Am. Chem. Soc.* **2010**, *132*, 14751–14753.
13. Whitesides, G. M.; Grzybowski, B. *Science* **2002**, *295*, 2418–2421.
14. Ercolani, G. *J. Phys. Chem. B* **1998**, *102*, 5699–5703.
15. Israelachvili, J. N. *Intermolecular and Surface Forces*; Academic Press: London, 1991; pp 291–294.
16. Riess, G. *Prog. Polym. Sci.* **2003**, *28*, 1107–1170.
17. Atanase, L.-I.; Riess, G. *Polym. Int.* **2011**, *60*, 1563–1573.
18. Golling, F. E.; Schuster, T.; Geidel, C.; Mammen, L.; Vollmer, D.; Müllen, K.; Klapper, M. The Power of Perfluorinated Amphiphilic Polymers at Interfaces. In *Advances in Fluorine-Containing Polymers*; Smith, D. W., Jr., Iacono, S. T., Boday, D. J., Kettwich, S. C., Eds.; ACS Symposium Series 1106; American Chemical Society: Washington, DC, 2012; pp 111–126.
19. Ryu, J.-H.; Hong, D.-J.; Lee, M. *Chem. Commun.* **2008**, 1043–1054.
20. Schmidt-Mende, L.; Fechtenkötter, A.; Müllen, K.; Moons, E.; Friend, R. H.; MacKenzie, J. D. *Science* **2001**, *293*, 1119–1122.
21. Jianqi, F.; Lixia, G. *Eur. Polym. J.* **2002**, *38*, 1653–1658.
22. Onoe, H.; Gojo, R.; Kuribayashi-Shigetomi, K.; Takeuchi, S. In *25th IEEE International Conference on Microelectro Mechanical Systems (MEMS)*, January 29–February 2, 2012, Paris France, pp 1065–1068.
23. Hsieh, A.; Zahir, T.; Lapitsky, Y.; Amsden, B.; Wan, W.; Shoichet, M. S. *Soft Matter* **2010**, *6*, 2227–2237.
24. Kamps, A. C.; Fryd, M.; Park, S.-J. *ACS Nano* **2012**, *6*, 2844–2852.

25. Ryu, J.-H.; Hong, D.-J.; Lee, D.-J. *Chem. Commun.* **2008**, 1043–1054.
26. Wunderlich, K.; Larsen, A.; Marakis, G.; Fytas, G.; Klapper, M.; Müllen, K. *Small* **2014**accepted.
27. Wunderlich, K. Ph.D. Thesis, Max Planck Institute for Polymer Research, Mainz, Germany, 2013.
28. Jiménez-García, L.; Kaltbeitzel, A.; Pisula, W.; Gutmann, J. S.; Klapper, M.; Müllen, K. *Angew. Chem., Int. Ed.* **2009**, *48*, 9951.
29. Hudson, S. D.; Jung, H.-T.; Percec, V.; Cho, W.-D.; Johansson, G.; Ungar, G.; Balagurusami, V. S. K. *Science* **1997**, *278*, 449–452.
30. Fei, J.; Zhang, Z.; Zhong, L.; Gu, L. *J. Appl. Polym. Sci.* **2002**, *85*, 2423–2430.
31. Wang, H.; You, W.; Jiang, P.; Yu, L.; Wang, H. H. *Chem.–Eur. J.* **2004**, *10*, 986–993.
32. Hudson, S. D.; Jung, H.-T.; Percec, V.; Cho, W.-D.; Johansson, G.; Ungar, G.; Balagurusami, V. S. K. *Science* **1997**, *278*, 449–452.
33. Hill, J. P.; Jin, W.; Kosaka, A.; Fukushima, T.; Ichihara, H.; Shimomura, T.; Ito, K.; Hashizume, T.; Ishii, N.; Aida, T. *Science* **2004**, *304*, 1481–1483.
34. Baram, J.; Shirman, E.; Ben-Shitrit, N.; Ustinov, A.; Weissman, H.; Pinkas, I.; Wolf, S. G.; Rybtchinski, B. *J. Am. Chem. Soc.* **2008**, *130*, 14966–14967.
35. Nikolic, M. K.; Olsson, C.; Salcher, A.; Kornowski, A.; Rank, A.; Schubert, R.; Frömsdorf, A.; Weller, H.; Förster, S. *Angew. Chem.* **2009**, *48*, 2752–2754.
36. Lvov, Y.; Decher, G.; Möhwald, H. *Langmuir* **1993**, *9*, 481–486.
37. Novoselov, K. S.; Jiang, D.; Schedin, F.; Booth, T. J.; Khotkevich, V. V.; Morozov, S. V.; Geim, A. K. *Proc. Natl. Acad. Sci. U.S.A.* **2005**, *102*, 10451–10453.
38. Eck, W.; Küller, A.; Grunze, M.; Völkel, B.; Götzhäuser, A. *Adv. Mat.* **2005**, *17*, 2583–2587.
39. Nottbohm, C. T.; Beyer, A.; Sologubenko, A. S.; Ennen, I.; Hütten, A.; Rösner, H.; Eck, W.; Mayer, J.; Götzhäuser, A. *Ultramicroscopy* **2008**, *108*, 885–892.
40. Turchanin, A.; Beyer, A.; Nottbohm, C. T.; Zhang, X.; Stosch, R.; Sologubenko, A.; Mayer, J.; Hinze, P.; Weimann, T.; Götzhäuser, A. *Adv. Mater.* **2009**, *21*, 1233–1237.
41. Rhinow, D.; Weber, N.-E.; Turchanin, A. *J. Phys. Chem. C* **2012**, *116*, 12295–12303.
42. Turchanin, A.; Weber, D.; Büenefeld, M.; Kisielowski, C.; Fistul, M. V.; Efetov, K. B.; Weimann, T.; Stosch, R.; Mayer, J.; Götzhäuser, A. *ACS Nano* **2011**, *5*, 3896–3904.
43. Angelova, P.; Vieker, H.; Weber, N.-E.; Matei, D.; Reimer, O.; Meier, I.; Kurasch, S.; Biskupek, J.; Lorbach, D.; Wunderlich, K.; Chen, L.; Terfort, A.; Klapper, M.; Müllen, K.; Kaiser, U.; Götzhäuser, A.; Turchanin, A. *ACS Nano* **2013**, *7*, 6489–6497.
44. Wang, E. N.; Karnik, R. *Nat. Nanotechnol.* **2012**, *7*, 552–554.
45. Yang, S.; Bachman, R. E.; Feng, X.; Müllen, K. *Acc. Chem. Res.* **2013**, *46*, 116–128.

Chapter 2

Poly(ionic liquid)-Derived Functional-Shaped Carbon Nanomaterials

Yan Yang and Jiayin Yuan*

Department of Colloid Chemistry,
Max Planck Institute of Colloids and Interfaces,
Potsdam, Germany 14476

*E-mail: Jiayin.Yuan@mpikg.mpg.de

Poly(ionic liquid)s or polymerized ionic liquids (PILs) are a class of polyelectrolytes that are composed of a polymeric backbone and repeating ionic liquid (IL) species. Combining the native properties of polymer and that of ILs, PILs have shown many advantages, such as negligible vapor pressure, high thermostability, ease of shaping and processing and heteroatoms doping. These features allow for easy access to carbon materials with smart-designed nanostructures, fine-shaped morphologies and well-controlled compositions. In this chapter, PIL-derived carbons, including hollow carbon spheres, nanoparticles, thin films and nanofibers, nanotubes and monolith were presented as examples. Meanwhile, these versatile carbons exhibited interesting applications, for example, as fire-retardant materials, adsorbents, stabilizers for carbon materials (carbon nanotubes) and supports for metal NPs. It is worth noting that, the nitrogen-doped carbon materials act as good support and stabilizer for metal NPs simultaneously, thus can generate fine and well-dispersed metal NPs in their matrix, which in turn show good catalytic activity in some reactions.

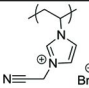
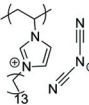
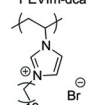
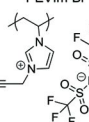
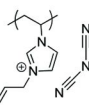
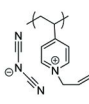
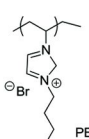
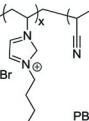
1. Introduction

PILs refer to a class of polyelectrolytes that have a polymeric backbone and repeating ionic liquid (IL) species along it. Compared to conventional polyelectrolytes, PILs exhibited adaptive solubility in organic solvents and a wider window of glass transition temperature, which expanded the potential application area of polyelectrolytes. Unlike ILs, the polymer nature endows PILs new properties, for example, they can be readily shaped and processed *via* some classical methods, such as spin-coating, electrospinning, wet spinning, extrusion, embossing, and so on. These features allow for easy access to carbon materials with well-designed nanostructures and fine-shaped morphologies, including spheres, nanoparticles, thin films, nanofibers, nanotubes and monolith which are of huge importance in material science.

PILs have shown broad applications in several fields, such as polymer electrolytes, liquid-crystal nanostructures, electrochemical devices, stimuli-responsive materials and precursors of carbon materials. Research on PILs is highly topical, and there are some good reviews available describing the nature and applications of PILs (1–5). In this chapter, we only focused on PILs as carbon precursors and the related applications of the derived carbon nanomaterials.

The requirements of the chemical structure for ILs as effective carbon precursors have been reviewed recently (6, 7). Similar requirements can also be applied to PILs. Table 1 summarizes the carbon yield and nitrogen content of the carbon materials produced from various PILs. Similar to ILs, PILs bearing nitrile or cyano groups generally produce N-doped carbons with higher yield than the ones without these groups. The cyano groups can be easily incorporated into PILs via anion exchange, such as dicyanamide (dca), tricyanomethinide (tcm) and tetracyanoborate (tcb). These condensable anions can couple different cations, such as pyridinium, pyrrolidonium, or imidazolium derivatives, to generate N-doped carbon in high yield. Alternatively, cyano-functionalities can be present in the cation, for example 1-cyanomethyl-3-methyl-imidazolium (MCNIM) or 1,3-bis(cyanomethyl)-imidazolium (BCNIM) in combination with classical anions, such as halides or bis(trifluoromethylsulfonyl)imide (Tf_2N). It is not surprising to find that the PIL, poly(1-cyanomethyl-3-vinylimidazolium bis(trifluoromethane sulfonyl) imide), (PCMVIm- Tf_2N), which contains a cyano group in the cation backbone gives a high carbon yield of 20 wt% at 1000 °C under an inert gas atmosphere (11). The yield is 6.7 times of that of PEVIm-Br (10). When carbonizing a copolymer (PB_xA_y) of acrylonitrile and 1-butyl-3-vinylimidazolium bromide, the carbon yield and nitrogen content increase linearly with the content of cyano groups (13). The carbon yield and nitrogen content is up to 54.8 wt% and 15.3 wt% for $\text{PB}_{1.5}\text{A}_{12}$ at 800°C, further proving the strong influence of the cyano group on the carbon yield and nitrogen content.

Table 1. Carbon yield and nitrogen content in carbons produced from different PILs as carbon precursors

Chemical Structure	Carbonization Temperature (°C)	Carbon Yield (wt%)	Nitrogen Content (wt%)	Reference
 <p>PCMVIm-Br</p>	900	n.d.	12	8, 9
 <p>PEVIm-dca</p>	1000	13	4.5	10
 <p>PEVIm-Br</p>	1000	3	n.d.	10
 <p>PCMVIm-Tf₂N</p>	1000	20	7.4	11
 <p>PAVIm-dca</p>	1000	n.d.	6.3	12
 <p>PAVP-dca</p>	1000	n.d.	8.0	12
 <p>PB</p>	800	5.8	8.27	13
 <p>PB_xA_y</p>	800	x=1, y=1, 26.3 x=1, y=4, 41.0 x=1, y=12, 54.8	x=1, y=1, 9.2 x=1, y=4, 11.5 x=1, y=12, 15.3	13

2. Carbon Nanomaterials with Variable Morphologies and Structures

PILs have showed several advantages in acting as carbon precursors. First of all, due to their polyelectrolytic nature, they exhibit no vapor pressure. This feature shows advantages in minimizing the mass loss of the precursor during carbonization process and simplifying the processing procedure at the same time. Secondly, the fluid state at certain temperature facilitates the easy incorporation of PILs into porous templates. Thirdly, they can act like “universal” surface-active molecules, because there are favorable interactions existing between PILs and the polar surfaces of inorganic materials, such as silica or alumina. That means, *via* a judicious choice of the backbone, anion and cation, they are able to form very homogeneous coatings or layers on most of the surfaces. Thus, carbon nanomaterials with well-designed shapes and porous structures can be easily prepared, such as hollow spheres, nanofibers, nanotubes, membranes and monolith. Fourthly, PILs, especially the imidazolium-type ones, contain tightly incorporated/conjugated heteroatoms, such as nitrogen, sulphur, boron, or phosphorus atoms in their molecular structures, thus inevitably yielding heteroatoms in the final carbon structures. Many reports have proven that some properties of carbon can be modified and enhanced through adjusting the respective nitrogen content, for example, the electrical conductivity, basicity, oxidation stability and catalytic activity.

The first example of using PILs as carbon precursor was demonstrated in 2009, in which highly graphitic, mesoporous, and conductive carbon nanostructures were produced by the pyrolysis of IL monomers or PILs (900 °C) under nitrogen in the presence of metal salts (14). With the assistance of the catalytic effect of the metal salts, the obtained carbon was highly porous and graphitic, meanwhile this synthetic route is template-free. A disadvantage of involving metal salt was the loss of all nitrogen atoms in the final carbon products. Considering that nitrogen content is very essential for enhanced electronic conductivity and catalytic activity, in recent research more attempts were focused on carbonization processes without metal or metal salts. In addition, to fully utilize the advantages of the polymeric nature, PILs were processed into various morphologies, which can in turn be converted into carbons of well designed shapes and structures.

2.1. Hollow Carbon Spheres

Hollow carbon spheres (HCSs) are unique carbon architectures that possess a high surface-to-volume ratio, high thermal and chemical stability, low apparent density, and a low percolation threshold. Some groups take them as “processable pores”. The versatile preparation and applications of HCSs have been widely investigated. Here, we only focused on HCS derived from PILs

The first report of using PILs as a carbon precursor for the fabrication of HCSs was published in 2011 by Guo *et al.* (15) They used commercially available SiO₂ particles as templates, whose surface was coated with a uniform layer of PILs upon *in situ* polymerization to form a core@shell structure. Subsequent carbonization and template removal generated HCSs. The HCSs possess good conductivity, high

surface area and porosity. All these features made it good candidate for acting as support for metal nanoparticle catalysts. Pt nanoparticles were prepared as an example. An average size of 2.8 nm of Pt nanoparticles was obtained, the small sizes and high dispersity of Pt nanoparticles mostly were caused by this unique structure, high surface area and porosity of the HCSs. The obtained Pt/HCS hybrids exhibited a significant catalytic activity in the oxidation of methanol.

In another example, the preparation of nitrogen-doped HCSs from PILs was fabricated similarly (8). Uniform and mono-dispersed SiO_2 spheres with different sizes made from Stöber method were chosen as templates. The PIL coating was achieved by one-step free-radical precipitation polymerization of the IL monomer in ethanol, in the presence of silica colloidal templates. Due to the insolubility of the PILs in ethanol and its attractive interaction with silica surfaces, it preferentially deposited onto the silica surface homogeneously. This thin layer was found to be able to hold its shape during the carbonization under high temperature (900 °C). After removing silica, HCSs with a homogeneous 5 nm-thin shell were obtained (Figure 1). Iron oxide nanoparticles could be further introduced into HCSs *via* post-carbonization deposition. This synthetic route further proved the excellent wetting properties of PILs on solid substrates.

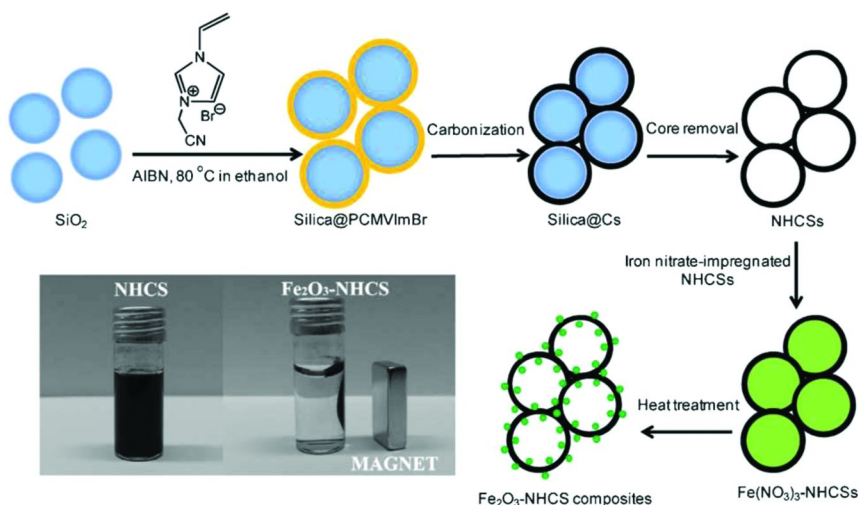


Figure 1. Schematic illustration of the formation of HCSs based on the polymerization of an IL monomer 3-cyanomethyl-1-vinylimidazolium bromide onto silica particle templates, and the further preparation of Fe_2O_3 -HCS composites via impregnation-thermal decomposition of iron nitrate. Reprinted with permission. Copyright 2013, Wiley-VCH (8).

Taking advantage of the polyelectrolytic nature, PILs can be fabricated by common methods. The layer-by-layer (LbL) technique is a well-known method for making coatings or films from oppositely charged polyelectrolytes or colloids. This technique provides an alternative approach to engineer silica particle surfaces with PIL coatings. A cationic PIL poly(3-cyanomethyl-1-vinylimidazolium bromide) and anionic poly(ammonium acrylate) were chosen for demonstration (9). During the carbonization process, the PIL fraction in the LbL layer mainly served as carbon precursor, because the poly(ammonium acrylate) underwent decarboxylation and fragmentation at high temperature. Carbon hollow spheres with variable sizes from 200 to 600 nm were prepared through this approach from differently sized silica particles. Both samples gave nitrogen content of 7.2 wt% and a satisfactory specific surface area of ca. 400 m²/g.

Ultra-Small HCSs (25–90 nm) with high conductivity and a distinctive atomic graphitic order were obtained by a silica nanocasting method (10). The obtained HCSs showed variable nitrogen doping amount and superior dispersability in water. This superior aqueous dispersability was mostly caused by the confinement effect of silica during the carbonization process.

The synthesis started with PIL nanoparticles, which act as sacrificial templates, carbon precursor and nitrogen source at the same time. The PIL nanoparticles were buried in bulk silica by adding silica precursor (TMOS or TEOS) into the aqueous nanoparticle dispersion dropwisely. The mass ratio of silica precursor/PIL nanoparticle was carefully chosen to satisfy a true confinement of each PIL nanoparticle into a chemically inert silica environment. Pyrolysis of the PIL/silica hybrid at 1000 °C under N₂ atmosphere converts the PIL nanoparticles into HCSs. After etching away silica, the carbon products were liberated into aqueous solution. Due to the confinement effect of silica, enhanced carbonization yields were observed for all samples (up to 30%), which is more than twice the value of a non-confined carbonization process (13%).

Another interesting point of this ultra-small HCSs is, the distinctive atomic graphitic order of the shell. High resolution transmission electron microscopy (HR-TEM) characterization was conducted to reveal details of the graphitic structure on the shell. Unlike the disordered graphitic planes of nitrogen-doped bulk carbon derived from ILs reported previously, here the crystalline phase could develop in an ultrathin circular shell of 5–10 nm. Figure 2 depicts the HR-TEM images of the edge and central views of a single nanosphere. The unique layered pattern stemming from the stacking of only slightly distorted graphene sheets was observed, perpendicular to the surface of the HCSs.

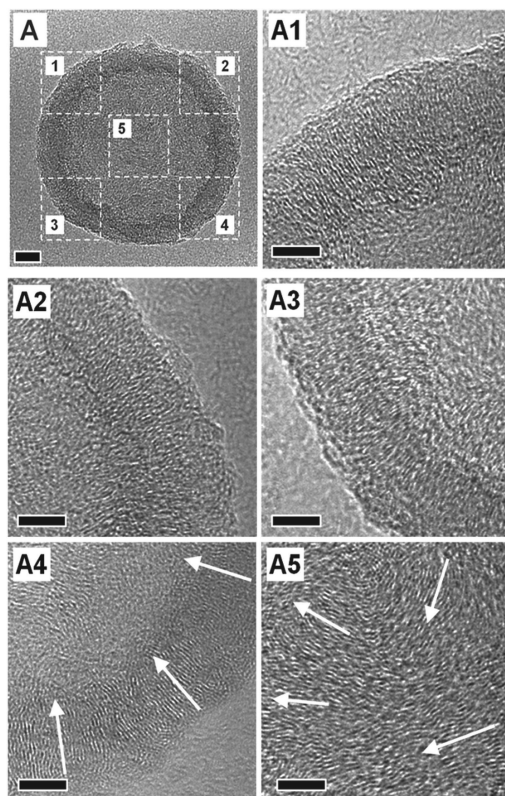


Figure 2. (A) A TEM image of a single HCS. (A1)–(A5) The HRTEM images of the selected parts in A. The white arrows indicate the planar direction of the stacked graphenes. The scale bar in (A) is 10 nm and in the rest is 5 nm. Reprinted with permission. Copyright 2013, Wiley-VCH (10).

2.2. Carbon Nanoparticles

Zhang *et al.* reported the synthesis of porous carbon nanoparticles through a hydrothermal carbonization (HTC) method (160–200 °C), using inexpensive, harmless and naturally available sugars as carbon source and PIL as additive (16). PIL was used to incorporate nitrogen atoms and minimize the particle size from 2.3 μm down to < 50 nm. In addition, PILs further improved the porous structure of the final materials in the post-HTC carbonization step. The porous carbon nanoparticles showed high surface area (S_{BET} up to 572 $\text{m}^2 \text{g}^{-1}$). The synthesis procedure is displayed in Figure 3. Here, the PIL chains act as a stabilizer for the primary nanoparticles formed by condensation/polymerization reactions of 5-hydroxymethyl furfural (dehydrated from fructose). The charged nature of the PILs introduces electrostatic repulsion to keep the primary nanoparticles stable in solution and minimize their further agglomeration. The porosity of the obtained carbon nanomaterials was further improved by post-synthesis carbonization processes.

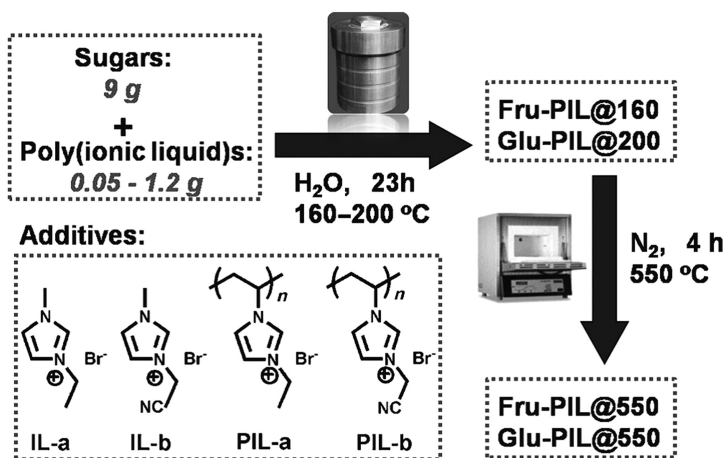


Figure 3. Synthetic route to porous nitrogen-doped carbon nanostructures by a HTC-PIL protocol. Reprinted with permission. Copyright 2013, Wiley-VCH (16).

2.3. Nanotube

The preparation of porous carbon nanotubes was conducted using anodic aluminum oxide (AAO) membranes (200 nm in channel size) as templates (11). The inner channel of AAO was filled with a poly[3-cyanomethyl-1-vinylimidazolium bis(trifluoromethanesulfonyl)imide] (PCMVI_mTf₂N) solution (10 wt%) in DMF. As PILs are surface active materials, as demonstrated recently by Texter *et al.*, they formed a thin coating on the inner wall surface (17). The thickness is in fact tunable via the polymer concentration. The PIL layer on the AAO wall was then converted to carbon nanotubes *via* carbonization process, and further characterized by TEM and scanning electron microscopy (SEM). Carbon nanotubes with micrometer in length, 200 nm in width and 5 nm in wall thickness were obtained. Their tubular shape and sizes were in coincidence with the AAO channels, thus indicating a good shape and structure replication from the AAO template. Interestingly, the tubes self-stabilize themselves by the formation of periodic cross-layers, which of course is not part of the original template. The specific surface area of these tubes was measured to be 400 m² g⁻¹. The pore size distribution curve derived from the nitrogen sorption isotherms proves the existence of rich micropores co-existing with mesopores.

2.4. Nanofiber and Film

To illustrate the feasibility of designing carbon materials with variable shapes from PILs, carbon nanofibers and films were further developed. Being polymer in nature, it is easy to find out ways to fabricate fibers and films, for example, electrospinning and spin-coating technique.

Electrospinning is a powerful way to shape polymers into nanofibers, this is a widely accepted approach in both academic research and industrial production. The general way to synthesize nitrogen-doped carbon nanofibers and films

via electrospinning is as follows: vinylimidazolium or vinylpyridinium-type PILs with an allyl functionality and a dicyanamide anion were prepared via quaternization of pre-synthesized poly(1-vinylimidazole) or commercially available poly(4-vinylpyridine) (12). The as-synthesized PIL polymers were mixed with a trithiol crosslinker molecule and a radical initiator, and electrospun into fibers and mats. The fibers were first radically crosslinked and then carbonized at 1000 °C. From the SEM image investigation, the carbon fibers were ca. 0.2 to 2 μm in diameter with a satisfactory conductivity of 200 S/cm. It is worth noting that, the same strategy obviously cannot be applied for ILs, because they cannot preserve a preformed morphology due to their uncrosslinked liquid nature.

In the case of generating porous carbon films with variable thicknesses, spin-coating is an ideal way. Zhao *et al.* reported the fabrication of carbon films with tunable thickness from 50 nm to 100 μm through spin-coating method (11). First of all, a PCMVImTf₂N solution in acetonitrile (0.5–2wt%) was prepared. KBr disks were utilized as substrate due to their insolubility in acetonitrile (≤ 0.02 wt%) and high thermal stability (a solid form up to 734 °C). In addition, it is easily removable by water. The spincoating was performed under different polymer concentration or spin speed to obtain films with variable thickness. Then the spin-coated KBr disks were carbonized at 600 °C. The carbonization yield is typically around 30 wt% for PILs at this processing temperature. After removing the KBr disk in water, a freestanding carbon film with different thicknesses were achieved. Carbonized PIL thin film (ca. 50 nm) prepared on the KBr disk was obtained under a low PIL concentration. The film is homogeneous and planar in a large scale. Pleats are observed when the films were very thin and flexible. It is worth noting that these carbon films were doped by nitrogen and rich of micro/mesopores in its structure (generating from a crosslinkable nitrile group in the imidazolium cation and a rather bulky anion in parallel), all these features made it very special and possessing great application potential.

2.5. Monolith

Besides carbon spheres, nanoparticles, nanotubes, nanofibers and films, another important morphology is monolith with well-defined shape and complex porosity. Men *et al.* reported a facile method for generating carbon monolith from biomass by lowering the activation temperature of bio(macro)molecules through PIL coating (18). The synthetic route is very simple and only a low-fraction of PILs is needed. Dried cotton was immersed in a PIL solution in acetonitrile (10 wt%) for 5 min. The wet cotton was then shaped into different morphology, and dried at 80 °C until constant weight. The carbonization was conducted at 400 °C, quite low compared to normal activation process (normally above 600 °C). This process is easy in operation, cheap in raw materials and quick in time consuming, all these advantages make it possible for large-scale production.

The obtained carbon monolith can still preserve its natural shape, high porosity and good mechanical performance. Carbonizing the PIL/cotton composites in its original form produces an irregularly shaped fluffy foam that can be conveniently cut into any well-defined geometry, such as a cuboid

geometry shown in Figure 4. The carbonaceous cuboid foam is also sponge-like and deformable like cotton itself. In a mechanical test shown in Figure 4D-F, it recovers itself readily after being compressed by 2000 times of its own weight.

Besides the sponge-like mechanical behavior, these cotton products are highly porous and deformable, and can be engineered into various shapes. Carbonaceous cylindrical monolith (Figure 4C) can be generated by densely pressing the coated cotton precursor into a tube.

It is interesting that essentially no changes in the microtexture were found in the interior microscopic texture of the cellulose throughout pyrolysis. Therefore, this low temperature carbonization process retains the morphology well, both macro- and microscopically. What is more surprising is, even at low PIL content (7 wt%), the carbonization process can still be efficiently promoted, generating large amount of micropores while maintaining the skeleton of the biotemplates.

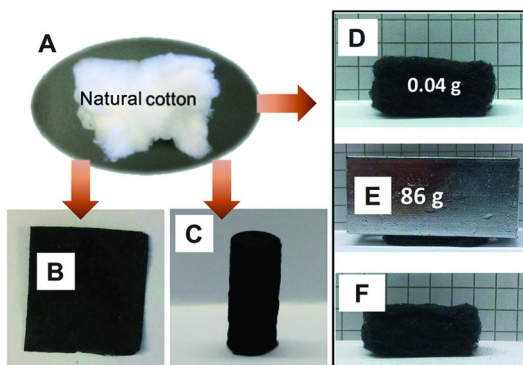


Figure 4. Photographs of (A) natural cotton, (B) carbonaceous thin film derived from a PIL/cotton composite film, (C) carbonaceous monolith derived from a PIL/cotton composite cylinder, and (D) cut carbonaceous cuboid from a carbonized PIL/cotton composite. (E and F) A shape retention test on the composite. Reprinted with permission. Copyright 2013, RSC (18).

3. Carbon Materials with Variable Chemical Compositions

3.1. Heteroatoms-Doped Carbon

The incorporation of heteroatoms is an effective way for the further functionalization of carbon materials. Variable heteroatoms have been incorporated into carbon materials, such as B, N, O, P, and S. The resulted carbon materials showed enhanced properties in electrochemical energy storage and as catalyst support. It is easy to find that all the PIL carbon precursors contain nitrogen (or boron/sulfur/phosphor) atoms in their backbone structure or as counter anions, which inevitably yields nitrogen (or boron/sulfur/phosphor) heteroatoms in the final carbon frameworks. Many of these PILs are rich in sp^2 hybridized N atoms, up to 50 wt%, which in turn can give high N doping under an appropriate condition. The nitrogen content is generally reduced with increasing carbonization temperature (11). At 800 °C, the nitrogen content is still as high as

18 wt%. However, at 1000 °C the nitrogen content has decreased to about 7-10 wt%. In spite of this, the carbon in this case is highly graphitized, possessing a metallic luster.

The nature of the nitrogens bound to the carbon structures can be analysed by X-ray photoelectron spectroscopy (XPS). Detailed studies indicated that, nitrogen atoms in PIL-derived carbons are predominantly bonded in pyridinic or quaternary-graphitic environments, thus as structural nitrogens incorporated into the graphitic microdomains. According to the intensity of the deconvoluted contributions from the XPS spectra, quaternary-graphitic nitrogen is the dominant species in most cases. Higher amounts of pyridinic species are found when high-surface-area carbons are created, which, in fact, could favor the formation of pyridinic carbon in plane termini.

In some cases, the nitrogen distribution in the carbon nanomaterials is homogeneous, which have been proved by STEM-based electron energy loss spectroscopy (EELS) (8). The EEL spectra intensity of the nitrogen K-edge cross the carbon shell indicates a homogeneous nitrogen distribution within the hollow carbon spheres along the scanning profile.

3.2. Metal NPs

Nitrogen is the most common impurity (donor) that can be found in carbon materials. Nitrogen atoms inserted in the carbon frameworks worked as electron donors, and can significantly reduce the work function of nitrogen-doped carbon materials, which in turn changed the position of the valence band or conduction band of the carbon materials, normally making the material more metallic. DFT studies reveal that carbon substrates containing moderate to high N-doping levels in the form of C–N defects and N interstitials can serve as local heterogeneous Pt nucleation sites. For instance, Lei *et al.* have obtained very uniform dispersion of Pt nanoparticles on nitrogen-doped carbon support, which is mostly due to the strong interaction between nitrogen atoms and Pt nanoparticles (19). Thus, nitrogen-doped carbon materials are considered as good candidate to support and stabilize metal NPs simultaneously. This is proved by a recent example. An IL monomer, 1-butyl-3-vinylimidazolium bromide ([Bvim][Br]), was copolymerized with acrylonitrile to produce poly([Bvim][Br]-co-acrylonitrile) (13). The Br anion of the as-synthesized PIL copolymer was exchanged with a Pt precursor anion PtCl_6^{2-} . This process led to a homogeneous distribution of the PtCl_6^{2-} anion throughout the copolymer matrix. After carbonization, nitrogen-doped carbons with well-dispersed Pt nanoparticles in very high loading amount were obtained. This hybrid material showed a high catalytic activity and stability in the electrocatalytic oxidation of methanol. The carbon yield, nitrogen content and nanostructure of the carbon materials were controllable in terms of the IL monomer content in the copolymer.

Metal NPs with more sophisticated nanostructure (supported on nitrogen-doped carbon materials) can also be obtained through similar one-pot method. The PIL-improved HTC process, as mentioned above, was further coupled with addition of metal salts before the HTC process to directly produce metal NPs in the nitrogen-doped porous carbon materials. Novel nanohybrids

(S_{BET} up to $255 \text{ m}^2 \text{ g}^{-1}$) with Au–Pd core-shell nanoparticles embedded in nitrogen-doped porous carbon were obtained (16). From the TEM image, the Au–Pd core-shell nanoparticles were well dispersed on the carbon support. As shown in Figure 5, the HRTEM, scanning electron transmission microscopy in high angular dark field mode (STEM-HAADF) and scanning electron transmission microscopy-X-ray energy dispersive spectroscopy (STEMXEDS) mapping analysis were carried out to analyse the structural and elemental information of the metal nanoparticle. All the results proved that the nanoparticle have a core-shell structure with Au as core and Pd as shell.

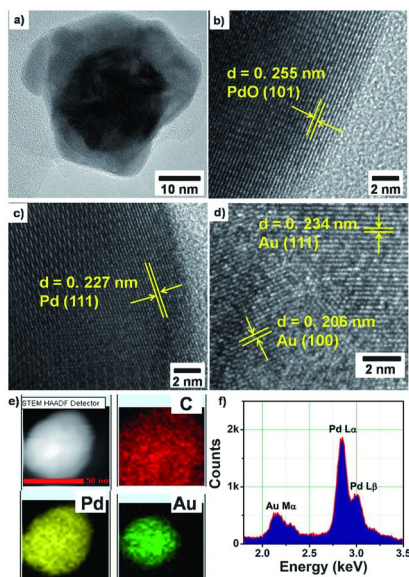


Figure 5. HRTEM images (a–d) of a representative Au–Pd particle embedded in 0.95%Au–1.1%Pd@N-Carbon. (e) A representative STEM-HAADF image of a Au–Pd particle in 0.95%Au–1.1%Pd@N-Carbon, and the corresponding STEM-XEDX maps of the C-K α , Pd-La, Au-La signals. Scale bar: 50 nm. (f) The corresponding STEM-EDX point spectra. Reprinted with permission. Copyright 2013, Wiley-VCH (16).

4. Potential Applications of Carbon Nanomaterials Derived from PILs

4.1. Fire-Retardant Material

Inertness against oxidation by oxygen is another classical feature of N-heterocycles and nitrogen-doped carbons. Men *et al.* reported the fire retardancy of nitrogen-doped carbon foams generated through a PIL-assisted low temperature carbonization/activation process of natural cotton (18). The carbon foams prepared at $400 \text{ }^\circ\text{C}$ from cotton with/without PILs, respectively,

were wetted with 500 wt% of ethanol, and burnt in air (Figure 6A). This test was repeated 4 times. The shape and mass change was monitored after each cycle. As observed, the carbon foam derived from pure cotton collapsed after the 1st cycle of burning, while the PIL/cotton carbon remained intact. The mass vs. firing cycle plot (Figure 6B) indicates that the 1st firing cycle burnt away 80.3 wt% of the cotton-based carbon product, while only 4.1 wt% of mass loss occurred for the cotton/PIL carbon foam. Within 3 cycles, only the cotton/PIL carbon foam preserved its shape and 85 wt% of its mass. Under even harsh conditions, when repeatedly exposed shortly to the flame of a butane/propane (70 : 30) gas burner, the foam maintained its shape and size well (Figure 6C). In a real-time video, it is observed that the foam bottom could be turned to a red blaze in the central flame (1300 °C), but quenched immediately when pulled out. This illustrates that the material is robust against co-firing, a really exceptional property for high surface area carbons.

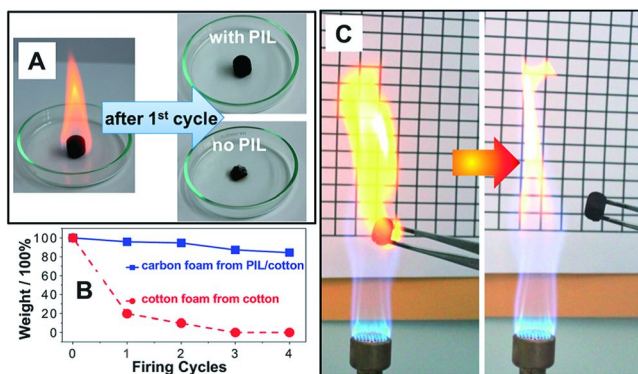


Figure 6. (A) Photographs of the 1st firing cycle test of the carbon foams (absorb 500 wt% of ethanol and burn in air). Left: a burning ethanol-wetted foam. Right: foams after the 1st firing cycle test. (B) Plot of the carbon foam mass vs. the firing cycle. (C) Photographs illustrating the fire-retardancy of a carbonaceous foam by repeatedly firing the sample using a butane/propane gas burner. Reprinted with permission. Copyright 2013, RSC (18).

4.2. Stabilizer

In 2013, our group reported the synthesis of nitrogen-doped carbon hollow nanospheres (named “nanobubbles”, denoted as CNB) through a confined silica nanocasting method. These CNBs have highly distinctive graphitic order, conductivity, variable nitrogen content and controlled sizes (25–90 nm) (20). An interesting property of these highly graphitic carbon nanobubbles is its superior dispersability in neutral water, which was mostly due to its spontaneous charge transfer and hydroxylate adsorption ability. In a recent study, the CNBs were found to be able to disperse CNTs in aqueous solution, as illustrated in Figure 7. This process relies on the π - π interaction between the relatively electron-poor

CNBs and the electron-rich CNTs. This process was easy and simple which can be processed in water with the assistance of sonication. Conductive filter membranes, and purely carbon-based ink and discs can also be fabricated through the same way without any other additives.

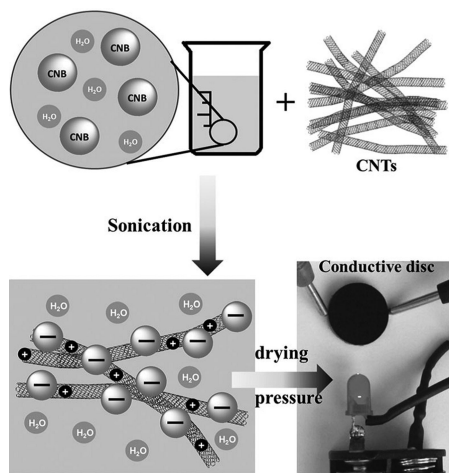


Figure 7. Stabilization of carbon nanotubes (CNTs) by water-dispersible carbon nanobubbles (CNBs) in the aqueous phase, and the preparation of the CNT/CNB composite conductive disc. Reprinted with permission. Copyright 2014, Wiley-VCH (20).

4.3. Adsorbent

The porous carbonaceous sponge derived from the cotton/PIL pad can absorb methylene blue dye molecules from aqueous solution quickly (18). This is a unique property of such hierarchical porous carbon structures, in which the macropores formed by the entanglement of the carbon fibers accelerates the liquid diffusion and the micropores in the carbon fibers effectively store the dye molecules. As shown in Figure 8, colorless water was released by squeezing it. In another example, an aqueous solution of methylene blue was decolorized after passing through a short column filled with the carbon sponge, which further demonstrates the efficient removal of organic dyes from the aqueous solution. The PILs added to the cotton played an important role in accelerating the absorption kinetics of organic dyes. In a control experiment of absorbing crystal violet from aqueous solution, the porous carbon foam derived from cotton/PIL (Figure 8F) presented a much faster kinetics in the dye sorption than the porous carbon foam derived from pure cotton (Figure 8E).

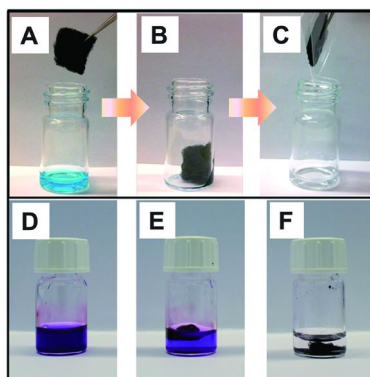


Figure 8. (A–C) Photographs illustrating the sorption of methylene blue dye from aqueous solution by a carbonaceous foam derived from the PIL/cotton composite. (D–F) Photographs of the initial aqueous solution of crystal violet (D), 5 min after treatment by pure cotton-based carbon foam (E), and 5 min after treatment by a cotton/PIL-based carbon foam (F). Reprinted with permission. Copyright 2013, RSC (18).

4.4. Catalysis

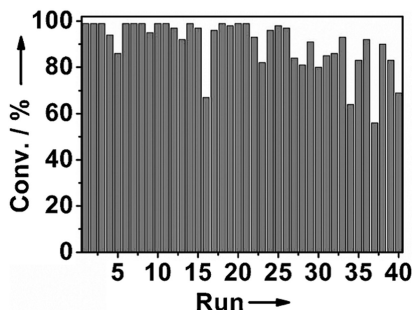


Figure 9. The reusing tests of the core-shell Au-Pt nanoparticle-doped nitrogen doped carbon (0.95%Au–1.1%Pd@N-Carbon) in the phenylacetylene hydrogenation. Reprinted with permission. Copyright 2013, Wiley-VCH (16).

The Au–Pd core-shell nanoparticles trapped in nitrogen-doped carbon materials, could serve as active and highly stable (reused forty times) catalysts for the selective semihydrogenation of phenylacetylene under mild reaction conditions (80 °C, H₂ 1 atm) (16). Due to its heterogeneous nature, the catalysts can be easily recycled by centrifugation. After careful washing with ethanol, the catalysts can be used directly for next recyclability tests. The activity of the recovered catalyst was fully retained in the first thirty runs (Figure 9). From the 31st to 40th run, a longer reaction time was needed to keep the phenylacetylene conversion above 80%. The gradually decrease in catalytic activity mainly attributed to the loss of catalyst during the recovery process, as only 46 wt%

of the initial catalyst was recovered after forty runs. The metal content of the recovered catalyst was investigated by ICP–AES, and the calculated leaching rate per run is rather low (<1%).

5. Summary and Outlook

PILs as carbon precursor are a new but increasingly growing topic, on which significant development and achievement have been obtained in the last five years. The interest in applying PILs as carbon precursors lies in the unique structural properties and functions of PILs, such as negligible vapor pressure, high thermostability, “universal” affinity towards variable surfaces and heteroatoms doping ability. The former three make it ease of shaping and processing, thus carbon nanomaterials with different morphologies were obtained. The heteroatoms doping ability is a very simple and efficient way to adjust the electrical conductivity, basicity, oxidation stability and catalytic activity of the carbon materials. In this chapter, PIL-derived carbon materials with different shapes including spheres, nanoparticles, nanofibers and films, nanotubes and monoliths were presented, and their compositions and applications were also illustrated.

A variety of applications for nitrogen-doped nanocarbons have been reported in literature. In this chapter, we presented that nitrogen-doped carbons derived from PILs can serve as fire-retardant materials, adsorbents, stabilizers for carbon materials (carbon nanotubes) and supports for metal NPs. The nitrogen-doped carbon materials are good support and stabilizer for metal NPs simultaneously, thus can generate fine and well-dispersed metal NPs in their matrix, which in turn show good catalytic activity in electrocatalysis and traditional catalysis.

In spite of the rapid progress, there is a lot to be tested in the future. So far developed carbon materials are based on simple models with normal shapes and structures. More sophisticated carbon nanostructures with unique properties are worth trying, such as double shell, core-shell and yolk-shell nanostructure. At the same time, the heteroatoms doping is mostly performed to N and S. PIL-derived carbon materials with dual- or multi-doping elements are highly interesting, which seems easily accessible through the PIL route.

References

1. Yuan, J.; Mecerreyes, D.; Antonietti, M. Poly(ionic liquid)s: An update. *Prog. Polym. Sci.* **2013**, *38*, 1009–1036.
2. Mecerreyes, D. Polymeric ionic liquids: Broadening the properties and applications of polyelectrolytes. *Prog. Polym. Sci.* **2011**, *36*, 1629–1648.
3. Lu, J.; Yan, F.; Texter, J. Advanced applications of ionic liquids in polymer science. *Prog. Polym. Sci.* **2009**, *34*, 431–448.
4. Green, O.; Grubjesic, S.; Lee, S.; Firestone, M. A. The design of polymeric ionic liquids for the preparation of functional materials. *Polym. Rev.* **2009**, *49*, 339–360.

5. Green, M. D.; Long, T. E. Designing imidazole-based ionic liquids and ionic liquid monomers for emerging technologies. *Polym. Rev.* **2009**, *49*, 291–314.
6. Fellingner, T. P.; Thomas, A.; Yuan, J.; Antonietti, M. 25th anniversary article: “Cooking carbon with salt”: Carbon materials and carbonaceous frameworks from ionic liquids and poly(ionic liquid)s. *Adv. Mater.* **2013**, *25*, 5838–5854.
7. Paraknowitsch, J. P.; Thomas, A.; Antonietti, M. A detailed view on the polycondensation of ionic liquid monomers towards nitrogen doped carbon materials. *J. Mater. Chem.* **2010**, *20*, 6746–6758.
8. Balach, J.; Wu, H.; Polzer, F.; Kirmse, H.; Zhao, Q.; Wei, Z.; Yuan, J. Poly(ionic liquid)-derived nitrogen-doped hollow carbon spheres: Synthesis and loading with Fe₂O₃ for high-performance lithium ion batteries. *RSC Adv.* **2013**, *3*, 7979–7986.
9. Zhao, Q.; Fellingner, T.-P.; Antonietti, M.; Yuan, J. Nitrogen-doped carbon capsules via poly(ionic liquid)-based layer-by-layer assembly. *Macromol. Rapid Commun.* **2012**, *33*, 1149–1153.
10. Soll, S.; Fellingner, T.-P.; Wang, X.; Zhao, Q.; Antonietti, M.; Yuan, J. Water dispersible, highly graphitic and nitrogen-doped carbon nanobubbles. *Small* **2013**, *9*, 4135–4141.
11. Zhao, Q.; Fellingner, T.-P.; Antonietti, M.; Yuan, J. A novel polymeric precursor for micro/mesoporous nitrogen-doped carbons. *J. Mater. Chem. A* **2013**, *1*, 5113–5120.
12. Yuan, J.; Marquez, A. G.; Reinacher, J.; Giordano, C.; Janek, J.; Antonietti, M. Nitrogen-doped carbon fibers and membranes by carbonization of electrospun poly(ionic liquid)s. *Polym. Chem.* **2011**, *2*, 1654–1657.
13. Pan, C.; Qiu, L.; Peng, Y.; Yan, F. Facile synthesis of nitrogen-doped carbon-Pt nanoparticle hybrids via carbonization of poly([Bvim][Br]-co-acrylonitrile) for electrocatalytic oxidation of methanol. *J. Mater. Chem.* **2012**, *22*, 13578–13584.
14. Yuan, J.; Giordano, C.; Antonietti, M. Ionic liquid monomers and polymers as precursors of highly conductive, mesoporous, graphitic carbon nanostructures. *Chem. Mater.* **2010**, *22*, 5003–5012.
15. Bo, X.; Bai, J.; Ju, J.; Guo, L. Highly dispersed Pt nanoparticles supported on poly(ionic liquids) derived hollow carbon spheres for methanol oxidation. *J. Power Sources* **2011**, *196*, 8360–8365.
16. Zhang, P.; Yuan, J.; Fellingner, T.-P.; Antonietti, M.; Li, H.; Wang, Y. Improving hydrothermal carbonization by using poly(ionic liquid)s. *Angew. Chem., Int. Ed.* **2013**, *52*, 6028–6032.
17. Ma, X.; Crombez, R.; Ashaduzzaman, M.; Kunitake, M.; Slater, L.; Mourey, T.; Texter, J. Polymer dewetting via stimuli responsive structural relaxation-contact angle analysis. *Chem. Commun.* **2011**, *47*, 10356–10358.
18. Men, Y.; Siebenburger, M.; Qiu, X.; Antonietti, M.; Yuan, J. Low fractions of ionic liquid or poly(ionic liquid) can activate polysaccharide biomass into shaped, flexible and fire-retardant porous carbons. *J. Mater. Chem. A* **2013**, *1*, 11887–11893.

19. Lei, Z.; An, L.; Dang, L.; Zhao, M.; Shi, J.; Bai, S.; Cao, Y. Highly dispersed platinum supported on nitrogen-containing ordered mesoporous carbon for methanol electrochemical oxidation. *Microporous Mesoporous Mater.* **2009**, *119*, 30–38.
20. Kuzmich, D.; Prescher, S.; Polzer, F.; Soll, S.; Seitz, C.; Antonietti, M.; Yuan, J. The colloidal stabilization of carbon with carbon: carbon nanobubbles as both dispersant and glue for carbon nanotubes. *Angew. Chem., Int. Ed.* **2014**, *53*, 1062–1066.

Chapter 3

Structural Control in Block Copolymer-Templated Nanoporous Carbon Films

Bryan D. Vogt,^{*,1} Zhe Qiang,¹ Jiachen Xue,^{1,2}
Guodong Deng,¹ Alamgir Karim,¹ and Kevin A. Cavicchi¹

¹Department of Polymer Engineering, University of Akron,
Akron, Ohio 44325, United States

²Current address: Material Science, Engineering, and Commercialization
Program, Texas State University, San Marcos, Texas 78666, United States

*E-mail: vogt@uakron.edu

Cooperative assembly of block copolymers (BCPs) with carbonizable polymer precursors is a viable route to nanoporous carbon materials with well-defined pore size and morphology. There is a subtle balance in reaction kinetics of the carbonizable precursor and ordering of the BCP that controls the extent and length scale over which the ordered structure persists. The use of low molecular weight precursors such as phenolic resin oligomers (resol) enable processing to further order and orient the ordered domains prior to “locking-in” the structure by thermally crosslinking the carbonizable precursor. Processing with solvent, either by exposure to their vapors or use of low volatility solvents in the casting solution, provides one low temperature route to markedly enhance order, but these nanostructures lack long-range orientation. Directional forces through application of a thermal gradient or shear enable large scale orientation of the nanostructures.

Introduction to Templated Nanoporous Carbons

Mesoporous carbon films and membranes have attracted significant interest (1–4) in recent years due to a variety of advantageous properties, such as chemical inertness, electrical conductivity, and high thermal stability, for a plethora of potential applications including membrane separations (5), sensors (6), electrodes for batteries (7) and supercapacitors (8), and absorbents (9) for purification. One challenge for applications of mesoporous carbons is sufficient control of the structure in terms of pore size, pore geometry and pore connectivity; these properties can be controlled through templating approaches. Since the initial report by Bein and coworkers for carbon filled in the pores of mesoporous silica (10) and the follow-up by Ryoo and coworkers (11) for the subsequent removal of the silica to fabricate mesoporous carbon, this hard templating or nanocasting (12) approach has been a mainstay for the synthesis of well-defined mesoporous carbons (13, 14), but this approach is difficult to translate to thin films (15) or membranes due to challenges associated with the filling of the pores without overfilling. Alternatively, colloidal crystals can act to template the nanopores through filling with carbon precursors to generate inverse opals (16), typically referred to as 3-dimensional ordered macroporous (3-DOM) materials (17). As the 3-DOM pores are templated by silica or polymer spheres, the size of the pores is limited by the synthetic ability to generate small colloids. As such, these are generally macroporous (>50 nm) (18), but recent reports have illustrated the potential to generate mesoporous materials with this method. The morphology of these porous carbons are generally limited to close-packed spherical pore structures, but hierarchical structures can be obtained by the combination of two different colloids (19) or in concert with soft templating (20, 21). These 3-DOM structures can be extended to thin films, but this requires excellent control to produce ordered thin films of colloidal crystals (22). The development of direct soft templating of carbonizable precursors using block copolymers by Dai and coworkers provides a facile route to fabricate mesoporous carbon films through cooperative assembly of a reactive resorcinol-formaldehyde (RF) sol with an amphiphilic block copolymer (23). This sol-gel route for self-assembly to generate mesoporous carbons is analogous to the typical evaporation induced self assembly route (24) for the fabrication of mesoporous metal oxides (25). One disadvantage with this route is the difficulty in manipulating the nanostructure once the film is formed due to the cross-linked network associated with the RF resin.

The use of block copolymers that contain one or more carbonizable segments (26–28) enables further manipulation of the nanostructure to provide additional orientational control of the mesoporous carbon. For example, Tang et al. have illustrated long range order of polyacrylonitrile (PAN)-containing block copolymers that can be converted effectively to carbon after oxidative stabilization of the PAN (29). Additionally, micelles of these block copolymers can be converted into carbon nanoparticles (30). As the carbonizable material is solely a block copolymer, it can be subjected to most processing techniques developed for other block copolymers, such as solvent vapor annealing (31), electric fields (32), magnetic fields (33), zone annealing (34), and chemical modification of

substrates to control orientation (35) and alignment (36). Despite these potential advantages associated with the processing of these block copolymers prior to conversion into mesoporous carbon, there exists one major drawback to this direct conversion method in that the morphology and pore size are directly determined by the original template. Thus to modulate the morphology, another block copolymer template needs to be synthesized; this is a major drawback in comparison to the cooperative assembly with RF discussed previously where commercially available materials can be utilized without any need for controlled polymer synthesis.

As an alternative, Zhao and coworkers have developed a non-reactive cooperative assembly route where oligomers of phenol-formaldehyde (resol) are utilized as the carbonizable precursor in combination with a non-ionic block copolymer template (37). Upon heating, the resol is cross-linked and hardened to enable carbonization, while the mesostructure evolves (38). For thin films, the evolution of nanostructure is even more dramatic transforming from a disordered homogeneous mixture to a well-ordered nanostructure as the resol is concurrently cross-linked when Pluronic surfactants act as the template (39). When high molecular-weight block copolymers are utilized as the template, the interplay between the reaction kinetics of crosslinking and the chain dynamics associated with ordering of the film turns unfavorable for the formation of well defined pore morphology (40). However, analogous mesoporous carbon powders yield highly ordered mesoporous structure (41).

In this chapter, we describe methodologies to exploit or overcome these observations regarding the ordering of block copolymer templated mesoporous carbon in thin films. First, we begin by describing some of the differences between thin films and bulk samples fabricated by the soft templating method using resol as the carbon precursor. In particular, we focus on the wetting characteristics at the air-film and film-substrate interfaces as well as the anisotropic structures that evolve from the pinning of the film at the substrates. Second, the modulation of the nanostructure including enhancing the ordering by use of solvents in the processing will be discussed. These include a standard protocol for the processing of block copolymer based on solvent vapor exposure, termed solvent vapor annealing (42), and the inclusion of low volatility solvents in the casting solution for the films that provide enhanced mobility. Finally, the alignment of the templated domains will be demonstrated by the application of a directional force to the templated film to provide a preferential orientation of the nanostructure.

Thin Film Effects for Soft Templated Carbons

The assembly behavior of block copolymers is known to be altered in thin films due to the fields imposed by the interfaces (43). These interfaces can impose alignment of anisotropic structures (44–46) and tune the equilibrium morphology (47) of neat block copolymers. The addition of carbonizable precursors and their cooperative assembly with block copolymers can further impact the structure and morphology developed in these thin films as full component segregation to the interfaces is possible. These interfaces can also be exploited to provide routes

to orientation during the structure self-assembly. In addition to the impact during self-assembly, there is an additional component associated with the maintenance of the ordered nanostructure through the chemical transformation of the framework to amorphous carbon. In particular, the stresses associated with volume reduction during carbonization imposed in the film are generally unidirectional (through the film thickness) and can induce changes in the size, shape and presence of pores in the films.

Influence of Interfaces on Structure

Even the initial block copolymer templated mesoporous carbon films reported by Dai and coworkers illustrated the potential power of interfaces on the structural arrangement of the nanopores in these systems (48). In this case, the assembly and crosslinking reaction were decoupled that allowed for perpendicular alignment of cylindrical nanopores through solvent vapor annealing (SVA) of the film (48). In this case, the solvent provides mobility to enable segmental re-arrangements and balances the interfacial properties to prevent preferential wetting of segments of the block copolymer at an interface as has been demonstrated for neat block copolymers in the past (49). Thus, although the interfaces have not been systematically examined for the direct conversion of block copolymers in mesoporous carbon films, this interfacial consideration should enable orientation control depending on substrate chemistry and/or drying conditions.

Figure 1 schematically illustrates the differences in block copolymer wetting and associated structural orientation for different nanostructures. In this case, both the air and substrate interfaces must be considered in the context of the conditions during which the nanostructure is developed. For reactive assembly systems consisting of resorcinol, formaldehyde, catalyst and block copolymer cast from alcohol or aqueous solutions (23, 50, 51), the solvent still present in the film as the system assembles will impact the wetting characteristics. The crosslinking of the RF resin prohibits further rearrangement of the nanostructure. Conversely, the cooperative assembly of block copolymers with phenolic resins in thin films does not typically spontaneously occur on evaporation and instead the films order on heating (39). In this case, the relative rates between ordering and crosslinking impact the morphology; if the rate of ordering is significantly greater than that for the crosslinking to a network solid, a long range ordered morphology can be obtained.

Depending on both the surface and substrate interactions, any preferred orientation (e.g., parallel versus perpendicular cylinders as shown in Figure 1) of the self-assembled structure evolves. A ‘neutral’ condition induced by surface modification has been utilized to generate perpendicular cylindrical nanopores in inorganic oxides (52), but this interfacial modification has not been successfully applied to mesoporous carbon films. In most cases, the hydrophobic segments of the block copolymer will preferentially wet the air-film interface, while the hydrophilic segments will preferentially wet the substrate-film interface (for quartz and silicon). This wetting condition will lead to parallel orientation of cylindrical mesopores as illustrated in Figure 2. In order to maintain the ordered

structure through the thickness of the film, the local film thickness must be an integer multiples of the lattice spacing for symmetric wetting and integer multiple + one half of the lattice spacing for asymmetric wetting as shown in Figure 1. If the total film thickness is not commensurate with these wetting conditions and the period of the mesostructure, islands and holes will typically form in the film so locally the film thickness is commensurate. For neat block copolymer films, the island and hole morphology typically occurs when the incommensurability between the periodicity of the block copolymer and the film thickness exceeds approximately 10-15% (53–55). The exact tolerable incommensurability depends on the relative energy difference between the formation of additional interfacial area (due to the terracing) and the stretching of the block copolymer segments required to expand or contract to the periodicity required to maintain the ordered morphology through the thickness of the film.

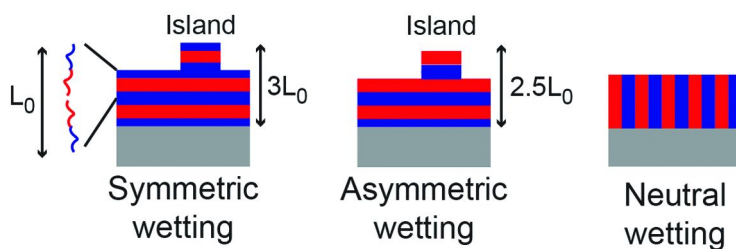


Figure 1. Schematic of wetting conditions associated with block copolymers and associated alignment of cylindrical domains.

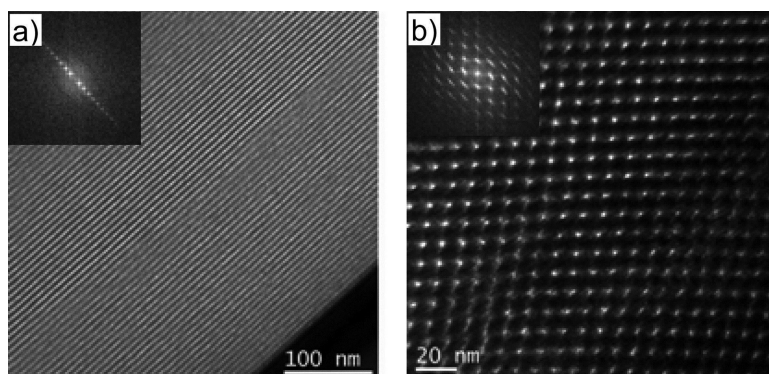


Figure 2. TEM micrograph of a cross section of a mesoporous cross-linked phenolic resin templated by Pluronic P123 after pyrolysis in nitrogen at 350 C. The micrographs show both the (a) (110) and (b) (001) planes of the ordered c2mm morphology. Reproduced with permission from ref (69). Copyright 2010 American Chemical Society.

In the case for parallel orientation illustrated in Figure 2, a phenolic resin oligomer was cooperatively assembled with a commercial poly(ethylene oxide)-*block*-poly(propylene oxide)-*block*-poly(ethylene oxide) surfactant (PEO₂₀-PPO₇₀-PEO₂₀, where the subscripts indicate the average degree of polymerization for each segment), Pluronic P123. The neat Pluronic P123 is predominately hydrophobic, but the interactions between PEO and PPO are insufficient to segregate the segments into ordered phases (56). It is the enthalpically favorable hydrogen bonding (56) between the PEO segments and the phenolic resin that leads to microphase segregation and the formation of ordered structures, which is similar to the bulk state. The morphology developed is strongly dependent on the relative volume fraction of hydrophilic and hydrophobic segments; additionally, the conformational asymmetry (57) associated with segmental size of the different components can shift the phase boundary for neat block copolymers. For these cooperatively assembled systems, the complexity associated with the thermodynamics of self-assembly increases as the interactions between components and the segments of the block copolymer are important and the added component is not subjected to the same cooperativity constraints as the block copolymer. In cases where the interactions are highly favorable for one segment, highly ordered mesopores can be assembled in thin films such as shown in Figure 2. The hydrophilic PEO and phenolic resin will selectively wet the silicon substrate, while wetting of the air interface by the hydrophobic PPO segments might be expected based on simple energetic arguments. By changing the block copolymer, the interactions with the carbonizable precursor are tuned. The hydrophilic segment does not need to be water soluble, but does need to have a preferential interaction with the carbonizable precursor. For example, polystyrene-*block*-poly(vinyl pyridine) has been utilized as a template for mesoporous carbon with RF (48) and phenolic resin (58, 59) as the carbon precursors. Figure 3 illustrates a porous carbon film templated by a weakly amphiphilic block copolymer of polystyrene-*block*-poly(methyl methacrylate).

In this case, resorcinol was blended with this block copolymer along with *p*-toluenesulfonic acid with the film spun cast from THF onto a silicon wafer. Exposure to formaldehyde vapor cross-linked the resorcinol as has been reported previously (48). A poorly ordered structure consisting of spherical pores and oblong worm-like micelles are observed on the surface. This illustrates that the preferential wetting of the hydrophobic domains, but also the subtleties involved with cooperative assembly. A block copolymer of poly(ethylene oxide)-*block*-poly(methyl methacrylate) has been shown to template mesoporous carbons using resol as the precursor (60). In this case, the methacrylate phase is sufficiently hydrophobic to template the mesopores. The difference in the selection of the carbonizable precursor changes the miscibility between phases; the entropy of mixing associated with the oligomers of phenolic resin is significantly less than for the small molecule resorcinol, which alters the solubility with the poly(methyl methacrylate) as immiscibility is common for polymer mixture in the absence of strong favorable interactions. The size of the precursor is also important – monomers such as resorcinol or phloroglucinol will be more miscible with mildly hydrophilic polymer segments than their oligomers due to the loss of the entropy of mixing with polymerization.

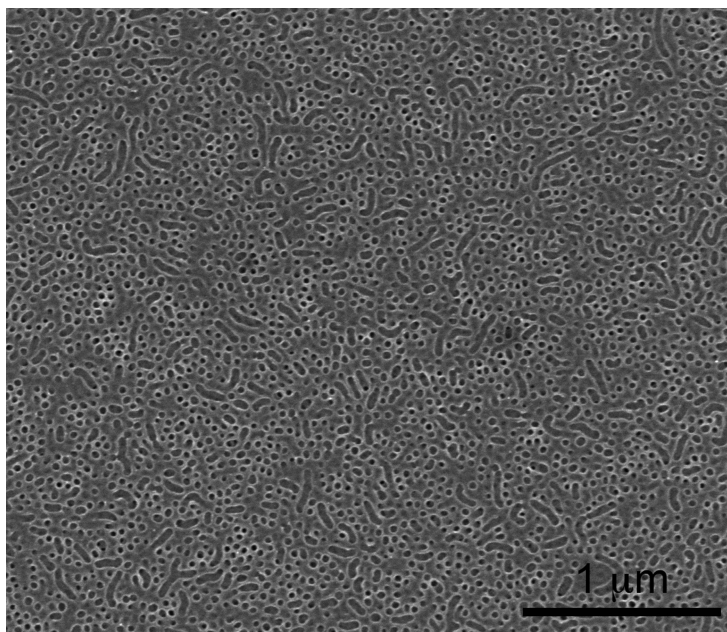


Figure 3. Top down FESEM of a mesoporous carbon film templated by the mildly amphiphilic polystyrene-block-poly(methyl methacrylate).

In addition to selective wetting induced by the interfaces that impacts the orientation of the ordered morphology, the phase behavior of the thin films can be altered in comparison to the analogous bulk mesoporous carbon. First, the crosslinking associated with the carbonizable precursor can alter the space group symmetry slightly by the combination of volumetric contraction from crosslinking and the pinning at the substrate. For both the reactive (RF) and non-reactive (resol) cooperative assembly pathways, this can lead to near uniaxial contraction through the thickness of the film, which also deforms the ordered structure. For spherical mesopores, this changes the morphology from body centered cubic (BCC, $Im3m$) for the bulk to a face centered orthorhombic ($Fmmm$) (50, 61); similarly, the bulk hexagonally packed cylinders ($p6mm$) transforms to rectangularly packed cylinders ($c2mm$). In sufficiently thin films (thickness $< 20 L_0$ as described in Figure 1), block copolymer morphology can be thickness dependent (62); for BCC bulk morphology, the favored 2-D packing is hexagonal. For cooperatively assembled mesoporous carbon films, this difference between 2-D and 3-D equilibrium packing can be satisfied more readily as the chain stretching associated with space filling is relaxed (63, 64) by the presence of the carbonizable precursor that is not tethered to the hydrophobic segments.

For the cooperative assembly of Pluronic F127 and resol to form BCC spheres in the bulk (FDU-16) (65), even thick ($>1 \mu\text{m}$) films exhibit hexagonal closed packing (HCP) at the surface, while the remainder of the film is face centered orthorhombic (FCO) as illustrated in Figure 4. In this case, the surface of the film has been partially scrapped by a razor blade to enable investigation into the

morphology through the film thickness. The bottom right of the image is the natural surface of this film, which is HCP as illustrated by the hexagons. However, the structure underneath this HCP layer exhibits square packing consistent with FCO, which is only slightly distorted from BCC oriented with the close packed (110) plane parallel to the substrate. These structures have been confirmed by grazing incidence small angle x-ray scattering (GISAXS) (61). The overall phase behavior can be thickness dependent for block copolymer thin films (66). The HCP persists through mono- and bi-layers ($2L_0$) of spheres, while a co-existence of HCP and FCO are obtained at $5L_0$ (67). These thickness dependencies for the cooperatively assembled resol-Pluronic F127 are strikingly similar to that for the neat triblock copolymers, so the addition of resol in this case does not appear to impact the thickness dependent phase behavior; thus in many cases, the neat block copolymer behavior can be utilized to predict the thin film behavior for cooperatively assembled resol for the fabrication of mesoporous carbon films. This similarity is not surprising as the ordering in these films proceeds on heating and is thermally induced (39), just as typically observed for block copolymer thin films when the casting solvent is a good solvent for both segments (68).

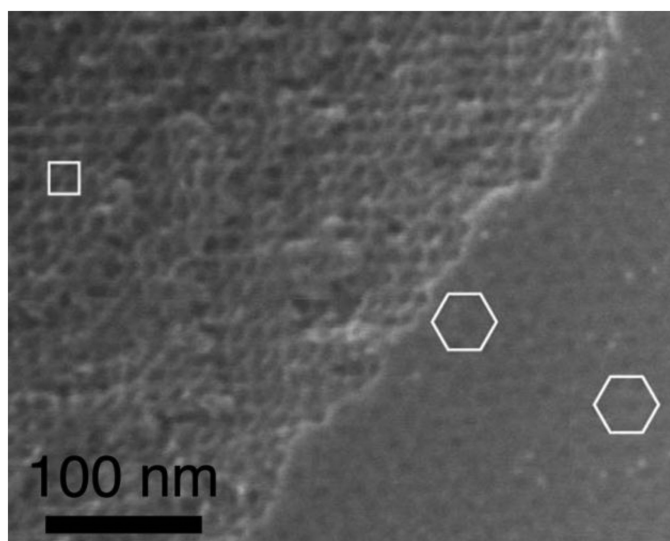


Figure 4. FESEM of the surface (bottom right) and underlying layers of a thick mesoporous carbon film with HCP surface and FCO bulk.

In addition to these shifts between HCP and FCO for the spherical mesopores, the overall phase behavior can be thickness dependent for block copolymer thin films (66). Additionally, the preferential wetting of components can, for sufficiently thin films, alter the local composition to change the processing windows (in terms of template to carbonizable precursor ratio) in comparison to bulk analogs. For the family of $p6mm$ mesoporous carbons from cooperative

assembly of Pluronic P123 and resol (FDU-15) (65), the morphology is altered on both boundaries with a disordered or wormlike morphology observed at high resol content and lamellae at low resol content in thin films for compositions within the bulk FDU-15 processing window (69). Thus it is important to note that if an ordered structure is not obtained in a thin film that the issue could be the alteration of phase boundaries relative to the bulk.

In addition to the substrate impacting wetting behavior, the substrate selection can also provide a route to enable additional functionality such as a current collector for electrochemical energy storage (70) or providing ease of release to generate free standing mesoporous carbon films after carbonization (71). However in selecting substrates, their influence on both wetting and potentially the phase behavior needs to be considered. For the generation of free standing films, the film can also be removed prior to carbonization but a hardener additive is required for mechanical stability through carbonization (72). Even in this case, the substrate will be important for structural control as self-assembly occurs with the substrate in place.

Film Issues Associated with Structure Formation and Maintenance through Carbonization

In addition to the complications that can arise in cooperatively assembled thin films due to thickness and interface effects, there are other deleterious factors that can impact the structure of these mesoporous carbon films that are not as pronounced for analogous powders when using resol as the carbonizable precursor. First, the ordering using high molecular weight block copolymer templates can be quite poor in the thin films, even when highly ordered mesostructures are obtained for the analogous powders (40). The ordering can be further degraded by the inclusion of ionic functionality in the block copolymer template (73). To explain these differences, the competition between cross-linking of the phenolic resin and the segmental dynamics of the block copolymer template for ordering can be considered. For block copolymer thin films, the ordering kinetics are significantly retarded in comparison to the bulk material (74). This decrease in ordering kinetics results in insufficient mobility prior to the kinetically trapping of the mesostructure by cross-linking. This effect is also observed for bulk powders to some degree when the cross-linking reaction is performed at significantly high temperature (65). This effect is also mitigated in bulk powders as the materials are initially somewhat ordered and the ordering only improves on heating while the phenolic resin crosslinks (38); this is different in thin films where the material does not appear to be ordered on casting and the full evolution from disorder to order is required (39).

Moreover even when the desired ordered structure is initially formed in the film, significant deformation of the mesostructure can occur during carbonization. For spherical nanopores, the span length of the unsupported area associated with the pore is relatively small; as the template degrades prior to carbonization, the volumetric contraction associated with the transformation from polymer to inorganic carbon provides stresses to deform these pores. This contraction in volume can be quite severe with > 60 % decrease in film thickness observed (50).

The pinning of the film at the substrate produces near uniaxial contraction of the film and space group. This can lead to slit-like pores in cases where the wall thickness is rather small (61). For cylindrical mesopores, this uniaxial contraction may lead to full collapse of the ordered structure if the framework walls lack sufficient mechanical integrity during the carbonization process (69). The selection of the carbon precursor (51), synthesis method (75), and wall thickness (69) appear to be critical factors; additionally, the co-assembly with inorganic sol gel materials (76) can also provide increased strength to the framework to minimize deformation of the ordered mesostructure.

Thus considerations associated with both the structure formation and the carbonization are important in fabrication of the desired morphology for these soft templated mesoporous carbon films. These issues are also present in direct formation for mesoporous carbon from a block copolymer (29). Methodologies to address the structure formation and provide additional control beyond simple heating of the films to induce order are addressed in the following two sections with a focus on solvent assistance and application of directional forces to align the nanostructures.

Solvent-Assisted Processing of Soft Templated Carbon Films

For the synthesis of mesoporous materials through cooperative assembly of sol-gel precursors and block copolymers, the addition of organic solvents swells the hydrophobic domains to subsequently increase the size of the mesopores (77). This technique has been also successfully applied to the synthesis of mesoporous carbons with large pores (78). From the perspective of neat block copolymers, the effect of solvents is dependent on the nature of its interaction with the segments of the copolymer (79). In the case where the solvent is neutral (e.g., the solvent is equally good for both segments), the presence of the solvent acts to screen the interactions between the segments and promote miscibility (80). For a good neutral solvent, it is possible for the overall domain spacing to decrease with addition of solvent as the segments of the block copolymer are not as stretched. Alternatively, a highly selective solvent will preferentially swell one domain of the block copolymer to increase the domain size without significant compatibilization of the copolymer interface (81). Irrespective, the added solvent will enhance the dynamics of the block copolymer and promote the kinetics of ordering (82). One common route to promote ordering in block copolymer thin films is solvent vapor annealing, where the block copolymer film is exposed to solvent vapor, which is sorbed into the film to promote ordering of the film (49, 83). These solvents can be utilized to promote non-equilibrium morphologies in the films (84, 85). These kinetically trapped morphologies can then be exploited for applications, but as the structures can be controlled (86), the structure can be extremely sensitive to small perturbations in the processing conditions. Although there has been considerable interest in solvent processing associated with block copolymer films (87), these advances associated with block copolymers have not been fully translated to mesoporous carbons to exploit the wealth of potential morphologies available.

Solvent Vapor Annealing

The first report for soft templated mesoporous carbon films (48) required an extended solvent vapor exposure step to provide sufficient mobility for the custom block copolymer template, polystyrene-*block*-poly(vinyl pyridine) (PS-*b*-PVP), to order in the presence of resorcinol. The primary factor that is likely important for why solvent vapor annealing (SVA) is utilized in this case is the high glass transition temperature (T_g) associated with both PS (≈ 105 °C) and PVP (≈ 110 °C); moreover, the mobility of PVP can be dramatically inhibited with the addition of salts that can associate with the pyridine moiety (88). The resorcinol associates with the pyridine, so highly reduced segmental mobility might be expected. Exposure to a mixed solvent vapor of dimethyl formamide (DMF) and benzene results in substantial sorption of solvent into the film that plasticizes the polymer segments to promote ordering of the block copolymer. The benzene effectively plasticizes the PS segments, while DMF is a good solvent for the PVP. Moreover, DMF can effectively replace the resorcinol in coordination with PVP to provide mobility to the complex. This example illustrates the wealth of possibilities associated with solvent vapor annealing through use of solvent mixtures to produce perpendicularly aligned cylindrical pores in the film (48). However control of solvent mixtures can be complex, especially when considering the vast difference in volatility between benzene and DMF. For block copolymers, a system independently controlling the relative vapor pressure of solvents has been demonstrated in several cases by use of mass flow controllers (49, 85).

Figure 5A illustrates schematically the general concept for this solvent vapor control system. The key aspect is saturating the gas streams flowing through the solvents of interest such that the relative flow rates between the air and two solvent streams enables direct determination of the vapor pressure of the head space surrounding the film of interest. The film is swollen by the solvents to alter the mobility of the templated film and allows for re-arrangement of the block copolymer and carbonizable precursor prior to crosslinking. It should be noted once highly crosslinked, the morphology will be challenging to alter, so this technique is most appropriate for cooperative assembly with phenolic resin. Figure 5B illustrates the rapid swelling of a templated film as the partial pressure is systematically increased. An *in-situ* swelling experiment indicates that it takes approximately 2 min to achieve the equilibrium swelling at each relative vapor pressure from $p/p_0=0$ to $p/p_0=0.85$.

This swelling provides mobility to the system to enhance the ordering of the mesoporous films templated by poly(styrene-*block*-*N,N*-dimethyl-*n*-octadecylamine *p*-styrenesulfonate) (PS-*b*-PSS-DMODA). Figure 6 illustrates the differences in the surface structure associated with different SVA conditions for mesoporous carbon films (73). Without SVA, the traditional thermal processing at 120 °C that leads to ordered resol/Pluronic surfactant composites (89) does not produce an ordered structure. There are very short range cylinder-like structures on the surface, but nothing approaching a highly ordered structure like illustrated in Figure 2. It should be noted that in this case electrostatic interactions between the template and resol are possible. This stronger interaction than the typical hydrogen bonding appears to inhibit the ordering. This is consistent with

the poorly ordered mesostructures illustrated for mesoporous carbon powders templated by ionic surfactants (90). Thus similar to the templating of mesoporous silicas (91), the mechanisms associated with the assembly and structure formation appears to be different for cooperative assembly with resol (and potentially other carbonizable precursors) when utilizing an ionic or a non-ionic template.

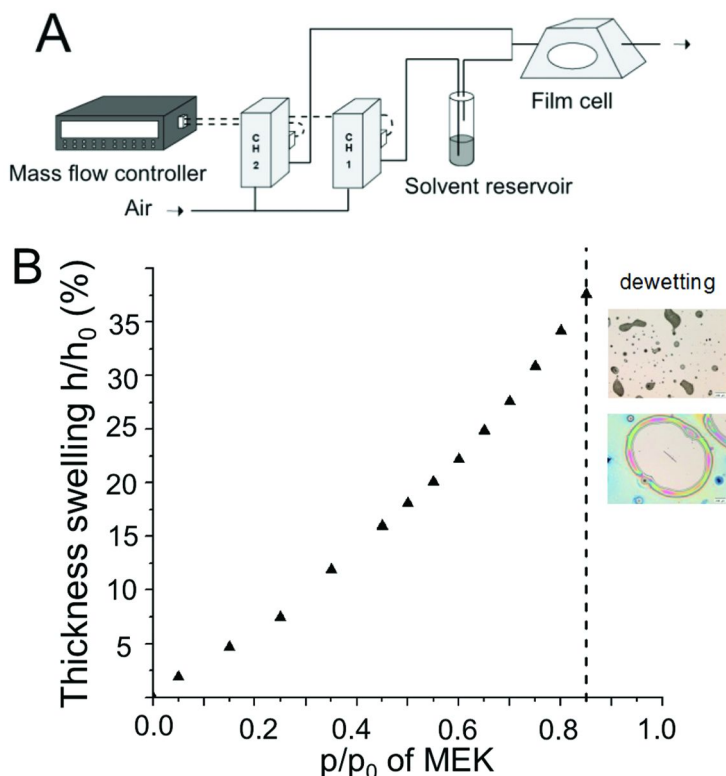


Figure 5. (A) Schematic of system to control the vapor pressure of solvent mixtures using mass flow controllers. (B) In-situ thickness measurement during SVA using spectroscopic ellipsometry. Adapted with permission from ref (73). Copyright 2013 American Chemical Society.

However for the cooperatively assembled PS-*b*-PSS-DMODA and resol films after SVA at low partial pressure of MEK, the cylinder structure begins to emerge (Figure 6B), but the ordering is still extremely limited. Increasing the partial pressure of MEK to further swell the film (Figure 5B) results in the formation of a fingerprint pattern (Figure 6C) that is consistent with the typical ordered morphology associated with ordered cylinders in neat block copolymers (92). In this case, the cylinders are aligned parallel to the substrate as a result of the preferential wetting of one of the segments of the block copolymer template. There is terracing associated with the non-commensurate thickness of the film

observed in the AFM images; there are islands of larger thickness formed (refer to the schematic in Figure 1), which infers that the parallel alignment of the cylinders relative to the substrate persist through the film thickness. This alignment has been confirmed by grazing incidence small angle x-ray scattering (GISAXS) (73).

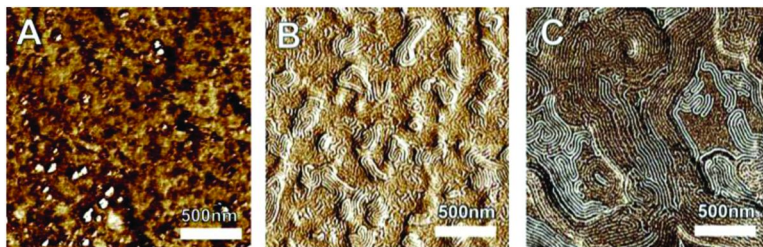


Figure 6. AFM micrographs of the surface of mesoporous carbon films with (A) no SVA, (B) SVA with MEK at $p/p_0 = 0.6$, and (C) SVA with MEK at $p/p_0 = 0.8$. Adapted with permission from ref (73). Copyright 2013 American Chemical Society.

In addition to the changes in ordering, the SVA process also impacts the pore size. MEK is a good solvent for both segments, but the incompatibility between them is sufficiently large to prevent loss of ordering at the conditions examined. The films are highly swollen by MEK (Figure 5), so the domains are likewise swollen. The average pore size increases from 3.8 nm without SVA to 5.4 nm after exposure to $p/p_0 = 0.6$ and to 8.6 nm after exposure to $p/p_0 = 0.8$ (73). This increase in pore size associated with the hydrophobic PS domains can be understood in terms of both the standard increase in d-spacing on ordering of a block copolymer due to chain stretching and the swelling by the solvent. The solvent is fully removed prior to crosslinking, so this effect is not analogous to the standard addition of low volatility solvents to enhance the pore size of block copolymer templated mesoporous materials (78). Instead the domain sizes are kinetically trapped as the solvent is removed due to vitrification of the block copolymer segments when the solvent content is insufficient to plasticize. The solvent selection is critical and will depend on the system details. For this example, the mobility of both segments in the block copolymer are limited, so it is important to plasticize both. Use of a highly selective solvent for one component such as toluene for PS segment or chloroform for PSS-DMODA segment does not appreciably improve the ordering after SVA as toluene and chloroform will not improve the mobility of the PSS-DMODA and resol phase. SVA provides a simple route to improve ordering and potentially tune the pore size. With the correct solvent mixture selection, the orientation of anisotropic phases such as cylinders can be flipped from parallel to perpendicular (48), which is desired for membranes as an example. Control of the solvent vapor annealing conditions and the selection of the solvent(s) are important to consider to achieve the desired orientation and ordering.

Residual Low Volatility Solvent

While SVA is relatively simple and has been successfully applied to numerous block copolymer systems, it is not readily extendable to manufacturing due to the flammable and toxic nature of many of the organic solvents utilized for SVA. However, the use of very low volatility liquid solvents in synthesis have been applied to expand the pore size of mesoporous carbons (78) by selection of a hydrophobic solvent, such as trimethylbenzene, that will be highly selective for the hydrophobic segments of the block copolymer template. As the hydrophobic phase provides the template for the pores, the addition of solvent can dramatically increase the pore size. Thus, this addition of solvent should enhance the chain dynamics in the hydrophobic regions. However for block copolymers with electrostatic interactions with phenolic resin, the dynamics of the phenolic resin containing phase can also be limited. Moreover as the size of the segments increase, the mobility of the associated chains and their ability to order decrease (93). From considerations of interactions between components and prior success with the ordering with SVA using solvent mixtures, it is possible to rationally select solvents to add to the casting solution to aid in the self-assembly process. First, the solvent should be highly selective for one of the phases to minimize compatibilization of the block copolymer, which could lead to lack of an ordered morphology. Second, the solvent must be low volatility such that evaporation does not occur during film formation and remains partially in the film as it is heated. These types of solvent mixtures have successfully been utilized in the RF-based templating of ionic vesicles with tert-butanol and 1,3,5-trimethylbenzene denoted as co-surfactants (94). As direct templating with ionic surfactants for mesoporous carbons have not typically yielded highly ordered systems, the uniform pore sizes obtained from this vesicle templating suggests that these added solvents may provide sufficient mobility to produce highly ordered mesoporous carbons.

To demonstrate the potential of this methodology, the same kinetically hindered system illustrated in the prior SVA section will be utilized. As shown in Figure 6, a highly ordered structure is not obtained after casting from MEK and thermopolymerization without the use of SVA with MEK. MEK is a relatively high volatility solvent and not highly selective solvent for this system, so it cannot easily promote ordering unless a modest fraction is maintained in the film through controlling the external vapor pressure such as in SVA. It is important to plasticize both the PSS-DMODA/resol and PS phases independently. In order to achieve this, dioctyl phthalate (DOP), a common plasticizer for thermoplastics, is added to the casting solution to enhance the mobility of the PS domains. DOP has a normal boiling point of 385 °C, so nearly all of the DOP in the casting solution remains in the film after the carrier solvent (MEK) is evaporated. For the resol containing domains, dimethyl sulfoxide (DMSO) provides an aprotic solvent that can effectively mediate the electrostatic interactions between the resol and PSS-DMODA. The high boiling point of DMSO (189 °C) ensures that sufficient solvent remains after the film casting. Figure 7 illustrates the influence of the addition of these solvents to the casting solution for the fabrication of mesoporous carbon films (95). Without any added low volatility solvents (DOP or DMSO), the film lacks significant order, although there are similar sized short

rod-like pores visible at the surface. With only plasticization of the PS phase by addition of DOP, there is a minimal change in the morphology. Conversely when only adding DMSO, the ordered structure is dramatically improved. This can be further improved using the combination of both DOP and DMSO.

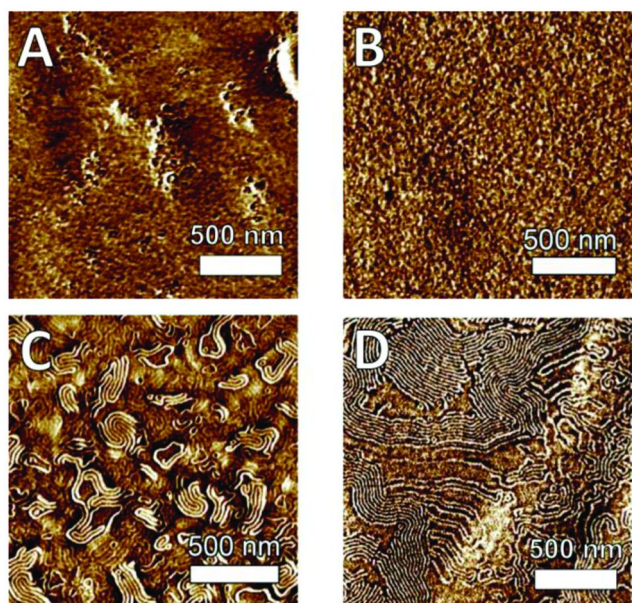


Figure 7. AFM micrographs of the surface of mesoporous polymer films after template removal at 400 °C for (A) no added solvent, (B) only DOP, (C) only DMSO, (D) both DOP and DMSO at 20 wt % relative to solids. Adapted with permission from ref (95). Copyright 2013 American Chemical Society.

The low volatility of the solvent means that exceedingly small quantities of DOP is required; for a 5 mL solution of 20 wt% solids (block copolymer + resol) in MEK, four drops of DMSO and one drop of DOP is effectively the additive amount included to observe the changes in the morphology from Figure 7A to Figure 7D. Thus, the solvent utilization for plasticizing these films is minimal. In addition to improving the long range order, these solvents impact other important characteristics of the mesoporous films. First when using the mixture of both DOP and DMSO (at a 1:4 mass ratio), increasing the amount of these solvents in the casting solution effectively increases the pore size. For mesoporous polymer films, the average pore size increases from 3.1 nm without this solvent mixture to 4.3 nm when only 5 wt% DOP and DMSO relative to the solids (PSS-DMODA and resol); this can be enlarged to 9.9 nm at 20 wt% DOP and DMSO. In addition to enlarging the pore size as expected associated with the added DOP that acts to swell the hydrophobic domains, there is also some enhancement in the pore size associated with the enhanced ordering that leads to a larger extent of chain stretching. Second, the porosity of the films is substantially increased with this solvent mixture (DOP and DMSO). The porosity can be more than doubled in this system going from no

added solvent to 20 wt % DOP and DMSO. Thus by selecting the ratio of solvents and their concentration, the ordering and pore size can be controlled in these soft templated mesoporous carbon films.

Large Area Alignment of Ordered Domains

One of the shortcomings of the previous attempts to improve the ordering is the lack of macroscopic alignment of the mesostructure. The large scale alignment and orientation of block copolymers in thin films has been extensively investigated over the past several decades due to their potential use as photoresists in microelectronics. Figure 8 illustrates the ability to direct the self-assembly of block copolymers on surfaces into desired patterns as pioneered by Nealey and coworkers (96). This directed self-assembly is driven by chemically patterning the substrate by optical lithography. The surface patterns provide selectivity to wetting of one of the segments of the block copolymer. Although this is effective and allows for pattern multiplication (46), the costs associated with the lithographic patterning are not typically compatible with potential applications of mesoporous carbon films.

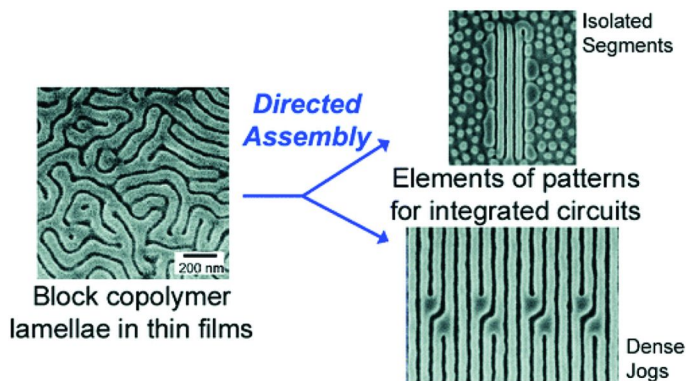


Figure 8. Illustration of use of chemically patterned substrates to direct the assembly of block copolymers in thin films. Without the chemical pattern, the block copolymer is ordered, but no directionality to the ordered structure is directed. Reproduced with permission from ref (96). Copyright 2007 American Chemical Society

There are a number of other techniques that have been developed for block copolymer alignment in thin films (32, 97–101); these typically do not allow for an arbitrary orientation of the domains, but can allow for unidirectional alignment over large areas. The deposition conditions can be controlled through zone casting (101) or controlled spray coating (102) to produce well aligned block copolymer films. Alternatively, topographical patterning of the surface produces edges to which the ordered block copolymer domains can align (103). For example, perfect registration of sphere forming block copolymers can be obtained over macroscopic lengthscales by the use of miscut sapphire, which

induces a sawtooth pattern on the substrate that can direct the assembly of a block copolymer (99). After film formation, electric (104) and magnetic (105) fields can induce preferential orientation of the block copolymer due to differences in the dielectric and magnetic susceptibility of their segments. A sweeping solidification front (98) or zone annealing (100) associated with the motion of a temperature gradient induces orientation. Application of a shear force to the surface of the polymer film can also produce orientation (97).

Due to the similarities between the ordering of block copolymers and soft templated mesoporous carbon based on phenolic resin cooperative assembly, it is likely that a majority of these techniques can be applied to the fabrication of mesoporous carbon films. To date several of these techniques have been demonstrated, here we will discuss three of the forces discussed previously for block copolymers and their application to ordered mesoporous carbon films. First, we will illustrate the work by Kowalewski and coworkers on the application of zone casting of block copolymer films and their direct conversion to mesoporous carbon films with highly aligned nanostructures (29). Second, we will show how a moving sharp temperature gradient can be utilized to produce highly aligned cylinders and spheres using common templating surfactants, Pluronic F127 and Pluronic P123, for mesoporous carbon films. Finally, a more recent development where shear is applied to the films during solvent vapor annealing is shown for alignment of larger pore sizes in mesoporous carbon films.

Zone Casting

Zone casting involves the deposition of the polymer solution on a moving substrate through a flat nozzle. The evaporation rate of the solvent is the key control variable to obtain the desired orientation and alignment of anisotropic materials such as liquid crystals (106) and block copolymers (101). Kowalewski and coworkers have extended this technique to the fabrication of mesoporous carbon films (29). In their case, a novel carbon-yielding block copolymer is utilized as both the template and the carbonizable precursor: polyacrylonitrile-*block*-poly(*n*-butyl acrylate), PAN-*b*-PBA. This block copolymer is cast from solution onto the moving substrate as illustrated in Figure 9. The solvent evaporates as the substrate moves to generate a solidification front that can template alignment of subsequent material being deposited. As shown in Figure 9, perpendicular lamellae are formed that are highly aligned in one direction that is orthogonal to the direction of motion of the substrate during deposition. The alignment can be quantified over macroscopic dimensions with GISAXS; the beam in GISAXS illuminates a strip of the film with the width of the beam, so it provides a global average of the orientation. Both AFM and GISAXS can be analyzed in Fourier space in terms of the Herman's orientational parameter, which provides a quantification of the extent of orientation. For an isotropic sample, the orientational parameter is 0; while for perfect alignment, the orientational parameter is 1. Qualitatively, this can be assessed from Figure 9E in terms of the width of the peak. For perfect alignment the normalized peak height should be a delta function, so as the peak broadens the extent of orientation is decreased. In this case, the alignment of the lamellae decreases on

carbonization. On the basis of the large change in volume on carbonization and the associated stresses, it is not surprising that the orientation degrades slightly after carbonization.

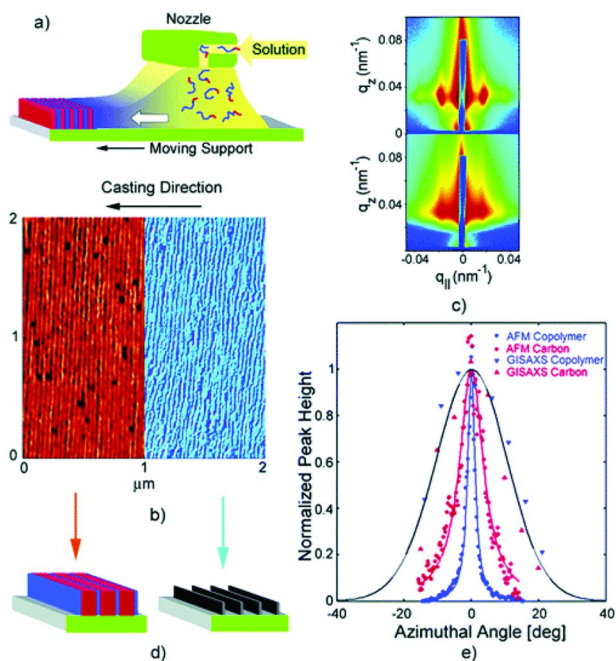


Figure 9. Long-range order in thin films of PBA-*b*-PAN block copolymers prepared by zone-casting (a) and in nanostructured carbons prepared by subsequent pyrolysis. (b) AFM phase images (left, copolymer; right, carbon); (c) GISAXS patterns acquired at 90° to casting direction (top, copolymer; bottom, carbon); (d) schematic illustration of lamellar order (left, copolymer; right, carbon); (e) azimuthal profiles of maxima in 2-D Fourier transforms of AFM images and maxima in GISAXS patterns corresponding to the lamellar period. Reproduced with permission from ref (29). Copyright 2005 American Chemical Society.

Cold Zone Annealing

As an alternative to zone casting, cold zone annealing (CZA) provides a post-casting processing route to produce highly aligned nanostructures. In CZA, the sample is passed through a controlled temperature gradient (\dot{T}) at a fixed velocity (l_{00}). This dynamic thermal field annealing technique is a modification of zone refining by Pfann for polycrystalline semiconductors (107). Recently, we have illustrated the application of CZA to the common FDU-15 and FDU-16 mesoporous carbon films (108). Figure 10 illustrates schematically the CZA method.

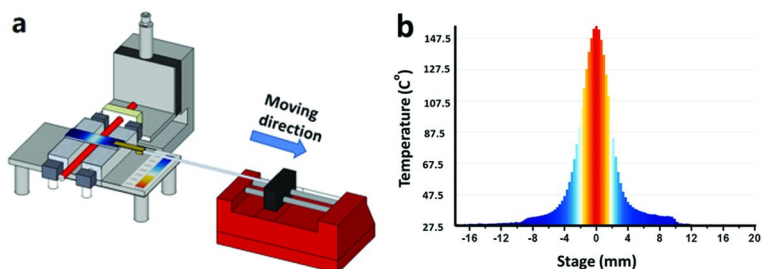


Figure 10. (a) Schematic representation of the zone annealing apparatus consisting of a hot filament, two cold blocks and a syringe pump to control the motion of the film through the hot zone. (b) Temperature gradient profile for the thermal zone used for alignment of the FDU films. Reproduced with permission from ref (108). Copyright 2013 the Royal Society of Chemistry.

The cooperatively assembled film consisting of Pluronic and resol at an appropriate ratio to yield either FDU-15 or FDU-16 on a quartz substrate is pulled through a sharp temperature gradient reaching a maximum temperature of 150°C with the temperature then sharply decreasing as illustrated by the temperature profile shown in Figure 10B. This gradient produces substantial forces on the molten pluronic-resol mixture, leading to flow of the material when Pluronic P123 is utilized as the templating agent (109). These directional forces also provide for directional alignment of the self-assembled structure. The alignment area is significantly larger than the typical TEM or FESEM field of view. To quantify the alignment, X-ray scattering with rotation of the sample is utilized to generate the angular dependent scattering intensity of the primary diffraction of the nanostructure (29, 108, 109). This can then be analyzed in terms of the Hermans' orientational parameter (S) (110), which is the 2nd order Legendre polynomial and provides a quantitative measure of the extent of alignment of the structure. For a perfectly isotropic sample, $S = 0$; while for a single crystal (perfect registration), $S = 1$.

Figure 11 illustrates the difference in the GISAXS patterns when the beam is aligned parallel or perpendicular to the alignment direction for FDU-15 film templated by Pluronic P123 (108). In the parallel direction, the diffraction pattern is well defined with multiple reflections as expected for a highly aligned sample (Figure 11A). For 2D structures such as cylinders, there are no correlations along the long axes of the FDU-15 films that would lead to diffraction peaks in the scattering profile. As expected, Figure 11B exhibits significantly less scattering peaks (note that the color scales are different) with the higher order reflections not as well defined. This is as expected for perpendicular direction of alignment relative to the X-ray beam. Figure 11C illustrates the normalized scattering intensity of the primary diffraction peak as a function of alignment angle of the GISAXS on the sample. The sharp peak associated with this film is representative of a highly aligned sample. In this case, the Hermans' orientational factor, S , is 0.98.

The orientation is strongly dependent on the rate at which the sample is pulled through the hot zone (109). At sufficiently slow rates, the orientation is modest from zone annealing with $S < 0.8$. This decrease in the optimal alignment is attributed to the time that the sample is exposed to elevated temperatures as sufficient to allow some relaxations in the chains. At intermediate velocities, highly aligned mesoporous carbon films with S as high as 0.98 can be obtained as shown in Figure 11. At high velocity, the alignment is also decreased to $S \sim 0.9$, which is attributed to the limited time in the hot zone that provides the energy requisite for re-organization of the template in the resol matrix. With appropriate processing, namely additional time for thermopolymerization, these aligned structures can be maintained in the carbonized films (108). Additionally, films processed by zone annealing appear to be more resilient to carbonization with the mesostructure remaining on carbonization for FDU-15 templated by Pluronic F127 when zone annealed (108), while the simple thermopolymerized sample collapses (69).

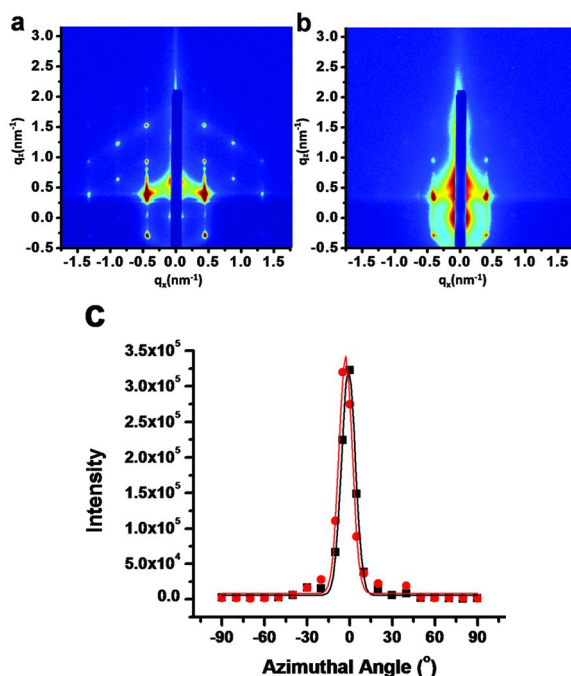


Figure 11. GISAXS profiles for FDU-15 film subject to zone annealing examining the structure (a) parallel ($\varphi=0^\circ$) and (b) perpendicular ($\varphi=90^\circ$) to the moving direction of the substrate. The color scales are different in (a) and (b) and span from highest intensity (red) to background incoherent scattering (blue). The orientation can be best illustrated by examination of the intensity of the primary diffraction peak in q_x as a function of azimuthal angle at incident angles of 0.07° (below critical angle, red circle) and 0.15° (above critical angle, black square). Reproduced with permission from ref (108). Copyright 2013 the Royal Society of Chemistry.

Elastomer Shear through Solvent Vapor Annealing

Alternatively, another simple method for fabricating highly aligned nanostructures is solvent vapor annealing with a soft, flexible elastomer capping layer such as crosslinked poly(dimethylsiloxane) (PDMS) (111); differential swelling of the PDMS and polymer produces a shear force at the polymer-PDMS interface to align the ordered domains. Interestingly, the orientation of the alignment can be controlled by the shape and placement of elastomer cap, which provides a simple route for controlling the alignment direction and to achieve macroscopic alignment in porous carbon thin films. Figure 12A shows the surface morphology of poly(ethylene oxide)-*block*-poly(ethyl acrylate)-*block*-polystyrene (PEO-*b*-PEA-*b*-PS) : resol film after annealed by MEK vapor, which consists of long-range ordered cylinders with a characteristic fingerprint morphology that is commonly observed in block copolymers with parallel cylindrical morphology. The isotropic properties of this mesostructure can be clearly confirmed by the FFT of the AFM micrographs as shown in the inset of Figure 12A which yields an isotropic ring and its radius is associated with the average cylinder to cylinder spacing. When the PEO-*b*-PEA-*b*-PS : resol film is capped with a crosslinked PDMS slab with same SVA conditions, the cylindrical domains of film is highly aligned along the shear direction with stripe patterns as shown in the micrograph (Figure 12B). From the FFT of the AFM phase images as the inset of Figure 12B, the alignment of the structure can be clearly confirmed by the two orders of diffraction spots. This highly aligned cylindrical morphology remains after crosslinking the resol during thermal annealing and subsequent carbonization. This provides a simple method for aligning the mesoporous carbon films that combines the common SVA to enhance ordering with a directional field due to the shearing associated with the drying of the PDMS.

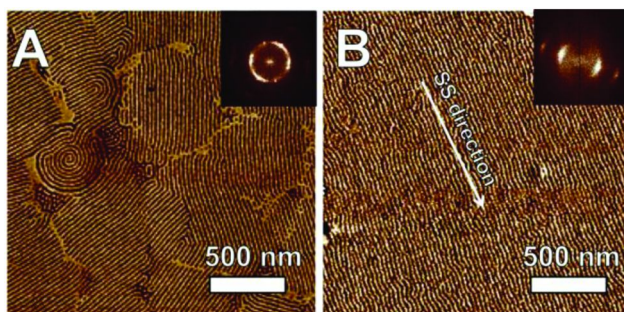


Figure 12. AFM micrographs of surface of PEO-*b*-PEA-*b*-PS:resol polymer films after (A) solvent vapor annealing (SVA) and (B) solvent vapor annealing with soft shear (SVA-SS). The inset FFT of the micrograph illustrates the orientation of the cylinders.

Outlook and Opportunities

Soft templating (23, 37) has enabled the facile fabrication of mesoporous carbon films (48, 89). Depending on the selection of precursor, the ordered structure can occur on casting (50) or may require heating (39). This later case provides significant opportunities for further manipulation of the structure as has been illustrated herein. However, there remains opportunities for improvements that occur be beneficial to potential applications. For example, perpendicular alignment of cylindrical mesopores through the film thickness would be beneficial for membrane separations; this orientation was obtained in the initial report for soft templated mesoporous carbons, but this approach required two separate vapor exposures (48). Methods for alignment of block copolymers (35, 102, 112–114) should be applicable to the cooperative assembly with resol approach, but have not been demonstrated. Additionally although free standing mesoporous carbon thin films have been synthesized (115, 116), these methods to separate the film from a substrate are time consuming and require specific surface chemistries for the substrate. A continuous approach mimicking carbon fiber production for mesoporous carbon films would also illustrate the scalability of these methods; kilogram scale synthesis of mesoporous carbon powders has been demonstrated (117), so it should be possible to scale to large area films. Additionally, the fabrication of mesoporous composites (118, 119) for added functionality in thin films has not been fully explored; one example in the literature illustrated a loss of ordering at modest loadings of metal oxide in thin films (70). It is unclear if there are routes to avoid the degradation in structural order for these composite materials.

References

1. Zhai, Y.; Dou, Y.; Zhao, D.; Fulvio, P. F.; Mayes, R. T.; Dai, S. *Adv. Mater.* **2011**, *23*, 4828.
2. Huang, Z.-h.; Wang, L.; Bai, Y.; Kang, F.-y. *New Carbon Mater.* **2012**, *27*, 321.
3. Stein, A.; Wang, Z.; Fierke, M. A. *Adv. Mater.* **2009**, *21*, 265.
4. Lee, J.; Kim, J.; Hyeon, T. *Adv. Mater.* **2006**, *18*, 2073.
5. Tanaka, S.; Nakatani, N.; Doi, A.; Miyake, Y. *Carbon* **2011**, *49*, 3184.
6. Dai, M.; Maxwell, S.; Vogt, B. D.; La Belle, J. T. *Anal. Chim. Acta* **2012**, *738*, 27.
7. Li, H.-Q.; Liu, R.-L.; Zhao, D.-Y.; Xia, Y.-Y. *Carbon* **2007**, *45*, 2628.
8. Lee, J.; Yoon, S.; Hyeon, T.; Oh, S. M.; Kim, K. B. *Chem. Commun.* **1999**, 2177.
9. Zhuang, X.; Wan, Y.; Feng, C.; Shen, Y.; Zhao, D. *Chem. Mater.* **2009**, *21*, 706.
10. Wu, C. G.; Bein, T. *Science* **1994**, *266*, 1013.
11. Ryoo, R.; Joo, S. H.; Jun, S. *J. Phys. Chem. B* **1999**, *103*, 7743.
12. Yang, H. F.; Zhao, D. Y. *J. Mater. Chem.* **2005**, *15*, 1217.
13. Ryoo, R.; Joo, S. H.; Kruk, M.; Jaroniec, M. *Adv. Mater.* **2001**, *13*, 677.
14. Lu, A. H.; Schuth, F. *Adv. Mater.* **2006**, *18*, 1793.

15. Lin, M.-L.; Huang, C.-C.; Lo, M.-Y.; Mou, C.-Y. *J. Phys. Chem. C* **2008**, *112*, 867.
16. Stein, A.; Wilson, B. E.; Rudisill, S. G. *Chem. Soc. Rev.* **2013**, *42*, 2763.
17. Wang, Z.; Li, F.; Ergang, N. S.; Stein, A. *Chem. Mater.* **2006**, *18*, 5543.
18. Cychoosz, K. A.; Guo, X.; Fan, W.; Cimino, R.; Gor, G. Y.; Tsapatsis, M.; Neimark, A. V.; Thommes, M. *Langmuir* **2012**, *28*, 12647.
19. Stein, A.; Li, F.; Denny, N. R. *Chem. Mater.* **2008**, *20*, 649.
20. Petkovich, N. D.; Stein, A. *Chem. Soc. Rev.* **2013**, *42*, 3721.
21. Deng, Y.; Liu, C.; Yu, T.; Liu, F.; Zhang, F.; Wan, Y.; Zhang, L.; Wang, C.; Tu, B.; Webley, P. A.; Wang, H.; Zhao, D. *Chem. Mater.* **2007**, *19*, 3271.
22. Snyder, M. A.; Lee, J. A.; Davis, T. M.; Scriven, L. E.; Tsapatsis, M. *Langmuir* **2007**, *23*, 9924.
23. Liang, C. D.; Dai, S. *J. Am. Chem. Soc.* **2006**, *128*, 5316.
24. Brinker, C. J.; Lu, Y. F.; Sellinger, A.; Fan, H. Y. *Adv. Mater.* **1999**, *11*, 579.
25. Brinker, C. J.; Dunphy, D. R. *Curr. Opin. Colloid Interface Sci.* **2006**, *11*, 126.
26. Nguyen-Thai, N. U.; Hong, S. C. *Carbon* **2014**, *69*, 571.
27. Ngoc, U. N. T.; Hong, S. C. *Macromolecules* **2013**, *46*, 5882.
28. Tang, C. B.; Kowalewski, T.; Matyjaszewski, K. *Macromolecules* **2003**, *36*, 1465.
29. Tang, C. B.; Tracz, A.; Kruk, M.; Zhang, R.; Smilgies, D. M.; Matyjaszewski, K.; Kowalewski, T. *J. Am. Chem. Soc.* **2005**, *127*, 6918.
30. Tang, C. B.; Qi, K.; Wooley, K. L.; Matyjaszewski, K.; Kowalewski, T. *Angew. Chem., Int. Ed.* **2004**, *43*, 2783.
31. Cavicchi, K. A.; Russell, T. P. *Macromolecules* **2007**, *40*, 1181.
32. Morkved, T. L.; Lu, M.; Urbas, A. M.; Ehrichs, E. E.; Jaeger, H. M.; Mansky, P.; Russell, T. P. *Science* **1996**, *273*, 931.
33. Gopinadhan, M.; Majewski, P. W.; Choo, Y.; Osuji, C. O. *Phys. Rev. Lett.* **2013**, *110*, 078301.
34. Bosse, A. W.; Douglas, J. F.; Berry, B. C.; Jones, R. L.; Karim, A. *Phys. Rev. Lett.* **2007**, *99*, 216101.
35. Mansky, P.; Liu, Y.; Huang, E.; Russell, T. P.; Hawker, C. J. *Science* **1997**, *275*, 1458.
36. Kim, S. O.; Solak, H. H.; Stoykovich, M. P.; Ferrier, N. J.; de Pablo, J. J.; Nealey, P. F. *Nature* **2003**, *424*, 411.
37. Meng, Y.; Gu, D.; Zhang, F. Q.; Shi, Y. F.; Yang, H. F.; Li, Z.; Yu, C. Z.; Tu, B.; Zhao, D. Y. *Angew. Chem., Int. Ed.* **2005**, *44*, 7053.
38. Florent, M.; Xue, C.; Zhao, D.; Goldfarb, D. *Chem. Mater.* **2012**, *24*, 383.
39. Schuster, J.; Koehn, R.; Doeblinger, M.; Keilbach, A.; Amenitsch, H.; Bein, T. *J. Am. Chem. Soc.* **2012**, *134*, 11136.
40. Labiano, A.; Dai, M.; Young, W.-S.; Stein, G. E.; Cavicchi, K. A.; Epps, T. H., III; Vogt, B. D. *J. Phys. Chem. C* **2012**, *116*, 6038.
41. Deng, Y.; Liu, J.; Liu, C.; Gu, D.; Sun, Z.; Wei, J.; Zhang, J.; Zhang, L.; Tu, B.; Zhao, D. *Chem. Mater.* **2008**, *20*, 7281.
42. Jung, Y. S.; Ross, C. A. *Nano Lett.* **2007**, *7*, 2046.
43. Albert, J. N. L.; Epps, T. H., III. *Mater. Today* **2010**, *13*, 24.

44. Hong, S. W.; Huh, J.; Gu, X.; Lee, D. H.; Jo, W. H.; Park, S.; Xu, T.; Russell, T. P. *Proc. Natl. Acad. Sci. U.S.A.* **2012**, *109*, 1402.
45. Yager, K. G.; Berry, B. C.; Page, K.; Patton, D.; Karim, A.; Amis, E. J. *Soft Matter* **2009**, *5*, 622.
46. Ruiz, R.; Kang, H.; Detcheverry, F. A.; Dobisz, E.; Kercher, D. S.; Albrecht, T. R.; de Pablo, J. J.; Nealey, P. F. *Science* **2008**, *321*.
47. Sohn, K. E.; Kojio, K.; Berry, B. C.; Karim, A.; Coffin, R. C.; Bazan, G. C.; Kramer, E. J.; Sprung, M.; Wang, J. *Macromolecules* **2010**, *43*, 3406.
48. Liang, C. D.; Hong, K. L.; Guiochon, G. A.; Mays, J. W.; Dai, S. *Angew. Chem., Int. Ed.* **2004**, *43*, 5785.
49. Albert, J. N. L.; Bogart, T. D.; Lewis, R. L.; Beers, K. L.; Fasolka, M. J.; Hutchison, J. B.; Vogt, B. D.; Epps, T. H. *Nano Lett.* **2011**, *11*, 1351.
50. Tanaka, S.; Katayama, Y.; Tate, M. P.; Hillhouse, H. W.; Miyake, Y. *J. Mater. Chem.* **2007**, *17*, 3639.
51. Tanaka, S.; Nishiyama, N.; Egashira, Y.; Ueyama, K. *Chem. Commun.* **2005**, 2125.
52. Koganti, V. R.; Dunphy, D.; Gowrishankar, V.; McGehee, M. D.; Li, X.; Wang, J.; Rankin, S. E. *Nano Lett.* **2006**, *6*, 2567.
53. Ji, S.; Liu, C.-C.; Liao, W.; Fenske, A. L.; Craig, G. S. W.; Nealey, P. F. *Macromolecules* **2011**, *44*, 4291.
54. Carvalho, B. L.; Thomas, E. L. *Phys. Rev. Lett.* **1994**, *73*, 3321.
55. Suh, H. S.; Kang, H. M.; Nealey, P. F.; Char, K. *Macromolecules* **2010**, *43*, 4744.
56. Tirumala, V. R.; Romang, A.; Agarwal, S.; Lin, E. K.; Watkins, J. J. *Adv. Mater.* **2008**, *20*, 1603.
57. Bates, F. S.; Fredrickson, G. H. *Phys. Today* **1999**, *52*, 32.
58. Valkama, S.; Nykanen, A.; Kosonen, H.; Ramani, R.; Tuomisto, F.; Engelhardt, P.; ten Brinke, G.; Ikkala, O.; Ruokolainen, J. *Adv. Funct. Mater.* **2007**, *17*, 183.
59. Kosonen, H.; Valkama, S.; Nykanen, A.; Toivanen, M.; ten Brinke, G.; Ruokolainen, J.; Ikkala, O. *Adv. Mater.* **2006**, *18*, 201.
60. Deng, Y.; Liu, C.; Gu, D.; Yu, T.; Tu, B.; Zhao, D. *J. Mater. Chem.* **2008**, *18*, 91.
61. Song, L.; Feng, D.; Campbell, C. G.; Gu, D.; Forster, A. M.; Yager, K. G.; Fredin, N.; Lee, H.-J.; Jones, R. L.; Zhao, D.; Vogt, B. D. *J. Mater. Chem.* **2010**, *20*, 1691.
62. Stein, G. E.; Kramer, E. J.; Li, X.; Wang, J. *Macromolecules* **2007**, *40*, 2453.
63. Matsen, M. W. *Macromolecules* **1995**, *28*, 5765.
64. Winey, K. I.; Thomas, E. L.; Fetters, L. J. *Macromolecules* **1992**, *25*, 422.
65. Meng, Y.; Gu, D.; Zhang, F.; Shi, Y.; Cheng, L.; Feng, D.; Wu, Z.; Chen, Z.; Wan, Y.; Stein, A.; Zhao, D. *Chem. Mater.* **2006**, *18*, 4447.
66. Tsarkova, L.; Knoll, A.; Krausch, G.; Magerle, R. *Macromolecules* **2006**, *39*, 3608.
67. Vogt, B. D.; Chavez, V. L.; Dai, M.; Arreola, M. R. C.; Song, L.; Feng, D.; Zhao, D.; Perera, G. M.; Stein, G. E. *Langmuir* **2011**, *27*, 5607.
68. Fasolka, M. J.; Mayes, A. M. *Ann. Rev. Mater. Res.* **2001**, *31*, 323.

69. Song, L.; Feng, D.; Fredin, N. J.; Yager, K. G.; Jones, R. L.; Wu, Q.; Zhao, D.; Vogt, B. D. *ACS Nano* **2010**, *4*, 189.
70. Dai, M.; Song, L.; LaBelle, J. T.; Vogt, B. D. *Chem. Mater.* **2011**, *23*, 2869.
71. Feng, D.; Lv, Y.; Wu, Z.; Dou, Y.; Han, L.; Sun, Z.; Xia, Y.; Zheng, G.; Zhao, D. *J. Am. Chem. Soc.* **2011**, *133*, 15148.
72. Wang, X.; Zhu, Q.; Mahurin, S. M.; Liang, C.; Dai, S. *Carbon* **2010**, *48*, 557.
73. Qiang, Z.; Xue, J. C.; Cavicchi, K. A.; Vogt, B. D. *Langmuir* **2013**, *29*, 3428.
74. Harrison, C.; Cheng, Z. D.; Sethuraman, S.; Huse, D. A.; Chaikin, P. M.; Vega, D. A.; Sebastian, J. M.; Register, R. A.; Adamson, D. H. *Phys. Rev. E* **2002**, *66*, 011706.
75. Jin, J.; Nishiyama, N.; Egashira, Y.; Ueyama, K. *Chem. Comm.* **2009**, 1371.
76. Song, L. Y.; Feng, D.; Lee, H. J.; Wang, C. Q.; Wu, Q. Y.; Zhao, D. Y.; Vogt, B. D. *J. Phys. Chem. C* **2010**, *114*, 9618.
77. Cao, L.; Man, T.; Kruk, M. *Chem. Mater.* **2009**, *21*, 1144.
78. Wickramaratne, N. P.; Jaroniec, M. *Carbon* **2013**, *51*, 45.
79. Lodge, T. P.; Pudil, B.; Hanley, K. J. *Macromolecules* **2002**, *35*, 4707.
80. Lodge, T. P.; Hanley, K. J.; Pudil, B.; Alahapperuma, V. *Macromolecules* **2003**, *36*, 816.
81. Lai, C. J.; Russel, W. B.; Register, R. A. *Macromolecules* **2002**, *35*, 841.
82. Chastek, T. Q.; Lodge, T. P. *J. Polym. Sci. B* **2006**, *44*, 481.
83. Xuan, Y.; Peng, J.; Cui, L.; Wang, H. F.; Li, B. Y.; Han, Y. C. *Macromolecules* **2004**, *37*, 7301.
84. Thomas, K. R.; Chenneviere, A.; Reiter, G.; Steiner, U. *Phys. Rev. E* **2011**, *83*, 021804.
85. Gotrik, K. W.; Hannon, A. F.; Son, J. G.; Keller, B.; Alexander-Katz, A.; Ross, C. A. *ACS Nano* **2012**, *6*, 8052.
86. Hayward, R. C.; Pochan, D. J. *Macromolecules* **2010**, *43*, 3577.
87. Sinturel, C.; Vayer, M.; Morris, M.; Hillmyer, M. A. *Macromolecules* **2013**, *46*, 5399.
88. Atornigitjawat, P.; Runt, J. *J. Phys. Chem. B* **2007**, *111*, 13483.
89. Schuster, J.; Koehn, R.; Keilbach, A.; Doeblinger, M.; Amenitsch, H.; Bein, T. *Chem. Mater.* **2009**, *21*, 5754.
90. Zhang, X. Y.; Wang, X. Y.; Su, J. C.; Jiang, L. L.; Wu, H.; Wu, C. J. *Power Sources* **2012**, *199*, 402.
91. Tanev, P. T.; Pinnavaia, T. J. *Chem. Mater.* **1996**, *8*, 2068.
92. Mastroianni, S. E.; Epps, T. H., III *Langmuir* **2013**, *29*, 3864.
93. RamachandraRao, V. S.; Gupta, R. R.; Russell, T. P.; Watkins, J. J. *Macromolecules* **2001**, *34*, 7923.
94. Fujikawa, D.; Uota, M.; Sakai, G.; Kijma, T. *Carbon* **2007**, *45*, 1289.
95. Qiang, Z.; Xue, J.; Stein, G. E.; Cavicchi, K. A.; Vogt, B. D. *Langmuir* **2013**, *29*, 8703.
96. Stoykovich, M. P.; Kang, H.; Daoulas, K. C.; Liu, G.; Liu, C. C.; de Pablo, J. J.; Mueller, M.; Nealey, P. F. *ACS Nano* **2007**, *1*, 168.
97. Angelescu, D. E.; Waller, J. H.; Register, R. A.; Chaikin, P. M. *Adv. Mater.* **2005**, *17*, 1878.
98. Angelescu, D. E.; Waller, J. H.; Adamson, D. H.; Register, R. A.; Chaikin, P. M. *Adv. Mater.* **2007**, *19*, 2687.

99. Park, S.; Lee, D. H.; Xu, J.; Kim, B.; Hong, S. W.; Jeong, U.; Xu, T.; Russell, T. P. *Science* **2009**, 323.
100. Berry, B. C.; Bosse, A. W.; Douglas, J. F.; Jones, R. L.; Karim, A. *Nano Lett.* **2007**, 7, 2789.
101. Tang, C.; Wu, W.; Smilgies, D.-M.; Matyjaszewski, K.; Kowalewski, T. *J. Am. Chem. Soc.* **2011**, 133, 11802.
102. Hu, H.; Rangou, S.; Kim, M.; Gopalan, P.; Filiz, V.; Avgeropoulos, A.; Osuji, C. O. *ACS Nano* **2013**, 7, 2960.
103. Segalman, R. A.; Yokoyama, H.; Kramer, E. J. *Adv. Mater.* **2001**, 13, 1152.
104. Mansky, P.; DeRouchey, J.; Russell, T. P.; Mays, J.; Pitsikalis, M.; Morkved, T.; Jaeger, H. *Macromolecules* **1998**, 31, 4399.
105. Gopinadhan, M.; Majewski, P. W.; Choo, Y.; Osuji, C. O. *Phys. Rev. Lett.* **2013**, 110, 078301.
106. Tracz, A.; Jeszka, J. K.; Watson, M. D.; Pisula, W.; Mullen, K.; Pakula, T. *J. Am. Chem. Soc.* **2003**, 125, 1682.
107. Pfann, W. G. *Science* **1962**, 135, 1101.
108. Xue, J.; Singh, G.; Qiang, Z.; Karim, A.; Vogt, B. D. *Nanoscale* **2013**, 5, 7928.
109. Xue, J. C.; Singh, G.; Qiang, Z.; Yager, K. G.; Karim, A.; Vogt, B. D. *Nanoscale* **2013**, 5, 12440.
110. Hermans, J. J.; Hermans, P. H.; Vermaas, D.; Weidinger, A. *Recl. Trav. Chim. Pays-Bas* **1946**, 65, 427.
111. Qiang, Z.; Zhang, L.; Stein, G. E.; Cavicchi, K. A.; Vogt, B. D. *Macromolecules* **2014**, 47, 1109.
112. Thurn-Albrecht, T.; DeRouchey, J.; Russell, T. P.; Kolb, R. *Macromolecules* **2002**, 35, 8106.
113. Yoo, M.; Kim, S.; Jang, S. G.; Choi, S.-H.; Yang, H.; Kramer, E. J.; Lee, W. B.; Kim, B. J.; Bang, J. *Macromolecules* **2011**, 44, 9356.
114. Phillip, W. A.; O'Neill, B.; Rodwogin, M.; Hillmyer, M. A.; Cussler, E. L. *ACS Appl. Mater. Interfaces* **2010**, 2, 847.
115. Fang, Y.; Lv, Y.; Che, R.; Wu, H.; Zhang, X.; Gu, D.; Zheng, G.; Zhao, D. *J. Am. Chem. Soc.* **2013**, 135, 1524.
116. Feng, D.; Lv, Y.; Wu, Z.; Dou, Y.; Han, L.; Sun, Z.; Xia, Y.; Zheng, G.; Zhao, D. *J. Am. Chem. Soc.* **2011**, 133, 15148.
117. Wang, J.; Xue, C.; Lv, Y.; Zhang, F.; Tu, B.; Zhao, D. *Carbon* **2011**, 49, 4580.
118. Wu, Z.; Lv, Y.; Xia, Y.; Webley, P. A.; Zhao, D. *J. Am. Chem. Soc.* **2012**, 134, 2236.
119. Gorka, J.; Jaroniec, M. *J. Phys. Chem. C* **2008**, 112, 11657.

Chapter 4

Soft-Templated Mesoporous Carbons: Chemistry and Structural Characteristics

Dipendu Saha,^{*1} Renju Zacharia,² and Amit K. Naskar³.

¹Chemical Engineering Department, Widener University,
Once University Place, Chester, Pennsylvania 19013, United States

²Institut de recherche sur l'hydrogène, Université du Québec à
Trois-Rivières, Trois-Rivières (QC), G9A 5H7, Canada

³Materials Science and Technology Division, Oak Ridge National
Laboratory, One Bethel Valley Road, M.S. 6053,
Oak Ridge, Tennessee 37821, United States

*E-mail: dipendus@gmail.com, dsaha@mail.widener.edu.
Phone +1 610 499 4056. Fax: +1 610 499 4059.

Soft-templated mesoporous carbon is a relatively newer variety of synthetic nanoporous carbon. This type of carbon is templated by the micellar actions of amphiphilic surfactants with the phenolic type of carbon precursors. The role of surfactants is similar to that of silica in the case of hard-templating, i.e., to dictate the structural characteristics and mesoporosity of the carbons. A wide variety of amphiphilic surfactants along with synthetic and natural precursors were employed for use as a carbon source. Despite being termed as mesoporous carbon, these materials usually contain a large fraction of micropore distribution which is clearly observed in the type IV nature of nitrogen adsorption-desorption plot. Because of the unique mesopore feature of such carbon, it has found wide application in several unique fields of science and technology. This particular review briefly discusses the synthesis protocols of mesoporous carbons, including the types of carbon precursors and surfactants along with their critical role in dictating the structural characteristics. It also introduces the role of physical and chemical activation in enhancing the porosity and the key structural features of soft-templated mesoporous carbons.

1. Introduction

Nanoporous materials have gained increased attention in today's scientific and technological advancement because of their broad range of applicability in numerous sectors. Amongst all types of nanoporous materials, carbon is probably the most ubiquitous material employed so far in scientific and technological fields. Several inherent advantages of carbon-based materials are chemical inertness of majority of chemicals, easy functionalization, hydrophobicity, high thermal and electrical conductivity, mechanical stability, low density and last but not the least, low cost and ease of fabrication. According to the classification of pores made by International Union of Pure and Applied Chemistry (IUPAC), the pores can be divided into three main categories (1), (i) Micropores (pore width less than 2 nm or 20 Å), (ii) Mesopores (pore width less than 2-50 nm or 20-500 Å) and (iii) Macropores (pore width greater than 50 nm or 500 Å). There are quite large fractions of research works that often referred to the term 'nanoporous' materials. There was no clear categorization of the exact dimension of a nanopore until recently, when IUPAC set the dimension of nanopores to be less than 100 nm. Generally, microporosity and mesoporosity are the most characteristic features of the carbon-based materials, which are also key application sites of the porous carbons.

Amongst all the carbon-based materials, so-called *activated carbons* are the most widely employed nanoporous carbon. While the root of the activated carbon can be linked with the historical origin, modern technology has improved both the quality and characteristic features of activated carbon materials. These materials can be synthesized from inexpensive natural (2) or synthetic (3) carbon-rich precursors, although several post-synthetic modifications, like physical and chemical activation provide the enhancement of the available surface area (4-6) thereby increasing the costs. Today, the Brunauer-Emmett-Teller (BET) (7) surface area of commercially available activated carbons may be as high as 3000 m²/g. The pores present in the activated carbons are mostly microporous in nature. Although the versatility of activated carbon materials can be reached in several industrial, scientific or household applications (8), several drawbacks of activated carbon materials still lie with its structural morphology. The key drawbacks of activated carbons materials are (i) difficulty to attain mesoporosity in the structure leading to inability to adsorb larger molecules, (ii) inability to tune the pore structure in terms of pore width and pore volume leading to the difficulty to attain the desired structural morphology for a particular application (iii) difficulty to attain the ordered porous structure and hierarchical porosity and (iv) almost definite collapse of porous structure upon graphitization. Because of these downsides of activated carbons, researchers made a series of efforts to artificially "*template*" nanoporous carbon structures to achieve the desired porosity and eliminate the majority of the problems of activated carbons.

The work of Gilbert *et al.* (9) and Knox *et al.* (10) established the first step towards the fabrication of ordered carbon by employing an inorganic mold or template. Several years later, in 1999, Ryoo *et al.* (11) demonstrated that ordered mesoporosity in the carbon materials can be successfully improved by utilizing a silica mold, more commonly known as 'hard template' with sucrose as the

carbon precursor; where the resultant carbon becomes the structural ‘negative’ of the template or mold (12). The templating process can be well explained by employing a metaphor with the casting process in the larger or macroscopic scale (13–15). In that scale, a ‘mold’ consisting of wood, plaster, wax or similar rigid materials is employed while its void spaces are filled with the precursor materials to be cast followed by several processing protocols. At the end of the process, the mold is removed and the recovered cast material becomes the negative of the mold. The similar concept can be scaled down to the nanometer level. At the nanoscale, the mold is termed a ‘template’ (13). In general, the growth in efforts of synthesizing templated porous carbons reached a steady rise after the discovery of the mesoporous silica M41S family (16). These are mesoporous silica formulated with an organosilicious material and a suitable surfactant for templating. The carbons generated from these precursors contain very large fractions of mesoporosity along with the associated microporosity in the pore wall. The carbons also possessed long range crystalline order of cubic to hexagonal shape as observed in the small-angle x-ray scattering (SAXS). The types of mesoporous silica employed for this study include SBA-1 (17)/3 (17)/15 (18, 19)/16 (20, 21), MCM-41/45 (18), FDU-5 (22, 23)/12 (24) or KIT-6 (23). Besides silica, zeolite (25, 26), alumina (27, 28) or even metal-organic frameworks (MOFs) (29, 30) were also employed for hard templating purposes where the porosity of the resultant carbon varied all along from ordered and controlled meso- to micro-porosity. Several types of carbon precursors were employed for hard templating, the most common ones were sucrose (17, 24), polyfurfuryl alcohol (18, 19) and a few aromatic precursors (22, 23), like pyrrole or acenaphthene. The majority of the mesoporous carbons generated from the silicious hard templates are typically termed as CMK-1 through 5 (13) along with CMK-8 and 9 (13). The steps associated with the hard templating techniques are (31) (i) synthesis of the organic template (ii) the impregnation of template with the organic carbon precursor (iii) polymerization of the precursor within the template (iv) carbonization and (v) removal or leaching of the template to generate pure templated carbon. Although the hard-templating strategy was the first successful effort to remove the majority of the drawbacks of activated carbons in terms of controlled and ordered meso- as well as micro-porosity, the underlying limitation of hard-templating are (32, 33)

- (1) *Highly tedious procedure*: The synthesis protocol in the hard-templating strategy is quite tedious and several steps are involved starting from synthesis of template to the sacrificial leaching of it.
- (2) *Low yield*: The final yield of the mesoporous carbon is very low. As the volume of carbon material is the negative of the template, the volume of it corresponds to the pore volume of the template. As the template materials do not possess a high pore volume, the yield of the resultant carbon is very low making it very difficult to scale-up for large-scale production at the commercial scale.
- (3) *Expensive in nature*: Owing to the involvement of an expensive sacrificial silica template that cannot be recovered after leaching and a low yield of carbon materials, hard templated carbons are very expensive in nature.

- (4) *Involvement of highly toxic chemicals*: Several toxic chemicals are required in the synthesis protocol of these hard-templated carbons. Organosilicious compounds, like alkyl orthosilicates, which are the precursors of the silica templates, are toxic in nature. But, the most toxic chemical involved in the hard-templating method is hydrofluoric acid (HF), which is most efficient towards dissolving silicate materials and hence rigorously employed during template removal. Because of extreme toxicity, HF requires additional safety protocols including personal safety gear and training.
- (5) *Instability during graphitization*: Although more resistant than activated carbons, which always collapse during graphitization, the resistance of the hard-templated carbons to the graphitization process is not improved to a significant degree.
- (6) *Difficulties in generating monolithic structures*: Owing to the presence of an additional template removal step, it is very difficult to achieve a monolithic structure in the hard-templated carbons.

2. Soft-Templated Mesoporous Carbon

2.1. Principles of Soft Templating

Soft templating is the newer strategy of synthesizing mesoporosity in carbons. Intuitively thinking, such a strategy, in fact, is not a completely new discovery in the field of templating. The soft-templating strategy was originally employed to synthesize mesoporous silica, which, in turn, was employed as a sacrificial hard template. However, directly employing soft templating in the case of carbon materials required several other stringent requirements, especially, narrowing down of the choice of carbon precursors. Typically, in this process, an amphiphile is required that can form a micelle in a suitable solvent when its concentration is above the critical micelle concentration (CMC). An amphiphile consists of a hydrophilic and a hydrophobic end; in a polar solvent like water, the Hildebrand solubility factor dictates the hydrophobic end to orient in the center of the micelle, whereas the hydrophilic end orientates on the periphery. Because of the interactions between the micelle and solution, often the micelles take different types of morphology, like cylindrical, spherical or ellipsoidal. When a suitable carbon precursor enters such a system, it can get attached with the external part, or the hydrophilic part of the surfactant through hydrogen bonding or electrostatic interactions. If the carbon precursor is a monomer, then an additional step of polymerization of the monomer is required to build a continuous carbon matrix. It is also noteworthy to mention that the ideal surfactants should possess zero to minimal char yield. At this point, upon pyrolysis or carbonization, the carbon precursor yields the carbon network. The hydrophobic part, which was at the center of micelle and not attached to the carbon precursor, provides the mesopores, as the surfactant does not give a char yield. This technique immediately eliminates the requirement of an additional step for the removal of templates. It also needs to be mentioned that one of challenging parts of this strategy is to attain the ideal polymerization or cross-linking of the carbon precursor while restricting

it to move away from the surfactant and lose the driving force of templating. Poor cross-linking will keep the polymer precursor below its glass-transition temperature (T_g) thereby allowing it to get soft or molten during carbonization resulting in the collapse of the pore whereas too high cross-linking will ‘force’ the precursor to detach from the surfactants. Figure 1 shows the schematic of soft templating from the research of our work (34).

Although the majority of the soft-templated mesoporous carbons are synthesized in bulk form, a few of them were generated by adopting a strategy, known as Evaporation Induced Self-Assembly (EISA), which is quite a powerful technique to induce highly ordered structure. The origin of EISA can be rooted to the solvent annealing or solvent-vapor annealing technique (35, 36). In the thin film of block copolymers, owing to micro phase separation, highly ordered periodic structures can be obtained at equilibrium and thus can be transferred to the other substances templated by the polymers. However, being a kinetically controlled process (36), the direct formation of the block copolymer film from its solvents results in a non-equilibrium disorganized structure. In order to induce equilibrium ordering, the polymer film is exposed to solvent vapor typically below the bulk T_g of both the blocks resulting in a swollen film and subsequent solvent evaporation resulting in a highly ordered structure. In this solvent-vapor annealing (SVA) technique, a gradient in concentration of the solvent exists along the direction normal to the film, as the solvent evaporates, the ordering propagates down through the film. The EISA technique links its root to the concept of SVA in terms of concentration gradient of solvent around the thin film thereby allowing the propagation of ordering in the template-precursor composite. However, one key difference with SVA is that it is reversible in nature, whereas EISA is inherently irreversible because of simultaneous cross-linking of the precursors at the time of solvent evaporation (37). Although EISA was incorporated rigorously in the case of mesoporous oxide fabrication (38), its utilization for mesoporous carbon is limited (39–41).

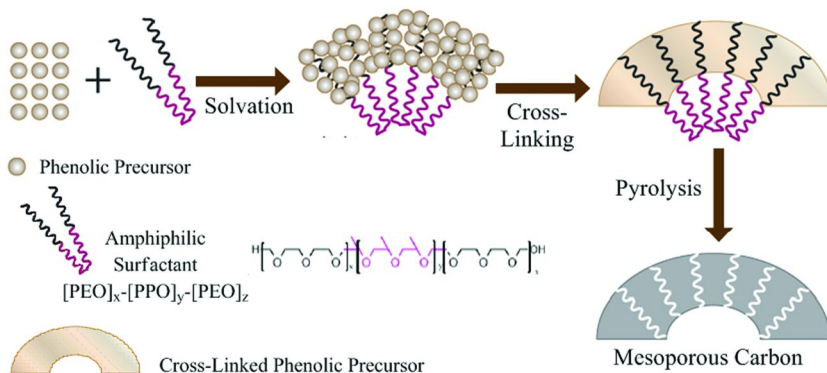


Figure 1. Schematic of mesoporous carbon synthesis from carbon precursor and surfactant. Reproduced with permission from reference (34). 2014 American Chemical Society.

2.2. Templates

Typically, the surfactants or the soft templates employed in the soft templating are either of the ionic or the non-ionic type. The most common ionic surfactants employed in this study is cetyl trimethylammonium bromide (CTAB) which can employ electrostatic interactions with the precursor. Probably, the first effort of synthesizing soft-templated mesoporous carbons was made by Moriguchi et al. (42), although it did not yield the porosity because of the collapse of the mesostructure at the elevated temperature. Employing CTAB also did not help to create porosity in the work of Li et al. (43) In a later period, the CTAB was successfully employed by Lee et al. (44) to synthesize the mesoporous carbons with a surface area as high as 501 m²/g and a pore volume of 0.41 cm³/g.

Amongst the non-ionic surfactants, Brij surfactants [C_nH_{2n+1}(EO)_x, EO=ethyleneoxy] were employed in the research of Z.J. Li et al. (45) Although ordered structure was observed in the precursor phase, no porosity was observed upon carbonization, most likely because of high carbon yield of the template itself (37). The di-block and tri-block copolymers ([A]-[B] or [A]-[B]-[C] type) with amphiphilic character have been widely employed to template mesoporous carbons. Pluronic F127 is probably the most extensively employed soft template reported in the literature (32, 40, 46–51). It has the molecular formula [(PEO)₁₀₆(PPO)₇₀(PEO)₁₀₆, PEO=polyethylene oxide, PPO=polypropylene oxide] and average molecular weight (MW) 12,600. Pluronic P123 is a similar surfactant with lower molecular weight [(PEO)₂₀(PPO)₇₀(PEO)₂₀, M_w=5750] and was reported to be employed for templating purposes (39, 52–54). Two reverse pluronic types of surfactants, pluronic 17R4 [(PPO)₁₉(PEO)₃₃(PPO)₁₉, M_w=2650] and 25R4 [(PPO)₁₄(PEO)₂₃(PPO)₁₄] were also employed as soft templated to synthesize mesoporous carbons (55), although the characterization of the resultant porous carbon was not reported. Successful mesostructured carbons by employing the reverse tri-block copolymers [(PPO)₅₃(PEO)₁₃₆(PPO)₅₃] were demonstrated by Huang et al. (56) where the resultant mesoporous carbons demonstrated face-centered cubic mesostructure. Polystyrene-*block*-poly-4-vinylpyridine (PS-*block*-P4VP, average molecular weights: M_{n,PS}=40,000, M_{n,P4VP}=5600) is a di-block non-pluronic surfactant that was successfully employed to synthesize mesoporous carbons by Liang et al. (57) and Kosonen et al. (58) The report by Liang et al. (57) was probably the first to describe synthesizing an ordered mesoporosity by surfactant templating. Hydrogen bonding between the template and precursor (resorcinol resin) and very low char yield of the template (1.05 %) were the key reasons for the successful templating. A highly ordered carbon film with a pore width of 33.7 nm and a wall thickness of 9.0 nm was obtained in the work. Similar ordered mesoporosity was also demonstrated in the work of Kosonen et al. (58) with phenolic precursor. Despite being an excellent template, not a large volume of reports are found on the utilization of PS-*block*-P4VP, most likely because of very limited commercial availability and expense (37). Two other type of di-block copolymers were also employed for soft-templating purposes, which are polyethylene oxide-*block*-polystyrene (PEO-*b*-PS) (59) and polyethylene oxide-*block*-polymethylmethacrylate (PEO-*b*-PMMA) (60). Because of the commercial unavailability, both the surfactants are synthesized in

the laboratory by the atom transfer radical polymerization (ATRP) method. Direct carbonization of block copolymers was also reported in the literature. Kowalewski et al. (61) employed the triblock copolymers of $[(AN)_{45}(BA)_{530}(AN)_{45}]$, AN=acrylonitrile, and BA=*n*-butyl acetate) as carbon precursors and the difference in carbon yielding properties of [AN] block and pore forming [BA] blocks were employed to deposit the film. However, no porosity data were reported of this work.

Choosing the template structures is the key option for controlling the mesoporosity. In general, the hydrophobic terminal of micelles composed of the surfactant provides the mesoporosity. Therefore, in fact, all the conditions that affect the size and shape of the micelle have a strong influence on the mesoporosity of the resultant carbon. The greatest contribution to the mesopore width originates from the ratio of hydrophobicity over hydrophilicity of the surfactant, typically, a larger hydrophobic group compared to that hydrophilic one provides the larger mesopore size. The other controlling factors are pH, temperature, and addition of a suitable swelling agent. These factors are, in fact, considered earlier to tune the porosity of the surfactant templated mesoporous silica (62, 63). Meng et al. (39) reported the increase of mesopore widths of FDU-16 from 28 to 43 Å when F108 $[(PEO)_{132}(PPO)_{50}(PEO)_{132}]$ is replaced with F127 $[(PEO)_{106}(PPO)_{70}(PEO)_{106}]$, definitely suggesting a higher hydrophobicity of F127 had the contributing factor. Custom synthesized large hydrophobic group containing diblock copolymers of $[PEO]_{125}$ -*b*- $[PMMA]_{144}$ and $[PEO]_{125}$ -*b*- $[PS]_{230}$ resulted in quite large mesopore widths of 105 and 230 Å, respectively (59, 64). The effect of temperature on the mesopore width was observed when lowering the reaction temperature from 55 °C to 15 °C resulted in enhancement of the mesopore width up to 160 Å (65). Enlargement of mesopore width from 40 to 80 Å by employing Brij 58, Brij 78 or F127 surfactants in the acidic conditions was the supporting factor of contribution of pH to increase the mesopore width in the report of Choma et al. (66) Addition of swelling agents, like 1,3,5-trimethyl benzene (TMB), heptane or hexane showed only limited success, while distorting the mesopore domains (47, 67). The success of adding swelling agents was reported in work of Deng et al. (64) where the addition of decane or hexadecane into the surfactant system of $[PEO]_{125}$ -*b*- $[PS]_{230}$ enhanced the pore width from 229 Å to 374 Å, which is the probably largest width of mesopores ever reported in literature.

Shrinkage of the pore width upon carbonization is a common problem of soft or organic templating strategy (39, 68). In order to restrict the shrinkage, Liu et al. (67) incorporated tri-constituent co-assembly of F127 as a template in the mixture of phenol-formaldehyde and tetraethyl orthosilicate (TEOS), which is a silica precursor. F127 was employed to template both carbon and silica whereas in the resultant carbon-silica composite, silica acted like a “reinforcing steel bar”, did not allow shrinkage upon carbonization, and was leached later with HF. Similar reinforcing strategy can be employed by the “brick and mortar” methods of synthesizing nanocomposites (69). In the soft-templating strategy, Fulvio et al. (70) methodically replaced the RF “mortar” in the synthesis gel of soft-templated carbon with nano-structures of carbon onions or carbon black as “brick”. Changing the brick and mortar ratio can alter the mesopore volumes and widths of the carbons.

2.3. Precursors

As mentioned earlier, the surfactant or soft templating possesses place some inherent limitations on the choice of the carbon precursors. The precursor should be selected in such a way that it can be involved in the interactions with the surfactant so that the driving force of the templating can evolve in the reaction mixture. Hydroxyl groups containing aromatic precursors were commonly employed in the soft-templating purposes, most common examples are the resins of phenol (47, 49–51, 54, 59), resorcinol (46, 48, 57) and phloroglucinol (32, 71–73). Quite obviously, the strong interaction between the hydroxyl groups of those resins with the surfactant is the common cause of choosing such a surfactant. For the pluronic or PS-*block*-P4VP type of templates, the hydrogen bond between the hydroxyl group of the precursor and oxygen atom of PEO (or nitrogen atom of PS-*block*-P4VP) is the driving force. Figure 2 shows the hydrogen bonded PS-*block*-P4VP and part of Pluronic with the phenolic resins.

In general, moving towards phenol to phloroglucinol, i.e., higher hydroxyl group density within the precursor enhances the driving force of templating resulting in faster reaction time. In the phenolic resins, the phenol monomers are polymerized or cross-linked, most typically by formaldehyde (HCOH) that attaches the two phenolic rings through an $-\text{CH}_2$ linkage. Such a kind of cross-linking takes place in the *ortho* position of phenolic ring and is typically catalyzed by acid (like HCl) or base (like NaOH or Na_2CO_3). In few occasions, the cross-linking is also performed by glyoxal (74) or hexamethylenetetramine (HMTA) (58). HMTA based cross-linking is typically performed on the base catalyst and the key advantage for employing HMTA can be attributed to its less toxic nature resulting in the advantage of less hazardous processing conditions. There are two strategies observed in literature regarding the addition of precursors to the reaction system. In one kind of synthesis, initially synthesized phenolic resins are added to the surfactant solution to introduce the templating followed by drying and carbonization. In the other strategy, the precursor monomer is first allowed to dissolve in the surfactant solution thereby allowing the hydrogen bonding and “locking” structure, followed by cross-linking and generating the continuous matrix. In addition to the phenol, resorcinol and phloroglucinol, Saha et al. (75) employed a rather unusual phenolic precursor, hexaphenol (also referred to as (5H)-10,15-dihydro-2,3,7,8,12,13-hexahydroxy-tribenzo[a,d,g]cyclononene) as the carbon precursor which was cross-linked by formaldehyde in the soft-templating strategy with Pluronic P123 as the surfactant.

All the phenolic precursors employed to synthesize soft-templated mesoporous carbons are synthetic in nature. Very recently, our group has employed a natural and renewable phenolic precursor, lignin, in the synthesis of mesoporous carbons (76). Lignin is a biopolymer and structural building block of wood, which is also a by-product of the pulp and paper as well as the biofuel industries. We employed different varieties of lignin and template them with pluronic F127 (76). In the synthesis of the mesoporous carbons, we employed both formaldehyde and hexamethylenetetramine as cross-linking agents. In a particular lignin (softwood type), it was demonstrated that the templating strategy

did not require any cross-linking as the natural precursor itself was cross-linked enough to provide the continuous matrix. All the carbons generated from lignin showed significant mesoporosity. Employing a natural and renewable precursor in the synthesis of mesoporous carbons will provide the advantages of (1) Lowering of cost (2) Employment of less hazardous chemicals (3) Approach towards more benign and green chemistry and (4) Provide a good market for the lignin downstream industry. Figure 3 shows the protocol of synthesizing soft-templated mesoporous carbons from lignin (76). Another key observation made in our report is the interactions between the precursor and surfactants during thermo-gravimetric analysis (TGA). The derivative of the TGA peak of pure Pluronic F127 appears at around 388 °C, but when it is present in the precursor polymer with lignin together, this peak shifts to the higher temperature of 393-400 °C. (Figure 4) Such a 5-12 °C shift of the decomposition temperature of Pluronic F127 is considered as the fingerprint of the hydrogen bonding between template and precursor.

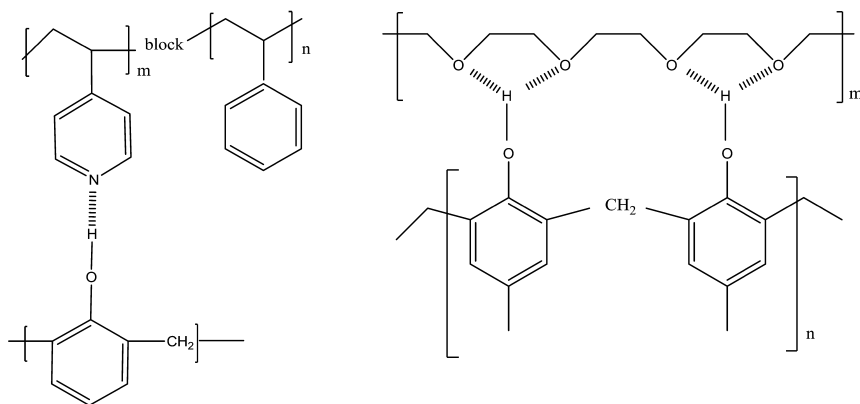


Figure 2. (a) Phenolic resin hydrogen bonded with PS-block-P4VP and (b) phenolic resin hydrogen bonded with pluronic (only [PEO] block is shown).

2.4. Activation

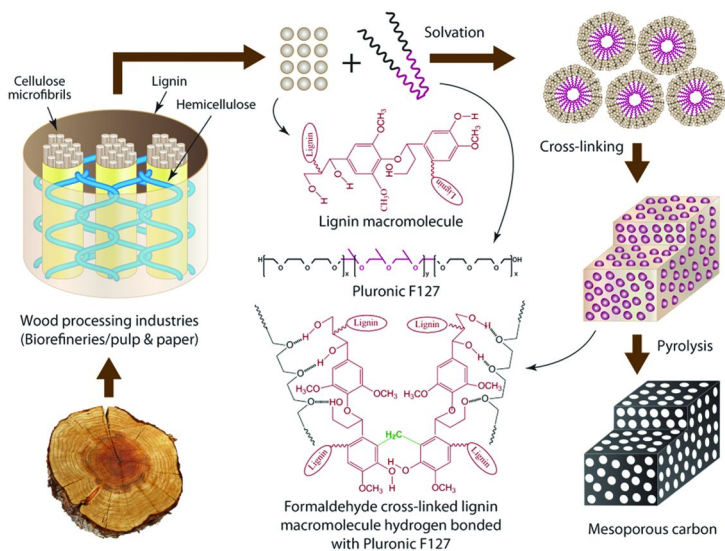


Figure 3. Strategy of synthesizing soft-templated mesoporous carbons from lignin. Reproduced with permission from reference (76). 2013 American Chemical Society

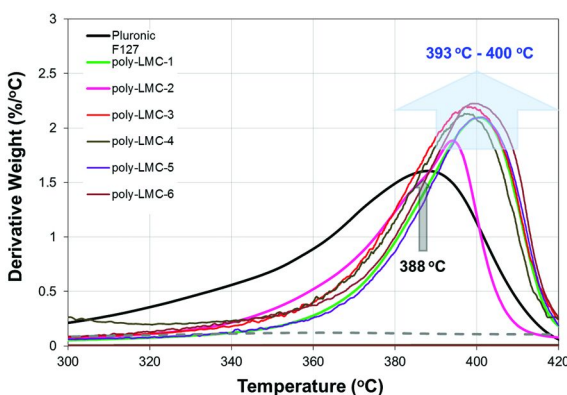


Figure 4. The comparison of derivative thermogravimetric plots of precursors of mesoporous carbon and Pluronic F127. The shift of peak decomposition temperature signifies hydrogen bonding between lignin and F127. Reproduced with permission from reference (76). 2013 American Chemical Society

Activation of carbon-based porous materials is a well-established strategy to enhance the porosity of those materials. There are two most common protocols for activation; one is activation by carbon dioxide (CO₂) at elevated temperature, also referred to as “*physical activation*” and the other technique is activation by heating the solid mixture of potassium hydroxide (KOH) and carbon in an inert atmosphere, commonly known as “*chemical activation*”.

In the physical or CO₂ activation protocol, the carbon sample is heated at moderate (600 °C) to high (about 1000 °C) temperatures in the regulated flow of CO₂ or a CO₂/N₂ mixture. It is commonly understood that CO₂ mildly oxidizes the carbon surface thereby creating the additional porosity in it with carbon monoxide (CO) as an off-gas. The reaction can be expressed as (77): $C + O_2 = 2CO$ ($\Delta H = +159$ kJ/mol). Because of this reaction, the carbon mass is significantly lost and the increase in porosity shows the dependence with degree of burn-off, temperature of activation, and CO₂ flow rate. Both hard- (78, 79) and soft-templated (80–82) mesoporous carbons have been reported to be activated with CO₂. The BET surface area of hexagonal mesostructured carbon FDU-15 is enhanced up to 2750 m²/g which is over four times that of its pristine state at 70% burn-off level (80). It is also reported that CO₂ mildly enhances the microporosity and slightly enlarges the mesopore volume. In one report (81), the enhancement of the porosity of a similar material is also observed by CO₂ activation at 65% burn-off level without significant alternation of structural integrity. CO₂ treatment demonstrated the increase of both micro- and meso-porosity upon activation. CO₂ activation of phloroglucinol derived soft-templated mesoporous carbons up to 900 °C and 3 h enhanced the BET surface area up to 1598 m²/g with significant increase in both micro- and meso-porosity (82). Our group (83) vividly examined the level of burn-off and its influence on BET surface area and pore volume in the lignin derived soft-templated mesoporous carbons. They found that the most optimum level of burn-off is 56% which enhances the BET surface area three times that of the pristine one accompanied by the simultaneous increase in both micro- and meso-pore volume (Figure 5a). This work also illustrated a linear relation between degree of burn-off and CO₂ exposure time revealing a zero order kinetics of CO₂ activation (Figure 5b).

Chemical activation by KOH is a more vigorous activation technique which results in higher porosity but at the expense of much faster alternation of ordered structure. In this technique, different proportions of solid KOH and pristine carbons are mixed and heated in an inert atmosphere. Similar to physical activation, the degree of activation is a strong function of KOH to carbon ratio, temperature of heat treatment and exposure time. The overall reactions between KOH and carbon are composed of different stages and are quite complex in nature (84, 85). KOH reacts with carbon to generate potassium and potassium carbonate, which further dissociates and/or reacts with carbon to generate potassium oxide, carbon dioxide and carbon monoxide. These reactions may be summed up to the following equations (84, 85):

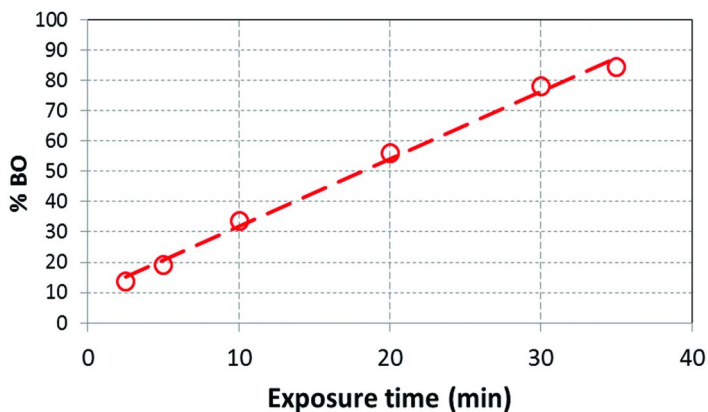
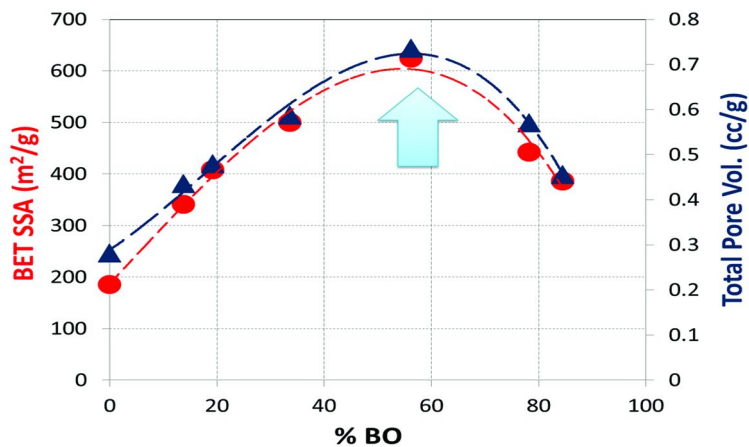
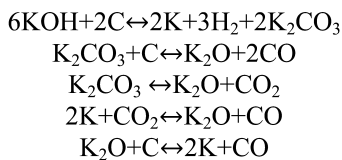


Figure 5. (a) Optimizing the degree of burn-off with BET SSA and pore volume. Reproduced with permission from reference (83). 2014 American Chemical Society. (b) Linear relation between burn-off and CO₂ exposure time suggesting a zero-order kinetics. Reproduced with permission from reference (83). Copyright 2014 American Chemical Society.

KOH activation of soft-templated mesoporous carbons is extensive in the literature (82, 86–88). Wang et al. (82) employed KOH activation of phloroglucinol-formaldehyde derived mesoporous carbons at 700–900 °C for 1 hour with a KOH/carbon ratio of 2 to 8. The BET surface area and the total pore volume were enhanced to 2037 m²/g and 1.59 cc/g along with a very high increase in both microporosity and mesoporosity. Our group (83) employed KOH activation for lignin derived mesoporous carbon with KOH/carbon ratio of 1 to 2 at the temperature of 1000 °C, in which enhancement of both micro- and meso-porosity are reported. Another key observation made by our group (83) is the monitoring of oxygen and oxygen containing functional groups on the carbon samples after activation. With the help of x-ray photoelectron spectroscopy (XPS) they quantified the oxygen containing groups in the activated samples and reported that C-O, C=O and O-C=O functionalities were enhanced upon both physical and chemical activation. Conservation of mesoporosity and mesopore width upon KOH activation is also mentioned elsewhere in literature (86, 88). The key difference between CO₂ and KOH activation is that KOH activation generally provides more micropore volume compared to that of CO₂. Therefore it results in better improvement over BET surface area as 70% of total surface area originates only from micropores (68).

Apart from CO₂ or KOH, oxygen (O₂) (80), water vapor (H₂O) (80, 89) and ammonia (NH₃) (90, 91) were also reported to be employed as activation agents. The principle of activation by oxygen is very similar to that of CO₂. Except, a quite strong oxidizing atmosphere of O₂ results in shorter exposure time and/or lower temperature. Yan et al. (80) employed this strategy to activate the ordered mesoporous carbon FDU-15 at 300–400 °C with the exposure time of 1–7 h. The optimum condition enhanced the BET SSA to 1600 m²/g and total pore volume to 1.09 cc/g. These values are two to three times that of the pristine carbon. However, the fingerprint of O₂ activation was found in the rapid destruction of the mesostructure owing to the fast burning capacity of oxygen. Activation by water vapor (steam) is also a mild activation strategy. The reaction between steam and carbon may be mimicked as (77) C+H₂O = CO +H₂ ($\Delta H=+117$ kJ/mol). Water activation of mesoporous carbon FDU-15 at the optimum condition of 800 °C/ 10 h enhanced the BET SSA and pore volume up to 2100 m²/g and 1.47 cc/g, respectively at 52% burn-off (80). Maintaining an ordered mesostructure of the silica-derived carbon by Gorka et al. (89) also serves as an illustrative feature of mildness of water activation on carbon based materials. Ammonia treatment on carbon at high temperature causes replacement of oxygen containing groups by nitrogen ones (91) and etching of carbon fragments by the radicals generated from ammonia at high temperature (92, 93). The nitrogen containing groups that are introduced by NH₃ treatment are pyridinic, pyrrolic, quaternary-N and N-oxides of pyridinc-N (90, 91). Ammonia activation of 2D hexagonal mesoporous carbon at 950–1050 °C for 1 h enhances the BET SSA, total pore volume and mesopore volume 2121 m²/g, 2.15 cc/g, 1.68 cc/g respectively, which are about three times that of pristine characteristics (91). Ammonia activation also increased the BET SSA of phloroglucinol derived mesoporous carbons from 500 m²/g to 1100 m²/g for activation conditions of 850°C/2 h (90). Ammonia activation is particularly useful for increasing the wettability for electrochemical activations or nitrogen

containing groups for catalytic activity. Nonetheless, ammonia treatment releases extremely hazardous HCN off-gas that may render a limitation in the applications of ammonia activation process (68).

2.5. Structural Characteristics of Soft-Templated Mesoporous Carbons

As mentioned earlier, the mesopores are the key characteristic feature of the mesoporous carbons that made them distinct from the traditional activated carbon materials. However, almost all the mesoporous carbon materials do have a certain micropore distribution, which are clearly observed in the N₂ adsorption-desorption plots. According to the IUPAC classifications, the N₂ adsorption-desorption plots at 77 K are type-IV in nature. This type of isotherm is characterized by a sharp rise in the lower pressure followed by a plateau in the higher-pressure regime. In the desorption plot, a distinct hysteresis loop is observed, *i.e.*, adsorption and desorption do not follow the same line. The sharp rise in the low-pressure regime is the characteristics of microporosity whereas the hysteresis loop is the fingerprint of mesoporosity. There is a significant amount of research that has dealt with shape of the hysteresis loop with the mesopore characteristics, but those are beyond the scope of this work. In the adsorption studies, the N₂ adsorption-desorption at liquid nitrogen saturation temperature (77 K) is the most common strategy of characterizing the porosity. To analyze very narrow pore size distribution, generally below 7-8 Å, CO₂ adsorption-desorption at 273 K is performed. The complement of N₂ adsorption-desorption is Argon (Ar) adsorption-desorption at saturated liquid Argon temperature (88 K). For the porosity analysis of very low surface area materials, krypton (Kr) adsorption-desorption is performed, although universality of the analysis is not well established. In order to calculate the pore size distribution (PSD) using other than BET analysis, several types of model fitting are usually performed on the N₂ adsorption/desorption data. In the classical approach, the Dubinin-Radushkevich (D-R), Dubinin-Astakov (D-A), α_s method, t-plot or *micropore analysis* (MP method) were employed to calculate the micropore distribution, whereas the Barrent-Joyner-Halenda (BJH) method was the most commonly employed technique to calculate the mesopore distributions. However, in modern times, non-local density functional theory (NLDFT) is employed to calculate both micropore and mesopore distributions and proved to be more accurate than the earlier techniques. Recently, another development, named as quenched solid-density functional theory (94, 95) (QSDFT) has been established which has been demonstrated to be more accurate for specific applications.

The hysteresis loop in the N₂ adsorption-desorption plot of mesoporous carbon was first explained by the Kelvin equation (96) with the help of theoretical perspectives in the macroscopic level. Later there have been several extensive studies on the hysteresis loops and IUPAC classified it into four broad categories of H1 to H4 (Figure 6).

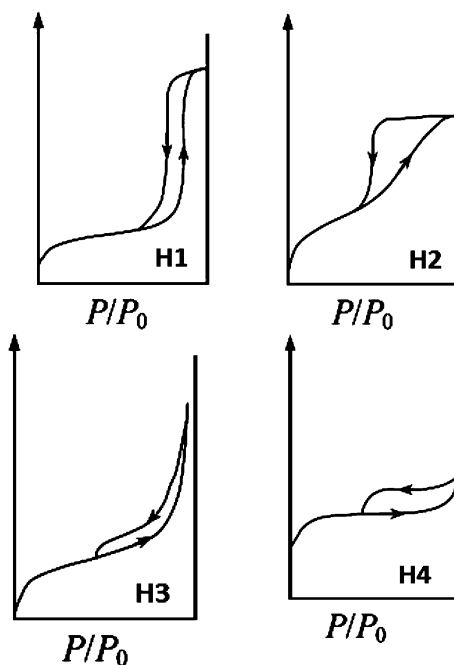


Figure 6. Types of Hysteresis loop.

H1 pore appeared from cylindrical pores whereas the H2 type of pores appear for both cylindrical to spherical pores. The cause of H3 hysteresis represents the disordered, slit or lamellar type of pores. The type of H4 hysteresis was not investigated in details, most likely it arises from both disordered micro-/mesoporosity. There is some additional research work published on hysteresis loops and their role in predicting the adsorption/adsorbent structure (97–99) but those are beyond the scope of this chapter.

Pore textural characteristics of lignin derived mesoporous carbons demonstrated moderate to low BET specific surface area and distributed pore size, as observed in our findings. Table 1 shows the pore textural properties of lignin derived carbons. We have measured surface area as high as 418 m²/g with total pore volume 0.50 cm³/g. All the nitrogen adsorption-desorption plots showed a hysteresis loop and pore size distribution revealed wide pore widths of 3 to 10 nm (Figure 7(a) and 7(b)). The cause of wide pore size distribution may be attributed to heterogeneity of lignin and inappropriate cross-linking.

Table 1. Pore textural properties of soft-templated mesoporous carbons (LMC-1 through LMC-6; LMC stands for Lignin Derived Mesoporous Carbon). Reprinted with permission from reference (76). Copyright 2013 American Chemical Society.

<i>Entity</i>	<i>Preparation (F127 content %)</i>	<i>BET SSA (m²/g)</i>	<i>Mesopore vol. (cm³/g)</i>	<i>Total pore vol. (cm³/g)</i>
LMC-1	HCHO/acid; (105)	418	0.34	0.50
LMC-2	HCHO/acid; (210)	205	0.13	0.20
LMC-3	HCHO/base; (160)	222	0.15	0.22
LMC-4	HMTA/base; (160)	214	0.17	0.19
LMC-5	Pre-cross-linked lignin/THF (116)	208	0.24	0.28
LMC-6	Pre-cross-linked lignin /DMF (116)	276	0.11	0.22

The mesostructure of ordered mesoporous carbon consists of lattices of long range ordering, walls of uniform thickness and mesopores whose dimensions, based on IUPAC classifications are between 2 and 50 nm. As mentioned earlier, these structures are typically formed by self-assembly between a carbon precursor and copolymer templates. The long range morphology of mesostructures can be hexagonal, cubic or lamellar. The micellization process of block copolymers that leads to the required structure is a complex phenomenon that results in diverse mesostructures due to their structural characteristics such as block length, composition, and architecture (49). Self-assembly of block copolymers is usually governed by three parameters including, composition, interfacial tension, and sequencing. For two-component block copolymers, there is one composition variable, one segment-segment interaction parameter, and one or two sequences (100). Differently, ABC-type tri-block copolymers have two independent composition variables, three SSI parameters, and three distinct sequences, resulting in a much richer structural behavior. Therefore, compared with AB or ABA block copolymers, amphiphilic ABC triblock copolymers are more adaptive candidates as templates for the creation of novel mesoporous materials with designable structures, compositions, and tunable pore/wall parameters (100). By effectively controlling the concentration of reactants, the amphiphilic nature of the copolymer, and the temperature, a wide variety of structures, such as 3D caged mesostructure, rhombohedral and body-centered structures are formed. For instance, evaporation-induced self-assembly between the phenolic resol precursor and the reverse amphiphilic triblock copolymer, such as [PPO]₅₃ [PEO]₁₃₆ [PPO]₅₃ (PPO: propyleneoxide; PEO: ethyleneoxide) results in 3D face centered cubic mesostructures (56). The type of mesostructures formed depends also on the hydrophilic/hydrophobic interfacial curvature (47). For example, a triblock copolymer with large PEO blocks leads to the structural shape with large interface curvature (47). To make the ordered structure with smaller interface curvature,

small PEO segments, such as those in Pluronic P123 can be employed. During synthesis, the hydrophilic carbon precursors interact with PEO segments, while the hydrocarbon molecules interact with the hydrophobic PPO side. In these cases, the ratio of carbon precursor to copolymer may dictate the interface curvature in such a way to minimize the energy barrier (47). Additionally, the sequence of segments on the copolymer can greatly influence the physicochemical behavior of the copolymers in the micellization process. During the self-assembly, when the concentration of copolymer reaches the critical micelle concentration (CMC), several possible configurations of polymer sequences may be formed (49). When a hydrophobic segment is exposed to the hydrophilic matrix the formation of mesostructure becomes energetically unfavorable. In certain instances, the entropic penalty arises from the folding of polymeric segments. Lowering of curving energy is made possible by deliberately using a longer segment, such as PEO in the reverse PPO-PEO-PPO tri-block copolymer (49).

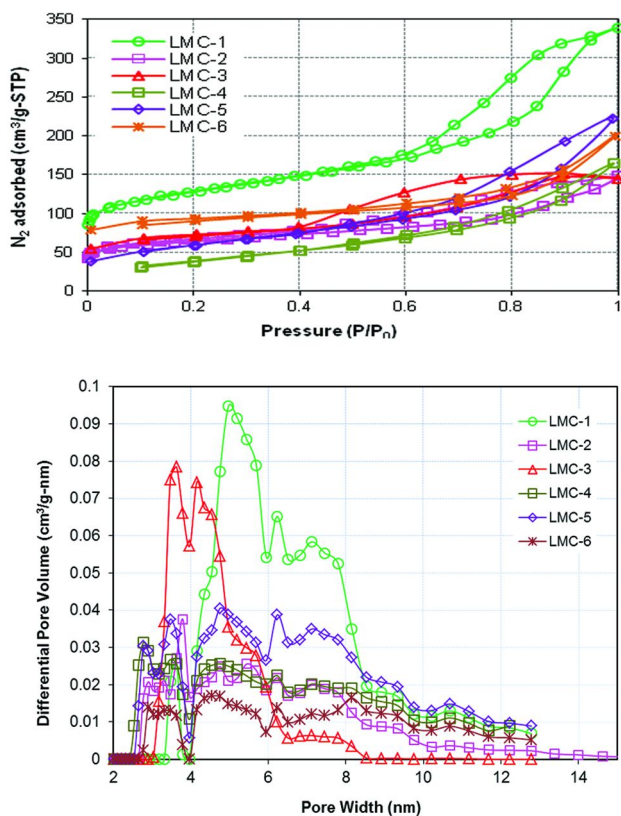


Figure 7. (a) N_2 adsorption-desorption plots of lignin derived mesoporous carbons (LMC-1 to LMC-6) at 77 K. Reproduced with permission from reference (76). Copyright 2013 American Chemical Society. (b) Pore size distribution of LMC samples calculated by NLDFT method. Reproduced with permission from reference (76). Copyright 2013 American Chemical Society.

As mentioned earlier, mesoporous ordered carbons invariably contain micropores, which are formed during the framework calcination. Evidence of silicate frameworks resisting the formation of micropores is observed in the synthesis of ordered mesoporous carbons by soft template synthesis using resorcinol, silicate oligomer and tri-block copolymer. When mesoporous carbons are prepared with and without silicate frameworks, this leads to a reduction in microporous BET surface area from 50% to almost zero (101). Additionally, etching of silicate frameworks with HF results in higher net specific surface area (101). Highly graphitized mesoporous carbons are formed by performing carbonization in non-neutral medium. The cross-linking leads to thicker walls which gives additional stability and adds rigidity. This will resist shrinkage and the formation of micropores (32). When these materials are calcined at increased temperature, a reduction of BET specific surface occurs. A method to preserve the mesoporosity and framework shrinkage is by using aco-polymer and organic precursor that leads to a high level of cross-linking (48). All these materials exhibit mesoporosity as evident from the hysteresis of adsorption and desorption branches at high relative pressure region. Evaporation Induced self-assembly organic molecules are also used to produce mesoporous resins and carbons (39). At higher activation temperatures, micropores are developed in these materials. But increased temperature calcination causes the reduction in pore size as indicated by the lower relative pressure for the hysteresis loop (39). A carbon sample activated in the presence of Ar, even though it shows a clear hysteresis loop, does not fully developed the desorption branch which probably indicates blocked pores. When treated thermally at elevated temperatures, the hysteresis loops shifted to lower relative pressure suggesting the reduction of the pore size. By calcination of these samples in the presence of little oxygen, cage windows can be easily opened. Removal of the co-polymer matrix by dissolving in sulfuric acid causes some shrinkage of the pores. Amphiphilic surfactants such as tri-block copolymers containing PEO segments contain many oxygen atoms which can interact with the templates. Additionally, due to the low glass transition temperature, the copolymers can be easily removed at low temperatures without destroying the resin framework. Thermal stability and chemical behavior differences of copolymer templates and phenolic resin causes controlled mesopores in the mesostructure of polymer resins. A copolymer, such as PEO-PPO-PEO has high oxygen content and hence has low thermal stability. On the contrary, the thermal stability of phenolic resins is high due to the 3D network structure constructed by covalent bonds. Mesoporous carbons (FDU-15) obtained by calcination at 350 °C nitrogen atmosphere shows a hysteresis loop at relative pressure 0.6-0.7 which indicated large mesopores with cylindrical channels (40). By controlling the temperature, we can have some control on structural shrinkage. Continuous removal of carbon, hydrogen and oxygen from the thick walls during the pyrolysis, etches out the wall and make larger pores (54). Mesoporous polymers and carbon materials were obtained by adjusting the ratios of F127, reverse $[PPO]_{53}[PEO]_{136}[PPO]_{53}$, and phenolic resorcinol precursors through a solvent evaporation-induced self-assembly (EISA) process (49). The mixed block copolymer system interacts with resorcinol and self-assembles into micellar structures, which provide a suitable template for mesostructures.

For these materials, broad capillary condensation with two increasing steps is observed. Bimodal pore distribution suggests that the carbonaceous sample has two types of mesopores. In some cases, tunable pore dimensions are achieved by using hydrocarbon swelling agents (47). Lattice enlargement occurs due to interaction of hydrocarbons with hydrophobic parts of tri-block polymers.

Soft-templated order mesoporous carbons can be graphitized completely upon heating to above 3000 °C, whereas hard carbons are very difficult to graphitize owing to the vulnerability of structural integrity at high temperature. In general, the BET surface area and pore volume increase to a great extent with the increase of the pyrolysis temperature. These results imply that numerous micropores are generated during the high temperature pyrolysis. It is caused by dehydrogenation and deoxygenation from the polymeric frameworks during the pyrolysis. Micropore volume can be tuned by varying the carbonization temperature of phenolic resins in the range from 400 to 1000 °C followed by the post-synthesis KOH activation at 700-1000 °C.

References

1. Sing, K. S. W.; Everett, D. H.; Haul, R. A. W.; Moscou, L.; Pierotti, R. A.; Rouquerol, J.; Siemieniewska, T. *Pure Appl. Chem.* **1985**, *57*, 603–619.
2. Ioannidou, O.; Zabaniotou, A. *Renewable Sustainable Energy Rev.* **2007**, *11*, 1966–2005.
3. Burket, C. L.; Rajagopalan, R.; Marencic, A. P.; Dronvajjala, K.; Foley, H. C. *Carbon* **2006**, *44*, 2957–2963.
4. Rodríguez-Reinoso, F.; Molina-Sabio, M. *Carbon* **1992**, *30*, 1111–1118.
5. Ahmadvpour, A.; Do, D. D. *Carbon* **1996**, *34*, 471–479.
6. Marciá-Agulló, J. A.; Moore, B. C.; Cazorla-Amorós, D.; Linares-Solano, A. *Carbon* **2004**, *42*, 1367–1370.
7. Brunauer, S.; Emmett, P. H.; Teller, E. *J. Am. Chem. Soc.* **1938**, *60*, 309–319.
8. Yin, C. L.; Aroua, M. L.; Wan Daud, M. A. W. *Sep. Purif. Technol.* **2007**, *52*, 403–415.
9. Gilbert, M. T.; Knox, J. H.; Kaur, B. *Chromatographia* **1982**, *16*, 138–146.
10. Knox, J. H.; Kaur, B.; Millward, G. R. *J. Chromatogr.* **1986**, *352*, 3–25.
11. Ryoo, R.; Joo, S. H.; Jun, S. *J. Phys. Chem. B.* **1999**, *103*, 7743–7746.
12. Stein; Wang, Z.; Fierke, M. A. *Adv. Mater.* **2009**, *21*, 265–293.
13. Lu, A. H.; Schüth, F. *Adv. Mater.* **2006**, *18*, 1793–1805.
14. Schüth, F. *Angew. Chem.* **2003**, *115*, 3730–3750.
15. Schüth, F. *Angew. Chem., Int. Ed.* **2003**, *42*, 3604–3622.
16. Kresge, C. T.; Leonowicz, M. E.; Roth, W. J.; Vartuli, J. C.; Beck, J. S. *Nature* **1992**, *359*, 710–712.
17. Ryoo, R.; Joo, S. H.; Jun, S.; Tsubakiyama, T.; Terasaki, O. *Stud. Surf. Sci. Catal.* **2001**, *135*, 150.
18. Joo, S. H.; Choi, S. J.; Oh, I.; Kwak, J.; Liu, Z.; Terasaki, O.; Ryoo, R. *Nature* **2001**, *412*, 169–172.
19. Che, S.; Lund, K.; Tatsumi, T.; Iijima, S.; Joo, S. H.; Ryoo, R.; Terasaki, O. *Angew. Chem.* **2003**, *115*, 2232–2235.

20. Guo, W.; Su, F.; Zhao, X. S. *Carbon*, **43**, 2423–2426.
21. Kim, T.-W.; Ryoo, R.; Gierszal, K. P.; Jaroniec, M.; Solovyov, L. A.; Sakamoto, Y.; Terasaki, O. *J. Mater. Chem.* **2005**, *15*, 1560–1571.
22. Che, S.; Garcia-Bennett, A. E.; Liu, X.; Hodgkins, R. P.; Wright, P. A.; Zhao, D.; Terasaki, O.; Tatsumi, T. *Angew. Chem.* **2003**, *115*, 2232.
23. Kleitz, F.; Choi, S. H.; Ryoo, R. *Chem. Commun.* **2003**, 2136–2137.
24. Fan, J.; Yu, C.; Gao, F.; Lei, J.; Tian, B.; Wang, L.; Luo, Q.; Tu, B.; Zhou, W.; Zhao, D. *Angew. Chem.* **2003**, *42*, 3146–3150.
25. Yang, Z.; Xia, Y.; Sun, X.; Mokaya, R. *J. Phys. Chem. B* **2006**, *110*, 18424–18431.
26. Nishihara, H.; Hou, P.-X.; Li, L.-X.; Ito, M.; Uchiyama, M.; Kaburagi, T.; Ikura, A.; Katamura, J.; Kawarada, T.; Mizuuchi, K.; Kyotani, T. *J. Phys. Chem. C* **2009**, *113*, 3189–3196.
27. Che, G.; Lakshmi, B. B.; Fisher, E. R.; Martin, C. R. *Nature* **1998**, *393*, 346–349.
28. Che, G.; Lakshmi, B. B.; Martin, C. R.; Fisher, E. R.; Ruodd, R. S. *Chem. Mater.* **1998**, *10*, 260–267.
29. Liu, B.; Shioyama, H.; Akita, T.; Xu, Q. *J. Am. Chem. Soc.* **2008**, *130*, 5390–5391.
30. Yang, S. J.; Kim, T.; Im, J. H.; Kim, Y. S.; Lee, K.; Jung, H.; Park, C. R. *Chem. Mater.* **2012**, *24*, 464–470.
31. Sakintuna, B.; Yürüm, Y. *Ind. Eng. Chem. Res.* **2005**, *44*, 2893–2902.
32. Liang, C.; Dai, S. *J. Am. Chem. Soc.* **2006**, *128*, 5316–5317.
33. Saha, D.; Deng, S. Self-Assembled Ordered Mesoporous Carbon: Synthesis, Characterization and Applications. In *Activated Carbon: Classifications, Properties and Applications*; Nova Publishers: Hauppauge, NY, 2011; pp 509–538.
34. Saha, D.; Warren, E. A.; Naskar, A. K. *Carbon* **2014**, *71*, 47–57.
35. Kim, S. H.; Misner, M. J.; Xu, T.; Kimura, M.; Russell, T. P. *Adv. Mater.* **2004**, *16*, 226–231.
36. Sinturel, C.; Vayer, M.; Morris, M.; Hillmyer, M. A. *Macromolecules* **2013**, *46*, 5399–5415.
37. Liang, C.; Li, Z.; Dai, S. *Angew. Chem., Int. Ed.* **2008**, *47*, 3696–3717.
38. Brinker, C. J.; Lu, Y. F.; Sellinger, A.; Fan, H. Y. *Adv. Mater.* **1999**, *11*, 579–585.
39. Meng, Y.; Gu, D.; Zhang, F. Q.; Shi, Y. F.; Cheng, L.; Feng, D.; Wu, Z.; Chen, Z.; Wan, Y.; Stein, A.; Zhao, D. *Chem. Mater.* **2006**, *18*, 4447–4464.
40. Meng, Y.; Gu, D.; Zhang, F. Q.; Shi, Y. F.; Yang, H. F.; Li, Z.; Yu, C. Z.; Tu, B.; Zhao, D. Y. *Angew. Chem.* **2005**, *117*, 7215.
41. Hu, Q. Y.; Kou, R.; Pang, J. B.; Ward, T. L.; Cai, M.; Yang, Z. Z.; Lu, Y. F.; Tang, J. *Chem. Commun.* **2007**, 601–603.
42. Moriguchi, I.; Ozono, A.; Mikuriya, K.; Teraoka, Y.; Kagawa, S.; Kodama, M. *Chem. Lett.* **1999**, *28*, 1171.
43. Li, Z. J.; Yan, W. F.; Dai, S. *Carbon* **2004**, *42*, 767–770.
44. Lee, K. T.; Oh, S. M. *Chem. Commun.* **2002**, 2722–2723.
45. Li, Z. J.; Yan, W. F.; Dai, S. *Carbon* **2004**, *42*, 767–770.

46. Tanaka, S.; Nishiyama, N.; Egashira, Y.; Ueyama, K. *Chem. Commun.* **2005**, 2125–2127.
47. Zhang, F. Q.; Meng, Y.; Gu, D.; Yan, Y.; Chen, Z. X.; Tu, B.; Zhao, D. Y. *Chem. Mater.* **2006**, *18*, 5279–5288.
48. Wang, X. Q.; Liang, C. D.; Dai, S. *Langmuir* **2008**, *24*, 7500–7505.
49. Huang, Y.; Cai, H. Q.; Yu, T.; Sun, X. L.; Tu, B.; Zhao, D. Y. *Chem.–Asian J.* **2007**, *2*, 1282–1289.
50. Yan, Y.; Zhang, F. Q.; Meng, Y.; Tu, B. D.; Zhao, Y. *Chem. Commun.* **2007**, 2867–2868.
51. Zhang, F. Q.; Gu, D.; Yu, T.; Zhang, F.; Xie, S. H.; Zhang, L. J.; Deng, Y. H.; Wan, Y.; Tu, B.; Zhao, D. Y. *J. Am. Chem. Soc.* **2007**, *129*, 7746.
52. Zhang, F.; Meng, Y.; Gu, D.; yan, Y.; Yu, C.; Tu, Bo.; Zhao, D. *J. Am. Chem. Soc.* **2005**, *127*, 13508–13509.
53. Linag, C.; Hong, K.; Guiochon, A.; Mays, J. W.; Dai, S. *Angew. Chem., Int. Ed.* **2004**, *43*, 5785–5789.
54. Zhang, F. Q.; Meng, Y.; Gu, D.; Yan, Y.; Yu, C. Z.; Tu, B.; Zhao, D. Y. *J. Am. Chem. Soc.* **2005**, *127*, 13508.
55. Jang, J.; Bae, J. *Chem. Commun.* **2005**, 1200–1202.
56. Huang, Y.; Cai, H. Q.; Yu, T.; Zhang, F. Q.; Zhang, F.; Meng, Y.; Gu, D.; Wan, Y.; Sun, X. L.; Tu, B.; Zhao, D. Y. *Angew. Chem., Int. Ed.* **2007**, *46*, 1089–1093.
57. Liang, C. D.; Hong, K. L.; Guiochon, G. A.; Mays, J. W.; Dai, S. *Angew. Chem., Int. Ed.* **2004**, *43*, 5785–5789.
58. Kosonen, H.; Valkama, S.; Nykanen, A.; Toivanen, M.; Brinke, G. T.; Ruokolainen, J.; Ikkala, O. *Adv. Mater.* **2006**, *18*, 201–205.
59. Deng, Y. H.; Yu, T.; Wan, Y.; Shi, Y. F.; Meng, Y.; Gu, D.; Zhang, L. J.; Huang, Y.; Liu, C.; Wu, X. J.; Zhao, D. Y. *J. Am. Chem. Soc.* **2007**, *129*, 1690–1097.
60. Deng, Y.; Liu, C.; Gu, D.; Yu, T.; Tu, B.; Zhao, D. *J. Mater. Chem.* **2008**, *18*, 91.
61. Kowalewski, T.; Tsarevsky, N. V.; Matyjaszewski, K. *J. Am. Chem. Soc.* **2002**, *124*, 10632–10633.
62. Zhao, D.; Feng, J.; Huo, Q.; Melosh, N.; Frederickson, G. H.; Chemelka, B. F.; Stucky, G. D. *Science* **1998**, *279*, 548–552.
63. Flodstrom, K.; Alfredsson, V. *Microporous Mesoporous Mater.* **2003**, *59*, 167–176.
64. Deng, Y. H.; Liu, J.; Liu, C.; Gu, D.; Sun, Z. K.; Wei, J.; Zhang, J. Y.; Zhang, L. J.; Tu, B.; Zhao, D. Y. *Chem. Mater.* **2008**, *20*, 7281–7286.
65. Gorka, J.; Fenning, C.; Jaroniec, M. *Colloids Surf., A* **2009**, *352*, 113–117.
66. Choma, J.; Zubrowska, A.; Gorka, J.; Jaroniec, M. *Adsorption* **2010**, *16*, 377.
67. Liu, R. L.; Shi, Y. F.; Wan, Y.; Meng, Y.; Zhang, F. Q.; Gu, D.; Chen, Z. X.; Tu, B.; Zhao, D. Y. *J. Am. Chem. Soc.* **2006**, *128*, 11652–11662.
68. Yun, J. M.; Yeo, J. S.; Kim, J.; Jeong, H. G.; Kim, D. Y.; Noh, Y. J.; Kim, S. S.; Ku, B. C.; Na, S. I. *Adv. Mater.* **2011**, *23*, 4828–4850.
69. Szeifert, J. M.; Fattakhova-Rohlfing, D.; Georgiadou, D.; Kalousek, V.; Rathouský, J.; Kuang, D.; Wenger, S.; Zakeeruddin, S. M.; Grätzel, M.; Bein, T. *Chem. Mater.* **2009**, *21*, 1260–1265.

70. Fulvio, P. F.; Mayes, R. T.; Wang, X.; Mahurin, S. M.; Bauer, J. C.; Presser, V.; McDonough, J.; Gogotsi, Y.; Dai, S. *Adv. Funct. Mater.* **2011**, *21*, 2208–2215.
71. Saha, D.; Wei, Z.; Velluri, S.; Deng, S. *J. Porous Media* **2008**, *13*, 39–50.
72. Saha, D.; Deng, S. *Langmuir* **2009**, *25*, 12550–12560.
73. Saha, D.; Deng, S. *J. Colloid Interface Sci.* **2010**, *345*, 402–409.
74. Mayes, R. T.; Tsouris, C.; Kiggans, J. O.; Mahurin, S. M.; DePaoli, D. W.; Dai, S. *J. Mater. Chem.* **2010**, *20*, 8674.
75. Saha, D.; Contescu, C. I.; Gallego, N. C. *Microporous Mesoporous Mater.* **2012**, *155*, 71–74.
76. Saha, D.; Payzant, E. A.; Kumbhar, A. S.; Naskar, A. K. *ACS Appl. Mater. Interfaces* **2013**, *5*, 5868–5874.
77. Wigmans, T. *Carbon* **1989**, *27*, 13–22.
78. Xia, K. S.; Gao, Q. M.; Song, S. Q.; Wu, C. D.; Jiang, J. H.; Hu, J.; Gao, L. *Int. J. Hydrogen Energy* **2008**, *33*, 116–123.
79. Xia, K. S.; Gao, Q. M.; Wu, C. D.; Song, S. Q.; Ruan, M. L. *Carbon* **2007**, *45*, 1989–1996.
80. Yan, Y.; Wei, J.; Zhang, F.; Meng, Y.; Tu, B.; Zhao, D. *Microporous Mesoporous Mater.* **2008**, *113*, 305–314.
81. Wu, D.; Liang, Y.; Yang, X.; Zou, C.; Li, Z.; Lv, G.; Zeng, X.; Fu, R. *Langmuir* **2008**, *24*, 2967–2969.
82. Wang, X.; Lee, J. S.; Tsouris, C.; DePaoli, D. W.; Dai, S. *J. Mater. Chem.* **2010**, *20*, 4602–4608.
83. Saha, D.; Li, Y.; Zi, B.; Chen, J.; Keum, J.; Hansley, D. K.; Grappe, H. A.; Meyer, H., III; Dai, S.; Paranthaman, M. P.; Naskar, A. K. *Langmuir* **2014**, *30*, 900–910.
84. Lillo-Ródenas, M. A.; Juan-Juan, J.; Cazorla-Amorós, D.; Linares-Solano, A. *Carbon* **2004**, *42*, 1371–1375.
85. Raymundo-Piñero, E.; Azaïs, P.; Cacciaguerra, T.; Cazorla-Amorós, D.; Linares-Solano, A.; Béguin, F. *Carbon* **2005**, *43*, 786–795.
86. Wang, Q. *Carbon* **2008**, *46*, 1159–1174.
87. Wang, L.; Song, Z.; Zhong, M.; Liu, W.; Yan, W.; Qin, F.; He, A.; Liu, B. *Appl. Surf. Sci.* **2010**, *256*, 5187–5190.
88. Jin, J.; Tanaka, S.; Egashira, Y.; Nishiyama, N. *Carbon* **2010**, *48*, 1985–1989.
89. Górka, J.; Jaroniec, M. *Carbon* **2011**, *49*, 154–160.
90. Shao, Y.; Wang, X.; Engelhard, M.; Wang, C.; Dai, S.; Liu, J.; Yang, Z.; Lin, Y. *J. Power Sources* **2010**, *195*, 4375–4379.
91. Wang, X.; Lee, J. S.; Zhu, Q.; Liu, J.; Wang, Y.; Dai, S. *Chem. Mater.* **2010**, *22*, 2178–2180.
92. Stohr, B.; Boehm, H. P.; Schlogl, R. *Carbon* **1991**, *29*, 707.
93. Mangun, C. L.; Benak, K. R.; Economy, J.; Foster, K. L. *Carbon* **2001**, *39*, 1809.
94. Ravikovitch, P. I.; Neimark, A. V. *Langmuir* **2006**, *22*, 11171–11179.
95. Neimark, A. V.; Lin, Y.; Ravikovitch, P. I.; Thommes, M. *Carbon* **2009**, *47*, 1617–1628.
96. Heimenz, P. C.; Rajagopalan, R. *Principles of Colloid and Surface Chemistry*, 3rd ed.; Marcel Dekker: New York, 1997; Chapter 6.

97. Nguyen, P. T. M.; Do, D. D.; Nicholson, D. *J. Phys. Chem. C* **2011**, *115*, 4706–4720.
98. Nguyen, P. T. M.; Do, D. D.; Nicholson, D. *J. Phys. Chem. B* **2011**, *115*, 12160–12172.
99. Ravikovitch, P. I.; Domhnail, S. C. O.; Neimark, A. V.; Schueth, F.; Unger, K. *Langmuir* **1995**, *11*, 4765–4772.
100. Zhang, J. Y.; Deng, Y. H.; Wei, J.; Sun, Z. K.; Gu, D.; Bongard, H.; Liu, C.; Wu, H. H.; Tu, B.; Schuth, F.; Zhao, D. Y. *Chem. Mater.*, *21*, 3996–4005.
101. Li, H. Q.; Liu, R. L.; Zhao, D. Y.; Xia, X. Y. *Carbon* **2007**, *45*, 2628–2635.

Chapter 5

Fractionation and Characterization of Carbonaceous Pitch Oligomers: Understanding the Building Blocks for Carbon Materials

Mark C. Thies*

Department of Chemical and Biomolecular Engineering,
Clemson University, 221 Earle Hall,
Clemson, South Carolina 29634-0909, United States

*E-mail: mcths@clemson.edu

The oligomeric constituents of a representative petroleum pitch precursor for carbon materials have been characterized in terms of their molecular structures. The most prevalent polycyclic aromatic hydrocarbon (PAH) monomer units, the extent of alkylation on each unit, and the nature of the linkages connecting monomer units to form oligomers have all been determined. The use of two relatively new techniques, supercritical fluid extraction (SCE) for isolating the pitch into its constituent oligomers to enable analytical characterization, and MALDI mass spectrometry for determining absolute molecular weights and the extent of alkylation, proved to be invaluable in determining the molecular structures of the pitch species. A number of independent analytical methods all confirm that the thermal polymerization process to form pitch oligomers has a minimal impact on the monomer unit building blocks: four hydrogens are lost between two monomer units to form a 5- or 6-membered connecting ring, and most of the alkyl groups on the monomer units are retained. A 97% trimer cut with an average molecular weight of 750 Da was isolated via SCE and was found to contain a significant proportion of bulk mesophase. To our knowledge, this is the first time that the true molecular weight of a petroleum or coal-tar pitch mesophase has been determined.

Introduction

Almost 50 years ago, Brooks and Taylor (1, 2) discovered that when carbonaceous, fossil-fuel materials such as petroleum tars and pitches, coal-tar pitches, and select pure polycyclic aromatic hydrocarbons (PAHs) are heated in an inert atmosphere at 400–450 °C, they undergo a transition from the isotropic to the liquid crystalline phase, as is described below: first, the material (i.e., the pitch) melts upon heating to become an isotropic liquid; second, with increasing temperature, spheres of liquid crystallinity appear in the pitch (see Figure 1a); third, the spheres grow larger with increasing time and/or temperature; finally, the spheres dominate the pitch, coalesce, and eventually form a mosaic of anisotropic, liquid-crystalline material (also called mesophase; see Figure 1b). Brooks and Taylor concluded that the mesophase spheres were composed of condensed PAHs in a planar configuration, which had formed by condensation and dehydrogenation reactions from the starting pitch compounds described above.

Over the ensuing years, a wide range of applications has been developed for carbonaceous pitches such as those Brooks and Taylor investigated, both in their isotropic and mesophase states. In general, there is significantly more interest in converting the pitch from the isotropic state to its mesophase form because of the graphitic orientation that develops when using mesophase pitches as the precursor for carbon materials. Because of this orientation, mesophase pitches can serve as precursors for advanced carbons such as high thermal conductivity carbon fibers, carbon electrodes, thermal heat pipes, and carbon–carbon composites (3, 4). Two newer applications that are showing promise include graphite foams (5, 6), which combine high thermal conductivity with very low weight, and mesophases produced *in situ* within a carbon–carbon composite (7). In fact, the latter application is the preferred method for densifying the thick (i.e., greater than 5 cm) composites needed for applications such as rocket nozzles and nose cones (7). More exotic applications, such as using mesophase pitch as the starting precursor for the generation of graphene-like materials, may also be possible.

New processes are still being developed for making mesophase pitches. For example, today they are produced not only by the original method of thermal polymerization (8), but also by catalytic polymerization (9, 10).

It is somewhat ironic that although our ability to produce versatile carbons from both isotropic and mesophase pitches has increased significantly since the Brooks and Taylor discovery of mesophase almost 50 years ago, our fundamental understanding of the role that molecular size, molecular structure, and mixture composition play in the properties of both the pitch precursor and the final carbon products continues to be quite limited. For example, the ideal molecular size for producing a mesophase pitch with a low melting point, which would be desirable from a processing standpoint, is not known. Also not known is the mixture composition that would enable one to produce a higher-melting isotropic pitch, which could be rapidly oxidized, minimizing processing costs. Researchers have of course recognized for decades that molecular weight and structure play a key role in the properties of a carbonaceous pitch and in its suitability for a given application, but this understanding has been primarily of a qualitative nature.

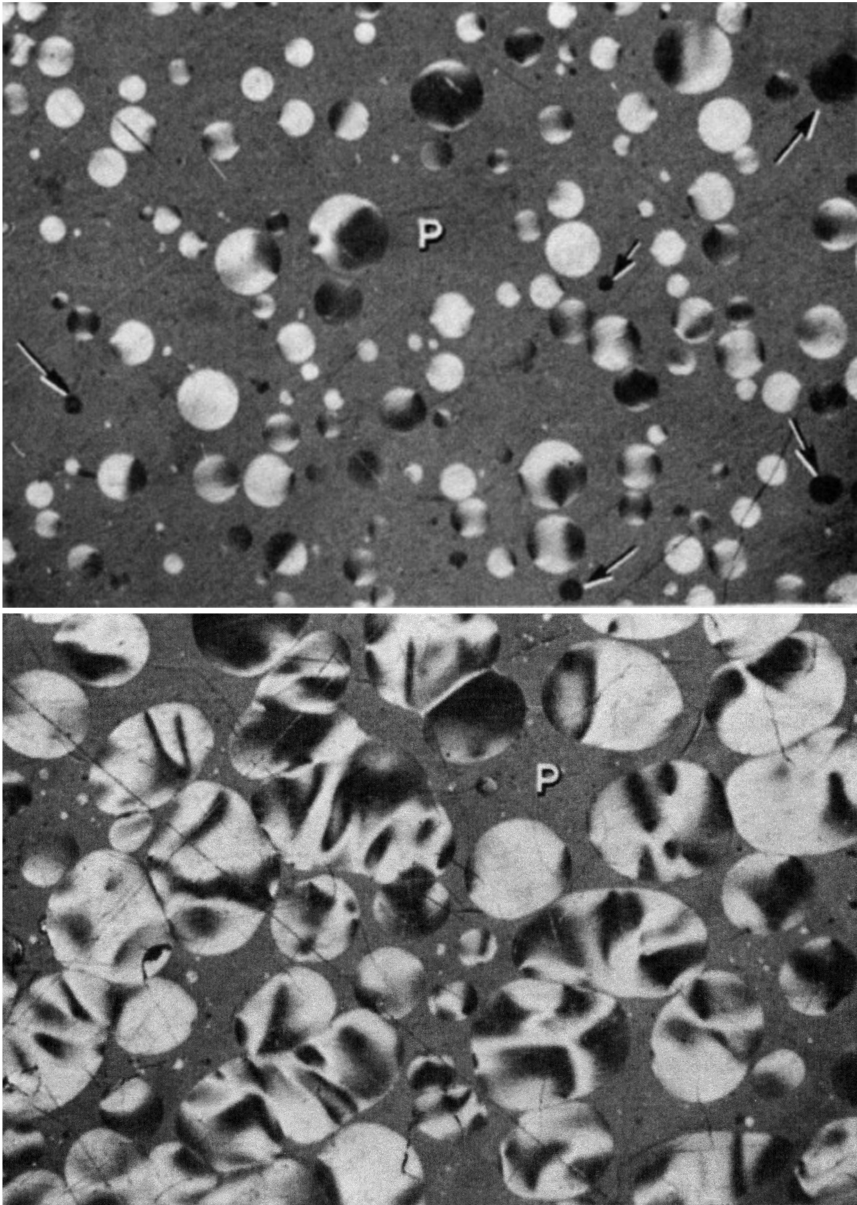


Figure 1. (a) Mesophase spheres in an early stage of development in isotropic pitch; (b) growth and coalescence of mesophase spheres to form continuous mesophase. Reproduced with permission from ref (2). Copyright 1965 Elsevier.

In reviewing the previous work in this area, our research group came to the conclusion that a significant barrier to developing an increased fundamental understanding of the structure–property relationships of carbonaceous pitches was the inability of previous workers to adequately characterize pitches at the molecular level. In particular, methods either did not exist or had not yet been developed for determining the molecular structures of the individual constituents in pitches. For example, in one of the earliest significant studies, Dickinson (11) fractionated a petroleum pitch into three fractions by conventional solvent extraction and then analyzed the fractions by NMR spectroscopy and vapor pressure osmometry (VPO). This information was used in conjunction with elemental analysis to propose average molecular structures for each isolated fraction. However, only these three structures could be used to represent the entire pitch. Kershaw and Black (12) performed analogous work to that of Dickinson, albeit primarily on coal-tar pitches; in addition, mass spectrometry (i.e., direct probe electron ionization) was applied to pitch for one of the first times.

Carbonaceous pitches can also be synthesized from pure PAHs. Here again, though, the analysis of these pitches has typically involved partitioning the pitch into a small number of fractions via conventional solvent extraction, followed by the analysis of these fractions via methods such as NMR and field desorption–mass spectrometry (13–15). As has been shown by our group, conventional solvent extraction methods produce fractions that are still quite broad in their molecular weight (mol wt) distribution (MWD). Thus, little information is gleaned concerning the individual species present in the pitches, other than the molecular weight if mass spectrometry is employed.

Kandiyoti and co-workers (16) were one of the first groups to propose the use of more innovative separation and analytical techniques that could enable one to characterize the higher mol wt portions of fossil fuels – and, by extension, the carbonaceous pitches that are of interest to us as precursors to carbon fibers. Based on more than a decade of research on coal-derived tars and pitches, they concluded (16) that the combination of size exclusion chromatography (SEC; also called gel permeation chromatography, or GPC) and matrix-assisted laser desorption/ionization mass spectrometry (MALDI–MS) provided the most accurate representation of the molecular weight of higher mol wt fossil fuels. However, mol wt information was the key focus of this work, so other types of molecular characterization information (e.g., molecular structure and functional groups) were generally not obtained.

Nevertheless, Kandiyoti et al.'s work with coal-derived materials laid the foundation for our subsequent research efforts with carbonaceous pitches derived from both petroleum and from pure PAHs. In particular, groundbreaking research by Conoco researchers (17) and follow-up efforts by our team (18) a few years later definitively established that petroleum pitches are oligomeric in nature. (By oligomeric, we mean that a pitch molecule consists of a relatively small number of monomer units linked together to form a larger species. Contrast this with a polymer, where in principle the number of monomer units can be essentially unlimited.) Referring to the MALDI of M-50 petroleum pitch in Figure 2, we denote the first broad peak as the monomers (210 to 390 Da), the second as the dimers (390 to 645 Da), the third as the trimers (645 to 890 Da), and the fourth

as the tetramers (890 to 1120 Da). (As we proceed through this chapter, the validity of these “assignments” will be demonstrated.) We pause for a moment here to emphasize that the above molecular weights are *absolute* (i.e., true) molecular weights, as they were obtained by (MALDI) mass spectrometry. To our knowledge, all previously reported molecular weights on petroleum pitches before those presented here (and which were first presented in References (17) and (18)) were *relative* molecular weights, that is, they were based on techniques such as GPC, where the molecular weights obtained were relative, being based on calibration standards that hopefully are (but many times are not) reliable.

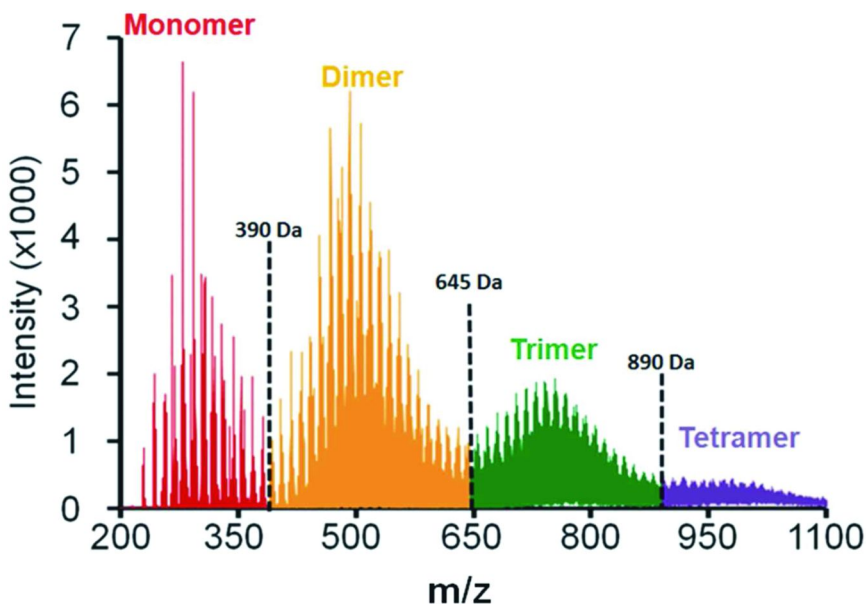


Figure 2. MALDI mass spectrum of an industrial-grade petroleum pitch, M-50.

Once the oligomeric nature of the pitch became known, our plan of action became clear: (1) Determine the molecular structure of the species comprising the monomer fraction of pitches. Quantitative, accurate monomer information was an obvious pre-requisite for the prediction of the molecular structures and sizes of the dimer and higher oligomers present in pitch. (The oligomers are the key constituents of any pitch that can be processed into desirable carbon materials, as the monomers are too volatile.) (2) Apply separation and analytical techniques such that the oligomeric species themselves, and not just the monomers, could be quantitatively analyzed in terms of molecular structure and size. Clearly our ability to analyze the higher oligomers would decrease as their molecular weight increased; nevertheless, our goal was to obtain quantitative molecular structure information on the highest “mer” numbers possible. As is discussed below, fractionation of the pitches into their respective oligomers by supercritical extraction has been a unique feature of the work done by our group and has led to breakthroughs in our ability to characterize the constituents of carbonaceous pitches. (3) Use the above characterization information to develop relationships

between the molecular structure and size of carbonaceous oligomers, their bulk properties, and the properties of the final carbon materials. As will be seen below, significant progress has been made on two of the above objectives, and a good foundation has been established for significant future progress on the third.

In this chapter, we discuss the work of our group over the past several years towards achieving the three objectives described above. Here our focus is on petroleum pitches, that is, those pitches derived from the heat-soaking of aromatic decant oil, a petroleum by-product of the processing of the heavier fractions of crude oil (8). Although other carbonaceous pitches (such as coal-tar pitches) are of interest and could have been investigated, petroleum-based pitches are the dominant type of pitch being used in the United States today for reasons of availability – and safety and health vs. coal-tar pitches (19). Also of interest to our research group are pitches derived from the polymerization synthesis of pure PAHs such as pyrene (20–22), but these are not the focus of this chapter.

Isolating Petroleum Pitch Oligomers via Supercritical Extraction

As discussed above, our understanding of the role that molecular size, structure, and MWD play on the bulk properties of carbonaceous pitches was quite limited at the beginning of this project. A significant barrier to an increased fundamental understanding of pitches was the difficulty in separating them into narrow mol wt fractions, which could both be more easily characterized and also serve as molecular calibration standards. The classic technique for both the analytical and prep-scale fractionation of pitches, GPC (23, 24), suffers from several disadvantages, including poor peak resolution and the very low solubility of higher oligomers in the GPC mobile phase.

We therefore proposed supercritical (fluid) extraction (SCE) as a solution to these problems (also known as dense-gas extraction (DGE)). As seen in Figure 3, the use of a supercritical fluid such as toluene ($T_c = 318.6\text{ }^\circ\text{C}$; $P_c = 41.1\text{ bar}$) has two advantages: First, it allows one to operate at elevated temperatures while still maintaining liquid-like densities, thus increasing pitch solubility; second, for toluene these elevated temperatures are also in the supercritical region; thus, changes in pressure allow one to effect large changes in solvent density and, consequently, solvent power. For example, note in the figure how for a given operating pressure (e.g., 60 bar) the density of toluene decreases significantly as the temperature is increased from 327 to 387 °C. Thus, if the column is operated with a positive temperature gradient, the solvent power of the solvent decreases as one moves up the column, effecting a separation between the components.

As was demonstrated by Edwards and Thies (26), SCE is an excellent method for obtaining concentrated, highly resolved mol wt cuts from materials having a broad MWD, such as petroleum pitches. Figure 4 shows the superiority of SCE vs both conventional solvent extraction and liquid chromatography (with the latter being impractically expensive except on the bench scale).

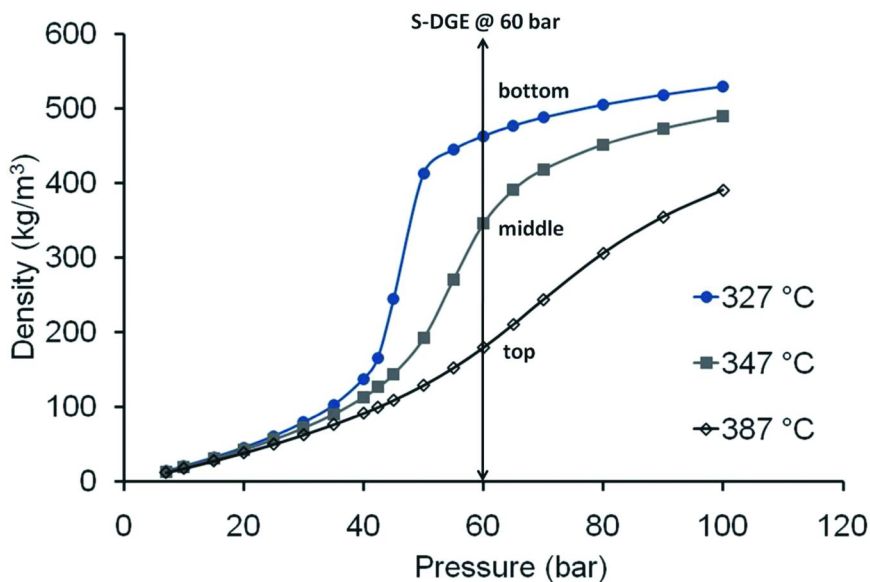


Figure 3. Supercritical toluene offers continuously varying density at elevated temperatures. Reproduced with permission from ref (25). Copyright 2012 American Chemical Society.

Our group designed and constructed a multi-stage SCE/DGE setup for the fractionation of petroleum pitches into 1-100+ g-sized cuts of controlled molecular weight. Two modes of operation were used in this work, continuous (see Figure 5) and semi-continuous (see Figure 6) operation. As details of the design, construction, and process control of this apparatus are given elsewhere (26, 28), the focus here is on the operating procedure, as well as on conceptually illustrating how SCE can be used to effect difficult separations.

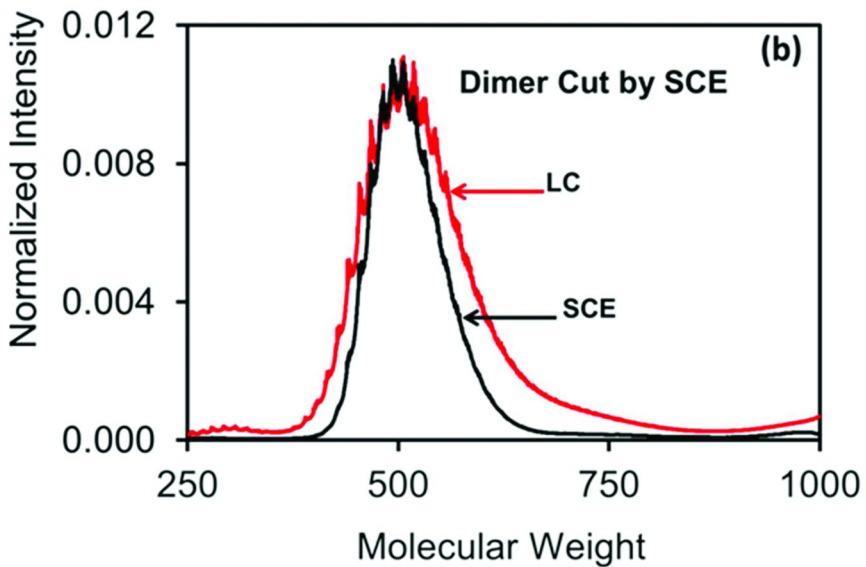
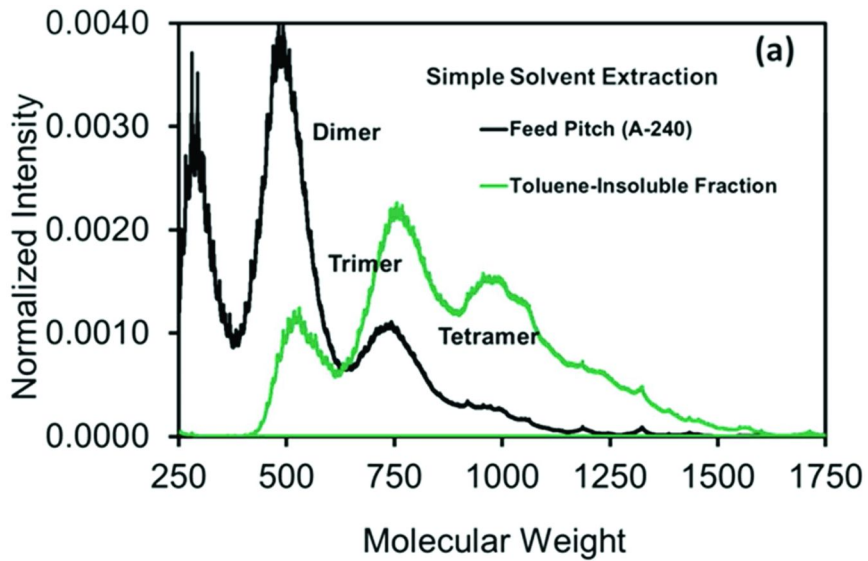


Figure 4. (a) Simple solvent extraction of a petroleum pitch gives a fraction with a broad MWD; (b) A narrow mol wt dimer cut can be produced by SCE – even narrower than by liquid chromatography (LC).

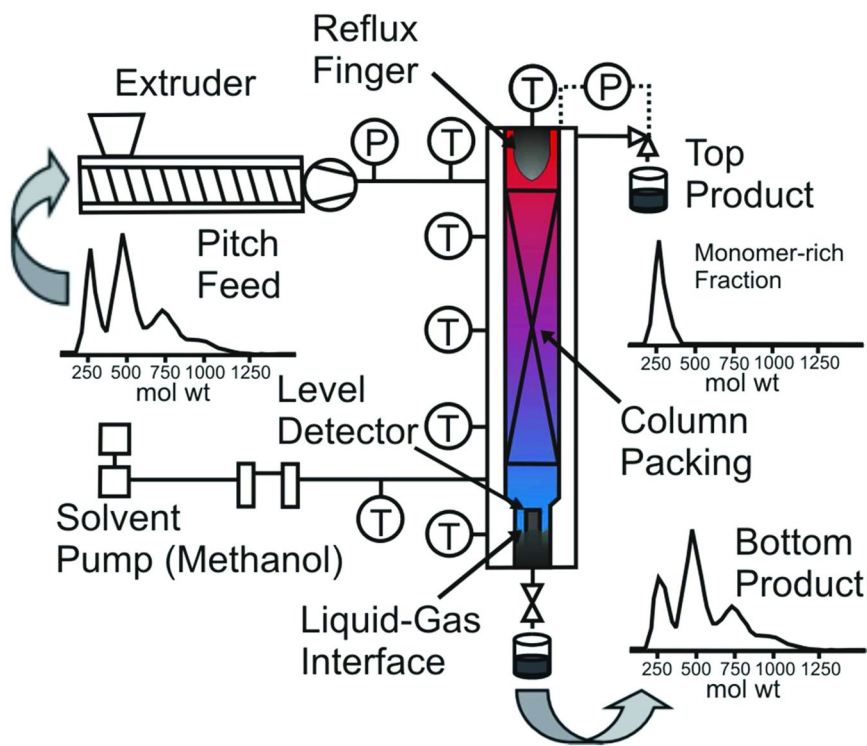


Figure 5. SCE/DGE apparatus for continuous fractionation of petroleum pitches. SC methanol is effective for isolating the monomer, but SC toluene is required for extracting oligomers. Reproduced with permission from ref (27). Copyright 2009 Elsevier.

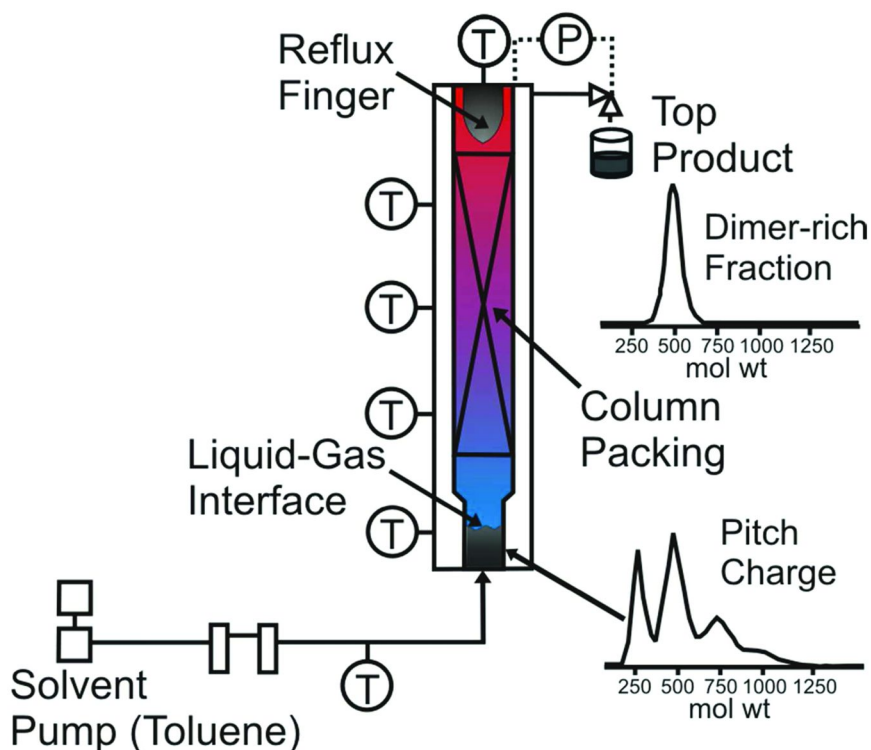


Figure 6. SCE/DGE apparatus for semi-continuous fractionation of petroleum pitches. This setup is best for isolating small amounts of high-purity, oligomeric pitch standards. Reproduced with permission from ref (27). Copyright 2009 Elsevier.

Continuous SCE Fractionation

The continuous SCE/DGE unit consists of a packed column with a total height of 2 m, a packed height of 1.5 m, and an inner diameter of 1.8 cm. The temperature and pressure rating of the column is 400 °C and 200 bar. For a typical experiment, molten M-50 pitch is fed to the top of the column at 50-125 g/h via a single-screw extruder, and supercritical solvent is delivered with an HPLC pump to the bottom of the column. Solvent-to-pitch ratios ranging from 5:1 to 15:1 have been employed. As pitch enters the column and flows down the packing, the supercritical solvent flows upwards. In this manner, selected pitch species are stripped out of the feed pitch and into the solvent-rich, light liquid phase, and a portion of the solvent is absorbed into the pitch-rich, heavy liquid phase. As would be expected, higher operating pressures increase the density of the solvent and increase the average molecular weight of the overhead extract. However, column operating temperature has been found to exhibit more complex behavior, with the establishment of a positive temperature gradient from the bottom to the

top of the column yielding the best purities (e.g., when toluene is used as the supercritical solvent, typically the bottom is held at 330, the middle at 350, and the top at 380 °C).

How such a temperature gradient can improve both product selectivity (i.e., improved separation between oligomers) and purity can be explained in terms of column operation as follows: at the bottom of the column where it enters, the supercritical solvent has a high density (and thus a high solvent power) at the lower temperatures (i.e., 330 °C). Thus, a relatively large portion of the feed pitch is extracted and dissolved in the liquid-like, supercritical solvent. However, as this solvent flows up the column, its solvent power continuously decreases with the increase in temperature (first to 350 °C and then to 380 °C), which decreases the solvent density (see Figure 3). This reduction in solvent power results in the precipitation of the heavier pitch species that were initially extracted, leading to the formation of a reflux flow down the column that increases the purity of the species collected out the top. The solvent-rich phase, containing the extracted pitch oligomers (e.g., the lower mol wt oligomers) is taken off as top product, and a pitch-rich phase containing the heavier oligomers, such as trimer and tetramer that were not extracted, is concentrated in the pitch charge. Liquid reflux of a portion of the top product back down the column is also enhanced by the use of a heated reflux finger ($T = 380\text{ °C}$) located above the top manifold. Cervo et al. (29, 30) have shown how such a temperature gradient leads to improved selectivity, even as good product yields are obtained.

A liquid-level detector (26) at the bottom of the column operates based on the difference in electrical resistivity between the top and bottom phases and ensures complete separation between the solvent-rich top liquid phase and pitch-rich bottom liquid phase. Steady-state operation is typically reached within an hour, and an experimental run takes 6-12 h, depending on how much pitch fraction is to be produced.

With continuous operation and the use of one column, operating conditions of temperature and pressure can be selected such that either the lowest mol wt oligomer (e.g., the monomer, as illustrated in Figure 5) or the highest mol wt oligomer is recovered in high purity. However, clearly the generation of high-purity intermediate oligomers (which are of the greatest interest for producing carbon materials) requires the use of two SCE columns operating in series. Such a setup for producing high-purity dimer has also been carried out (30) and is shown in Figure 7. Here, the feed pitch was delivered to the lower third of the packing in Column 1 (Col-1) in the molten state via the single-screw extruder (not shown), and the supercritical solvent (in this example, toluene) was delivered to the bottom of Col-1. As before, the pitch feed flowed down the packing and the supercritical solvent feed flowed upwards, with lighter pitch species being stripped out of the feed pitch and into the solvent-rich liquid phase, and a portion of the solvent being absorbed into the pitch-rich liquid phase. The operating pressure of both columns was 70 bar. To improve selectivity, a positive temperature profile (in this case, the top was set to 400, the middle to 380, and the bottom to 350 °C) was established. As described previously, a retrograde (i.e., positive) temperature gradient across the length of the column was created, enhancing the purity of the oligomer recovered in the top, solvent-rich phase. The solvent-rich phase,

containing the extracted pitch oligomers (in this case monomer and dimer), was taken off as Col-1 top product, and a pitch-rich phase containing the heavier, unextracted molecules, that is, a portion of the dimer and all of the trimer and tetramer, was taken off as the bottom product of Col-1.

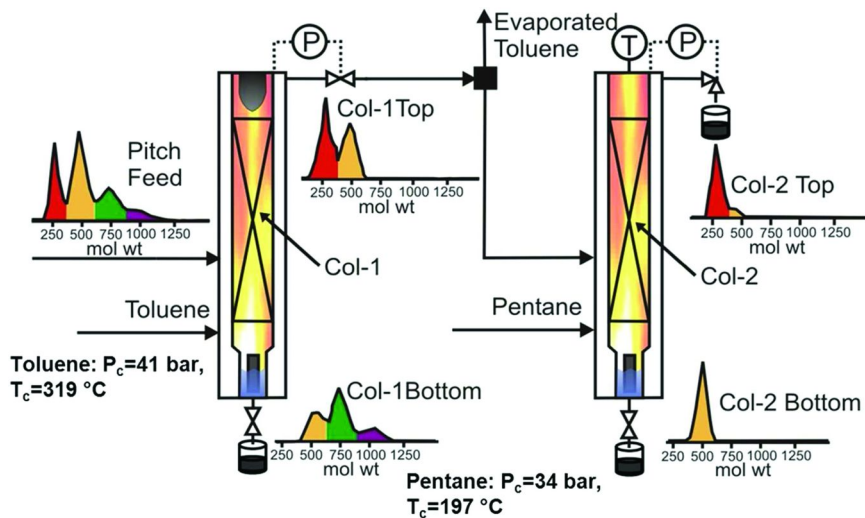


Figure 7. Two-column SCE for the isolation of intermediate oligomers of high purity, for example, dimer or trimer.

Next, the top product from Col-1 was sent to a second SCE column to effect a separation between the monomer and the dimer. But first, this stream had to be flashed in a gas-liquid separator to evaporate off a large portion of the toluene, as toluene is too powerful a supercritical solvent to separate monomer and dimer (it completely dissolves both of them). In this example, we found that operating the flash at 123 °C and 1 atm evaporated enough of the toluene to produce a 64 wt % concentrated pitch solution from the top product of Col-1 (a 6 wt % pitch solution). As shown in Figure 7, this 64% pitch solution then served as the feed pitch to Col-2 and was delivered at 70 bar to the lower quarter of Col-2. The supercritical solvent for Col-2, pentane ($T_c = 196.6$ °C; $P_c = 33.7$ bar), was delivered to the bottom of Col-2. A positive temperature gradient (260 top, 255-250 middle, 240 °C bottom), commensurate with the critical properties of pentane, was established along the height of Col-2 to enhance product purity. The monomer was taken off as the top product at 96% purity, and the dimer was taken off the bottom at 99% purity, as measured by MALDI (30).

In a related study (30), trimer-rich pitches were also produced from the above two-column unit, albeit at very different conditions from those described above. In particular, operating conditions in Col-1 were adjusted such that a significant percentage of the trimer (i.e., not just monomer and dimer) was also extracted into the top product. In this setup, the top product exiting Col-1 was not flashed to

remove the toluene; instead, this stream was fed directly into Col-2 along with an additional pure toluene stream, which served as the feed solvent for Col-2. Both the monomer and dimer were extracted into the supercritical solvent in Col-2, resulting in a trimer-rich bottom product.

For continuous, one-column operation, monomer purities of 98+% can readily be obtained at yields (as a percentage of the feed pitch) of ~50% (27). Thus, one can typically produce 50 g/h of pure monomer per 100 g/hr of petroleum pitch feed. (Careful mass balances taken during continuous SCE runs have shown that for M-50 petroleum pitch, 49±1 wt % of the mother pitch is monomer, 26±1 wt % is dimer, and 25±1 % consists of trimer and higher oligomers (30). Similar oligomer percentages have been obtained for the composition of other petroleum pitches, including Ashland A-240 and Koppers KP-100.) For continuous, two-column operation, a typical product from the second column would be a 97% pure dimer stream being generated at a flow rate of 20 g/h from an M-50 pitch of 100 g/h. Much lower trimer flowrates (7 g/h) and purities (60%) have thus far been obtained by two-column, continuous SCE/DGE of petroleum pitches (30).

In general, less aggressive supercritical solvents such as methanol ($T_c = 239.5\text{ }^\circ\text{C}$; $P_c = 81.0\text{ bar}$) and pentane ($T_c = 318.6\text{ }^\circ\text{C}$; $P_c = 41.1\text{ bar}$) are best for extracting the monomer from the rest of the pitch (27, 30), but toluene ($T_c = 318.6\text{ }^\circ\text{C}$; $P_c = 41.1\text{ bar}$) is preferred for isolating dimer and higher-oligomer species (27–30). Furthermore, Esguerra et al. (21) recently showed that the extraction of higher oligomers can be significantly improved by the addition of the co-solvent N-methyl-2-pyrrolidone (NMP) ($T_c = 450.9\text{ }^\circ\text{C}$; $P_c = 47.2\text{ bar}$) to toluene at the 15 mol % level, with trimer and higher solubilities being increased by a factor of three.

We have typically used continuous SCE for producing pitch cuts in the bulk quantities (i.e., up to several hundred grams per run) needed for processing into carbon products such as fibers (31). However, as discussed in the **Results and Discussion** sections herein, continuous SCE has also proven to be invaluable as an important first step in the generation of pitch molecular standards, as it is here that the oligomer of interest is concentrated from the raw “mother” pitch before the final purification step is carried out via semi-continuous SCE operation.

Semi-Continuous SCE Fractionation

For semi-continuous operation (see Figure 6), essentially the identical equipment is used as for continuous operation, but the procedure is a little different (and a bit easier too), as is described below. For a given experimental run, the bottom section (also called the manifold) of the column must first be detached and filled with 2–20 g of the sample to be fractionated. Typically, the sample is either raw M-50 pitch or an oligomeric fraction of that pitch previously concentrated via continuous SCE. Continuous flow of the supercritical solvent is then initiated. The solvent flows through the pitch charge, extracts a portion of the pitch depending on the operating temperature and pressure, flows up the column, and removes the extracted pitch out as top product. As with continuous DGE, a positive temperature gradient (e.g., 330/350/380 °C bottom/middle/top when toluene is used as the supercritical solvent) is typically established along

the length of the column to enhance product purity. Such a gradient, along with the use of a reflux finger, creates liquid reflux of a portion of the product back down the column, enhancing overhead-product purity. (Although reflux in our SCE unit has not actually been physically observed, Edwards and Thies (32) performed process simulations on a semi-continuous SCE column with a positive temperature gradient, and a liquid reflux phase was seen to exist due to retrograde condensation.) However, unlike continuous SCE where the pressure is maintained constant throughout an entire run, the pressure with semi-continuous SCE is typically increased stepwise. Thus, at the lowest pressures the lower mol wt oligomers are extracted from the pitch charge and are collected as top product; at moderate pressures, dimer is collected; and at the highest pressures, trimer and tetramer oligomers are collected. A stepwise increase to a higher operating pressure is typically implemented when the extraction of pitch/oligomer significantly decreases at a given pressure. This decreased extraction is typically marked by the color of the collected sample changing from nearly opaque to transparent and slightly tinted.

Whether the SCE fractionation is carried out continuously or semi-continuously, the method of sample collection is essentially the same. After exiting the pressure-regulating valves (shown in Figures 5-7), the overhead and bottom fractions (i.e., top and bottom products) are cooled to completely condense the samples and are then collected in sample collection jars with a volume of ~1L. Collected samples are typically dried to completely remove the solvent before analysis: The collection jars are placed in a vacuum oven, the temperature is set to 140 °C, and nitrogen at 5 scfh (0.14 m³/h) is purged through the oven during sample drying, with or without a slight vacuum, to ensure the complete removal of solvent.

Identification of the Monomeric Constituents of Petroleum Pitches

As stated above in the **Introduction**, our first objective was to determine the molecular structures of the key monomeric constituents present in petroleum pitches. Marathon M-50 pitch (CAS no. 68187-58-6) was chosen as a representative pitch for this study. Work in our lab had shown that this pitch is similar in terms of both molecular weight and chemical composition to its predecessor, Ashland A-240, and to a pitch that is currently available on the market, Koppers KP-100 (all of these pitches have the same CAS number).

Previous work focused on identifying the monomers in a petroleum pitch had been limited. Basova et al. (33) used gas chromatography–MS (GC–MS) to determine the identity of the monomeric components present in both a Korean and a Conoco petroleum pitch. With GC-MS, however, species with molecular weights above 250 Daltons (Da) become increasingly difficult to both elute and resolve (34), and the mol wt range of monomers in petroleum pitches extends up to almost 400 Da, see Figure 2. Previous work on the characterization of FCC decant oils is also of interest to us. Because decant oils are in essence the starting monomers for petroleum pitch, we would expect their molecular

constitution to be similar to the monomer fraction of pitch, although the process of heat-soaking decant oil to make petroleum pitch results in both polymerization and volatilization, which would be expected to create at least some changes in the molecular composition. Eser and co-workers (35, 36), recognized leaders in the analysis of decant oils, have used GC-MS, high pressure liquid chromatography (HPLC) combined with UV-vis/photodiode array detection (UV-vis/PDA), HPLC/MS/MS, and laser desorption-mass spectrometry (LD-MS) to characterize a number of different decant oils. Their work has shown that decant oils are composed primarily of methylated derivatives of 3-6 ring PAHs, including phenanthrene, pyrene, chrysene, perylene, the benzopyrene isomers, and benzo[ghi]perylene.

The Monomeric Constituents: Experimental

Pre-Fractionation and Concentration of Petroleum Pitch into Monomer Cuts via Supercritical Extraction

A unique feature of our work is the use of multi-stage supercritical extraction (SCE) to fractionate the carbonaceous pitches into cuts of relatively narrow molecular weight. At first glance one might think that such a pre-fractionation step before the subsequent analytical step is simply a waste of time, as the succeeding analytical step should be able to effect the separation on its own. However, in this work we found that the SCE pre-fractionation step frequently presented significant advantages, as will be noted throughout this chapter as appropriate.

SCE was used to both concentrate and resolve the monomer portion of the M-50 pitch (see Figure 8) into three cuts, namely, low (270 Da and below), medium (270-335 Da), and high (335-388 Da) mol wt monomer cuts. In this manner, samples were generated for prep-scale GPC analysis that were many times more concentrated in specific monomers than the original pitch, facilitating their identification. The versatility of SCE in the processing of petroleum pitches is nicely illustrated here, as we see how the various pitch cuts were produced: SCE Monomer Cut 1 was generated from M-50 pitch via continuous SCE using methanol as the supercritical solvent (27); SCE Monomer Cut 2 was generated from M-50 pitch via semi-continuous DGE, using toluene as the supercritical solvent; and SCE Monomer Cut 3 was also generated via semi-continuous DGE, but here the feed was the “Dimer-Rich B” cut obtained via continuous DGE by Cervo et al. (29). Additional details on how the above cuts were obtained is given elsewhere (27, 32).

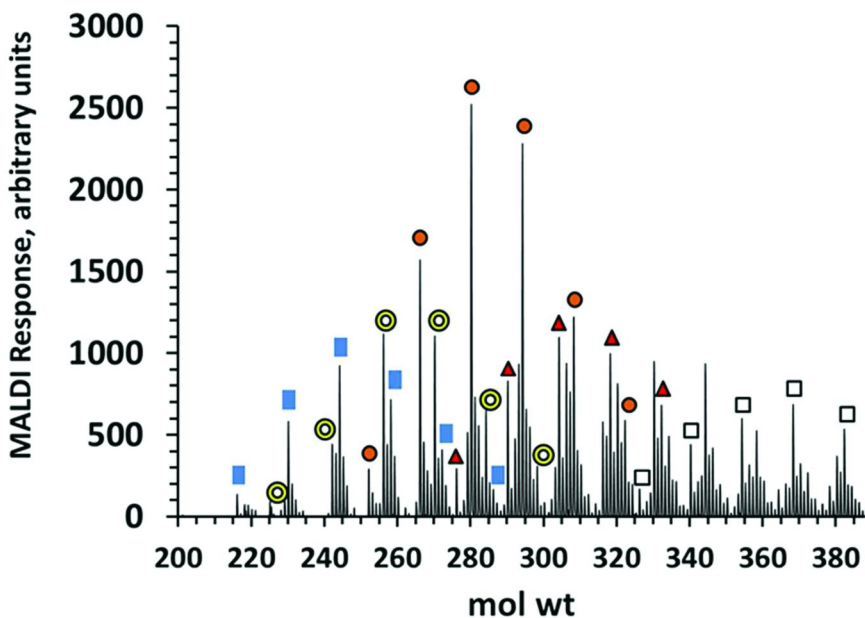


Figure 8. MALDI mass spectrum of M-50 pitch, showing the mol wt range of the monomer (210-388). The blue rectangle symbols are for pyrene (not shown) with increasing methyl substitution; the red triangles are for benzo[ghi]perylene with increasing methyl substitution. The other series are identified in the text. Reproduced with permission from ref (34). Copyright 2010 American Chemical Society.

GPC Fractions via Prep-Scale GPC from SCE Monomer Cuts 1-3

Prep-scale GPC was used to generate very narrow mol wt fractions from SCE Monomer Cuts 1-3, using hot 1,2,4-trichlorobenzene (TCB) as the mobile phase at 140° C. The choice of TCB as the mobile phase for fractionation of the monomer cuts of M-50 pitch was based on the fact that (1) Hutchenson et al. (37) had found ideal elution behavior with hot TCB and (2) solubility tests in our lab had shown that petroleum pitch is greater than 99% soluble in hot TCB over a concentration range of 1.5 to 100 mg/mL (38). An analytical-scale Waters Alliance GPCV 2000 modified for prep-scale work was used for this work. The two prep-scale GPC columns run in series (part no. PL1210-6125, pore size 500 Å column followed by part no. PL1210-6120, pore size 100 Å column) were supplied by Polymer Laboratories. Two GPC fractions were obtained from SCE Monomer Cut 1, five GPC fractions were obtained from SCE Monomer Cut 2, and five GPC fractions were obtained from SCE Monomer Cut 3. The GPC chromatogram for the fractionation of SCE Monomer Cut 2 is given as an example in Figure 9.

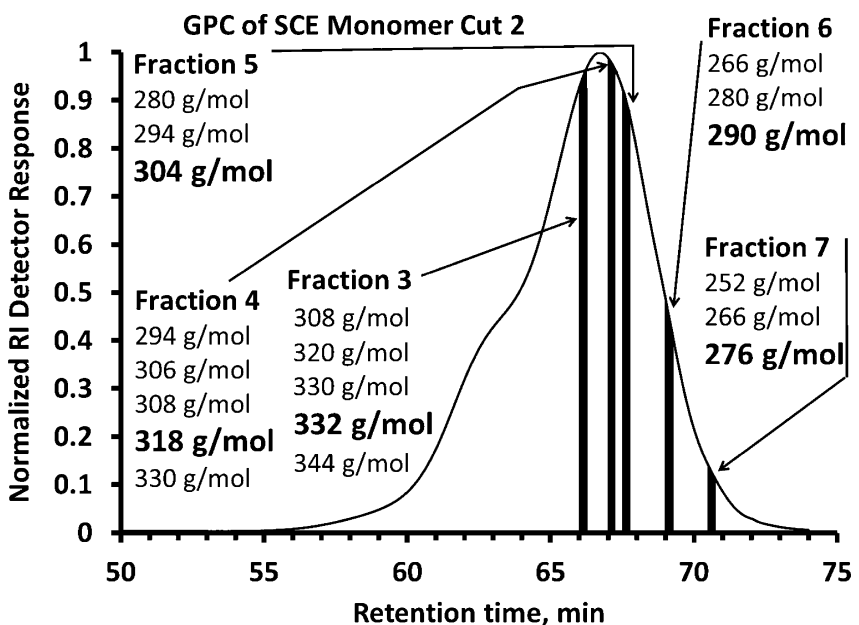


Figure 9. GPC Fractions 3-7 were obtained from the prep-scale GPC fractionation of SCE Monomer Cut 2, which encompasses the mid mol wt range of the monomers present in M-50 pitch. Adapted with permission from ref (34). Copyright 2010 American Chemical Society.

Individual Monomer Species Identification by HPLC + UV-Vis/PDA

HPLC + UV-vis/PDA (abbreviated HPLC/PDA) was used to unequivocally identify the monomeric species present in three pitch fractions: SCE Monomer Cut 1 (generated via SCE) and GPC Fractions 6 and 7, which were isolated from SCE Monomer Cut 2 via prep-scale GPC. In brief, the samples were first dried and then dissolved in acetonitrile (ACN)/water mixtures at concentrations resulting in desirable UV-vis spectra. Reversed-phase HPLC was used because of the success of previous workers (39-41) in using this technique to separate mixtures of PAHs with mol wts up to 450 Da. Here, a C18 reversed-phase column manufactured by Restek (Pinnacle II, product no. 9214575, 250 mm long) was used. The mobile phase was delivered to the column and PDA detector using a quaternary Waters model 626 solvent pump. The initial makeup of the mobile phase was 30/70 v/v ACN/water, with the ACN concentration being increased by 1 vol % per min until pure ACN was the eluent. A Waters Model 996 PDA detector was used to obtain the UV-vis spectra of the eluent exiting the column every 1.0 s. Species eluting from the HPLC column were identified by comparison with reference standards. For SCE Monomer Cut 1, fractions of the column eluent were collected every 20 s for follow-up MALDI analysis.

Conventional UV-vis analyses in cyclohexane (which has a much lower cutoff range than TCB) were performed on selected GPC fractions with a Spectral Instruments 400 Series spectrophotometer.

MALDI and PSD

Both MALDI and MALDI–post-source decay (PSD) analyses were performed on GPC fractions 1-12, using a Bruker Daltonics Autoflex MALDI mass spectrometer with a 337 nm nitrogen laser. MALDI was used to obtain the absolute molecular weight of the most prominent species in a given fraction; this was followed up with PSD on said prominent species, in order to obtain specific molecular structure information on those species. We have previously described the operating parameters for MALDI in detail elsewhere (27). Because of the very small (μg) quantities of pitch in each GPC or HPLC eluent fraction, a special sample preparation technique had to be used for MALDI to minimize the amount of sample used as follows: first, the matrix TCNQ (tetracyanoquinodimethane, CAS no. 1518-16-7, supplied by TCI America) was ground into a fine powder with the aid of a mini-ball mill (Thermo Electron Corp., Wig-L-Bug model). The TCNQ was then deposited onto the MALDI target using water spotting, a method developed by our group at Clemson (18). Next, a drop of the fraction of interest was spotted onto the dried TCNQ, and the sample was ready for analysis upon drying.

The Monomeric Constituents: Results and Discussion

Determination of PAH Backbones for M-50 Pitch Monomers

The HPLC chromatogram obtained for SCE Monomer Cut 1 is given as Figure 10. Here, the average absorbance from 200-450 nm was plotted, as different compounds absorb strongly at different wavelengths. Thus, we are able to show the HPLC retention times for virtually all identified components on this single plot. The five PAH backbone structures (i.e., the “A” through “E” series) shown in Figure 10 were definitively identified by UV-vis/PDA. For example, the “A” peak (at 48.82 min) was identified via UV spectral match as pyrene and the “B” peak (at 51.52 min) as triphenylene. Other key species identified (e.g., chrysene and benz[a]anthracene) are listed in the figure caption. However, specific information about the alkyl substituent groups located on the PAH backbones frequently also required information obtained via other analytical methods, as is illustrated next. Referring to Figures 11a-c, we see that Peaks A1, A2, and A3 from Figure 10 are UV spectral matches for pyrene, albeit with a small bathochromic shift. This is what one would expect for alkylpyrenes, and definitive identification of A1 and A2 as 4- and 2-methylpyrene, respectively, was obtained by comparison to reference UV spectra (42). Definitive confirmation was obtained from the MALDI spectra of Figures 11d-e, which show that the mol wts of the HPLC eluents were 216 Da, corresponding to an alkylpyrene. Other di- (A3 and A5) and tri-methyl pyrenes (A6) (mol wt = 244 Da) shown in Figure 10 were also identified through

spectral match and confirmed by MALDI. No reference was available for the UV-vis spectrum given in Figure 11f, but the HPLC eluent gave a strong MALDI signal at 230 Da, so the species must be a dimethylpyrene. This latter example shows how the combination of HPLC with MALDI can be a powerful tool for the unambiguous identification of PAH species, when good separation is achieved with the SCE pre-fractionation and concentration step.

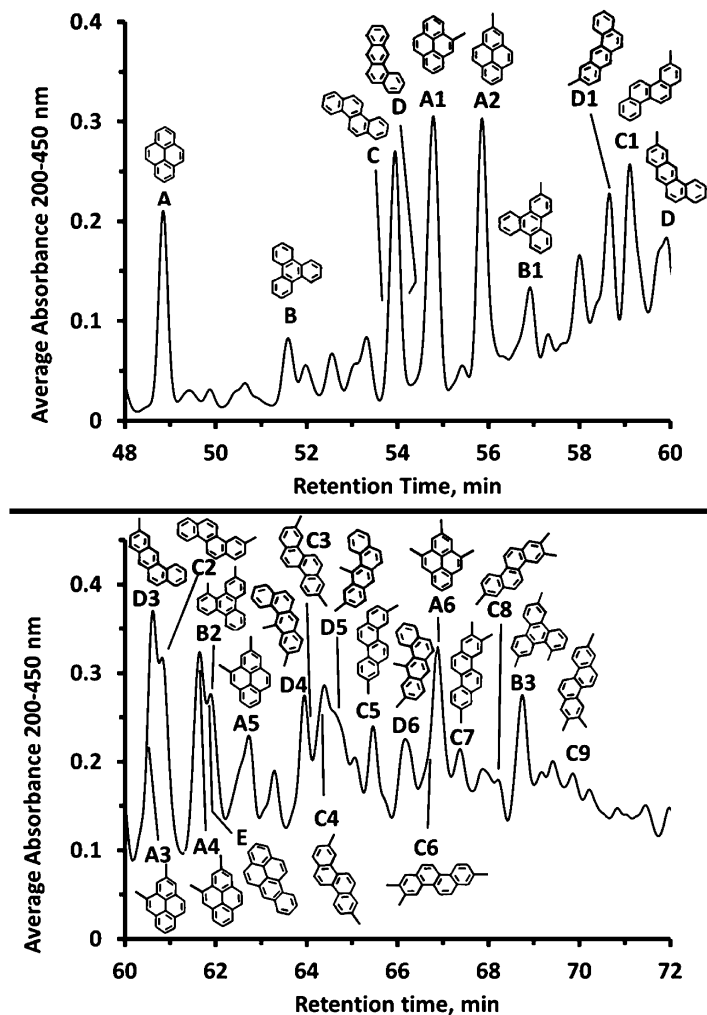


Figure 10. HPLC chromatogram of SCE Monomer Cut 1, the low mol wt portion of the monomers in M-50 pitch. The “A” series is for pyrene (A) (mol wt = 202 Da) with increasing degrees of methylation (A1–A6); similarly, the “B”, “C”, and “D” series are for triphenylene, chrysene, and benz[a]anthracene (all with mol wt = 228 Da), respectively, and their methyl substituents; and the “E” series is for benzo[a]pyrene and its methyl substituents. Reproduced with permission from ref (34). Copyright 2010 American Chemical Society.

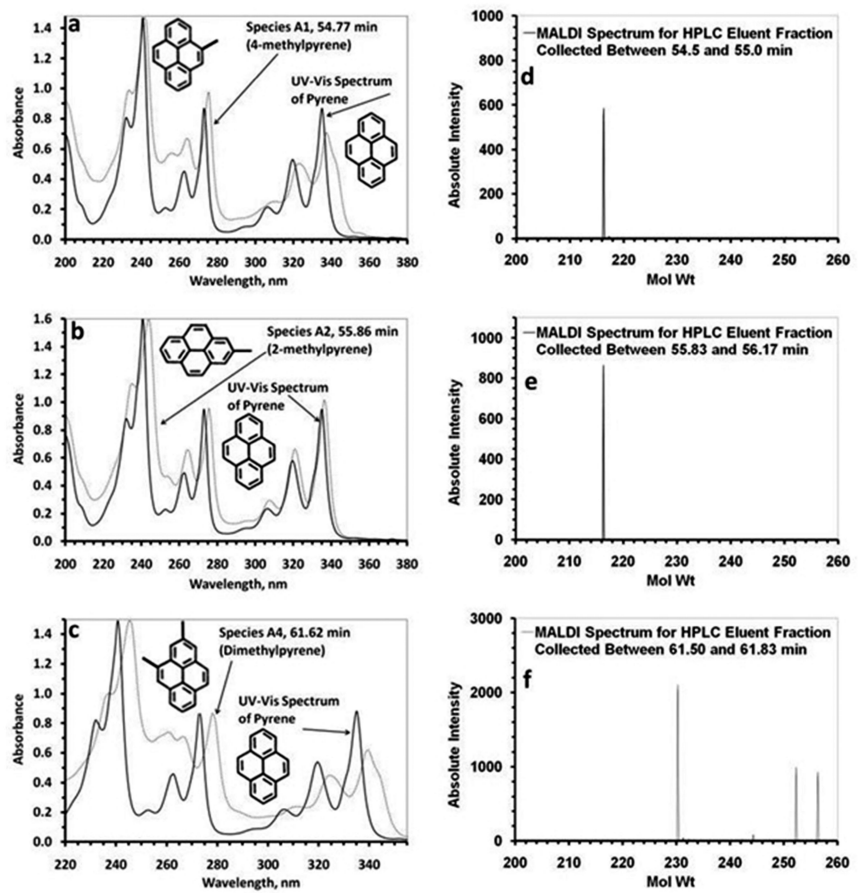


Figure 11. UV-vis spectra (obtained by HPLC/PDA) for the alkylpyrenes are very similar to those for pyrene, albeit with a slight bathochromatic shift. MALDI serves as a critical confirmation that the species are, indeed, alkylpyrenes. Reproduced with permission from ref (34). Copyright 2010 American Chemical Society.

Referring again to Figure 10, the “backbone” along with multiple alkylated versions of triphenylene (the B series), chrysene (the C series), and benz[a]anthracene (the D series) were identified by UV spectral match. Based on FTIR spectroscopy by Cristadoro et al. (27) on an SCE monomer cut of M-50 pitch, the monomers are preferentially substituted at a position β from an “inner” carbon atom that bonds with three other carbons. Thus, for the structures shown in Figure 10, we have placed most methyl groups in that position. In general, no UV library was available with such information.

Recall that SCE Monomer Cut 1 was for the lower mol wt portion of the monomer cut of M-50 pitch (270 Da and below). To identify key species in the medium mol wt portion (i.e, from 270-335 Da, see Figure 8), GPC Fractions 6 and 7, which were isolated from SCE Monomer Cut 2 (see Figure 9), were analyzed by both HPLC/PDA and MALDI, see Figure 12. These fractions were particularly suitable for analysis, as relatively few species were present (as shown by MALDI). As before, the PAH backbone structures were determined by spectral match (see Figure 13), and the presence of methyl-substituted analogs were deduced from the MALDI spectra of the GPC fraction of interest (see Figure 12). Shown are the identification of the benzo[e]pyrene, benzo[a]pyrene, and benzo[ghi]perylene backbones and several of their alkyl-substituted analogs.

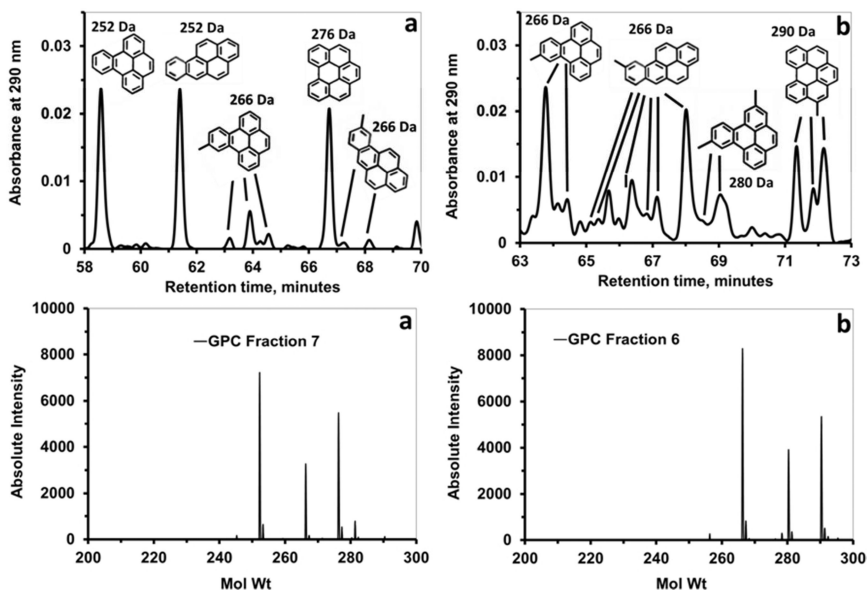


Figure 12. HPLC chromatograms and MALDI spectra of GPC Fractions 7 (see a) and 6 (see b). Adapted with permission from ref (34). Copyright 2010 American Chemical Society.

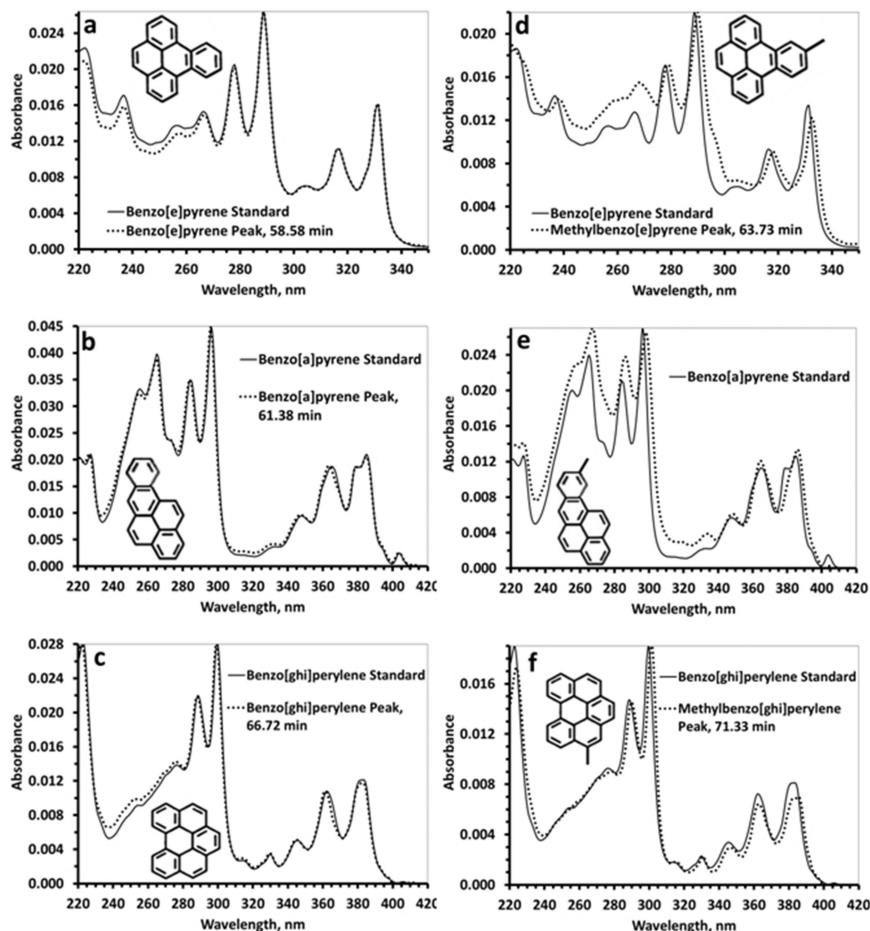


Figure 13. UV-vis spectra (from HPLC/PDA) and MALDI spectra (see Figure 12) of GPC Fractions 7 and 6 indicate that the PAHs (a) benzo[e]pyrene, (b) benzo[a]pyrene, and (c) benzo[ghi]perylene are predominant in Fraction 7, while their methyl substituents (see d, e, and f) are predominant in Fraction 6. Reproduced with permission from ref (34). Copyright 2010 American Chemical Society.

Determination of Degree of Alkyl Substitution on M-50 Pitch Monomers

Referring to the MALDI mass spectrum in Figure 8, we see that the monomer is approximately Gaussian in terms of its MWD (except perhaps at the highest molecular weights). More importantly, (1) the molecular weights corresponding to the PAH backbones identified above by HPLC/PDA can be located, (2) the peak signals for these species are relatively intense, and (3) they are part of a patterned response. For example, the blue rectangles mark the peaks consistent

with methyl and dimethylpyrene at 216 and 230 Da, respectively; the yellow rings at 228 and 242 Da are consistent with the “C” series of PAHs and their methyl substituents (see Figure 10); the red circles at 252 and 266 Da match the molecular weights of the benzopyrenes and their methyls, and the red triangles at 276 and 290 match benzo[ghi]perylene and its methyl (see Figures 12 and 13). In fact, looking at all of the colored symbols as a group, if we look for signal responses 14 Da greater than those mentioned above (corresponding to the addition of even more methyl groups to the PAH backbone), we find that they comprise the dominant species in the MALDI spectra and form a well-behaved Gaussian distribution, with the distribution beginning with the bare PAH backbone. (An exception is that bare pyrene is not observed, but we know from previous experience that in small amounts it is simply too volatile to be observed by MALDI.)

Therefore, MALDI-PSD was used to determine whether alkyl substitution was indeed the cause of the patterned responses described above, and to distinguish the extent to which the responses were due to methyl groups, or to larger alkyl (e.g., ethyl) groups. Specifically, PSD analysis was carried out on the twelve GPC fractions isolated from SCE Monomer Cuts 1, 2, and 3 (e.g., five are shown in Figure 9), with selected results from these analyses being given in Figures 14a-o. (Actually, 31 GPC fractions were generated, but only 12 peaks of interest that were sufficiently isolated such that they could be analyzed for molecular structure by PSD fragmentation analysis. For example, Figure 15 shows that for GPC fraction 5, PSD analysis could have been carried out on the peaks at 280.4, 294.4, and 304.4 Da, as they are sufficiently isolated from peaks of comparable size, but the peak at 316.4 Da could not have been analyzed, as it had a similarly sized peak nearby at ~318 Da whose fragmentation pattern would have interfered with that produced by the peak at 316.4.)

PSD results for the signal distribution marked by the blue rectangles are given in Figures 14a-e. The spectrum in panel **a** with a signal at $m/z = 216.3$ is consistent with our previous identification of methyl pyrene (see Figure 11), as no fragmentation pattern occurs with either an unsubstituted PAH backbone or one with a single methyl group (43, 44). In panel **b**, the spectrum shows a parent ion at $m/z = 230.4$ and a demethylated ion at 215.3, a pattern consistent with dimethylpyrene (a PAH ion with at least one methyl group is particularly stable (43, 44)). Panels **c** and **d**, then, are consistent with pyrene substituted with three and four methyl groups, respectively, with the parent and demethylated ions observed at $m/z = (244.3, 229.2)$ and $(258.4, 243.3)$, respectively. In panel **e**, a de-ethylated ion is also observed ($m/z = 243.6$), albeit at an intensity only 10% of that of the demethylated ion. This result is also consistent with proton NMR work on the monomer fraction of M-50 pitch (27), which indicates that ethyl substituent groups are relatively rare. Considering both the PSD and HPLC/PDA results, then, we were able to unequivocally identify Peaks A1-A6 in Figure 10 as alkylpyrenes.

An analogous process was followed for identification of the “yellow ring” compounds in Figure 8. Referring to Figures 14f-j, we see that the signals at $m/z = 228.3$ and 242.3 exhibit no fragmentation, so they must refer to the parent and monomethylated groups for triphenylene, chrysene, or benz[a]anthracene, as they all have molecular weights of 228. (Unequivocal identification of the PAH

backbones (labeled as the B, C, and D series, respectively) was made possible only by HPLC/PDA, see Figure 10.) Thus, Figures 14h-j shows fragmentation patterns for the dimethyl, trimethyl, and tetramethyl versions of the parent PAH backbones mentioned above. The peak at 269.8 in Figure 14j indicates that small amounts of ethyl groups are also present, as was described earlier for pyrene. The “orange circle and “red triangle” compounds identified in Figure 8 were identified in an analogous manner to that described above, with PSD providing the molecular weight and the alkyl-substituted nature of the species (see Figure 14), and HPLC/PDA providing unambiguous identification of the PAH backbones (see Figures 12 and 13). PSD for the benzo[ghi]perylene series are given elsewhere (34).

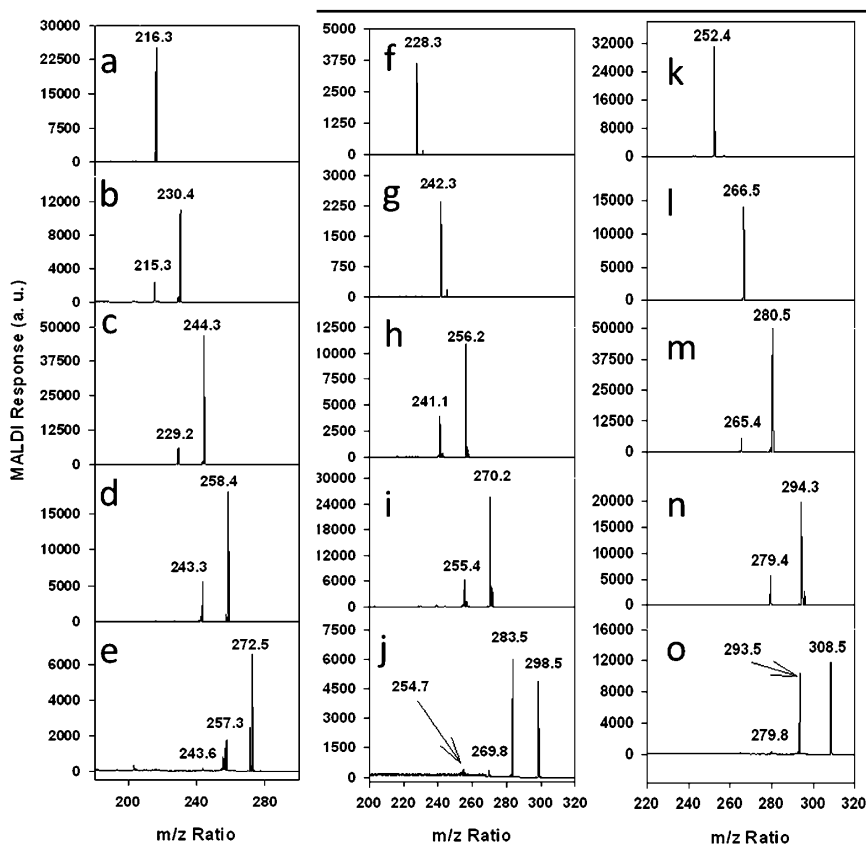


Figure 14. MALDI-PSD fragmentation analysis for the individual species comprising the “blue rectangle” (a-e), “yellow ring” (f-j), and “orange circle” (k-o) series in Figure 8 are given. The “red triangle” series is given elsewhere (34). The results show that alkylated PAHs are prevalent constituents in the monomer portion of M-50 pitch.

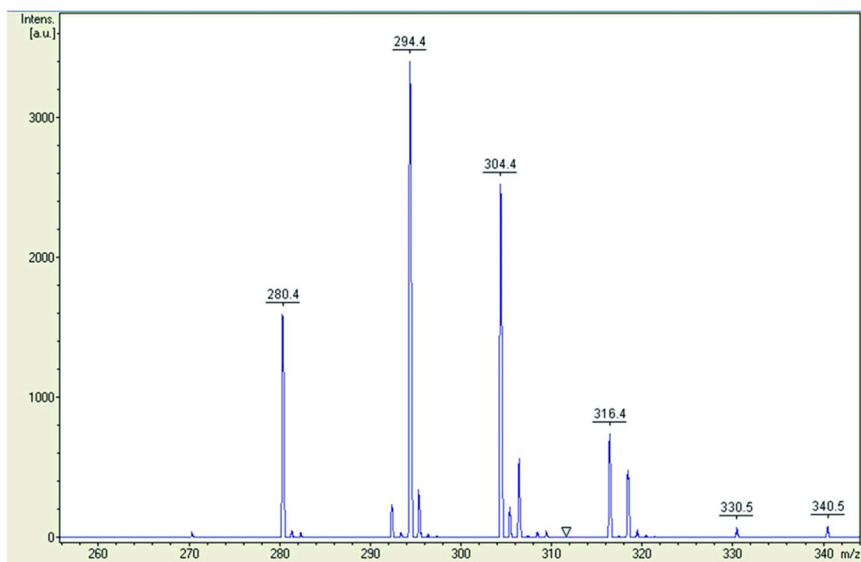


Figure 15. Adequate separation between dominant species in an SCE-, HPLC-, or GPC-generated pitch fraction is required to carry out PSD fragmentation analysis. GPC Fraction 5 is shown here as an example.

It is important to emphasize the importance of us having information available from multiple analytical techniques for the unambiguous characterization of the monomeric constituents of petroleum pitches. For example, in early work because we did not use HPLC/PDA for the analysis of SCE + GPC fractions (27), we mistook the blue rectangle series in Figure 8 as being for alkylated fluoranthenes. But subsequent HPLC/PDA work (34) revealed that in fact there are relatively few fluoranthene species in the monomer fraction of M-50 pitch – but lots of alkylated pyrenes, which have the same molecular weight as alkylated fluoranthenes. As another example, the presence of benzo[a]- and benzo[e]pyrenes and their alkylated substituents was determined by HPLC/PDA (see Figures 12a-b and 13a-b, d-e)), but the number of these alkyl groups, and the fact that they were predominantly methyl, could only be determined by also applying MALDI and MALDI-PSD. And finally, without the use of sequential SCE + GPC to produce truly narrow cuts of the pitches that contained isolated, individual species, little of the analytical work discussed above would have been possible.

Estimating the Species Compositions of the Monomer Fraction of M-50 Pitch

Accurately estimating the concentration of the monomeric species present in M-50 pitch proved to be a difficult task. Our original intent was to use the UV-vis results from HPLC/PDA to estimate these quantities, as UV-vis responses are recognized as being much more linear than those obtained via MALDI mass spectrometry (45). However, the problem was that HPLC/PDA was applied to

several different fractions prepared at greatly different sample concentrations, for example, SCE Monomer Cut 1 and GPC Fractions 6 and 7, so it would have been difficult to estimate the quantity of a given species given only HPLC/PDA information. The use of internal or external standards to enable quantification of the UV-vis results was considered, but we decided against it because the effort to carry out such a plan would have been excessive relative to the benefits achieved. As an alternative, we used the MALDI spectrum given in Figure 8 to estimate the concentrations of the major monomer constituents. These estimates were obtained as follows: (1) the monomer area under the peaks located between 216 and 318 Da was determined; (2) the area and mole fractions of the monomeric constituents were assumed to be equal; (3) a number average molecular weight was calculated ($M_n = 280$); and (4) the desired information, a weight percentage for each identified species, could then be calculated. The calculated concentrations are given in Table I, and the PAH backbones for the listed species are given in Figure 16. Estimates of monomer concentrations for species above 318 Da were not attempted for two reasons: dimer species start to appear in the spectrum above 320 Da (see next section), and species become increasingly difficult to isolate via SCE + GPC or SCE + HPLC so that they can be positively identified.

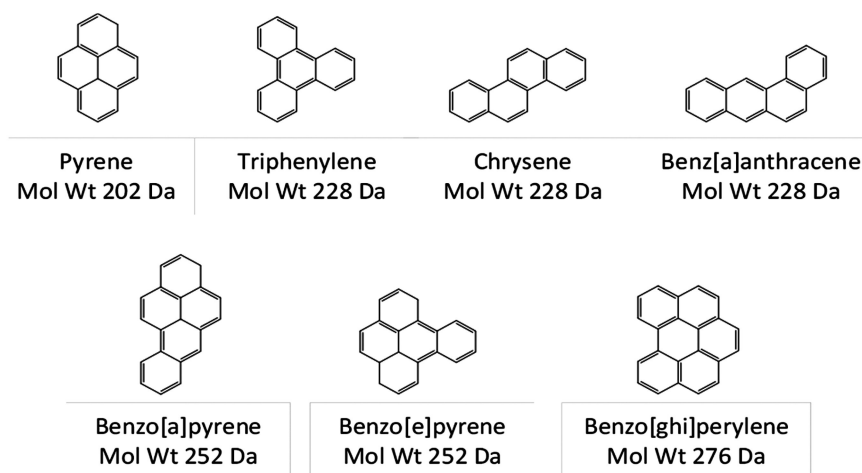


Figure 16. The most prevalent PAH backbones in the monomer portion of M-50 petroleum pitch (see Figure 8 and Table I).

The species concentrations presented in Table I should be regarded as estimates only. The use of MALDI mass spectrometry to quantitatively determine the concentration of species in a mixture is not a generally accepted method the way that, for example, GC-MS is, because different species have different propensities to ionize and thus “fly”. In particular, Burgess (45) has shown that alkylated PAHs produce signal responses 6-8 times higher than the same PAH backbone with no alkyl substitution. Cristadoro et al. (46) also reported on

this behavior and gave two reasons for the phenomenon: (1) the π electrons of alkylated PAHs associate more weakly with neighboring PAHs, resulting in easier desorption from the MALDI target plate, and (2) as was observed previously in our PSD work, the ionization energy of alkyl-substituted PAHs is lower than their “bare” PAH backbone counterparts, producing higher signal intensities. Fortunately, though, Burgess (45) has shown from a careful analysis of the HPLC data on SCE Monomer Cut 1 and GPC Fraction 7 that nonsubstituted PAHs are a relatively small percentage of the monomer portion of M-50 pitch. (For example, more than 85% of all pyrenes and chrysenes are alkylated.) In terms of MALDI response, the intensity doesn’t change much with increasing alkyl substitution past the first methyl group. Finally, species with molecular weights less than 250 are volatile enough that there is some loss from the target in the high-vacuum environment of the MALDI. In summary, then, the values given can be regarded as generally being accurate to within ± 25 -35%.

Table I. The major species present in the monomeric portion of M-50 pitch, their concentrations in the monomer, their molecular weights, and the color and symbol ID of their associated signal distributions (see Figure 8)

<i>Compound</i>	<i>Wt % in Monomer</i>	<i>Mol % in Monomer</i>	<i>Mol Wt (Da)</i>	<i>Signal Distribution</i>
Methylpyrenes (A1, A2)	0.16	0.20	216	Blue rectangle
Dimethylpyrenes (A3, A4, A5)	1.28	1.56	230	Blue rectangle
Trimethylpyrene (A6)	2.16	2.48	244	Blue rectangle
Triphenylene, chrysene, benz[a]anthracene (B, C, D)	0.11	0.14	228	Yellow ring
Methylated triphenylene, chrysene, and benz[a]anthracene (B1, C1, C2, D1, D2, D3)	1.02	1.18	242	Yellow ring
Dimethylated triphenylene, chrysene, and benz[a]anthracene (B2, C3, C4, C5, D4, D5, D6)	2.69	2.94	256	Yellow ring
Trimethylated triphenylene and chrysene (B3, C6, C7, C8, C9)	3.30	3.42	270	Yellow ring
Benzopyrenes	0.18	0.20	252	Orange circle
Methylbenzopyrenes	4.20	4.42	266	Orange circle
Dimethylbenzopyrenes	8.45	8.45	280	Orange circle
Trimethylbenzopyrenes	7.88	7.51	294	Orange circle
Methylbenzo[ghi]perylene	2.68	2.59	290	Red triangle

Continued on next page.

Table I. (Continued). The major species present in the monomeric portion of M-50 pitch, their concentrations in the monomer, their molecular weights, and the color and symbol ID of their associated signal distributions (see Figure 8)

<i>Compound</i>	<i>Wt % in Monomer</i>	<i>Mol % in Monomer</i>	<i>Mol Wt (Da)</i>	<i>Signal Distribution</i>
Dimethylbenzo[ghi]perylene	4.15	3.83	304	Red triangle
Trimethylbenzo[ghi]perylene	3.74	3.30	318	Red triangle
Totals	42.0	42.2	-----	-----

Identification of the Dimer Constituents of Petroleum Pitches

Once the key monomeric constituents in M-50 petroleum pitch had been established, the prediction of the molecular structures of the key dimers in this representative pitch was the next task. Two of the most obvious questions that we wanted to resolve were (1) to what extent is the molecular structure of the monomer unit altered as dimers are created and (2) what type of structure is used to link two monomer units to form a dimer? From the standpoint of understanding the molecular structures of pitch oligomers in general, dimers are the key constituents in many ways. That is, if you can figure out what their monomer units look like and how monomers link to form dimers, then there's a good chance that you can extrapolate this knowledge to the higher-order oligomers and be correct.

The procedure for analyzing the dimer portion of M-50 pitch was to first isolate relatively large amounts of specific pitch oligomers by continuous SCE, then obtain fractions of narrower molecular weight via semi-continuous SCE, and finally use preparative-scale (prep-scale) GPC to produce pitch subfractions containing several well-separated, individual species encompassing a total mol wt range of about 50 Da. Those individual species could then be analyzed by MALDI and by MALDI-PSD to determine absolute molecular weights and the degree of alkylation present on the dimers. Next, UV-vis was used to try and determine the molecular structure of the dimer molecule, including the nature of the bonds linking the monomer units. Finally, the above information was combined with our knowledge of the most common monomer units present in M-50 pitch (see previous section) to propose actual molecular structures for the most common dimer units present in M-50 pitch.

As was mentioned earlier in the **Introduction**, previous work on the characterization of petroleum and other carbonaceous pitches was significantly limited by the fact that individual species or even narrow mol wt cuts of the pitches were not obtained, as the only separation methods employed were typically simple solvent and solvent-mixture extractions (11-15). Thus, any mass spectra obtained were crowded, so that individual species could not be isolated for additional analysis by other characterization methods that would yield molecular- or chemical-structure information.

The Dimer Constituents: Experimental

Pre-Fractionation and Concentration of M-50 Petroleum Pitch into Dimer Cuts via Continuous + Semi-Continuous Supercritical Extraction

SCE was used to both concentrate and resolve the dimer portion of the M-50 pitch (see Figure 17) into a lower and a higher mol wt cut of the dimer. SCE Dimer Cuts 1 and 2 (see Figures 18 and 19) were produced by first recovering a dimer-rich portion from the M-50 raw pitch in a 2-column, continuous setup conceptually similar to that shown in Figure 7; the exact setup is described elsewhere (29). The “Dimer-Rich B” (29) fraction that was recovered also contained some heavy monomer and light trimer species. This fraction then served as the feed to a semi-continuous SCE setup (see Figure 6). The setup used is generally described earlier in this chapter; a column gradient of 330/350/380 °C bot/mid/top was used at a column pressure of 29 bar for SCE Dimer Cut 1, in order to recover and concentrate the lower mol wt dimers, and the same temperature profile with a pressure of 42 bar was used for SCE Dimer Cut 2 in order to recover the mid-range of the dimers; additional details are given elsewhere (47).

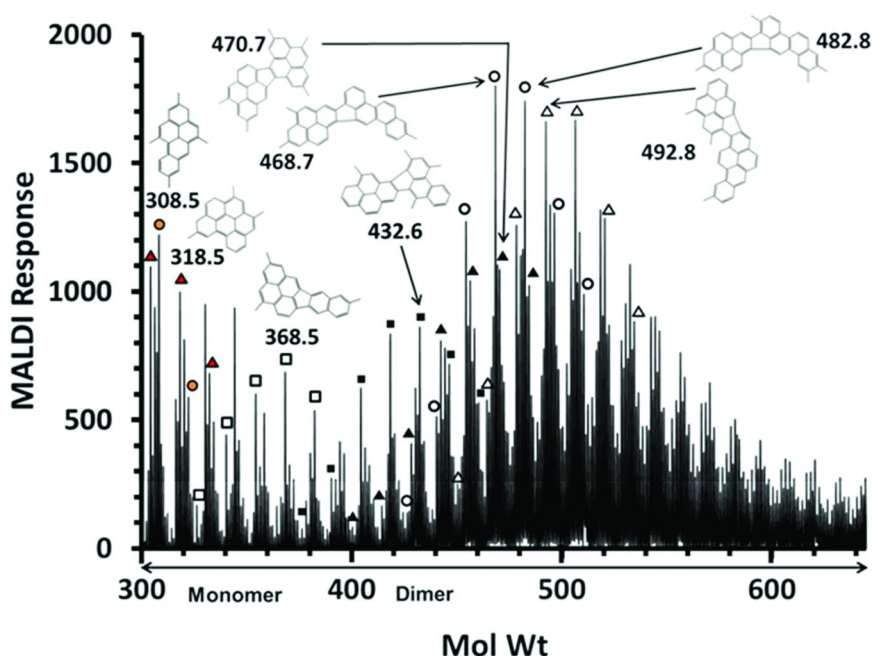


Figure 17. MALDI of M-50 pitch, focused in on the heavy monomer and dimer region. The major dimers are denoted with symbols, with mol wt increases for a given symbol being due to increasing methylation. Representative molecular structures, as deduced from structural characterization data, are also given.

Adapted with permission from ref (47). Copyright 2011 Elsevier.

GPC Fractions via Prep-Scale GPC from SCE Dimer Cuts 1-2

Prep-scale GPC was used to generate narrow mol wt fractions from SCE Dimer Cuts 1-2, using hot TCB as the mobile phase at 140° C. The equipment and procedure used were essentially the same as those used for the SCE Monomer Cuts, and are described in detail elsewhere (47). As shown in Figures 18 and 19, GPC Fractions 4-11 were obtained from SCE Dimer Cut 1, and GPC Fractions 12-19 were obtained from SCE Dimer Cut 2. Recall that the goal of the GPC fractionation work is to obtain pitch species that are isolated enough to be analyzed and thus identified. Up to 45 GPC fractions were collected every 15 seconds per Dimer Cut in order to obtain the 16 fractions shown that produced adequately isolated peaks.

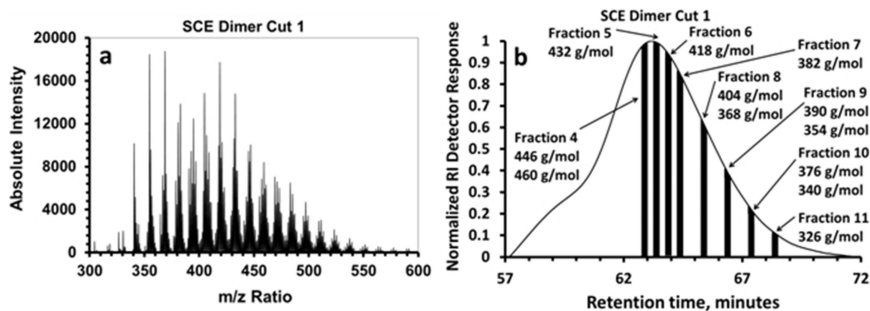


Figure 18. (a) MALDI mass spectrum for SCE Dimer Cut 1, concentrated in the lower mol wt dimer species. (b) GPC chromatogram for SCE Dimer Cut 1, where GPC Fractions 4-11 were collected. Molecular weights of the species subjected to MALDI-PSD are listed for each fraction. Adapted with permission from ref (47). Copyright 2011 Elsevier.

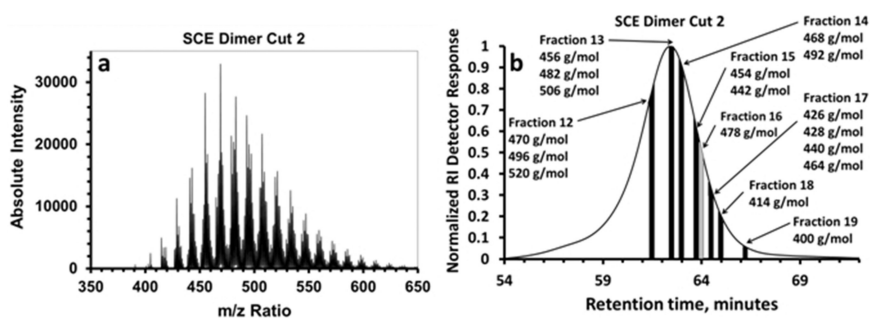


Figure 19. (a) MALDI mass spectrum for SCE Dimer Cut 2, concentrated in mid-range dimer species. (b) GPC chromatogram for SCE Dimer Cut 2, where GPC Fractions 12-19 were collected. Molecular weights of the species subjected to MALDI-PSD are listed for each fraction. Adapted with permission from ref (47). Copyright 2011 Elsevier.

UV-vis analyses of the collected GPC fractions were carried out using a Spectral Instruments 400 Series spectrophotometer. GPC fractions subjected to UV-Vis analysis were either run directly, or were dried to remove the TCB mobile phase before re-dissolving in cyclohexane, the UV cutoff wavelength of which is ~110 nm less than that of TCB. Typically, cyclohexane was used as the UV-Vis solvent for the dimer-range GPC fractions. In all cases, the concentrations of the GPC fractions analyzed were adjusted by adding solvent until the maximum light absorbance value measured was less than 2.0.

MALDI and PSD analyses were obtained using a Bruker Daltonics Autoflex MALDI mass spectrometer with a 337 nm nitrogen laser. We have previously described both the sample preparation method (18) and the operating parameters for MALDI and PSD (27) in detail elsewhere.

The Dimer Constituents: Results and Discussion

MALDI and PSD for Dimer Molecular Weights and Degree of Alkyl Substitution

The MALDI spectrum of M-50 pitch, albeit now focused in on the heavy monomer and dimer region, is given as Figure 17. In the **Monomeric Constituents** portion of this chapter, we learned how the monomers in M-50 pitch are comprised of a relatively small number of PAH backbones, with those backbones typically decorated in an approximately Gaussian distribution with 1-5 methyl groups. Note that the tail end of the “orange circle” (i.e., the benzopyrenes) and “red triangle” (the benzoperlyenes) series of monomers (see Figure 8) are repeated here for clarity. As was the case for M-50 monomer, we see that the dimer portion of M-50 pitch also is dominated by Gaussian signal distributions consisting of peaks separated by 14 Da. As before, we have highlighted the major distributions with symbols for ease of identification. For example, the “black triangle” signal distribution starts at $m/z = 400.4$ Da and extends in increments of 14 Da (corresponding to the addition of yet another methyl group to the dimer backbone) all the way to 470.6 Da. Four other Gaussian signal distributions (the “white square”, originating at $m/z = 326.5$; the “black square”, originating at $m/z = 376.4$; the “white circle”, originating at $m/z = 426.2$; and the “white triangle”, originating at $m/z = 450.6$, are also shown.

As for the monomers, MALDI-PSD was used to determine whether alkyl substitution was indeed the cause of the patterned responses described above, and to distinguish the extent to which the responses were due to methyl groups, or to larger alkyl (e.g., ethyl) groups. In Figure 20a-l and 21a-r, MALDI-PSD fragmentation analyses are shown for the species in each of the aforementioned distributions. For every series, the PSD fragmentation patterns for the first two species exhibit no fragment peaks, an observation that is in agreement with reference mass spectra (43) for unsubstituted and single-methylated PAHs. However, PSD spectra for all other isolated species exhibit a sharp fragment peak at 15 Da less than that of the parent species, indicating a species that has lost a methyl group (e.g., 418.5 and 403.3 in Figure 20i). In addition, many of the most

alkylated PSD spectra (i.e., those of higher mol wts) in each distribution exhibit fragment peaks at a mol wt 29 Da less than that of the parent species, indicating a species that has lost an ethyl group (e.g., 446.5, 431.5, and 417.6 in Figure 20k). It is encouraging to note that these trends are the same as those observed in the PSD spectra for the monomer species (see Figure 14).

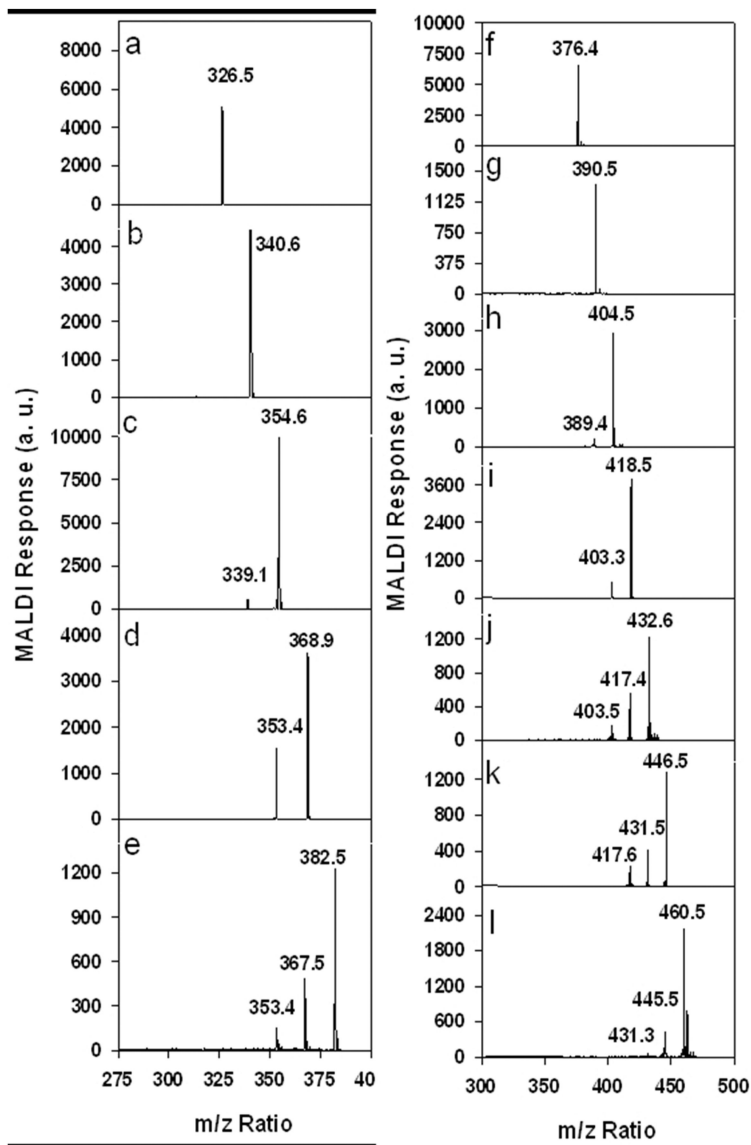


Figure 20. MALDI-PSD fragmentation analysis for the “white square” (a-e) and “black square” (f-l) species distributions given in Figure 17. Note that methyl substituent groups are the dominant fragment. Spectra are from the analysis of GPC Fractions 4-11.

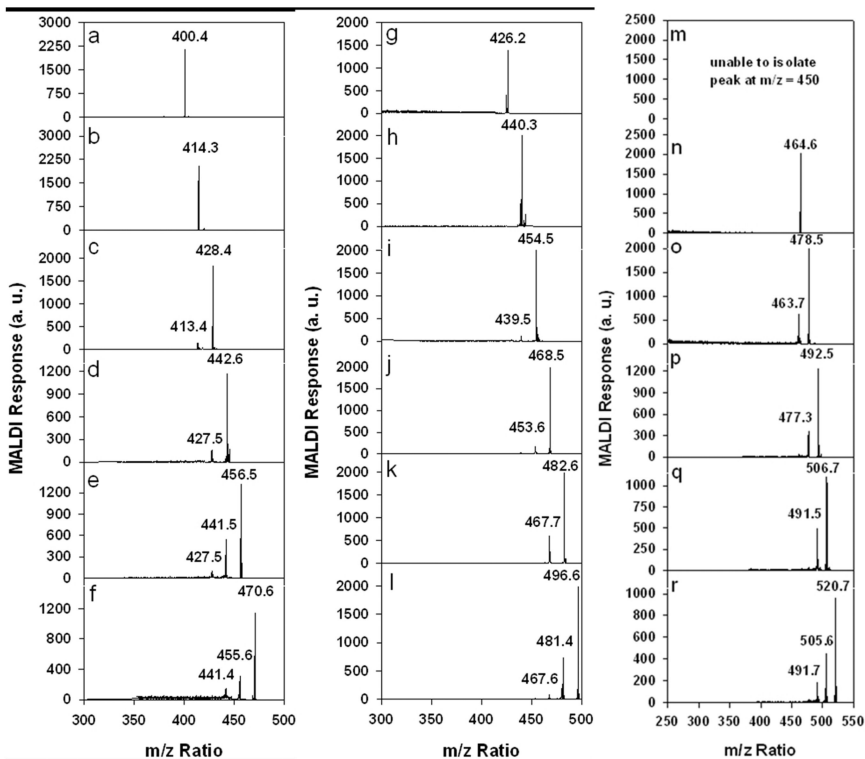


Figure 21. MALDI-PSD fragmentation analysis for the “black triangle” (a-f), “white circle” (g-l), and “white triangle” (m-r) species distributions given in Figure 17. Note that methyl substituent groups are the dominant fragment. Spectra are from the analysis of GPC Fractions 12-19.

MALDI-PSD analyses could not be performed on the signal at 450.6 Da (see Figure 21m) because of interference from closely neighboring signals (i.e., species) with stronger MALDI responses. However, we consider it likely that the “white triangle” series (see Figures 17 and 21m-r) begins at 450.6 Da. Similarly, PSD could not be applied to the portion of M-50 dimer above ~520 Da, as prep-scale GPC could not be used in this region to isolate species for PSD analysis.

MALDI and PSD for Molecular Structure of Dimers

HPLC/PDA could be used to unambiguously determine the molecular structures of the monomer species present in M-50 pitch because (1) we were able to isolate the monomer species and (2) because UV reference standards existed for the monomers. However, such a definitive identification of the dimers was *not* possible because even if we had been able to adequately isolate the dimer species

by HPLC (not a given), the needed UV reference dimer standards simply did not exist. Thus, we were forced to draw our conclusions about the molecular structure of the dimers based on alternative information, including MALDI, MALDI-PSD, and UV-vis measurements on selected GPC fractions obtained from our dimer cuts (see Figures 18 and 19).

The first evidence that little structural change was occurring to the monomer units in the dimer was the PSD information given in Figures 20 and 21. As noted above, the fragmentation patterns observed are strikingly similar to those previously obtained for the monomers, with the number and types of alkyl substituent groups being largely unchanged. In addition, no fragmentation patterns indicative of naphthenic groups or of biphenyl linkages between the monomer units were observed (43), so the evidence suggests that all “backbone” and “linking” carbons are still PAHs. Taken together, these two observations provided strong evidence that the monomer units are essentially undisturbed by the process of heat-soaking, in which the FCC decant oil is thermally polymerized to create the oligomers that constitute petroleum pitch. (Of course we were not able to determine whether perhaps some methyl groups are being ejected during the polymerization process, but the fragmentation patterns indicated that many substituent groups remain.)

If the above conclusions were correct, then the dimer species shown in the MALDI spectrum of Figure 17 would have been created by the loss of two aromatic hydrogen atoms per monomer and the subsequent formation of a 5- or 6-membered connecting ring. Thus, we proposed dimer structures based on the polymerization of the most common monomer units identified above, and then looked for those molecular weights in Figure 17. For example, by combining two pyrene monomers ($m/z = 202.3$), we would obtain a pyrene dimer ($m/z = 400.4$), see Figure 21a. And since alkylated pyrene was a common monomer constituent, we would expect to see a series of alkyl-substituted pyrene dimers. Indeed, such a signal distribution is found, see the black triangles in Figure 17 and also see Figure 21a-f. Using this same rationale, we proposed dimer structures for all of the series marked by symbols in Figure 17, with all proposed PAH backbones containing only monomer units previously identified in significant quantities. Examples of the resulting molecular structures, associated with their symbols, are given in Figure 17. A summary of the possible dimer combinations consistent with the MALDI and PSD spectra of Figures 17 and 20-21 are given in Table II. Two lower mol wt series in Figure 17 that are only partly consistent with this rationale were the white and black squares, the PSDs of which are given in Figure 20a-l. We concluded that the condensation of naphthalene or phenanthrene with pyrene to form a small dimer were the most likely structures for these two series, as both naphthalene and phenanthrene are present in decant oil (35, 36).

MALDI and UV-Vis To Determine the Nature of the Linkages Connecting the Monomer Units in Dimers

Once we had established with a reasonable degree of certainty that the monomeric PAH backbones were essentially unchanged by the thermal

polymerization process to form oligomers, we wanted to determine the nature of the bonds linking the monomer units to form the dimers. In our early work (27), we had assumed that all linkages were via 6-membered rings to form what are called alternant PAHs (48), but another possibility that we had not previously considered was linkage via a 5-membered ring (PAHs with 5-membered rings are called nonalternant PAHs).

Table II. Molecular weights of both the precursor monomer units and the resultant major oligomers that comprise M-50 pitch

<i>Oligomer Type</i>	<i>Monomer Unit 1</i>	<i>Monomer Unit 2</i>	<i>Monomer Unit 3</i>	<i>Monomer Unit 4</i>	<i>H Atom Loss^a</i>	<i>Mol Wt of Oligomer Product (g/mol)</i>
Dimer	220 ^b	216 ^c	-----	-----	4	432.6
Trimer	220 ^b	216 ^c	266 ^d	-----	8	694.9
Dimer	244 ^e	230 ^f	-----	-----	4	470.7
Trimer	244 ^e	230 ^f	266 ^d	-----	8	732.9
Tetramer	244 ^e	230 ^f	266 ^d	244 ^e	12	973.4
Tetramer	244 ^e	230 ^f	266 ^d	256 ^g	12	985.4
Dimer	230 ^f	242 ^h	-----	-----	4	468.7
Trimer	230 ^f	242 ^h	266 ^d	-----	8	730.9
Tetramer	230 ^f	242 ^h	266 ^d	270 ⁱ	12	997.5
Dimer	270 ^h	216 ^c	-----	-----	4	482.8
Trimer	270 ^h	216 ^c	266 ^d	-----	8	744.9
Tetramer	270 ^h	216 ^c	266 ^d	270 ⁱ	12	1011.5
Dimer	266 ^d	230 ^f	-----	-----	4	492.8
Trimer	266 ^d	230 ^f	266 ^d	-----	8	754.9

^a Four hydrogen atoms are lost for each condensation reaction between monomeric units as a five- or six-membered connecting ring is formed.

^b Trimethylphenanthrene.

^c Methylpyrene.

^d Methylbenzo[a]pyrene, methylbenzo[e]pyrene.

^e Trimethylpyrene.

^f Dimethylpyrene.

^g Dimethylchrysene, dimethylbenz[a]anthracene, dimethyltriphenylene.

^h Methylchrysene, methylbenz[a]anthracene, methyltriphenylene.

ⁱ Trimethylchrysene, trimethylbenz[a]anthracene, trimethyltriphenylene.

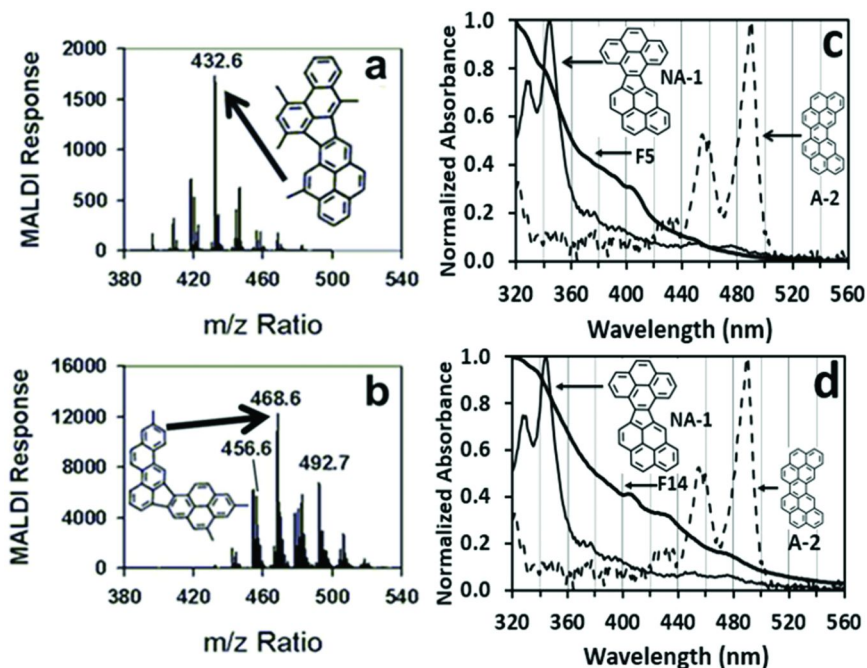


Figure 22. MALDI (a and b) and UV-vis spectra (c and d) for GPC Fractions 5 (a and c) and 14 (b and d). Comparison of the UV-vis spectra for each fraction (labeled F5 and F14) with those of a nonalternant (NA-1) and an alternant (A-2) pyrene dimer suggest that dimers form primarily via 5-membered ring linkages.

GPC Fractions 5 and 14 were among those selected for UV-vis analysis because each fraction contained only one major species (see their MALDI spectra in Figure 22a-b): The signal at 432.6 Da belongs to the black square series, and the signal at 468.6 belongs to the white circle series (see Figure 17). The UV-vis spectra of these two GPC fractions, which exhibit strong absorption below 360 nm and little absorption above 500 nm, are compared with those of an alternant (A-2) and nonalternant dimer (NA-1) of pyrene in Figure 22c and d, respectively. (Esguerra et al. recently generated these spectra by isolating them via SCE + HPLC from a pyrene pitch (21).) Clearly, the M-50 dimer spectra are more similar to the nonalternant vs. the alternant pyrene dimer. (Not all possible pyrene dimers (5 isomers exist) are shown, but those shown are representative of the two types.) UV-vis spectra for the other dimer GPC fractions (which contained more components and thus were even more heterogeneous) were similar in appearance to those shown here. Based on these results, then, we concluded that nonalternant PAHs are the more dominant form in M-50 pitch. However, Esguerra's HPLC analysis of a pyrene dimer that was isolated via SCE from a thermally polymerized pyrene pitch (see Figure 23) indicate that significant amounts of alternant pyrene dimer (i.e., A-1 and A-2) are present along with nonalternant pyrene dimers (NA-1 and NA-2). (As M-50 pitch is also produced via thermal polymerization, albeit from highly multicomponent FCC decant oil, we make this comparison

with a model dimer that was also produced thermally.) In summary, the prevailing evidence indicates that both the alternant and nonalternant forms are present in M-50 pitch dimers, with the nonalternant form probably being more prevalent. Thus, additional representative dimer structures to those shown in Figure 17 can be generated simply by replacing some of the 5-membered with 6-membered linkages.

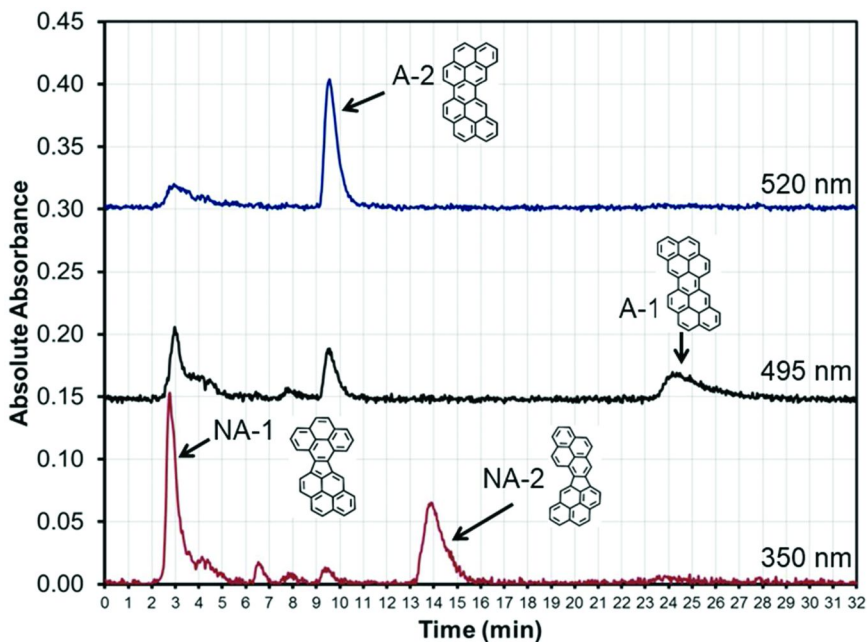


Figure 23. HPLC chromatogram for a thermally produced pyrene dimer fraction, monitored over three different wavelengths. Mol wts of all dimers shown (i.e., 400 Da) was obtained via MALDI. Adapted with permission from ref (21). Copyright 2014 Elsevier.

Identification of the Trimer and Tetramer Constituents of Petroleum Pitches

Analysis of the trimer and tetramer constituents of M-50 pitch proceeded in a manner essentially analogous to that followed for the dimer constituents: continuous SCE for concentration of relatively large amounts of the heaviest portion of M-50 pitch (i.e., that containing the trimers and tetramers), followed by semi-continuous SCE to obtain an even narrower cut focused on a certain mol wt range, and then finally prep-scale GPC for the isolation of individual species or groups of species that could then be analyzed by MALDI, PSD, and UV-vis. Recall from our previous discussions that for the monomers, definitive

identification of species through UV-vis was possible; however, for the dimers, both the inadequacy of the species isolation achieved via GPC along with the lack of all but a few UV-vis reference standards made dimer identification significantly more difficult (but not impossible). The aforementioned problems with dimer identification were of course exacerbated even more with the trimers and tetramers. Nevertheless, as seen below, analysis of our results via several independent means continued to be consistent with our proposed structures for thermally polymerized (i.e., heat-soaked) petroleum pitches: essentially undisturbed alkylated monomer units linked together by 5- and 6-membered rings to form petroleum pitch.

Trimer and Tetramer Constituents: Experimental

Pre-Fractionation and Concentration of M-50 Petroleum Pitch into Trimer + Tetramer Cuts via Continuous + Semi-Continuous Supercritical Extraction

SCE was used to both concentrate and resolve the trimer + tetramer portion of the M-50 pitch (see Figure 2) as follows: First, one-column, continuous SCE operating at a constant temperature of 330 °C and 49 bar was used to generate a heavy bottoms cut from the column rich in trimer and tetramer. Then ~2 g of this pitch was fractionated by semi-continuous DGE, with the column set at 330/350/380 °C for the bot/mid/top sections, respectively. The column was first set to a pressure of 56 bar, and the remaining dimer was removed as top product. Then the column pressure was raised to 112 bar, and the trimer and tetramer were taken off as the top cut, which we referred to as SCE Trimer Cut 3 (see Figure 24).

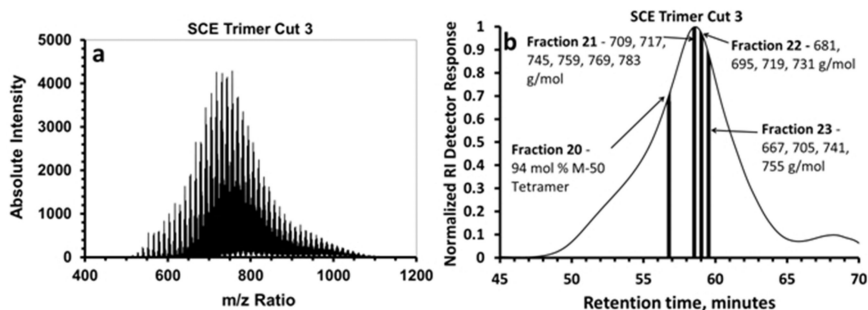


Figure 24. (a) MALDI mass spectrum for SCE Trimer Cut 3, concentrated in trimer and tetramer species. (b) GPC chromatogram for SCE Trimer Cut 3, where GPC Fractions 20-23 were collected. Molecular weights of the species subjected to MALDI-PSD are listed for each fraction. Adapted with permission from ref (47). Copyright 2011 Elsevier.

GPC Fractions via Prep-Scale GPC from SCE Dimer Cut 3

Prep-scale GPC was used to generate GPC Fractions 20-23 from SCE Trimer Cut 3, using hot TCB as the mobile phase at 140° C (see Figure 24); details of the equipment and procedure were given previously herein and also elsewhere (47).

MALDI, MALDI-PSD, and UV-Vis Analysis of GPC Trimer and Tetramer Fractions

MALDI and PSD analyses were obtained using a Bruker Daltonics Autoflex MALDI mass spectrometer with a 337 nm nitrogen laser. We have previously described both the sample preparation method (18) and the operating parameters for MALDI and PSD (27) in detail elsewhere.

UV-Vis analyses of the collected GPC fractions were carried out using a Spectral Instruments 400 Series spectrophotometer. The GPC fractions (dissolved in TCB) had to be run directly, as the trimer and tetramer fractions have a very low solubility in cyclohexane. In all cases, the concentrations of the GPC fractions analyzed were adjusted by adding solvent until the maximum light absorbance value measured was less than 2.0.

Trimer and Tetramer Constituents: Results and Discussion

MALDI, PSD, and UV-Vis for Trimer and Tetramer Molecular Weight, Degree of Alkyl Substitution, and Molecular Structure

The MALDI spectrum for GPC Fraction 22, which encompasses most of the mol wt range for the trimer portion of M-50 pitch (see Figure 2), is given as Figure 25. As was the case for the dimer portion of M-50 pitch, the major peaks are in Gaussian distributions separated by 14 Da; as before, the most prominent of these have been highlighted by color symbols. However, PSD analysis could not be carried out on all of the major peaks because of signal interference from neighboring peaks (i.e., those closer than 6-9 Da away). (Such an increase in signal density was of course expected for the higher oligomers.) Nevertheless, the PSD results that could be obtained (see Figure 26) were quite useful in elucidating the molecular structure of the trimers. For those signals in the “red triangle”, “green square”, and “blue circle” distributions that could be analyzed via PSD, we observed that the increments in molecular weight are caused by increasing methyl substitution, as was reported herein earlier for the monomers and dimers. The weak intensity of the de-methylation peaks and lack of de-ethylation peaks (vs. those PSD results shown earlier) occurred because a lower laser power had to be used for the more crowded signal field, so that the total number of ions to be analyzed did not overload the ion gate and thus make the isolation of individual ions infeasible.

UV-vis analysis of GPC Fraction 22 gave a spectrum quite similar to that already shown for the dimer fractions in Figure 22, exhibiting a steady decrease in absorption with increasing wavelength, and weak absorption in the area where

alternant PAHs typically have strong absorption. No significant change in the types of linkages between monomer units was expected for trimers vs. dimers, and these results confirmed that assumption.

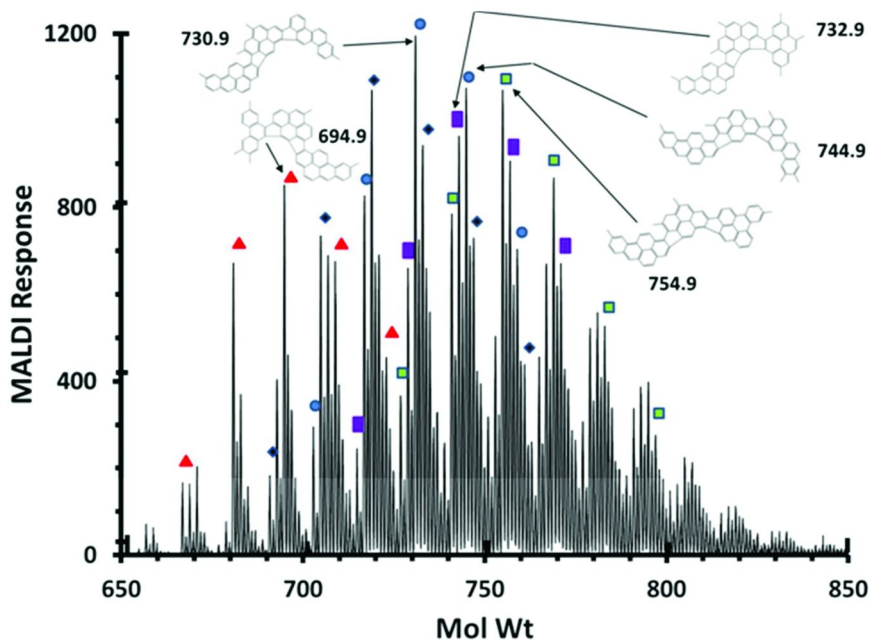


Figure 25. MALDI spectrum for the trimer portion of M-50 pitch, as obtained from GPC Fraction 22. The major trimers are denoted with symbols, with mol wt increases for a given symbol being due to increasing methylation. Representative molecular structures, as deduced from structural characterization data, are also given. Adapted with permission from ref (47). Copyright 2011 Elsevier.

Molecular structures for some of the most prominent trimer signals in Figure 25 were then constructed by assuming that some of the most prominent dimer species (signals) in Figure 17 underwent a condensation reaction with some of the most abundant monomer species (see Figure 8). As was the case for the dimers, this procedure was successful in predicting the molecular weights of some of the most prominent trimer signals. For example, consider the reaction of dimers of molecular weight 432.6, 470.7, 482.8, and 492.8 in Figure 17 with the methylbenzopyrenes, denoted by the orange circle at 266 Da in Figure 8. Connecting the dimers to the monomers with the elimination of 4 hydrogens gives us some of the most prominent trimer signals in Figure 25. Note that many

variations on the reactions proposed above are possible. In fact, any species from the “black square”, “black triangle”, “white circle”, or “white triangle” dimer signal distributions in Figure 17 can be reacted with any alkylated benzopyrene to produce the trimer structures shown in Figure 25, as long as the total number of methyl substituent groups on the final trimer in question remained unchanged. Finally, we note that, unlike the dimer distributions shown in Figure 17, the first trimer in a series distribution in Figure 25 does not consist of a bare PAH backbone, as these precursors were not among the most abundant ones. Examples of representative molecular structures for trimers are given in Figure 25. For the trimers, the limited evidence available suggests that 5-membered linkages between the monomer units dominate, but based on the dimer results above, we probably need to assume that 6-membered linkages are also present in the trimers. Thus, some of the nonalternant rings in the structures depicted in Figure 25 could be replaced with alternant rings if desired. Finally, a summary of the most prevalent trimers, their mol wts, and their monomer precursors, is given in Table II.

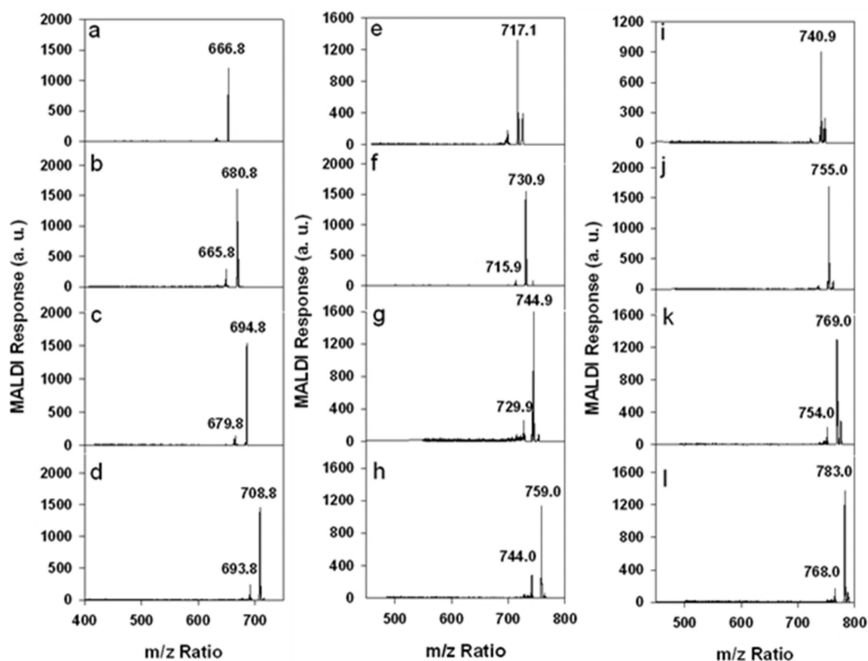


Figure 26. MALDI-PSD fragmentation analysis for the “red triangle” (a-d), “green square” (e-h), and “blue circle” (i-l) species distributions given in Figure 25. Note that methyl substituent groups are the only observed fragment. Spectra are from the analysis of GPC Fractions 21-23.

Identification of the molecular structures present in the tetramer portion of M-50 pitch was, as expected, the most difficult of all, but fortunately here our experience with the monomers and lower mol wt oligomers proved to be helpful. The MALDI spectrum for GPC Fraction 20, which encompasses more than 90% of the tetramer in M-50, is given as Figure 27. As was the case for the other oligomers present in M-50 pitch, the major peaks are in Gaussian distributions separated by 14 Da. Thus, by applying the same principles developed above for dimers and trimers, we can classify many of the most prominent signals in the tetramer spectrum into signal distributions. Three of these, denoted by white rectangles, white diamonds, and black circles, are given in Figure 27. Although the more continuous nature of the mol wt distribution of the M-50 tetramer (so that neighboring peaks are far too close for isolation) makes the application of PSD for fragmentation analysis infeasible, there is no reason to believe that the observed increments of 14 Da could be anything but increasing levels of methylation on a base PAH backbone.

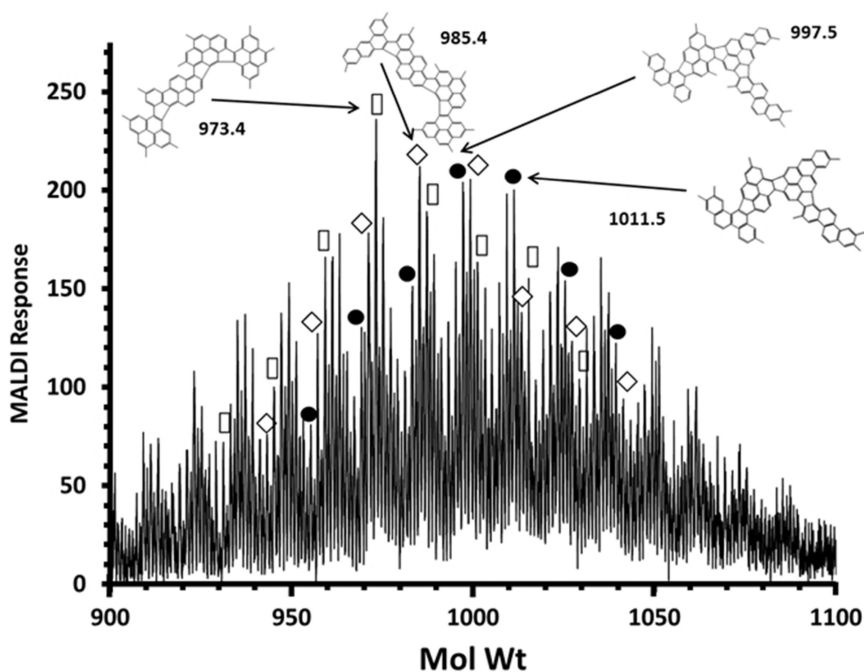


Figure 27. MALDI spectrum for the tetramer portion of M-50 pitch, as obtained from GPC Fraction 20. Some of the major tetramers are denoted with symbols, with mol wt increases for a given symbol being due to increasing methylation. Representative molecular structures, as deduced from structural characterization data, are also given. Adapted with permission from ref (47). Copyright 2011 Elsevier.

UV-vis analysis of GPC Fraction 20 produced a spectrum very similar to that observed for the trimer-rich GPC Fraction 22, so no new information was obtained here with respect to the types of bonds linking the monomer units.

Molecular structures for some of the most prominent tetramer signals in Figure 27 were constructed by assuming a condensation reaction between two common dimers, or the reaction of a common monomer and trimer; these structures are given in Figure 27 along with their associated molecular weights and signals. The molecular weights and monomer constituent units for these species are summarized in Table II.

FT-IR Spectroscopy of the Oligomers of Petroleum Pitch

Previous work on the molecular structures of the constituents of petroleum pitches had generally portrayed these species as being highly condensed (49–51). Yet the work discussed herein largely contradicts these claims, as our evidence is consistent with petroleum pitches consisting of relatively small monomer units, no bigger than 4–6 aromatic rings, linked together by a single 5- or 6- membered ring. With our results being somewhat different from those previously published, we sought yet another, independent analytical method to verify our somewhat surprising results. The method chosen was transmission FT-IR spectroscopy. For the monomer and dimer cuts of M-50 pitch, analysis was performed on bulk analyte samples with a Nicolet 730 spectrometer. For the trimer and tetramer cuts, a Nicolet Magna 550 FT-IR spectrometer equipped with a Thermo-Spectra Tech Nic-Plan FT-IR microscope was used to perform the analyses on thin films of dried GPC fractions. Two additional GPC fractions of higher concentration had to be obtained from SCE Trimer Cut 3 for trimer and tetramer analysis. In particular, tetramer-rich GPC Fraction 24 was collected for a longer time period than normal, that is, from 55.9 to 57.4 min, and trimer-rich GPC Fraction 25 was collected from 58.4 to 59.9 min. These samples were all dried and prepared for FT-IR analysis by the methods previously described (27, 47).

FT-IR absorption spectra for each of these four oligomers in M-50 pitch are directly compared in Figure 28. Note that all fractions have significant aryl content, as exhibited by the strong absorption between 900 and 700 cm^{-1} . The fact that aryl content does not decrease with increasing oligomer number is consistent with our observations concerning the formation of oligomers in petroleum pitch: namely, that linkage between monomer units does *not* occur by large-scale condensation or significant rearrangement between monomer units to form highly condensed, graphitic structures. Instead, the condensation process is relatively mild, with 4 hydrogens being lost to form a connecting 5- or 6-membered ring, with most of the alkyl groups on the monomer units being retained. Thus, FT-IR results for the monomer and oligomers are consistent with our proposed molecular structures and provide yet another degree of confirmation of the validity of our work.

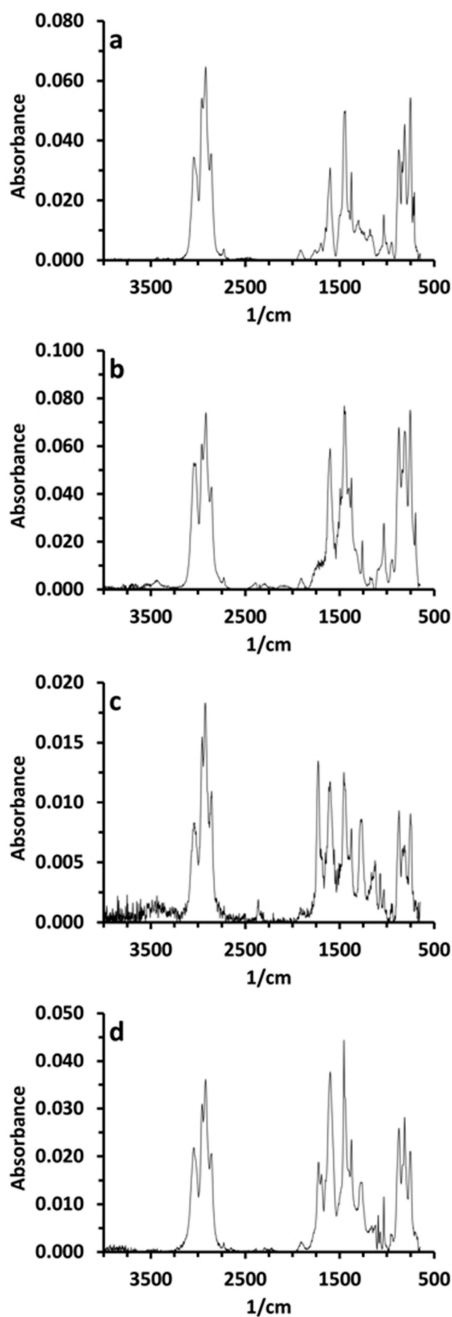


Figure 28. Transmission FT-IR analysis for (a) 98% monomer, (b) 97% dimer, (c) trimer-rich GPC Fraction 25, and (d) tetramer-rich GPC Fraction 24. Note that all fractions have significant aryl content, as exhibited by the strong absorption between 900 and 700 cm^{-1} . Thus, linkage between monomer units does not occur by large-scale condensation.

Onset of Mesophase in Petroleum Pitches: Liquid Crystallinity Discovered in a Trimer Fraction of M-50 Pitch

We opened this chapter by discussing the seminal work of Brooks and Taylor (1, 2) and their discovery that a liquid crystalline phase can be formed from carbonaceous materials such as petroleum/coal-tar pitches and tars. Based on the work described herein, we now have a reasonably good understanding of the constituents of petroleum pitch on a molecular level. Thus, we conclude this chapter by attempting to answer a question that has been asked since the days of Brooks and Taylor, but has yet to be adequately answered: what molecular weight and size are required in a petroleum pitch before it can form mesophase? Before our molecular characterization work began in earnest, Cervo et al. (52) used SCE/DGE to fractionate M-50 pitch in order to control the oligomeric composition. The MALDI mass spectra of the fractions obtained in their work are given as Figure 29; the arrows indicate how the concentrations of the various oligomeric constituents in the isolated pitch fractions increase/decrease with increasing extraction pressure. In Figure 30, we see how increasing the extraction pressure decreases the dimer concentration and increases the trimer and tetramer concentrations, resulting in increasingly oriented bulk mesophases. However, all of these fractions were mixtures of the three oligomers, so we really could not draw any conclusions about the minimum molecular weight and size required for mesophase formation.

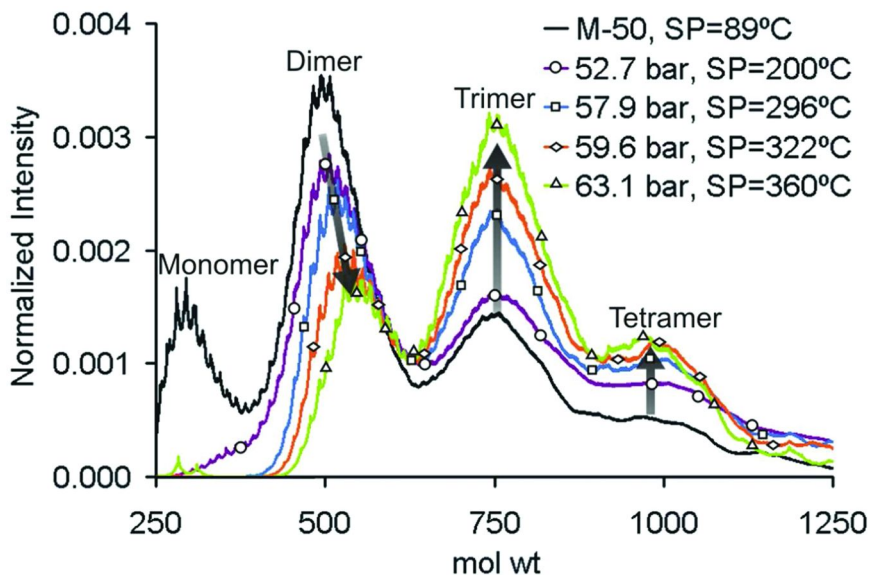


Figure 29. SCE extraction of M-50 pitch at 350 °C and selected pressures allows us to control the oligomeric composition (and thus softening points (SP)) of the resulting pitch fractions. Reproduced with permission from ref (52). Copyright 2007 The American Ceramic Society.

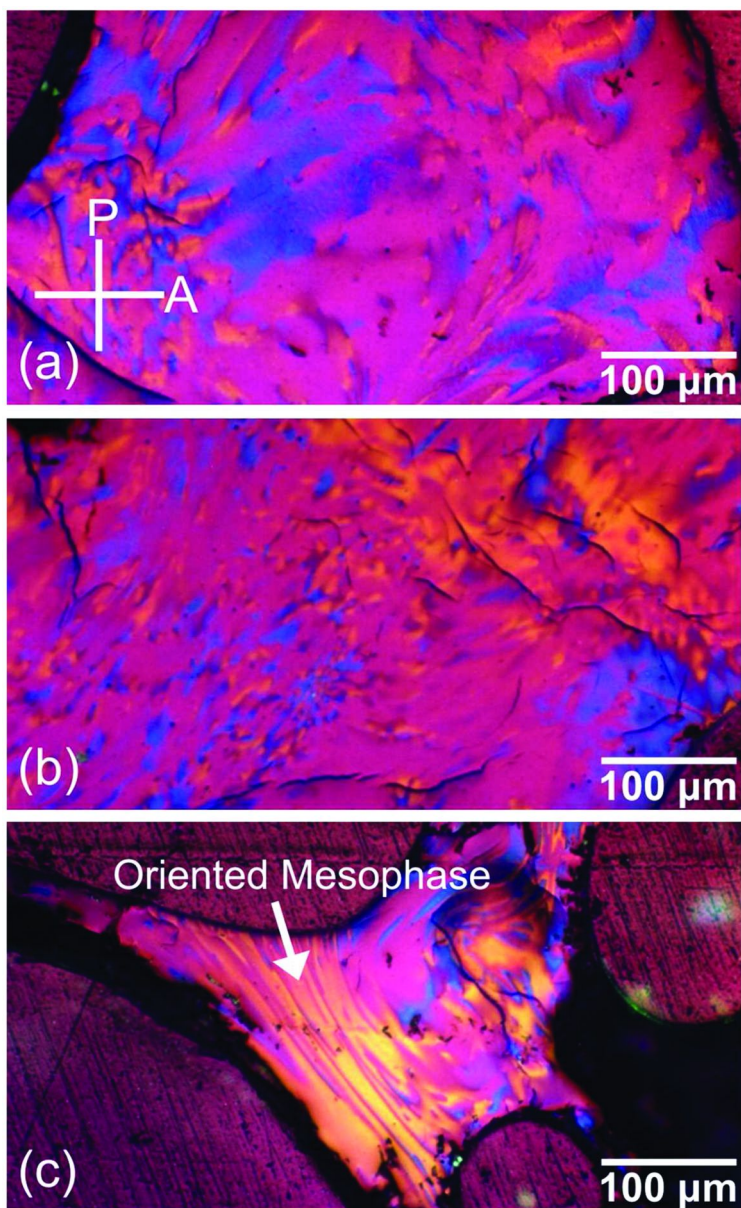


Figure 30. For the SCE extraction shown in Figure 29, increasing extraction pressures, from (a) 59.6 bar to (b) 61.3 bar to (c) 63.1 bar, produces bulk mesophases of increasing orientation, as shown in these cross-polarized light photomicrographs. Reproduced with permission from ref (52). Copyright 2007 The American Ceramic Society.

Previous work had already shown us that a pure dimer fraction was completely isotropic (29–31), as would be expected from Hurt's (53) seminal paper that discussed the role of PAH molecular weight and size on mesophase formation. But what about trimer? To address this issue, an M-50 trimer fraction was produced with the highest purity achievable with our current setup. The procedure was previously described herein and also in detail elsewhere (22, 25, 52), so only a brief sketch is given here. First, continuous SCE/DGE was used to remove the monomer and dimer portions of the M-50 pitch, resulting in an isotropic pitch fraction consisting of 66% trimer (by MALDI area). Several grams of this trimer fraction were then charged to a semi-continuous SCE setup, and a 97% pure trimer (by area) fraction was generated as the top product. (The MALDI spectrum for this trimer looked very similar to Figure 25.) In both SCE steps, toluene was used as the supercritical solvent. Complete removal of the toluene from the 97% trimer fraction was then carefully performed to insure that no solvent-induced effects interfered with mesophase analysis. Afterwards, the softening point of the trimer was measured with a Fisher-Johns, hot-plate melting-point apparatus and found to be 330 °C. The trimer was then analyzed for mesophase using cross-polarized optical microscopy; the resulting photomicrograph is given as Figure 31 and indicates that bulk mesophase formed from the trimer portion of M-50 pitch. About 60% of the trimer remained in the isotropic state; nevertheless, this is the first time that mesophase with a well-defined molecular weight has ever been isolated from a carbonaceous pitch. Also for the first time, a mesophase pitch was formed from a single oligomer, not a mixture of oligomers. With an average molecular weight of ~750 Da, to our knowledge this is also the lowest mol wt carbonaceous pitch fraction for which mesophase has ever been reported.

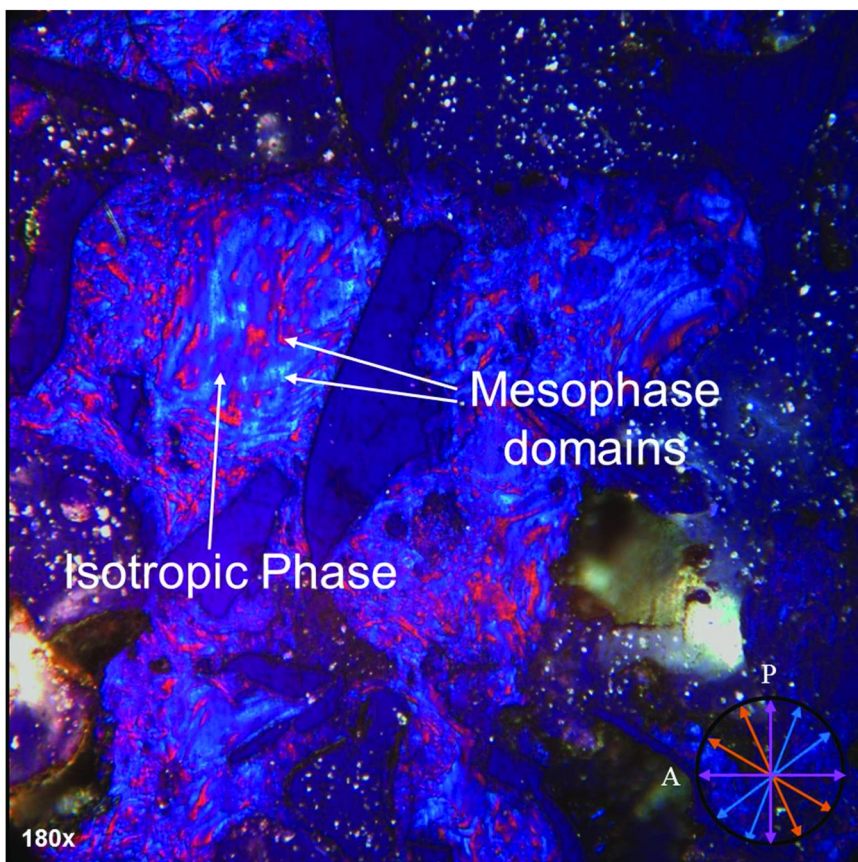


Figure 31. Cross-polarized light photomicrograph of a 97% pure trimer cut of M-50 pitch, as obtained by SCE. The trimer contains about 40% bulk mesophase. To our knowledge, this is the first time that a mesophase of well-defined molecular weight has been formed from a petroleum pitch, and is also the lowest mol wt petroleum pitch fraction for which mesophase formation has been reported.

Conclusions

A significant barrier to developing an increased fundamental understanding of carbonaceous pitches has been our inability to adequately characterize these pitches on the molecular level. As discussed in this chapter, our group has made significant progress over the past 5+ years in improving this situation. The application of two relatively new techniques, one processing and the other analytical, made much of the work discussed herein possible. In particular, the processing of pitches via supercritical/dense-gas extraction (SCE/DGE) enabled us to fractionate pitches into cuts of well-defined, controllable molecular weight. Once a complex mixture such as pitch could be fractionated in such a manner in significant quantities, it opened up new opportunities for analytical characterization.

MALDI mass spectrometry was the analytical technique that radically changed our way of analyzing carbonaceous pitches. With the notoriously low solubility of higher pitch oligomers in solvents, the ability of MALDI to obtain mol wt information from the solid state was a game-changer. For the first time, we could examine the entire mol wt range of a pitch, regardless of component solubilities. Furthermore, MALDI and SCE proved to be highly complementary when used together, as more quantitative molecular information was obtained when narrow mol wt pitch cuts isolated via SCE were used as MALDI analytes.

Although we have a high degree of confidence in the molecular structures proposed herein for the monomers and various oligomers in petroleum pitches, the nature of the linkages connecting the monomeric units continues to be only partly resolved. Measurements via several different methods are not consistent with respect to the extent to which the linkages are 5-membered (nonalternant) or 6-membered rings. Thus, this remains an area of future work.

Finally, the fact that, when isolated, the trimer portion of M-50 pitch forms mesophase with a reasonably low softening point is good news. We have the techniques at our disposal to produce mol wt cuts of trimer even narrower than what was obtained in this first reported experiment, and investigating both the properties and potential applications of single-oligomer, mesogenic pitches could form the basis of an interesting new research area for carbon materials.

Acknowledgments

The outstanding work of several former and present students, including Drs. Billy Edwards, Eduardo Cervo, Ward Burgess, Sourabh Kulkarni, David Esguerra, and Julian Velez, who made the writing of this chapter possible is gratefully acknowledged. I would also like to acknowledge the assistance of Ms. Diana Stamey in helping with the preparation of this manuscript.

References

1. Brooks, J. D.; Taylor, G. H. Formation of graphitizing carbons from liquid phase. *Nature* **1965**, *206*, 697–699.
2. Brooks, J. D.; Taylor, G. H. The formation of graphitizing carbons from the liquid phase. *Carbon* **1965**, *3*, 185–193.
3. Edie, D. D.; Fain, C. C.; Robinson, K. E.; Harper, A. M.; Rogers, D. K. Ribbon-shape carbon fibers for thermal management. *Carbon* **1993**, *31*, 941–949.
4. Fathollahi, B.; Mauldin, M.; Chau, P. C.; Wapner, P. G.; Hoffman, W. P. Integrated mesophase injection and in situ transformation in fabrication of high-density carbon-carbon composites. *Carbon* **2006**, *44*, 854–858.
5. Zweben, C. *Thermal Management Market/Business Study: Qualification of High Thermal Conductivity Pitch Based Graphite Fibers for Thermal Management*; Final Report; Composite Consultant, Devon, PA, 2003.
6. Klett, J. W. Carbon Foams. In *Cellular Ceramics*; Scheffler, M., Columbo, P., Eds.; Wiley-VCH: Weinheim, Germany, 2005; pp 137–157.

7. Wapner, P. G.; Hoffman, W. P.; Jones, S. Carbon and Ceramic Matrix Composites Fabricated by a Rapid Low-Cost Process Incorporating in-Situ Polymerization of Wetting Monomers. U.S. Patent 6,309,703, October 30, 2001.
8. Greenwood, S. H. Treatment of Pitches in Carbon Artifact Manufacture. U.S. Patent 4,277,324, July 7, 1981.
9. Mochida, I.; Shimizu, K.; Korai, Y.; Otsuka, H.; Sakai, Y.; Fujiyama, S. Preparation of mesophase pitch from aromatic hydrocarbons by the aid of HF/BF₃. *Carbon* **1990**, *28*, 311–319.
10. Mochida, I.; Kudo, K.; Fukuda, N.; Takeshita, K.; Takahashi, R. Carbonization of pitches.—IV: Carbonization of polycyclic aromatic hydrocarbons under the presence of aluminum chloride catalyst. *Carbon* **1975**, *13*, 135–139.
11. Dickinson, E. M. Average structures of petroleum pitch fractions by ¹H/¹³C n.m.r. spectroscopy. *Fuel* **1985**, *64* (5), 704–706.
12. Kershaw, J. R.; Black, K. J. T. Structural characterization of coal-tar and petroleum pitches. *Energy Fuels* **1993**, *7* (3), 420–425.
13. Mochida, I.; Shimizu, K.; Korai, Y.; Sakai, Y.; Fujiyama, S. Mesophase pitch derived from isotropic anthracene pitch produced catalytically with HF/BF₃. *Bull. Chem. Soc. Jpn.* **1990**, *63*, 2945–2950.
14. Mochida, I.; Shimizu, K.; Korai, Y. Preparation of mesophase pitch from aromatic hydrocarbons by the aid of HF/BF₃. *Carbon* **1990**, *28*, 311–319.
15. Sasaki, T.; Jenkins, R. G.; Eser, S.; Schobert, H. H. Carbonization of anthracene and phenanthrene. 2. Spectroscopy and mechanisms. *Energy Fuels* **1993**, *7* (6), 1047–1053.
16. Herod, A. A.; Bartle, K. D.; Kandiyoti, R. Characterization of heavy hydrocarbons by chromatographic and mass spectrometric methods: An overview. *Energy Fuels* **2007**, *21* (4), 2176–2203.
17. Southard, W. M.; Snow, T. A.; McEwen, C. N.; Lavin, J. G.; Romine, H. E.; Nanni, E. J. Molecular weight characterization of isotropic and meso-phase pitches by matrix assisted laser desorption ionization mass spectrometry. In *Extended Abstracts, 23rd Biennial Conference on Carbon*, Penn State, PA, U.S.A., 1997.
18. Edwards, W. F.; Jin, L.; Thies, M. C. MALDI-TOF mass spectrometry: Obtaining reliable mass spectra for insoluble carbonaceous pitches. *Carbon* **2003**, *41*, 2761–2768.
19. Sima, L.; Blanco, C.; Santamaria, R.; Granda, M.; Slaghuis, H.; Menendez, R. Relationship between chemical composition and pyrolysis behaviour of a medium temperature pitch (or Lurgi-gasifier pitch). *Fuel Process. Technol.* **2003**, *84*, 63–77.
20. Esguerra, D. F.; Hoffman, W. P.; Thies, M. C. Fractionation of an oligomeric pyrene pitch via supercritical extraction. *J. Supercrit. Fluids* **2013**, *79*, 170–176.
21. Esguerra, D. F.; Hoffman, W. P.; Thies, M. C. Molecular structures for the constituents of pyrene pitches. *Fuel* **2014**, *124*, 133–140.

22. Esguerra, D. F.; Thies, M. C. Liquid crystallinity in trimer oligomers isolated from petroleum and pyrene pitches. *Carbon* **2014**, DOI: 10.1016/j.carbon.2014.07.067.
23. Greinke, R. A. Kinetics of petroleum pitch polymerization by gel permeation chromatography. *Carbon* **1986**, *24* (6), 677–686.
24. Greinke, R. A.; Singer, L. S. Constitution of coexisting phases in mesophase pitch during heat treatment: Mechanism of mesophase formation. *Carbon* **1988**, *26* (5), 665–670.
25. Kulkarni, S. U.; Esguerra, D. F.; Thies, M. C. Isolating petroleum pitch oligomers via semi-continuous supercritical extraction. *Energy Fuels* **2012**, *26* (5), 2721–2726.
26. Edwards, W. F.; Thies, M. C. Fractionation of pitches by molecular weight using continuous and semibatch dense-gas extraction. *Carbon* **2006**, *44* (2), 243–252.
27. Cristadoro, A.; Kulkarni, S. U.; Burgess, W. A.; Cervo, E. G.; Raeder, H. J.; Muellen, K.; Bruce, D. A.; Thies, M. C. Structural characterization of the oligomeric constituents of petroleum pitches. *Carbon* **2009**, *47*, 2358–2370.
28. Cervo, E. G.; Thies, M. C. Control of the molecular weight distribution of petroleum pitches via dense-gas extraction. *Chem. Eng. Technol.* **2007**, *30*, 742–748.
29. Cervo, E. G.; Thies, M. C. Control of molecular weight distribution of petroleum pitches via multistage supercritical extraction. *J. Supercrit. Fluids* **2010**, *51*, 345–352.
30. Cervo, E. G.; Kulkarni, S. U.; Thies, M. C. Isolating polycyclic aromatic hydrocarbon (PAH) oligomers via continuous, two-column supercritical extraction. *J. Supercrit. Fluids* **2012**, *66*, 120–128.
31. Tekinalp, H. L.; Cervo, E. G.; Fathollahi, B.; Thies, M. C. The effect of molecular composition and structure on the development of porosity in pitch-based activated carbon fibers. *Carbon* **2013**, *52*, 267–277.
32. Edwards, W. F.; Thies, M. C. Dense-Gas Fractionation and MALDI characterization of carbonaceous pitches. *Energy Fuels* **2005**, *19*, 984–991.
33. Basova, Y. V.; Edie, D. D.; Lee, Y. S.; Reid, L. K.; Ryu, S. K. Effect of precursor composition on the activation of pitch-based carbon fibers. *Carbon* **2004**, *42*, 485–495.
34. Burgess, W. A.; Pittman, J. J.; Marcus, R. K.; Thies, M. C. Structural identification of the monomeric constituents of petroleum pitch. *Energy Fuels* **2010**, *24*, 4301–4311.
35. Wang, G.; Eser, S. Molecular composition of the high-boiling components of needle coke feedstocks and mesophase development. *Energy Fuels* **2007**, *21*, 3563–72.
36. Eser, S.; Wang, G. A laboratory study of a pretreatment approach to accommodate FCC high-sulfur decant oils as feedstocks for commercial needle coke. *Energy Fuels* **2007**, *21*, 3573–82.
37. Hutchenson, K. W.; Roebbers, J. R.; Thies, M. C. Fractionation of petroleum pitch by supercritical extraction. *Carbon* **1991**, *29* (2), 215–223.
38. Geiculescu, A. C. M.S. Thesis, Clemson University, Clemson, SC, 1994.

39. Somers, M. L.; Wornat, M. J. UV spectral identification of polycyclic aromatic hydrocarbon products of supercritical 1-methylnaphthalene pyrolysis. *Polycyclic Aromat. Compd.* **2007**, *27*, 261–80.
40. McClaine, J. W.; Oña, J. O.; Wornat, M. J. Identification of a new C₂₈H₁₄ polycyclic aromatic hydrocarbon as a product of supercritical fuel pyrolysis: Tribenzo[cd,ghi,lm]perylene. *J. Chromatogr. A* **2007**, *1138*, 175–83.
41. Fetzer, J. C.; Kershaw, J. R. Identification of large polycyclic aromatic hydrocarbons in a coal tar pitch. *Fuel* **1995**, *74*, 1533–6.
42. Friedel, R. A.; Orchin, M. *Ultraviolet Spectra of Aromatic Compounds*; John Wiley and Sons: New York, 1951.
43. CAS SciFinder. <http://www.cas.org/products/scifindr/index.html> (accessed May 2014).
44. McLafferty, F. W. *Interpretation of Mass Spectra*, 3rd ed.; University Science Books: Mill Valley, CA, 1980; p 187.
45. Burgess, W. A. Ph.D. dissertation, Clemson University, Clemson, SC, 2010; Chapter 5.
46. Cristadoro, A.; Raeder, H.-J.; Muellen, K. Clustering of polycyclic aromatic hydrocarbons in matrix-assisted laser desorption/ionization and laser desorption mass spectrometry and LD mass spectrometry. *Rapid Commun. Mass Spectrom.* **2007**, *21*, 2621–2628.
47. Burgess, W. A.; Thies, M. C. Molecular structures for the oligomeric constituents of petroleum pitch. *Carbon* **2011**, *49*, 636–651.
48. Zander, M. On the composition of pitches. *Fuel* **1987**, *66*, 1536–9.
49. Lewis, I. C. Chemistry of carbonization. *Carbon* **1982**, *20*, 519–529.
50. Mochida, I.; Yoon, S.-H.; Korai, Y.; Kanno, K.; Sakai, Y.; Komatsu, M. Carbon fibers from aromatic hydrocarbons. *CHEMTECH* **1995**, *25*, 29–37.
51. Fitzer, E.; Kompalik, D.; Mayer, B. Influence of Additives on Pyrolysis of Mesophase Pitch. *Proceedings of International Conference on Carbon: Carbon '86*, Baden-Baden, Federal Republic of Germany, pp 842–845.
52. Cervo, E. G.; Thies, M. C.; Fathollahi, B. Controlling the oligomeric composition of carbon-fiber precursors by dense-gas extraction. *J. Am. Ceram. Soc.* **2008**, *91*, 1416–1422.
53. Hurt, R. H.; Hu, Y. Thermodynamics of carbonaceous mesophase. *Carbon* **1999**, *37*, 281–292.

Chapter 6

Carbon Fibers Derived from Acetylated Softwood Kraft Lignin

Meng Zhang and Amod A. Ogale*

Chemical and Biomolecular Engineering and
Center for Advanced Engineering Fibers and Films, Clemson University,
Clemson, South Carolina 29634, United States

*E-mail: ogale@clemson.edu

A commercial softwood kraft lignin (SKL, Indulin AT) was processed into precursor fibers after acetylation of SKL to different degrees of substitution. The acetylated SKL (Ace-SKL) with higher extent of substitution was extracted with acetic acid resulting in a material that could be melt-spun, but those fibers became tacky during thermo-oxidation. Ace-SKL with lower substitution extent was chosen for solution spinning using acetone as solvent. It was found that both softening point and glassy transition temperature of Ace-SKL increased as the extent of acetylation decreased, which is favorable for the subsequent stabilization step. The Ace-SKL fibers derived from lower extent of substitution were successfully thermo-oxidatively stabilized and subsequently carbonized at 1000°C under tension to retain molecular orientation within the fibers. These carbon fibers displayed low crystallinity as investigated by WAXD and Raman spectroscopy. Resulting carbon fibers displayed a tensile modulus, strength, and strain-to-failure values of 52 ± 2 GPa, 1.06 ± 0.07 GPa, and $2.0 \pm 0.2\%$, respectively. Because of solvent diffusion during dry-spinning, fibers displayed a crenulated surface, which can provide a larger specific interfacial area for enhanced fiber/matrix bonding in composite applications.

Introduction

Currently, three precursor materials are used for commercial production of carbon fibers: polyacrylonitrile (PAN), pitch and rayon (1, 2). Of these, PAN is used almost exclusively in structural composite applications from a wet spinning process. However, this process involves generation of certain toxic by-products such as hydrogen cyanide (HCN) and other toxic gases during the thermal stabilization and carbonization steps, and wet-spinning process necessitates use of hazardous solvents. This problem of toxic by-product can potentially be overcome by the use of naturally occurring biomass. Amongst biomass-based alternatives, lignin shows the potential of being a carbon fiber precursor because of its high aromatic content. Over 3×10^{11} tons of lignin exists in the biosphere with approximately 2×10^{10} tons generated annually (3).

The first lignin based carbon fiber was patented in 1969 by Otani (4). The patent described both melt spinning and dry spinning using different type of lignin precursor. The strength of carbon fiber produced from melt spun precursor ranged up to 800 MPa. In the examples for dry spinning, water or sodium hydroxide aqueous solutions were used as solvent for both alkali lignin and thiolignin. Carbon fiber produced from this dry spinning process possessed strength that ranged only up to 300 MPa. Since 1990's, researchers have continued to focus on producing carbon fiber from different types of lignin precursors by melt spinning. Sudo and Shimizu (5) obtained lignin from steam exploded birch wood and modified the lignin into a fusible material by hydrogenolysis and extraction. Uraki converted a lignin precursor obtained from aqueous acetic acid pulping of hardwood into carbon fiber. The resulting organosolv lignin has good melt spinnability (6). Similarly, Kubo and coworkers applied atmospheric acetic acid pulping on softwood and removed a large molecular weight fraction from it by fractionation with aqueous acetic acid to obtain a fusible material for melt spinning (7). Also, hardwood kraft lignin and Alcell organosolv lignin can be converted into carbon fibers without any chemical modification (8). Above lignin based carbon fibers have exhibited relatively low tensile properties, with published tensile strengths of 660 MPa or lower.

Carbon fibers derived from softwood kraft lignin by melt-spinning of its acetylated form were patented by Eckert (9). However, in their example, only a small batch of about 200 mg acetylated lignin was melt-spun without any characterization of resulting carbon fibers. A recent study on a selected type of softwood kraft lignin demonstrated continuous melt spinning and fast stabilization of the precursor fiber but the carbonized fiber had large diameter (above $50 \mu\text{m}$) (10). The large cross-section area of those carbon fibers would lead to poor tensile strength as proposed by Chae, et al. (11). In 2010, Baker and coworkers reported their carbon fibers produced from an organic-purified hardwood lignin with tensile strength of 0.51 GPa and a modulus of 28.6 GPa (12). Also, a value of 1.07 GPa was attributed in a review article to a DOE presentation (13). Recently, we produced carbon fibers from acetylated softwood kraft lignin using dry spinning. The resulting carbon fiber displayed a tensile strength of 1.04 GPa (14).

Finally, a summary of tensile properties of carbon fibers obtained from different precursors are listed in Table I. All the listed lignin-derived carbon fibers

have significantly lower mechanical properties as compared with those of pitch or PAN based carbon fiber. The low strength may be attributed to the fact that melt-spun precursor fibers are inherently difficult to stabilize by thermo-oxidative means, and often partially fuse together during the stabilization-carbonization processes that lead to surface defects on the resulting carbon fibers. On the other hand, due to its three-dimensional aromatic structure, certain types of lignin are intractable in their unmodified state, and must be suitably modified into components or products that can be converted into fibers. Therefore, research on modification of lignin is of topical interest. In this chapter the conversion of a commercially available softwood lignin into carbon fiber through acetylation is reported; both melt spinning and dry spinning processes were investigated for obtaining precursor fibers.

Experimental

Materials

Softwood kraft lignin, Indulin AT™ (SKL), was obtained from Mead-Westvaco, Charleston, SC (USA). As-received SKL had a ash content about 2.9% as measured by ASTM D5630, so it was washed repeatedly with acidified DI water (pH=2) until ash content approached about 0.15%. Elemental analysis was done by Agricultural Service Laboratory of Clemson University. The elemental result of SKL before and after wash is shown in Table II.

Acetylation was carried out by reacting dry SKL lignin powder with acetic anhydride (Ac₂O) in a round-bottomed flask. The flask was connected with a reflux condenser and dipped into a water bath set at around 85-90°C with continuous stirring. After reaction, solvent present in SKL reaction mixture was removed directly under reduced pressure to obtain the acetylated lignin (Ace-SKL). FT-IR spectroscopy of Ace-SKL was performed in the transmission mode with a Nexus spectrophotometer, using KBr pellets containing 1% samples. Further, Ace-SKL was also fractionated with 75% aqueous acetic acid, and the dissolved fraction was obtained by evaporation of the aqueous acetic acid under reduced pressure.

Softening point was measured using a METTLER TOLEDO FP900 Thermosystem by the Mettler Cup and Ball method ASTM D3461. Low shear rate rheological testing of lignin melt was carried out on an ARES rheometer (TA Instruments) using cone-and-plate fixture at a steady shear rate of 1 s⁻¹. Lignin melt was tested at a temperature nominally 5°C higher than its melting point with an inert gas purge. High shear (300-30000 s⁻¹) rheological testing of lignin solution was conducted using a ACER 2000 capillary rheometer.

Table I. A summary of tensile properties of carbon fibers obtained from different precursors in prior studies

<i>Precursor Type</i>	<i>Diameter (μm)</i>	<i>Elongation (%)</i>	<i>Modulus (GPa)</i>	<i>Tensile strength (MPa)</i>	<i>Reference</i>
Various types of lignin	N/A	N/A	N/A	150-800	Otani, 1969 (4)
Steam exploded hardwood	8 ± 3	1.6 ± 0.2	40.7 ± 6.3	660 ± 230	Sudo, 1992 (5)
Organosolv hardwood	14 ± 1	1.0 ± 0.3	39.1 ± 13.3	355 ± 53	Uraki, 1995 (6)
Kraft hardwood	46 ± 8	1.1 ± 0.2	40 ± 11	422 ± 80	Kadla, 2002 (8)
Oganic purified hardwood	10 ± 1		28.6 ± 3.2	520 ± 182	Baker, 2011 (12)
Oganic purified hardwood		2.0	82.7	1070	Baker, 2013 (13)
Acetylated softwood	7	2.0 ± 0.2	52 ± 2	1040	Zhang, 2014 (14)
PAN	5-10	2	100-500	3000-7000	Various
Mesophase pitch	5-15	0.6	200-800	1000-3000	Various

Table II. Elemental analysis result of SKL before and after wash

	<i>K</i>	<i>Ca</i>	<i>Mg</i>	<i>Fe</i>	<i>S</i>	<i>Na</i>	<i>Al</i>	<i>Si</i>
	<i>wt.%</i>	<i>wt.%</i>	<i>wt.%</i>	<i>wt.%</i>	<i>wt.%</i>	<i>wt.%</i>	<i>wt.%</i>	<i>wt.%</i>
SKL	0.105	0.014	0.017	0.005	1.219	0.753	0.015	0.023
Washed SKL	0.003	0.008	0.012	0.004	0.684	0.007	0.014	0.018

Fiber Spinning

Melt spinning of lignin precursors was performed using an INSTRON capillary rheometer equipped with a 0.25 mm diameter die. The unit was preheated to about 5°C higher than the softening point of lignin sample. When temperature reached the target value, sample was loaded into the barrel. The plunger was fitted into the barrel, and the melt was extruded out of the capillary die. A take-up roll was positioned below to draw down the melt into fibers. The total heating time was controlled in this manner to prevent the formation of high viscosity material before spinning.

For solution spinning, 50 g of Ace-SKL dry powder was fully dissolved in 100 ml acetone. The mixture was stirred continuously and solvent evaporated until solution was concentrated to suitable concentration for spinning. The viscous solution was transferred into a spinning barrel equipped with a 12-hole die, with each hole having diameter of 75 μm . Spinning was performed with a batch unit from AJA Inc. (Greenville, SC). In this lab-scale process, the solvent was vented, but in continuous commercial processes, the solvent can be routinely condensed and recycled.

Thermal Treatment

Lignin fibers were placed in a programmable air oven and thermo-oxidatively stabilized. A heating rate of 0.10-0.25 $^{\circ}\text{C}/\text{min}$ was used to heat the precursor fibers to 220 $^{\circ}\text{C}$. Dwell time at certain temperature was necessary to prevent melting and sticking of fibers. Carbonization was performed using a heating rate of 4.5 $^{\circ}\text{C}/\text{min}$ up to 1000 $^{\circ}\text{C}$ or 2400 $^{\circ}\text{C}$ (HP50 furnace, Thermal Technology LLC).

Fiber Characterization

For tensile testing of monofilaments, individual fibers were tested in a Phoenix tensile testing device following the ASTM test method D-3379-75. The load cell of the MTS apparatus has a maximum capacity of 500 grams, and the cross head speed was set to 0.5 mm/min. Individual fibers were mounted on paper tabs for tensile tests, and nominally 25 samples per group of fibers were tested using a gage length of 10 mm. The fiber diameters were calculated via single slit laser diffraction. Each paper tab was secured in the upper and lower jaws of the MTS. To prevent the accidental breakage of fiber prior to test failure, an electric hot wire (instead of scissors) was used to burn the paper tab.

Raman spectra were recorded on a Renishaw System (Gloucestershire, UK) using a near infrared 780 nm-diode laser. The Raman shift was calibrated with a silicon standard centered at 520 cm^{-1} . Raman spectra was analyzed using WiRE software v3.2 to intergrated the peaks. Wide angle X-ray diffraction (WAXD) patterns were obtained from a Rigaku $\text{CuK}\alpha$ X-ray source at wavelength of 0.15406 nm, and the X-ray source was operated at 45 kV and 0.65 mA. Fiber bundles were mounted on a paper tab and sprinkled with NIST-grade silicon standard powder for accurate identification of 2 θ position on integrated azimuthal scan. The exposure time per sample was 1 h. The spacing of (0 0 2) plane (d_{002}) were calculated according to Bragg's law with the following equation:

$$d_{002} = \frac{\lambda}{2 \sin \theta}$$

where λ corresponds to the wavelength of the X-ray beam (0.15406 nm), and θ is the angle of incidence of the X-ray beam. According to the model given by Maire and Mering (15), degree of graphitization was calculated using the following equation:

$$g(\%) = \frac{0.3440 - d_{002}}{0.3440 - 0.3354} \times 100$$

where g is the degree of graphitization (%).

Results and Discussion

Melt Spinning of Ace-SKL with High Acetylation Content

As-received SKL had a glass transition temperature of 155°C as observed from DSC but showed no fusing behavior during the entire heating procedure even when the temperature reached 300°C at the end of the softening point test. Instead, degradation was observed, and the residue after heating was in a foamed state indicating the generation of volatiles during heating. Above results are in agreement with those reported in previous literature studies in which softwood lignin has been shown to possess poor thermal mobility because it has higher cross-linked structure than does hardwood lignin (7). The hydroxyl groups results in dehydration reaction between molecules. Thus, SKL cannot be melt-spun without appropriate modification.

In the current studies, SKL was reacted with Ac₂O for 2 hours to convert the hydroxyl group into acetyl group using a reaction solution of 15 ml of Ac₂O per gram of SKL. The Ace-SKL showed a softening temperature between 156 and 167°C. However, the viscosity of molten Ace-SKL at 170°C increased from around 80 Pa·s to 8,000 Pa·s within 30 min as shown in Figure 1 (a). The test finally ended due to overloading of the torque transducer. During heating, several types of reactions can occur including dehydration, condensation, and addition, that induce an increase of molecular weight. Consequently, the viscosity increases significantly and caused the failure of rheology test.

Ace-SKL was extracted with 75% acetic acid, and a fraction with relatively large molecular weight was removed. A similar study has been reported by Saito et al. (16) using methanol to obtain a hardwood lignin fraction with a much lower molecular weight, which displayed a softening point. After extraction, the fraction soluble in 75% acetic acid in the current study had a softening point between 136-145°C. The viscosity remained below 500 Pa·s for the first 30 min at 145°C, as shown in Figure 1 (b), as a result of the lower molecular weight, which indicates that subsequent melt spinning may proceed as a stable process.

The extracted Ace-SKL was successfully melt-spun into fibers, as illustrated in Figure 2 (a). Although the extracted Ace-SKL fibers were easy to spin, it was virtually impossible to stabilize them by thermo-oxidative stabilization. Substitution of hydroxyl groups by the stable acetyl groups prevented any significant crosslinking and thermal stabilization of the macromolecules within the precursor fibers. Although a slow ramp heating rate, as low as 0.01°C/min was applied, the fibers could not be maintained in their glassy state and became tacky at around 150°C, as shown in Figure 2 (b). Once the precursor becomes tacky, it is not possible to retain individual precursor fibers. Therefore, this composition is not well-suited for producing carbon fibers.

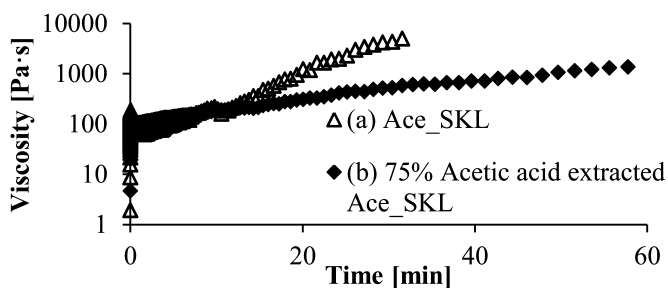


Figure 1. Transient shear viscosity of (a) Ace-SKL and (b) 75% acetic acid extracted Ace-SKL.



Figure 2. (a) as-spun Ace-SKL fibers; (b) tacky Ace-SKL fibers after thermal stabilization.

Controlled Acetylation of Ace-SKL

Consequently, SKL was reacted with a significantly lower Ac_2O concentration (0.66 ml $\text{Ac}_2\text{O}/\text{g}$ SKL) and shorter reaction time of only 0.25 hour to preserve more hydroxyl group in resulted Ace-SKL.

Figure 3 displays the FTIR spectra of SKL at different acetylation levels. All the spectra were normalized with respect to the peaks at 856 cm^{-1} , which is attributed to C-H bending on aromatic rings. As the amount of Ac_2O decreased from 15 ml to 0.66 ml, intensity of the hydroxyl peak at 3400 cm^{-1} increased significantly. Also, the weight gain of lignin after reaction with Ac_2O moderated from 18% to 5%. Larger content of hydroxyl group increased the reactivity and enabled crosslinking during thermo-oxidation, and fiber shape was preserved without fibers becoming tacky. At the same time, Ace-SKL resulted from limited acetylation was fully soluble in acetone, which enabled its solution spinning. Thus, 0.66 ml $\text{Ac}_2\text{O}/\text{g}$ SKL concentration and 0.25 hour reaction time with a weight gain around 5% were chosen as the conditions for producing precursor for all subsequent experiments.

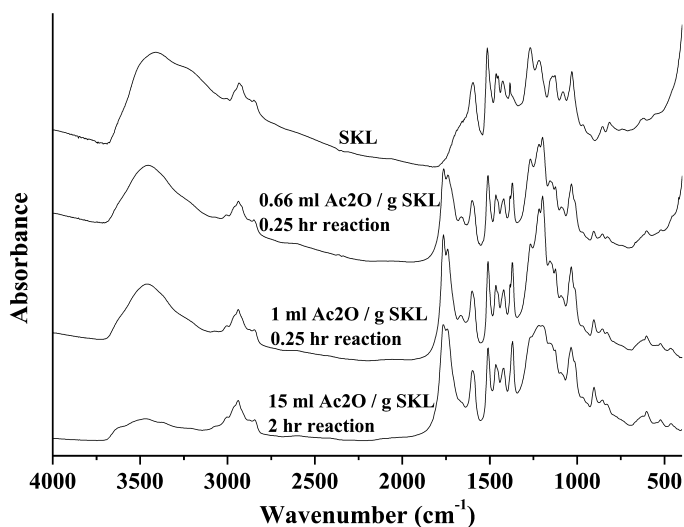


Figure 3. FT-IR spectra of acetylated lignin (Ace-SKL) produced from various compositions and reaction times. (Reproduced with permission from reference (14). Copyright 2014 Elsevier.)

Softening point was also tested for Ace-SKL with different reaction composition. As displayed in Figure 4, as the extent of acetylation decreased, resulting material had elevated softening point, which is also favorable for subsequent thermo-oxidative stabilization.

Glass transition temperature, as estimated using DSC, is displayed in Figure 5. T_g of Ace-SKL reacted from 1.5-15 ml acetic anhydride per gram SKL were all between 90-105°C, but was noticeably higher at 112°C for Ace-SKL obtained using 0.66 ml acetic anhydride per gram of SKL. The increase of softening point and T_g was attributed to stronger intermolecular hydroxyl group interactions when less hydroxyl groups were reacted away with acetic anhydride. The presence of such interactions is favorable for the following thermo-oxidative stabilization reactions.

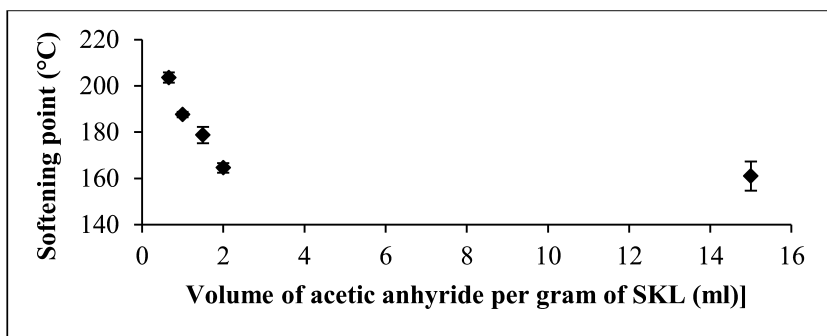


Figure 4. Softening point of Ace-SKL with different reaction composition.

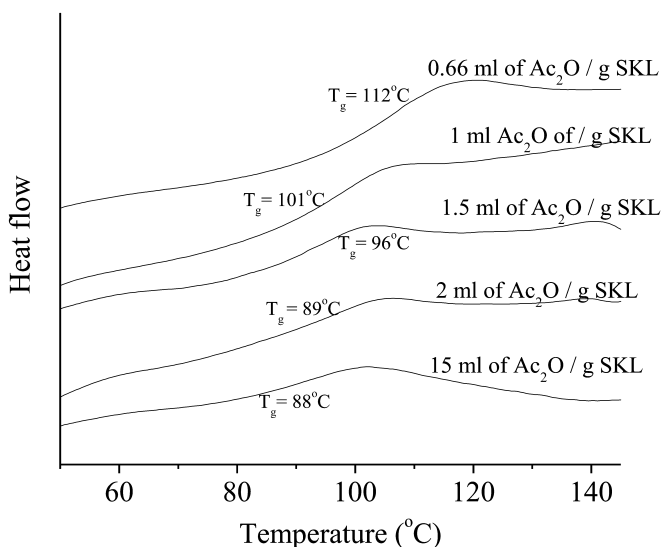


Figure 5. DSC of Ace-SKL with different reaction composition.

Dry Spinning of Ace-SKL

Ace-SKL was dissolved in acetone to obtain a homogeneous viscous solution with about 75% solids content. This solution concentration is optimal for spinning, because adequate viscoelasticity was needed for extension of filaments, whereas a low viscosity is preferred for lower spin pack pressure. Using a capillary rheometer, the viscosity at shear rate between 300-30000 s⁻¹ is shown in Figure 6. At 45°C which is slightly below the boiling point of acetone, spinning solution had a lower viscosity and acetone evaporate faster compared with room temperature.

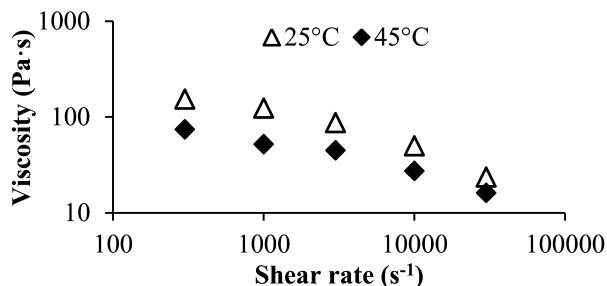


Figure 6. Capillary rheometer test of 75% solid content Ace-SKL solution.

Figure 7 shows the SEM images of as-spun fiber cross-sections obtained from dry spinning at 25 and 45°C, respectively. Both fibers displayed crenulation of the surface. For spinning at 45°C, a larger number of small-sized crenulations on each fiber were observed due to faster evaporation of acetone. In contrast, at 25°C, fibers developed fewer, but larger and smoother crenulations per fiber.

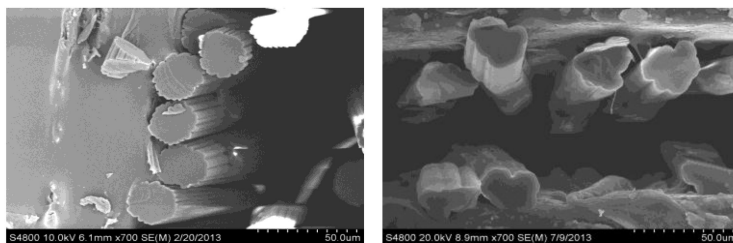


Figure 7. Ace-SKL as spun fibers from dry spinning at 45°C (left) and 25°C (right). (Adapted with permission from reference (14). Copyright 2014 Elsevier.)

Thermal Treatment of Ace-SKL Fibers and Characterization of Ace-SKL Based Carbon Fibers

Ace-SKL fibers were thermo-oxidatively stabilized using a temperature ramp of 0.2°C/min with several hours of dwell time from ambient to a maximum temperature of 220°C. The slow ramp heating program allowed the fibers to maintain their shape without becoming tacky. During thermostabilization, Ace-SKL precursor fibers were maintained under a tension of the order of 0.01 g/denier that resulted in an extension of up to 800%. Carbonization was also performed under tension using the same customized graphite rack, as illustrated in Figure 8.



Figure 8. Fiber tow suspended on a customized graphite rack and tungsten weight loaded at the bottom.

Ace-SKL Carbon Fiber Cross Section Shape Analysis

SEM micrographs of carbon fibers produced from a heat treatment of 1000°C are shown in Figure 9. From a comparison of cross-sectional shapes of as-spun fiber (shown earlier in Figure 7) and carbon fibers, it is evident that the cross-section pattern was preserved after carbonization. The average number of crenulations per fiber (C), number of crenulations/fiber perimeter (C/P), aspect ratio (a/b), and fiber perimeter/perimeter for equivalent circular

fiber with same cross-section area (P/Pe) values are listed in Table III. Fibers spun at a higher temperature undergo a rapid out-diffusion of solvent that can be achieved by a larger number of finer crenulations, which has 35% larger surface area as compared with equivalent circular fiber (same cross-sectional area) that are typically obtained by melt-spinning. Fiber spun at a lower temperature of 25°C undergo a slower out-diffusion of solvent and result in fewer but larger crenulations, which result in about 20% larger surface area.

The average tensile strength from single filament test were 1.05 ± 0.07 GPa and 1.06 ± 0.07 GPa for 45°C and 25°C spinning temperatures, respectively; these values are statistically not different. However, the fibers resulting from spinning at 45°C result in larger interfacial area, and this could ultimately lead to higher fiber-matrix interfacial bond strength in composites.

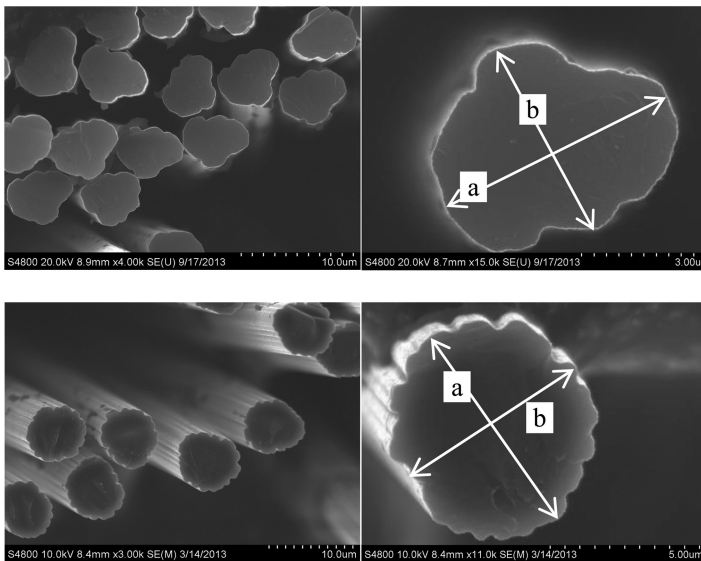


Figure 9. Ace-SKL carbon 25°C spinning (top) and 45°C spinning (bottom). (Adapted with permission from reference (14). Copyright 2014 Elsevier.)

Table III. Analysis of the SEM images of Ace-SKL carbon fibers from different spinning condition

Temperature	C	C/P (μm^{-1})	a/b	P/Pe
45°C	19 \pm 1	0.68 \pm 0.01	1.10 \pm 0.03	1.35 \pm 0.03
25°C	5 \pm 1	0.27 \pm 0.03	1.32 \pm 0.04	1.20 \pm 0.01

Tension Effect during Carbonization

When carbonization was conducted under tension, an extension of up to 25% could be achieved during with adequate tensile stress. Figure 10 displays modulus and strength of various carbon fibers as a function of fiber extension-during-carbonization (EDC). As expected, carbon fibers with larger EDC displayed better tensile properties, due to higher molecular orientation within the fibers.

Table IV lists the tensile properties of Ace-SKL derived carbon fiber from different batches stabilized and carbonized with or without tension; the values are before compliance correction. With applied tension, fibers with thinner diameter and better tensile properties were obtained. Fibers processed without any tension during both stabilization and carbonization displayed only half of the tensile strength as compared with fibers processed with tension during both steps. After compliance correction for modulus (using gage lengths of 5, 10, and 25 mm per ASTM D-3379-5), carbon fibers that underwent significant EDC displayed a tensile modulus, strength, and strain-to-failure values of 52 ± 2 GPa, 1.06 ± 0.07 GPa, and $2.0 \pm 0.2\%$, respectively. The largest individual filament tensile strength was 1.3 GPa. It is noted that, even when a similar extent of positive extension was obtained during carbonization of a previous Ace-SKL batch having a higher ash content of 0.3%, a much lower tensile strength of only 0.60 GPa was obtained for the resulting carbon fibers. This clearly indicates that low ash content is also critical for attaining higher performance of the resulting carbon fibers in addition to the tension.

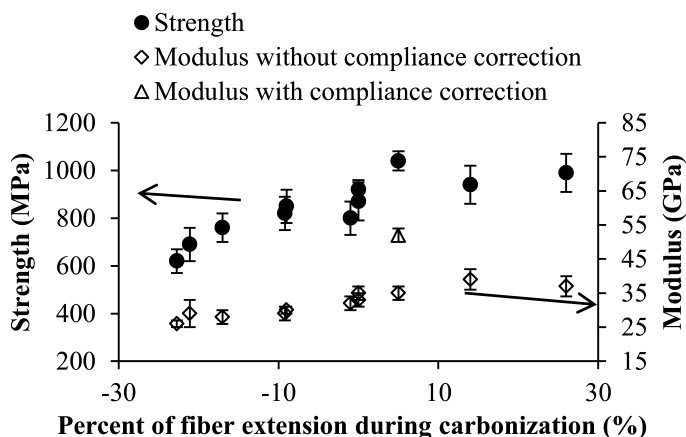


Figure 10. Tensile strength and modulus of Ace-SKL carbon fibers under various levels of tension during carbonization. (Reproduced with permission from reference (14). Copyright 2014 Elsevier.)

Table IV. Ace-SKL carbon fiber properties of fiber processed with and without tension

	<i>Diameter (μm)</i>	<i>Strength (MPa)</i>	<i>Apparent Modulus (GPa)</i>	<i>Apparent strain to failure (%)</i>
Stabilized and carbonized without tension	22.5 ± 0.4	510 ± 50	30 ± 2	1.7 ± 0.1
Stabilized with tension, carbonized without tension	8.6 ± 0.2	700 ± 30	28 ± 1	2.5 ± 0.1
Stabilized and carbonized with tension	5.9 ± 0.2	1050 ± 70	35 ± 3	3.0 ± 0.2

Characterization of Ace-SKL Carbon Fibers Crystallinity

To study the crystallinity development during carbonization, one group of Ace-SKL carbon fibers were further heat treated to 2400°C. After this high temperature carbonization, the tensile strength dropped to 210 ± 30 MPa. This is consistent with other precursors (such as PAN), where out-diffusion of noncarbonaceous elements leave behind voids and defects.

Representative Raman spectra for Ace-SKL carbon fibers carbonized at 1000 and 2400°C are displayed in Figure 11. The ratio of integrated intensity value of disordered (D) to graphitic (G) peaks (I_D/I_G) was measured to be about 2.88 and 1.02 for 1000 and 2400°C treated fibers respectively. Both values indicate a low degree of graphitic crystallinity development within the carbon fibers. This is consistent with the nonhomogeneous chemical structure of the lignin precursor, which is not as conducive to formation of the hexagonal carbon form as is mesophase pitch. It should be noted that a higher graphitic crystallinity enhances lattice-dominated properties such as the modulus and thermal conductivity, but adversely affects the tensile strength.

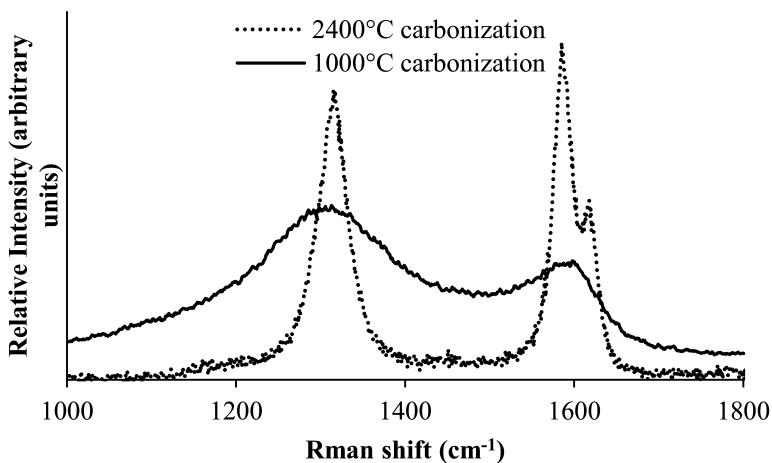


Figure 11. Raman spectra of Ace-SKL carbon fibers carbonized at 2400 and 1000°C. Intensity values on the ordinate scale are in arbitrary units.

For 1000°C carbonized fibers, the integrated azimuthal profiles from WAXD for fibers carbonized with and without tension are similar, with their (0 0 2) peaks located at 2θ value of approximately 24.3° as shown in Figure 12 (a). The three small, sharp peaks (first appearing at 28.4°) are from NIST-grade silicon powder sprinkled on the carbon fiber samples for accurate location of 2θ peak positions. For 2400°C carbonized fibers, the (0 0 2) peak was located at 26.0° , with d_{002} spacing calculated as 0.3424 nm, and the corresponding degree of graphitization at 18%. These WAXD results are consistent with those obtained from Raman spectroscopy. Further, the azimuthal profile of the (0 0 2) peak, Figure 12 (b), showed virtually no molecular orientation in fibers carbonized without tension. The Herman's orientation factor ($f_a = [3\langle \cos^2\phi \rangle - 1]/2$) was measured at about 0.1. In contrast, for fibers carbonized under tension, the peak at $\phi \sim 0^\circ$ indicates an observable extent of molecular orientation with a significantly higher Herman's orientation factor of about 0.3. The 2400°C carbonized fiber also preserved the orientation with Herman's orientation factor still as 0.3.

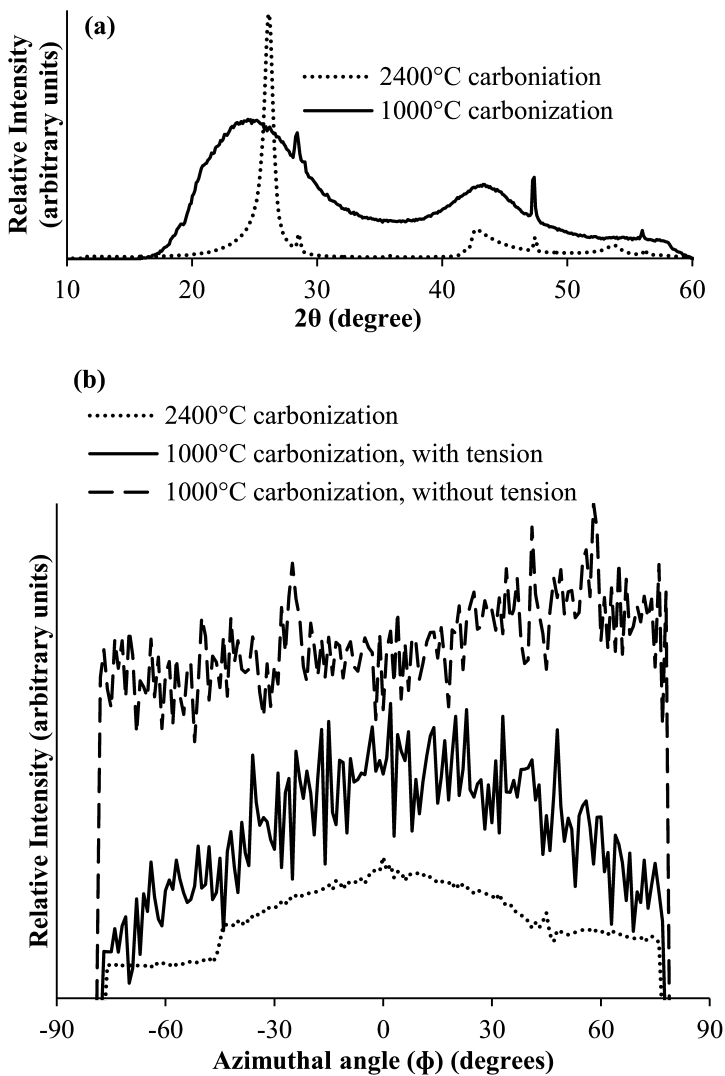


Figure 12. Wide-angle x-ray diffraction of Ace-SKL carbon fibers. Intensity values on the ordinate scale are in arbitrary units. Azimuthal scans have been shifted vertically for visual clarity. (Adapted with permission from reference (14). Copyright 2014 Elsevier.)

Conclusions

Acetylated lignin (Ace-SKL) obtained from higher extent of acetylation was capable of being melt-spun, but due to the difficulty of stabilization, it was not regarded as a suitable carbon fiber precursor. By limited acetylation, Ace-SKL could be dry-spun, and was capable of stabilization. Tension was applied during thermal treatment, and resulted in a tensile strength, modulus and strain-to-failure of 52 ± 2 GPa, 1.06 ± 0.07 GPa, and $2.0\pm 0.2\%$, respectively. These mechanical properties are amongst the highest values reported in the literature for lignin-derived carbon fibers. It is also noted that the cross-section shape can be controlled during dry-spinning, and crenulated carbon fibers obtained in this study have up to 35% larger surface area as compared with equivalent circular fibers that are typically obtained by melt-spinning. Due to the lack of graphitic crystallinity in these lignin-derived carbon fibers, their surface is expected to be more reactive than that of carbon fibers processing from graphitic precursors. Surface reactivity and larger surface area could both lead to better fiber-matrix interfacial bonding in composites.

References

1. Edie, D. D.; Diefendorf, R. J. In *Carbon-Carbon Materials and Composites*; Buckley, J. D., Edie, D. D., Eds.; Noyes Publications: Park Ridge, NH, 1993; pp 20–33.
2. Fitzer, E.; Manocha, L. M. *Carbon Reinforcements and Carbon/Carbon Composites*; Springer: Berlin, 1998; pp 17–28.
3. Sandermann, H., Jr.; Scheel, D.; Trenck, T. *J. Appl. Polym. Sci.: Appl. Polym. Symp.* **1983**, *37*, 407–420.
4. Otani, S.; Fukuoka, Y.; Igarashi, B.; Sasaki, K. U.S. Patent 3,461,082, 1969.
5. Sudo, K.; Shimizu, K. *J. Appl. Polym. Sci.* **1992**, *44*, 127–134.
6. Uraki, Y.; Kubo, S.; Nigo, N.; Sano, Y.; Sasaya, T. *Holzforschung* **1995**, *49*, 343–350.
7. Kubo, S.; Uraki, Y.; Sano, Y. *Carbon* **1998**, *36*, 1119–1124.
8. Kadla, J.; Kubo, S.; Venditti, R.; Gilbert, R.; Compere, A.; Griffith, W. *Carbon* **2002**, *40*, 2913–2920.
9. Eckert, R. C.; Abdullah, Z. U.S. Patent 7,794,824, 2010.
10. Norberg, I.; Nordström, Y.; Drougge, R.; Gellerstedt, G.; Sjöholm, E. *J. Appl. Polym. Sci.* **2012**, *128*, 3824–3830.
11. Chae, H. G.; Choi, Y. H.; Minus, M. L.; Kumar, S. *Composites Sci. Technol.* **2009**, *69*, 406–413.
12. Baker, D. A.; Gallego, N. C.; Baker, F. S. *J. Appl. Polym. Sci.* **2012**, *124*, 227–234.
13. Baker, D. A.; Rials, T. G. *J. Appl. Polym. Sci.* **2013**, *130*, 713–728.
14. Zhang, M.; Ogale, A. A. *Carbon* **2014**, *69*, 626–29.
15. Maire, J.; Mering, J. *Chem. Phys. Carbon* **1970**, *6*, 125–190.
16. Saito, T.; Perkins, J. H.; Vautard, F.; Meyer, H. M.; Messman, J. M.; Tolnai, B.; Naskar, A. K. *ChemSusChem* **2014**, *7* (1), 221–228.

Chapter 7

Solvent Fractionation of Lignin

Sabornie Chatterjee and Tomonori Saito*

Chemical Sciences Division, Oak Ridge National Laboratory,
Oak Ridge, Tennessee 37831-6210, United States

*E-mail: saitot@ornl.gov. Tel: 865-576-6418.

Lignin is a highly abundant source of renewable carbon that can be considered as a valuable sustainable source of biobased materials. The major issues for the commercial production of value added high performance lignin products are lignin's physical and chemical heterogeneities. To overcome these problems, a variety of procedures have been developed to produce pure lignin suitable for high performance applications such as lignin-derived carbon materials. However, most of the isolation procedures affect lignin's properties and structure. In this chapter, a short review of the effect of solvent fractionation on lignin's properties and structure is presented.

Introduction

Lignin, the largest biomass source with aromatic structure and a carbon content above 60%, can be considered as the most attractive sustainable precursor for carbonaceous materials (1–5). The use of lignin for the production of bio-based products has minimal environmental effects and, more importantly, this sustainable feedstock does not belong to the human food chain (6, 7). Lignin accounts for about 15-30% dry weight of woody plant materials (8). The estimated natural production of lignin on earth is in the range of $5\text{--}36 \times 10^8$ tons annually (5, 9). The annual production of commercial lignin is more than 70 million tons (10). Commercial lignins are mainly obtained as by-products from various industrial processes such as the enzymatic hydrolysis of biomass to produce bioethanol, and the sulfite pulping process used in the paper and pulp industry. The U.S. Renewable Fuels Standard (RFS) sets a mandatory target of producing 16 billion gallons of lignocellulosic biofuels (mainly ethanol) by 2022 (11). Similarly, the European Union as a whole has set a target to increase

the number of bio-refineries (2). These policies would thus result in a sustained abundant supply of enormous amounts of lignin at low cost.

In recent years, a great deal of research has focused on the development of lignin derived carbon fibers, activated carbons, and others (3, 10, 12–16), which are discussed in the other chapters in this symposium series. However, the use of lignin in different products other than inexpensive fuel is still very limited due to the presence of heterogeneity in lignin's molecular weight, functionality and thermal properties that vary with source and isolation process of lignin (17).

Chemical Compositions of Lignin

The molecular weight and composition of any particular lignin type largely depend on the plant source and the environmental and developmental factors (1, 5, 18–20). In general, lignin is a polyphenol with a three dimensional structure of randomly cross-linked phenyl propane units such as *p*-hydroxyphenyl (H), guaiacyl (G) and syringyl (S) (Figure 1) (21). The relative distributions of these monomeric units in any lignin type depend on the plant source. The typical S/G ratios in hardwood and softwood lignins are 2:1 and 1:2-1:3, respectively (13). Lignins from grasses have S/G ratio about 1:1 to 1:2 (22). The general structure of lignin contains a variety of carbon-oxygen and carbon-carbon bonds such as β -O-4, 5-5, 4-O-5, β - β and so on where the β -O-4 is the most common one (Figure 2) (1, 5, 23).

Isolation of Lignin

The isolation of lignin from biomass involves complex physical and chemical processes primarily due to the complex structures of the cell wall and the interactions of its components (19). Due to highly linked structures of lignin and carbohydrates in plant materials, it is impossible to isolate pure lignin without any chemical mediated cleavage (20). Isolation of lignin from plants generally can be performed in two ways (21). In the first case, carbohydrate is hydrolyzed using enzymes and dissolved away from lignin, where lignin is obtained as an insoluble material. This method requires a pre-treatment of the feedstock to facilitate the enzymatic hydrolysis. A variety of pretreatment methods such as ball milling, mechanical treatments, acid treatments, alkali treatments, hydrogen peroxide treatments, or an enzymatic hydrolysis are used to open up the biomass structure (1, 5)

The second method of lignin isolation uses chemical reagents to isolate carbohydrates from lignin. Several processes under this category such as acid sulfite process, alkaline kraft process, organosolv process are available for the production of lignin. Methods such as alkaline kraft process produce lignin with high sulfur content. Among all chemical methods, organosolv process produces relatively pure lignin. This process is more environment friendly than kraft or sulfite process because it does not involve environmentally hazardous compounds.

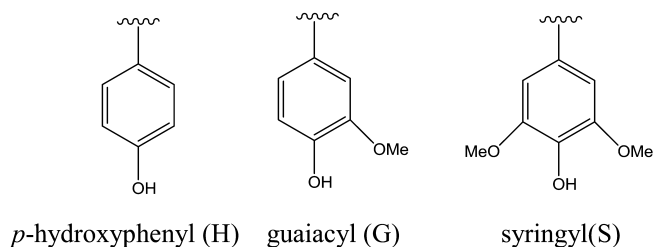


Figure 1. Structural units of lignin.

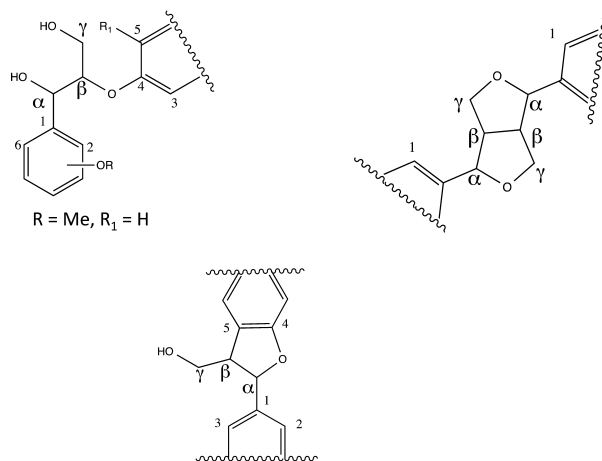


Figure 2. Common chemical bonds in lignin.

Most of the isolation methods used to produce lignin from biomass were initially developed to obtain high quality cellulose with great yields. Therefore, these methods were not focused on the production of highly pure lignin in general. Thus, treatments such as solvent fractionations of lignins, that are prepared in various methods, are necessary to generate pure lignin that can be used in modern high performance applications.

In our recent work, we performed the synthesis of a hardwood solvent extracted (Alcell) lignin based novel thermoplastic copolymer that showed two phase behavior in dynamic mechanical analysis (DMA) (9, 24). These studies indicate the lignin content and the glass transition temperature (T_g) could be tuned to achieve desired properties in the synthesized copolymers. In fact, the tunability of T_g of lignin is crucial in lignin-based material processing including the manufacturing of lignin-based carbon fibers, because T_g directly correlates to the thermal processing temperature. In the synthesis of lignin-based multiphase thermoplastic copolymers, the use of high molecular weight (HMW) lignin fraction was essential to allow an effective connection between the hard segment (lignin) and the soft segment. The ‘as-received lignin’ contained a large portion of low molecular weight (LMW) fraction (Figure 3a) and the HMW lignin fraction was prepared by formaldehyde crosslinking. Selective crosslinking

of lignin with formaldehyde not only increased the T_g of the material but also reduced its polydispersity index (PDI), that resulted in two different phases in the thermoplastic copolymer. Similar increase of T_g and molecular weight of lignin can also be obtained via solvent fractionation (9, 25).

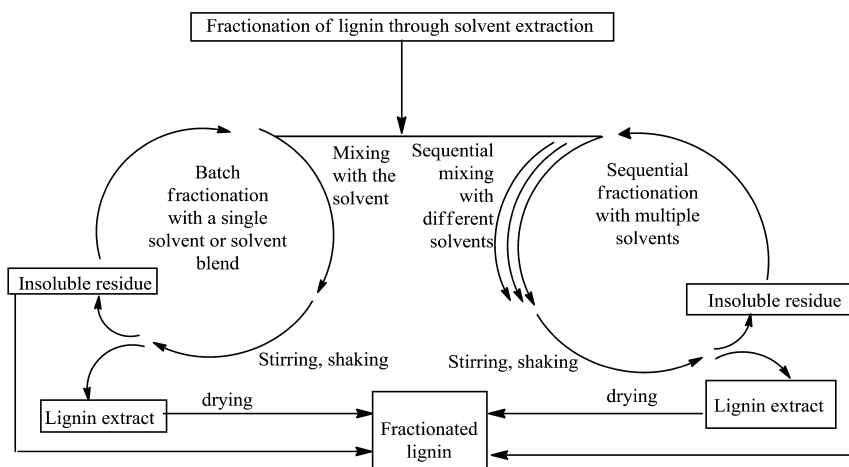
Solvent Fractionation of Lignin

Solvent fractionation is the process of isolating components of any mixture based on their different solubilities in a solvent or mixture of solvents. This process employs the interactions (such as hydrogen-bonding) of those components with solvent molecules to fractionate them. Commercial lignins, such as those isolated from acid sulfite process or organic solvent-based processes, have undergone extensive fragmentation and degradation (21, 22, 26). As a result, lignins with variable chemical properties and structures are generally obtained. Also, most industrial lignins contain significant amounts of impurities, which might create problems for many manufacturing process such as the production of carbon fibers. Using solvent fractionation, various pure fractions of lignin can be obtained. Solvent fractionation of lignin has been used in industry and explored with different types of lignin with a variety of solvents under different conditions (27–32). The recent detailed study of the solvent fractionation of lignin reveals that solvent fractionation has pronounced effects on lignin's properties such as molecular weight, molecular weight distribution, chemical structures, T_g , carbon yield, and thermal decomposition temperatures (25).

Solvent fractionation of lignin can be conducted primarily in two ways. In one case, lignin is extracted by a single solvent or a sequential use of multiple solvents. In the other case, a solvent is used to dissolve lignin and then precipitated using chemical (mostly acid) treatments. In this chapter, lignin fractionation by solvent extraction (case 1) is discussed. Solvent fractionation of lignin is generally conducted by mixing lignin with organic solvents followed by steps of stirring, shaking at ambient temperature for ideally 20-30 mins in each step (Scheme 1). Next, the mixture is centrifuged or filtered to isolate the soluble part or the extract from the non-soluble part and the supernatant is collected. The solids are re-extracted several times (generally 3-4 times) with fresh solvent and supernatants are collected. All supernatants are combined with the primary extract. These steps are repeated in the case of sequential solvent fractionation with different solvents or mixture of solvents. Further, the residual lignin and all extracts are evaporated to dryness under convection flow or vacuum.

In solvent fractionation method, the yields of various lignin fractions vary with the solvents and conditions used. Wang et al. reported the fractionation of Kraft-AQ (anthraquinone) lignin with different solvents. In their study, hexane and diethyl ether based fractionation gave very low yield of the starting lignin (Table 1) (33). On the other hand, methylene chloride and methanol, due to their strong hydrogen bonding ability, dissolved and subsequently gave large amounts of the starting lignin. Pas et al. observed similar trend with various steam exploded and organosolv lignins (34). When fractionation of these lignins were performed with ether, acetone and ether-acetone (4:1) mixture, highest lignin recovery was

made in the case of acetone (Table 2) (34). Zhao and Wilkins found that in the extraction of hardwood organosolv lignin with methanol and diethyl ether, higher amount of lignin was obtained when methanol was used. This also supported the previous result obtained by Thring et al. (31) All these reports indicate that polar solvents give higher yields in the fractionation of lignin. Wool et al. also reported solubility parameter for hardwood kraft lignin as $\delta_{\text{total}} = 24.3 \text{ J}^{1/2}/\text{cm}^{3/2}$ (35). The estimated solubility parameter fits in the similar range to these polar solvents used for extraction of lignin.



Scheme 1. Solvent fractionation of lignin.

Table 1. Yields (% dry matter, w/w) of the lignin fractions from *Eucalyptus pellita* derived Kraft-AQ lignin (33). [Adapted from reference (33)]

	<i>Lignin fractions</i>				
	<i>Hexane</i>	<i>Ethyl ether</i>	<i>Methylene chloride</i>	<i>Methanol</i>	<i>Dioxane</i>
Yield ^a	0.2	1.6	33.4	59.1	4.4

^a Standard deviation is less than 2%.

**Table 2. Yields of lignin fractions after sequential solvent fractionation (34).
[Adapted from reference (34)]**

<i>Lignin</i>	<i>Ether</i> (%)	<i>Ether/acetone</i> (%)	<i>Acetone</i> (%)	<i>Residual</i> (%)	<i>Total</i> (%)
Pine SE ^a	10	24	50	14	98
Eucalyptus SE ^a	4.7	12	48	34	99
Alcell OS ^b	2.8	27	57	12	99
Birch OS ^b	8.1	4.9	27	56	96

^a Solvent exploded. ^b Organosolv.

Effect of Solvent Fractionation on Molecular Weights of Lignin

Determination of lignin molecular weight is quite complex due to the heterogeneous chemical structures within the same batch of lignin. Size exclusion chromatography (SEC) is typically used to determine lignin molecular weight; however, the accuracy of the reported molecular weights via different mobile phases and detectors by various researchers is still open to discussion. It is important to be aware that the trend of molecular weights in the same method of SEC should be accurate but the value and polydispersity index (PDI) may be completely different in different methods. In all of our previous studies (9, 24, 25), SEC data from neat dimethylformamide (DMF) correlated very well with other physical properties, although the lignin peak from SEC data from neat DMF most likely represents both single lignin molecules and lignin aggregates in DMF. For example, as-received hardwood Alcell lignin and as-received softwood kraft lignin showed very high PDI of 120 and 110, respectively in DMF SEC without lithium bromide (LiBr) (Figure 3a, Table 3). All the correlated physical data as discussed below indicate that the significantly high PDI represents heterogeneities existing in lignin sample, and these SEC data in neat DMF (without LiBr) reflect lignin properties better than other methods. When the same as-received softwood kraft lignin was analyzed in DMF SEC with LiBr using the same column, single and monomodal peak with PDI 3.05 was obtained (Figure 3a and Table 4). Although researchers in this field tend to report monomodal SEC data similar to this data obtained from DMF SEC with LiBr (PDI 3.05), a multimodal SEC curve from DMF SEC without LiBr (PDI 110) corresponds better to lignin physical properties in our studies.

Solvent extraction-based lignin fractionation can produce lignin with varying molecular weights. In our recent study, the MeOH solvent fractionation was able to isolate low molecular weight (LMW) fraction of lignin from high molecular weight (HMW) lignin fraction effectively (25). In this work, the starting kraft lignin (as-received lignin) has a number average molecular weight (M_n) = 10000 g/mol and PDI = 110 (Table 3). The SEC curve of the starting lignin showed the presence of HMW and LMW peaks where the area percents of the HMW and LMW peaks were 93.6 and 6.4, respectively (Figure 3a and 3b). Repetitive extraction with MeOH extracted out the LMW phase from the lignin, which was clearly confirmed by

SEC, showing a reduced LMW peak (Table 3 and Figure 3b). Due to the removal of LMW fraction by this process, the PDI of the residual lignin was decreased to 3.5 and molecular weight (M_n) was increased to 443000 g/mol (Table 3). On the other hand, due to the presence of relatively large amount of LMW portion in the MeOH extracted lignin (Figure 3b), the PDI increased to 129 and the molecular weight (M_n) decreased to 3800 g/mol. This fraction also contained a large peak of HMW lignin that might be present in a colloidal form.

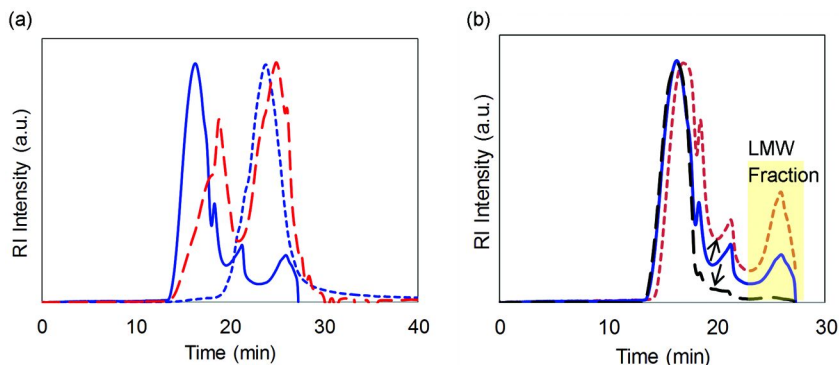


Figure 3. (a) SEC curves of as-received kraft lignin without LiBr (blue solid line), as-received kraft lignin with LiBr (blue dashed line), and as-received Alcell lignin without LiBr (red dashed line), (b) SEC curves (without LiBr) of as-received lignin (blue solid line), MeOH insoluble lignin (black dashed line), and MeOH soluble lignin (red dashed line) (9, 25). [Adapted from references (9) and (25)].

Similar SEC studies of these fractions were performed in the presence of LiBr (25). The addition of LiBr was performed to eliminate the influence of the lignin aggregations in the SEC mobile phase. All the SEC curves showed monomodal peak (Figure 3a and Table 4) and both MeOH soluble lignin fraction and MeOH insoluble residual lignin had lower PDI than the starting lignin (Table 4), indicative of accomplishing effective fractionation. The single, monomodal peaks of these lignin samples obtained in these DMF SEC with LiBr indicates that the size of lignin corresponds to a single distribution. However, combined results of DMF SEC both with and without LiBr suggest that the chemical structure and compositions among as-received, MeOH insoluble, and MeOH soluble lignins are significantly altered. The molecular weight (M_n) of the starting lignin, residual lignin and MeOH soluble lignin from refractive index (RI) detector were 2360, 6520 and 1590 g/mol, respectively. Absolute molecular weights were measured using light scattering (LS) detector where the weight-average molecular weight (M_w) of the starting lignin, residual lignin and MeOH soluble lignin were 96100, 188000 and 86600 g/mol, respectively. The dn/dc values were carefully measured off-line and these M_w values should be more accurate than the molecular weight from RI detectors. If this is a regular polymer, the absolute molecular weight from the LS detector should represent actual molecular weight of the polymer. However for lignin samples, these values might be still slightly off from an actual

molecular weight value due to the lignin's heterogeneity and branched structures. It is probably true that the molecular weights from RI detector (2360, 6520 and 1590 g/mol) are too low to be consistent with other physical characteristics.

Table 3. Molecular weight of lignin via MeOH fractionation (without LiBr) (9, 25). [Adapted from references (9) and (25)]

	<i>Washing</i>	M_n (g/mol)	M_w (g/mol)	<i>PDI</i>	<i>HMW</i> <i>Area (%)</i>	<i>LMW</i> <i>Area (%)</i>
Alcell Lignin (Hardwood)						
As-received Lignin		1,840	225,000	122		
MeOH Insoluble Lignin	1 st	8,960	664,000	74.2		
Kraft Lignin (Softwood)						
As-received Lignin		10,000	1,110,000	110	93.6	6.4
MeOH Insoluble Lignin	1 st	28,200	1,310,000	46.3	97.2	2.8
	2 nd	60,600	1,400,000	23.1	98.8	1.2
	3 rd	63,800	1,530,000	24.0	98.8	1.2
	4 th (last)	443,000	1,550,000	3.5	100	0.0
MeOH Soluble Lignin		3,800	492,000	129	84.7	15.3

Determined from refractive index detector.

Table 4. Molecular weight of lignin with addition of LiBr in SEC solvent (25). [Adapted from reference (25)]

	M_n^a (g/mol)	M_w^a (g/mol)	PDI^a	M_w^b (g/mol)	dn/dc^c (mL/g)
As-received Lignin	2,360	7,190	3.05	96,100	0.1867±0.0011
MeOH Insoluble Lignin	6,520	14,900	2.28	188,000	0.1837±0.0092
MeOH Soluble Lignin	1,590	3,000	1.90	86,600	0.1636±0.0028

^a Determined from refractive index detector. ^b Determined from light scattering detector. ^c Determined off-line.

The MeOH fractionation of hardwood Alcell lignin showed the same effect (9) as the softwood kraft lignin. The MeOH washing removed MeOH soluble fraction and MeOH insoluble fraction showed increased molecular weight (Table 3). Due to the presence of large low molecular weight peak in SEC without LiBr in the as-received starting lignin (Figure 3a), the isolated yield of the MeOH insoluble residual lignin after 1st washing showed 17% yield and further washing was not performed. Due to the unrepeated MeOH extraction and the presence of more LMW fraction in the starting lignin resulted in PDI of 74.2 (9). The isolated yield observation agrees well with SEC data since the yield of MeOH insoluble residual lignin for the softwood kraft lignin after 4th washing was 50%. The significant heterogeneity of the Alcell lignin was also reported by Harton et al. (22) They used the exact same batch of Alcell lignin as our team used (Figure 3a and Table 3) and they reported somewhat rigid and complex molecular architectures of the Alcell lignin, ranging from nanogels to hyperbranched macromolecules. Also, their acetylated Alcell lignin showed molecular weight of ~3000 g/mol with PDI ~3 from RI detector, while electrospray ionization (ESI) mass spectrometry showed M_w ~18,000–30,000 g/mol. The direct comparison is not possible since the Alcell lignin was not analyzed with SEC in DMF LiBr in our previous study. However, the discrepancy of the molecular weight range between RI detector and absolute molecular weight from the ESI mass spectrometry is consistent with what we observed in the study for the softwood kraft lignin as discussed above.

In another study, Wang et al. reported the use of solvent fractionation of lignin to effectively separate lignin fractions based on their molecular weight (Figure 4) (33). The sequential extraction of Kraft-AQ (anthraquinone) lignin with hexane, ethylether, methylene chloride, methanol and dioxane produced lignin fractions with molecular weight (M_w) 490, 690, 1170, 2470 and 13700 g/mol (Table 5). Eang et al. suggested that the successful separation of the low molecular weight to high molecular weight fractions of Kraft-AQ lignin using various organic solvent, which was controlled by the hydrogen-bonding capacity of different solvents.

In the solvent fractionation of organosolv lignin, Thring et al. found the molecular weights decreased in the order $fraction_{insoluble} > fraction_{MeOH} > fraction_{diethylether}$ (Table 6). The highest molecular weight from the insoluble fraction is consistent with our observation (9, 25). Poor solvent for lignin, i.e. diethylether only dissolved low molecular weight of lignin probably because low molecular weight lignin is more susceptible to solubilization. Zhao et al. also performed the diethylether and methanol fractionation and found a similar trend. Although they did not report molecular weight, diethyl ether fraction contained the highest amount of water soluble lignin probably due to its low molecular weight (Table 7) (31, 32).

Table 5. M_w , M_n , and PDI of the lignin fractions from *Eucalyptus Pellita* derived Kraft-AQ lignin (33). [Adapted from reference (33)]

	<i>Lignin fractions</i>				
	<i>Hexane</i>	<i>Ethyl ether</i>	<i>Methylene chloride</i>	<i>Methanol</i>	<i>Dioxane</i>
M_w	490	690	1170	2470	13700
M_n	490	670	1010	1680	3050
M_w/M_n	1.00	1.03	1.16	1.47	4.47

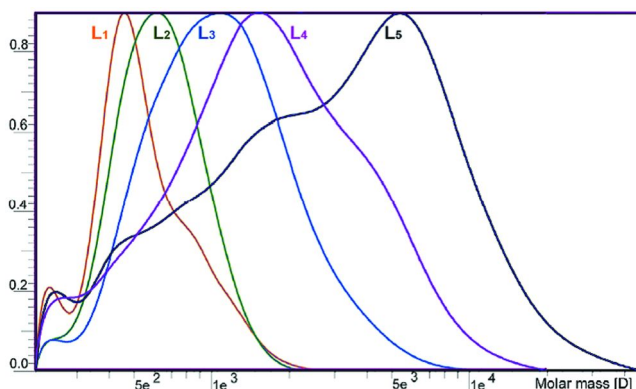


Figure 4. Molecular weight distributions for lignin fractions hexane (L_1), ethyl ether (L_2), methylene chloride (L_3), methanol (L_4) and dioxane (L_5) (33). [Reproduced from reference (33)].

Table 6. Fractionation of organosolv (Alcell) lignin by sequential solvent extraction (31, 36). [Adapted from references (31) and (36)]

<i>Lignin</i>	<i>Solvent</i>	<i>Yield (w/w, %)</i>	M_w^a (g/mol)	M_n^b (g/mol)
Fraction 1	Diethyl ether	27	720	480
Fraction 2	MeOH	53	2410	1040
Fraction 3	Insolubles	18	6950	2400
Original lignin		100	3300	900

^a Weight average molecular weight. ^b Number average molecular weight.

Table 7. Fractionation of organosolv (Alcell) lignin by sequential solvent extraction (3I). [Adapted from reference (3I)]

<i>Lignin</i>	<i>Solvent</i>	<i>Yield (w/w, %)</i>	<i>Water soluble lignin content^a (w/w, %) ± SD</i>
Fraction 1	Diethyl ether	17.5	39.1 ± 0.31
Fraction 2	MeOH	62.1	14.1 ± 0.13
Fraction 3	Insolubles	17.6	0.79 ± 0.05
Original lignin		100	16.5 ± 0.79

^a Values were recorded at 30°C.

Chemical Properties

Solvent fractionation of lignin separates its different parts based on their molecular weights and various bonding and non-bonding interactions with the solvents. These differentiations inevitably change some properties of lignin in each fraction.

During MeOH extraction of softwood kraft lignin (25), MeOH soluble fraction showed the lowest dn/dc value (Table 4), which suggested that its chemical compositions were most affected. In the same work, ^{13}C and ^{31}P NMR showed MeOH-soluble lignin contained more aliphatic carbon-carbon bonds than the MeOH-insoluble and the starting lignins (Table 8) (25). X-ray photoelectron spectroscopy also supported this result and showed the decrease of sp^2 carbon content and increase of sp^3 carbon content in the MeOH-soluble lignin. It was also found that the sp^2 carbon content increased and the amount of C-O-R groups decreased in MeOH-insoluble fraction (25). Higher sp^2 carbon and lower C-O-R group contents resulted in high char yield and higher T_g value of MeOH-insoluble lignin compared to the MeOH-soluble lignin (Table 9). Aliphatic groups facilitates free volume expansion and volatilization during heat treatment compared to aromatic groups (25). Thus, increase of aliphatic groups in a lignin fraction decreases the T_g and char yield. The NMR analysis also showed that MeOH-soluble lignin contained less amount of aliphatic hydroxyl groups that were mostly responsible for the formation of hydrogen-bonds. Thus, lowering of aliphatic hydroxyl groups further lowered the T_g of the MeOH-soluble extract.

Compared to the starting lignin, an increase in the amount of guaiacyl groups was observed in the MeOH-soluble lignin whereas a slight decrease was observed in case of MeOH-insoluble lignin. A higher phenolic content suggests the presence of higher number of chains or more depolymerised lignin. This explained the lower molecular weight and enhanced branched structure of MeOH-soluble lignin compared to the MeOH-insoluble lignin. During heating, guaiacyl types of groups volatilize more easily through the conversion of catechol structures by releasing methoxy groups. Thus, the presence of high amount of guaiacyl group in MeOH-soluble extract indicated that MeOH-soluble fraction would be more susceptible to volatilization and would form less char. NMR analysis of both MeOH-soluble and MeOH-insoluble lignins showed presence

of carboxylic acid groups and higher amount of C5 condensed units compared to the starting lignin. These properties resulted in lower thermal degradation temperature of these lignin extracts compared to the starting lignin.

Table 8. Hydroxyl group contents (mmol/g) of lignin calculated from ^{31}P NMR spectra (25). [Adapted from reference (25)]

Chemical Shift δ	Assignment	mmol/g Lignin		
		As-received	MeOH Insoluble	MeOH Soluble
150.0-145.5	aliphatic OH	1.71	1.68	1.24
136.6-144.7	phenols	3.43	3.45	4.21
140.0-144.7	C5 substituted "condensed" and syringyl	1.57	1.84	1.83
139.0-140.0	guaiacyl	1.45	1.23	2.04
138.2-139.0	catechol	0.28	0.25	0.22
137.3-138.2	<i>para</i> - hydroxyphenol	0.17	0.11	0.10
133.6-136.6	carboxylic acid OH	0.00	0.18	0.25
	total OH	5.15	5.31	5.70

Thermal Properties

Due to its aromatic structure, lignin is the most thermally stable material among lignocelluloses (33). While heating, the thermal degradation of lignin occurs in a stepwise manner. On heating from room temperature to 100-150°C, lignin first releases water vapor and other volatiles trapped in it. At around 150-300°C, cleavage of β -aryl ether linkages occurs. On further heating, around 300-400°C, fragmentation of aliphatic side chains and other carbon-carbon bonds of the lignin structure happens. Decomposition of lignin's aromatic structure occurs at 500-600°C. Generally, lignin fractions with high molecular weight have higher lignin degradation temperature than fractions with low lignin molecular weight.

Wang et al. observed the correlation of lignin's thermal stability and molecular weight in the fractionation of kraft AQ lignin (33). Among ethylether, methylene chloride, and methanol fractions of lignin, the thermal degradation temperature and the temperature of highest weight loss decreased in the order $fraction_{\text{MeOH}} > fraction_{\text{methylene chloride}} > fraction_{\text{ethylether}}$, which was the same as the decreasing order of the molecular weight. Similar influence of solvent fractionation was also observed in the fractionation of softwood kraft lignin with MeOH (25). MeOH-soluble lignin, due to its lower molecular weight, high sp^3 carbon content and low hydroxyl group content showed fast thermal degradation

(Figure 5a). The maximum of the decomposition derivative peak of its TGA curve located at 354 °C (Table 9). More importantly, the char yield (residual weight) at 1000 °C increased for MeOH insoluble lignin (47 wt%) and decreased for MeOH soluble lignin (32 wt%) from that of as-received starting lignin (41 wt%). The increase of char yield is highly beneficial in the application of lignin as a carbon precursor such as for carbon fibers and activated carbons. High char yield of MeOH insoluble lignin makes it valuable carbon precursor than low molecular weight MeOH soluble lignin. Interestingly, the char yield followed a linear regression with the area of LMW fraction obtained from SEC without LiBr (Figure 3b, Figure 5b). Considering an area of LMW fraction in SEC via RI intensity corresponds to the mass ratio, such a good fit with a linear regression indicates that the majority of the LMW fraction does not form char (25).

Table 9. T_g and thermal degradation properties of MeOH fractionated lignin (25). [Adapted from reference (25)]

	T_g (°C)	10 wt% weight loss (°C)	Derivative weight peak (°C)	Residual weight % at 1000 (°C)
As-received Lignin	153	301	384	41
MeOH Insoluble Lignin	211	293	362	47
MeOH Soluble Lignin	117	260	354	32
LMW Lignin Fraction	-89 ^a	-	-	-

^a Estimated from Fox equation.

In lignin-based material processing, T_g is one of the most important parameters. Thus, tunability of T_g is crucial for getting optimized properties in lignin materials. Fractionation of lignin offers the ability to alter the T_g of lignin. In the fractionation of softwood kraft lignin with MeOH (25), the T_g of the residual MeOH-insoluble part increased almost 50° C (211 °C) from the starting lignin (Table 9) (25). On the other hand, T_g of the MeOH-soluble lignin was decreased to 117 °C, which was lower than the starting lignin. This approximately 100 °C difference of T_g from the same batch of lignin indicates that lignin fraction with a desired T_g could be obtained by an application of a proper solvent in the fractionation. More importantly, the trend of these T_g values agrees very well with the Fox equation (25) (Figure 5b) using the LMW area from RI peaks converting to the weight fraction, which indicates that the LMW lignin oligomer fraction contributes to lowering its T_g , and the estimated T_g of LMW fraction from the Fox equation is -89 °C. The Fox-equation-derived T_g value of oligomeric lignin was so low that it justified the plasticization effect by the LMW lignin fraction (25). The extremely well correlation of char yield and T_g to LMW peaks (Figure 5b) from SEC without LiBr (Figure 3b) suggests that neat DMF SEC represents better for lignin properties. This statistical analysis of correlation also suggests that DMF SEC without LiBr might enable its use as one of the diagnostic tool to identify heterogeneities existing in lignin and correlates to its T_g and char yield.

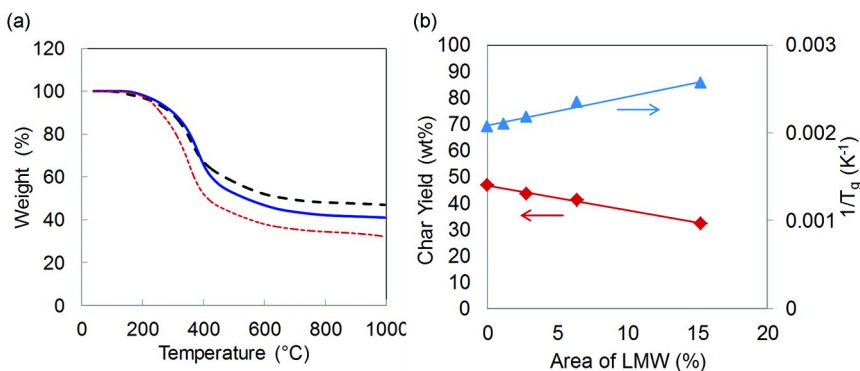


Figure 5. (a) TGA curves of as-received lignin (blue solid line), MeOH insoluble lignin (black dashed line), and MeOH soluble lignin (red dashed line), (b) The linear regression of char yield and $1/T_g$ as a function of LMW fraction from the SEC curve (25). [Adapted from reference (25)].

Conclusions

The use of lignin to make carbonaceous materials that fulfill consumer needs and maximize the environmental sustainability is rapidly developing. However, several challenges remain in associated with processing of lignin materials. The majority of lignin materials are prepared using melt-processing and thus, tuning thermal properties is very crucial. Solvent fractionation gives the ability to generate lignins with optimized thermal properties. In solvent fractionations of lignin, various interactions with the solvent used in the fractionation isolate lignin of completely altered properties. The solvent fractionation also enables separating lignin with respect to the molecular weights. As previously discussed, the detailed study of MeOH-based solvent fractionation revealed that efficient separation of low molecular weight lignin from high molecular weight lignin and could correlate to various other physical properties of lignin. In general, lignin fraction with higher molecular weight generates high amount of char and high T_g . Thus, solvent fractionation is very useful to make products like lignin carbon fiber where high char yield is beneficial. Moreover, empirical correlation in SEC data to char yield and T_g could suggest that lignin properties can be predicted based on one of the analyses such as SEC and the method can potentially produce lignin fraction with exact target properties.

Acknowledgments

This research was sponsored by the Laboratory Directed Research and Development Program of Oak Ridge National Laboratory, managed by UT-Battelle, LLC, for the U. S. Department of Energy.

References

1. Riaz, U.; Ashraf, S. M. In *Lignin Properties and Applications in Biotechnology and Bioenergy*, 1st ed.; Paterson, R. J., Ed.; MNova Science Publishers, Inc.: New York, 2012; pp 69–137.
2. Zakzeski, J.; Bruijninx, P. C. A.; Jongerius, A. L.; Weckhuysen, B. M. *Chem. Rev.* **2010**, *110*, 3552–3599.
3. Chatterjee, S.; Clingenpeel, A.; McKenna, A.; Rios, O.; Johs, A. *RSC Adv.* **2014**, *4*, 4743–4753.
4. Wang, S.-X.; Yang, L.; Stubbs, L. P.; Li, X.; He, C. *ACS Appl. Mater. Interfaces* **2013**, *5*, 12275–12282.
5. Gellerstedt, G.; Henriksson, G. In *Monomers, Polymers and Composites from Renewable Resources*, 1st ed.; Belgacem, M. N., Gandini, A., Eds.; Elsevier: Amsterdam, The Netherlands, 1998; pp 201–224.
6. Chatterjee, S. *Biofuels* **2013**, *4*, 571–573.
7. Bhattacharya, P.; Steele, P. H.; Hassan, E. B. M.; Mitchell, B.; Ingram, L.; Pittman, C. U., Jr. *Fuel* **2009**, *88*, 1251–1260.
8. Dhillon, G. S.; Gassara, F.; Brar, S. K.; Verma, M. In *Lignin Properties and Applications in Biotechnology and Bioenergy*, 1st ed.; Paterson, R. J., Ed.; Nova Science Publishers, Inc.: New York, 2012; pp 1–34.
9. Saito, T.; Brown, R. H.; Hunt, M. A.; Pickel, D. L.; Pickel, J. M.; Messman, J. M.; Baker, F. S.; Keller, M.; Naskar, A. K. *Green Chem.* **2012**, *14*, 3295–3303.
10. Lora, J. In *Monomers, Polymers and Composite from Renewable Resources*, 1st ed.; Belgacem, M. N., Gandini, A., Eds.; Elsevier: Amsterdam, The Netherlands, 2008; pp 225–241.
11. Cateto, C. A.; Barreiro, M. F.; Rodrigues, A. E.; Brochier-Salon, M. C.; Thielemans, W.; Belgacem, M. N. *J. Appl. Polym. Sci.* **2008**, *109*, 3008–3017.
12. Luo, J.; Genco, J.; Cole, B.; Fort, R. *BioResources* **2011**, *6*, 4566–4605.
13. Baker, D. A.; Gallego, N. C.; Baker, F. S. *J. Appl. Polym. Sci.* **2012**, *124*, 227–234.
14. Braun, J. L.; Holtman, K. M.; Kadla, J. F. *Carbon* **2005**, *43*, 385–394.
15. Sudo, K.; Shimizu, K. *J. Appl. Polym. Sci.* **1992**, *44*, 127–134.
16. Kadla, J. F.; Kubo, S.; Venditti, R. A.; Gilbert, R. D.; Compere, A. L.; Griffith, W. *Carbon* **2002**, *40*, 2913–2920.
17. Serrano, L.; Toledano, A.; Garcia, A.; Labidi, J. In *Lignin Properties and Applications in Biotechnology and Bioenergy*, 1st ed.; Paterson, R. J., Ed.; MNova Science Publishers, Inc.: New York, 2012; pp 139–182.
18. Bhattacharya, P.; Penmetsa, V.; Steele, P.; Mitchell, B. *J. For. Prod. Ind.* **2013**, *2*, 47–57.
19. Bozell, J. J.; Chatterjee, S. International Patent Application WO2013036911 A1, 2013.
20. *Biotechnological Application of Lignin: Sustainable Alternative to Non-Renewable Materials*; 1st ed.; Dhillon, G. S., Gassara, F., Brar, S. K., Verma, M., Eds.; Nova Science Publishers, Inc.: New York, 2012; pp 1–34.

21. Bozell, J. J.; O'Lenick, C. J.; Warwick, S. *J. Agric. Food Chem.* **2011**, *59*, 9232–9242.
22. Harton, S. E.; Pingali, S. V.; Nunnery, G. A.; Baker, D. A.; Walker, S. H.; Muddiman, D. C.; Koga, T.; Rials, T. G.; Urban, V. S.; Langan, P. *ACS Macro Lett.* **2012**, *1*, 568–573.
23. Heitner, C.; Dimmel, D.; Schmidt, J. A., Eds.; *Lignin and Lignans*; CRC Press: Boca Raton, FL, 2010.
24. Saito, T.; Perkins, J. H.; Jackson, D. C.; Trammel, N. E.; Hunt, M. A.; Naskar, A. K. *RSC Adv.* **2013**, *3*, 21832–21840.
25. Saito, T.; Perkins, J. H.; Vautard, F.; Meyer, H. M.; Messman, J. M.; Tolnai, B.; Naskar, A. K. *ChemSusChem* **2014**, *7*, 221–228.
26. Sarkanen, S.; Teller, D. C.; Hall, J.; McCarthy, J. L. *Macromolecules* **1981**, *14*, 426–434.
27. Toledano, A.; Serrano, L.; Balu, A. M.; Luque, R.; Pineda, A.; Labidi, J. *ChemSusChem* **2013**, *6*, 529–536.
28. Pan, X.; Gilkes, N.; Kadla, J.; Pye, K.; Saka, S.; Gregg, D.; Ehara, K.; Xie, D.; Lam, D.; Saddler, J. *Biotechnol. Bioeng.* **2006**, *94*, 851–836.
29. Thring, R. W.; Chornet, E.; Overend, R. P. *Fuel* **1993**, *72*, 1355–1356.
30. Vanderlaan, M. N.; Thring, R. W. *Biomass Bioenergy* **1998**, *14*, 525–531.
31. Zhao, J.; Wilkins, R. M. *J. Agric. Food Chem.* **2000**, *48*, 3651–3661.
32. Zhao, J.; Wilkins, R. M. *J. Agric. Food Chem.* **2003**, *51*, 4023–4028.
33. Wang, K.; Xu, F.; Sun, R. *Int. J. Mol. Sci.* **2010**, *11*, 2988–3001.
34. Pas, D. v. d.; Hickson, A.; Donaldson, L.; Lloyd-Jones, G.; Tamminen, T.; Fernyhough, A.; Mattinen, M. L. *BioResources* **2011**, *6*, 1105–1121.
35. Thielemans, W.; Wool, R. P. *Biomacromolecules* **2005**, *6*, 1895–1905.
36. Thring, R. W.; Vanderlaan, M. N.; Griffin, S. L. *J. Wood Chem. Technol.* **1996**, *16*, 139–154.

Chapter 8

Pyrolysis and Thermal Stability of Carbon Fiber Polymer Precursors with Different Microstructures

G. Santhana Krishnan*

Materials Science Division, CSIR-National Aerospace Laboratories,
Bangalore-560017, India

*E-mail:santhana@nal.res.in

Acrylonitrile based polymers have emerged as one of the preferred precursors for the production of high tensile carbon fibers. The salient feature of the poly(acrylonitrile) is that it is not stable upto its melting point and tends to decompose prior to melting with sudden release of heat and gas. Therefore it is important to control this thermal degradation and exotherm which is determinant in tensile characteristics of resulting carbon fibers. In this account, the influence of triad tacticity of poly(acrylonitrile) microstructure on the structural changes during the thermal oxidative degradation reactions was investigated applying hyphenated thermal techniques namely Pyrolysis-Gas Chromatography-Mass spectrometry, Evolved gas analysis-Mass Spectrometry, and thermal gravimetric analyzer-FT infrared spectrometry(TGA-FTIR) in the temperature range 200-600°C. The thermal analysis results revealed that nitrile polymerization of pendant cyano functionalities precedes cyclization reaction in case of isotactic rich poly(acrylonitrile) leading to a steady and stable thermal oxidative degradation reaction as compared to atactic rich poly(acrylonitrile). The mass loss accompanying the thermal reactions was accounted for the evolution of hydrogen cyanide, ammonia, and homologs of alkyl nitrile having molar masses between 47 and 147 m/z. The simultaneous TGA-FTIR results of evolved gas analysis also confirm the pyrolysis experimental data.

Introduction

Poly(acrylonitrile) (PAN) based carbon fibers are recognized as a critical part of modern aviation and aerospace applications. They constitute primary, secondary structures of commercial aircrafts, the international space station, satellites, rocket motor casings and expendable launch vehicles. Because of their high specific tensile properties, compressive strength, and increased resistance to corrosion under saline conditions, their use is being extended to other civil applications such as compressed natural gas tanks, anti-seismic reinforcing members of buildings and tethers in oil field rigs apart from traditional domains (1–5). These high tensile carbon fibers (Tensile strength higher than 4.0 GPa) enable the fabrication of light weight, durable, and cryogenic high pressure vessels for storage of compressed hydrogen gases in space launch vehicles (6–8). This kind of trend necessitate further understanding and continuous improvements to the physical characteristics of carbon fiber polymer precursors.

The industrial production of high tensile grade carbon fiber includes polymer synthesis, fiber spinning, thermal oxidative stabilization, and carbonization (9). The tensile properties of carbon fiber are highly sensitive to the internal and surface flaws such as voids and defects (10). Hiramatsu Touru studied the dependence of tensile strength of carbon fiber on the sizes of defects and voids formed during their production and reported that the surface defect sizes vary from 2.5μ to less than 0.5μ as tensile strength of carbon fiber filament increases to a value higher than 4.0 GPa (11). Therefore the control of formation of defects and voids becomes significant during the manufacture of high tensile grade carbon fibers. One of the critical stages in the carbon fiber fabrication process is the thermal oxidative stabilization, which involves controlled heat treatment of carbon fiber precursor fiber made of PAN in air at temperatures in the range 200 to 300 °C.

Further in the carbonization process, the stabilized fibers are further heated to the temperature up to 3000°C. There exists a trade-off relationship among the density of the oxidized PAN fibers and the subsequent heat treatment temperature and tensile characteristics (12, 13). Figure 1a and b shows the variation of density of PAN fiber precursor during the stabilization process and its influence on the change of limiting oxygen index (14). The high density oxidized PAN fiber leads to a defect free aromatic structure which facilitates the improvement of tensile characteristics in the carbon fibers.

The physical characteristics of high tensile carbon fibers with tensile strength above 6000 MPa, is known to depend critically on the surface and internal defects of fiber precursors (14, 15). The carbon fiber failure follows a brittle failure mechanism as predicted by the Griffith model. This model relates the surface free energy of the fracture surface formed on the surface of carbon fiber filament to its breaking strength (16). The Griffith equation is represented as in eq 1.

$$\sigma = (2\varepsilon / \pi C)^{1/2} \times \gamma^{1/2} \quad (1)$$

Here, “ σ ” is the breaking strength; “ ε ”, the ultrasonic elastic modulus of the carbon fiber filament; and the ‘C’ is the size of the flaw or defect.

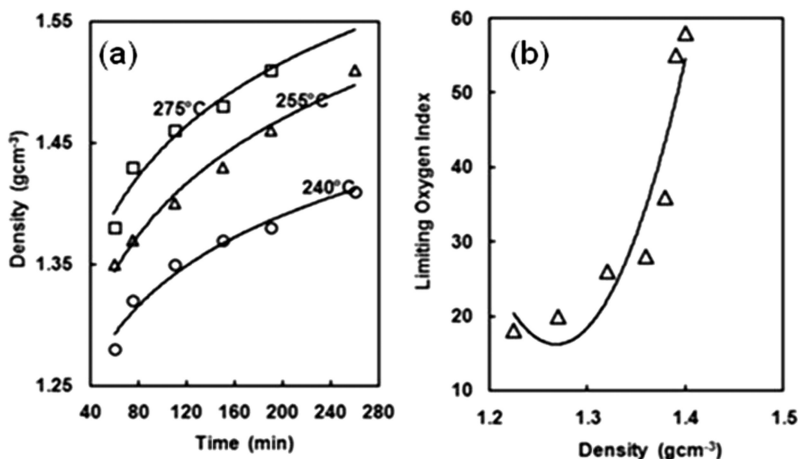


Figure 1. (a) Variation of PAN fiber density with thermal stabilization time, (b) Limiting Oxygen index of oxidized PAN fibers plotted against oxidized PAN fiber density. Source: Drawn from unpublished experimental data.

In general, every single filament of a carbon fiber strand has uneven surface structure with a length greater than $0.7 \mu\text{m}$. These kind of surface flaws have an assembly of several fibrils extending along the longitudinal axis of the fiber tow known as wrinkle structures. One of the several strategies of the strength improvement mechanisms in the carbon fiber manufacture is to prevent the formation of surface flaws, both internal as well as external. If the sizes of these flaws or defects are on the order of $0.6 \mu\text{m}$ or less, the tensile strength of the carbon fiber tow is more likely to be improved. The other commonly adopted method is to develop a highly dense structure of the oxidized PAN fiber with a density to a level in excess of 1.35 gcm^{-3} , wherein the defect point formation is suppressed. The thermal oxidative stabilization of PAN fiber precursor before precarbonization is carried out to endure the high temperature treatment. The oxidative stabilization process offers many scopes for the optimization of the quality of resulting carbon fibers in terms of tensile characteristics. This process is usually accompanied by the release of gaseous molecules such as ammonia, hydrogen cyanide, and oxides of carbon in substantial quantities, leading to the formation of large sized surface defects, thereby reducing the tensile strength of the subsequently obtained carbon fibers.

Erich Fitzer observed that tensile properties of carbon fibers are heavily influenced by the release of gases during the heat treatment processes up to 1800°C (17). Various techniques of thermal analysis, such as differential thermal analysis (DTA), thermogravimetry (TG) and differential scanning calorimetry (DSC) have become more and more conventionally used for thermal characterization studies of fiber forming high polymers. However, these techniques do not provide direct information on the qualitative and quantitative changes accompanying thermal degradation or cyclization reactions as the method lacks the capability of structural identification. Many research articles discussed the thermal degradation behavior and stability of acrylonitrile based copolymers with different monomers

(18–25). Grassie and McGuachan investigated the thermal degradation of PAN giving particular attention to the influence of environment, additives and comonomers on the overall process using conventional thermal techniques (26). This chapter describes the beneficial influence of microstructure, in terms of the triad tacticity content of cyano functionalities of poly(acrylonitrile) on their thermal degradation behavior. The detailed thermal investigations were performed applying hyphenated thermal techniques such as Pyrolysis-Gas chromatography-Mass spectrometry (Py-GC-MS), Evolved gas analysis-Mass spectrometry (EGA-MS), and TGA-FTIR, in addition to the confirmation of stereochemical configuration of PAN polymers.

Synthesis of Poly(acrylonitrile) with Different Microstructures

Materials

Acrylonitrile, (AN) (Sigma Aldrich), was used as monomer in the polymer synthesis. Acrylonitrile was washed with a sodium hydroxide solution of concentration 0.5 wt. % and distilled at its boiling range just before polymerization to remove the inhibitor content if any. The hexagonal crystalline metal salts (Nickel chloride or Magnesium chloride) (Sigma Aldrich) was used as a template compound in the solid state polymerization techniques. Commercially available α , α azoisobutyronitrile (AIBN) (Wako Co.) was used as initiator after crystallization in methanol. Analytical grade dimethylformamide, dimethyl sulphoxide and dimethyl acetamide (Sigma Aldrich) were used for the measurements of polymer solution properties.

Synthesis of Isotactic Poly(acrylonitrile) (I-PAN) and Atactic Poly(acrylonitrile) (A-PAN)

Polymerization experiments were carried out in a 500 mL three-necked round bottom flask, equipped with mechanical stirrer and a reflux condenser. The flask was bubbled with ultra-pure N₂ gas for 30 min at a flow rate of 30 mL/min. to ensure an oxygen-free atmosphere. The polymerization procedures as described in references were followed for the synthesis of I-PAN and A-PAN (27, 28). The resulting polymer was filtered and washed with methanol and dried at 60°C under vacuum to a constant mass.

Molecular Characterizations

Average Molecular Weight Determinations

Solution Capillary Viscometry

Solution viscometry is one of the simplest and elegant methods of molecular weight determination techniques. It also provides considerable insight on physical

characteristics of polymer molecules. Sufficient amount of PAN sample was dried in an oven at 75°C for 3h and dissolved in dimethyl sulphoxide at 50 °C. The flow time of the obtained solution between gauge marks is measured at an accuracy of 1/100 seconds using Ubbelohde viscometer at a temperature of 25°C. The measured dropping time is expressed as t (sec). Similarly the dropping time of dimethyl sulphoxide (DMSO) is expressed as t₀. Intrinsic viscosity (η) was obtained according to the following eq (2) using the data in the concentration range from 0.1 to 0.5g/dl (29).

$$[\eta] = \left\{ (1.44 \times \eta_{sp} + 1) \right\}^{1/2} - 1 / 0.36 \quad (2)$$

Where $\eta_{sp} = t/t_0 - 1$. The viscosity average molecular weight of PAC was calculated by eq (3) (30).

$$[\eta] = 3.35 \times 10^{-4} [M_v]^{0.72} \quad (3)$$

Membrane Osmometry

Membrane osmometry is one of the established primary methods for the determination of number average molecular weight of polymer molecules. Osmotic pressure (Π) measurements of polymer solutions were carried out in the range of polymer concentration (C) from 0.3 to 0.9 g/dl in DMSO at 60°C with Osmomat 090, Gonotec GmbH. Asymmetric two-layer cellulose triacetate membranes, with a diameter of 40 mm and a molecular weight cut off (MWCO) of 5,000 or 20,000 g/mol (type SM 14549, Sartorius GmbH, Gottingen, Germany), were used. Number average molecular weight (M_n) was obtained as Π/C extrapolated to C = 0 according to eq (4).

$$\lim_{C \rightarrow 0} \Pi C^{-1} = RT (M_n^{-1}) + A_2 C \quad (4)$$

Where R is gas constant.

Size Exclusion Chromatography (SEC)

The chromatography parameters (average molecular weights, molecular weight distribution (Mw/Mn)) were determined by SEC-TDA max instrument of Malvern Viscotek TDA 305 (Triple Detector Array) equipped with I-MBHMW-3078 column, a differential refractometer, a precision low angle light scattering detector, and a viscometer. The molecular weight parameters were computed using SEC data processing system (OmniSEC software). The carrier solvent was DMF containing 0.05 M lithium bromide with a flow a rate of 1 mL/min and injection volume of 100µL at 50 °C. A concentration of ~4mg/ml was

maintained in all samples. Before the injection, samples were filtered through a PTFE membrane with 0.2 μ m pore. A set of polymethyl methacrylate standards of narrow molecular weight distribution (PolyCALTM, Viscotek, US) of molecular weight 2.0×10^4 - 4.51×10^5 g/mol was used to generate conventional calibration curve.

¹³C Nuclear Magnetic Resonance Spectroscopy (¹³C NMR)

The ¹³C NMR (Bruker AMX-400) spectra of the polymers were recorded in deuterated DMSO using tetramethylsilane (TMS) as an internal standard. Samples were concentrated in dimethyl sulphoxide about 5% (w/w) for ¹³C NMR by using a 5 mm NMR tube at room temperature. ¹³C NMR spectra were acquired using 24996 data points, spectral width 22 kHz, broadening 3 Hz, pulse delay 2s, pulse width 90°, and 1024 scans. Nuclear overhauser effect (NOE) was suppressed by gating the decouple sequence. Heteronuclear multiple quantum coherence (HMQC) was performed by using the standard Bruker pulse sequence with a pulse program. The spectrum was obtained with 256 increments in the F1 dimension and 1024 data points in the F2 dimension, with 200 scans and relaxation delay 1.5.

Thermal Characterizations

Pyrolysis-Gas Chromatography-Mass Spectrometry

The configuration of Py-GC/MS as developed by Chuichi Watanabe et.al. (31), was employed for the evaluation of thermal -oxidative degradation of the polymer samples under investigation. A small amount of powdery sample was taken in a deactivated stainless steel sample cup and then mounted in to the pyrolyzer. The multifunctional pyrolyzer EGA/PY-3030D model (Frontier Laboratories, Japan) which is capable of heating a sample from near room temperature to 800 °C. In single shot pyrolysis, the column was first hold at 40 °C for 2 min. and heated at 20 °C /min. to 320 °C and hold there for 14 min. The pyrolysis temperature was 700 °C at a heating rate 20°C /min. Evolved gases released during the heat-up was directly separated and analyzed by the GC/MS (GC-MS-QP2010, GC-MS ITF temp.280°C, m/z: 27-600 IS temp.: 200). The remaining residue in the sample cup was analyzed on the same system by EGA-MS single shot analysis. In the GC-MS system, the evolved gas mixture was continuously introduced to the sample loops and separated in to the constituents by the chromatographic column. The carrier gas is removed by the separator and only the components to be determined are introduced directly in to the mass spectrometer to obtain mass spectrum. The pattern of thermal degradation and the structural changes accompanying degradation were estimated from the obtained thermogram and pyrograms.

TGA-Fourier Transform Infrared Spectrometry

The analysis of evolved gases from polymer samples was carried out using a hyphenated system of the TGA 4000/ Pyris 6 (Perkin Elmer) coupled to a frontier FT IR spectrometer. The typical analysis conditions are as follows: wave number, 400-4000 cm^{-1} , resolution, 2 cm^{-1} ; purging gas, N_2 (flow rate, 20 mL/min). Heating rate, 20 $^\circ\text{C}$, Temperature range, 40 to 650 $^\circ\text{C}$. Specimen mass 12.00 mg.

Molecular Characteristics and Microstructural Elucidation

The reaction scheme as in Figure 2 shows the synthetic routes followed for the preparation of PAN polymers with predominantly isotactic and atactic stereo-structures. Different types of molecular weight averages such as viscosity average, number average and weight average molecular weights were estimated with solution viscometry, membrane osmometry and SEC-TDAmx system.

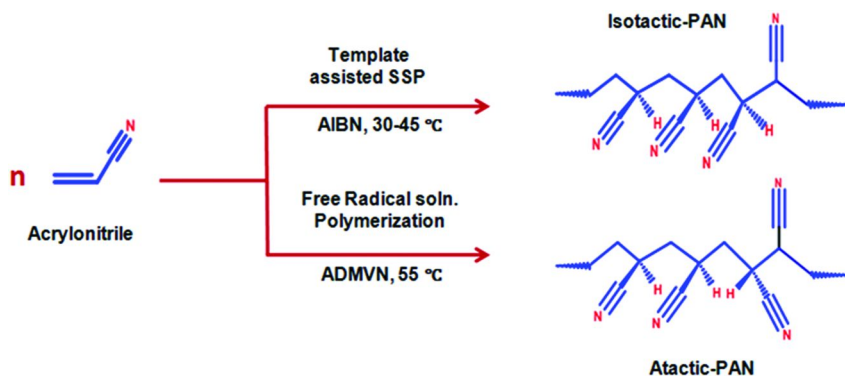


Figure 2. Synthesis pathways for poly(acrylonitrile) with different microstructures.

Figure 3 shows the elution curves generated using SEC triple detector system. The retention volumes observed for the PAN polymer samples ranges from 7.6 to 8.1 mL, the different molecular weight averages of the I-PAN and A-PAN under study is given in Table I. The number and weight average molecular weights of the PAN samples are $10.2\text{-}14.3 \times 10^4$ and $1.61\text{-}2.25 \times 10^5$, respectively.

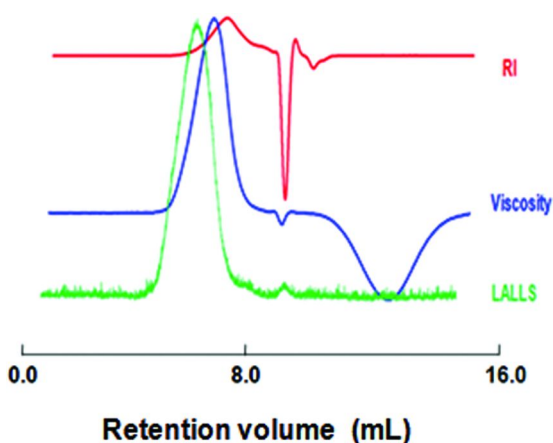


Figure 3. The SEC triple detector elution curves for PAN samples.

Table I. Different molecular weight averages of I-PAN and A-PAN under study

Sample ID	$M_v^a \times 10^{-5}$ ($g\text{mol}^{-1}$)	$M_n^b \times 10^{-4}$ ($g\text{mol}^{-1}$)	$M_n^c \times 10^{-4}$ ($g\text{mol}^{-1}$)	$M_w^c \times 10^{-5}$ ($g\text{mol}^{-1}$)
I-PAN/01	2.21	10.2	9.8	2.25
I-PAN/02	2.06	14.3	12.3	2.13
I-PAN/03	1.76	11.2	10.7	1.83
A-PAN/01	1.86	12.7	11.1	1.92
A-PAN/02	1.69	13.6	12.8	1.72
A-PAN/03	1.57	13.9	12.4	1.61

a = Solution viscometry, b = membrane Osmometry, c = SEC I-PAN = Isotactic Poly(acrylonitrile), A-PAN = Atactic poly(acrylonitrile) samples.

The stereoregularities in terms of triad tacticity contents were estimated using ^{13}C -NMR spectroscopic techniques. ^{13}C -NMR spectra of I-PAN and A-PAN are shown in Figure 4a and b. Triad tacticity contents were estimated from the intensities of methine carbon functionality observed at a chemical shift value of 26.50-28.00 ppm. Only methine carbon regions are expanded in Figure 5a and b (bottom). Stereochemical features of vinyl polymer systems are often calculated in terms of triad tacticity (32, 33). The measurement of tacticity in polymers is an area characterization. The areas corresponding to three bands, viz., syndiotactic A(rr), atactic A(mr), and isotactic A(mm) are estimated. The number fraction of each type of triad (mm),(mr), and(rr) is then obtained by dividing the area of each individual band by total area A(T). The triad tacticity contents of I-PAN and A-PAN used in this study are presented in Table II. The I-PAN synthesized was found to have a isotactic content of maximum 51.4 wt. % whereas atactic triad tacticity of A-PAN was 48.5 wt. %.

Table II. Triad tacticity contents of I-PAN and A-PAN

<i>Sample Code</i>	<i>Chemical Shift (ppm)</i>			<i>Triad tacticity (%)</i>			
	<i>mm</i>	<i>mr</i>	<i>rr</i>	<i>I</i>	<i>A</i>	<i>S</i>	<i>4IS/A²</i>
I-PAN/01	26.77	27.39	27.86	51.4	33.9	14.7	2.629
I-PAN/02	26.76	27.39	27.85	50.1	35.6	14.3	2.261
I-PAN/03	26.75	27.37	27.90	48.7	36.2	15.1	2.214
A-PAN/01	26.76	27.36	27.86	26.4	48.5	25.1	1.121
A-PAN/02	26.76	27.37	27.84	28.1	47.0	24.9	1.245
A-PAN/03	26.74	27.39	27.88	29.7	46.2	24.1	1.232

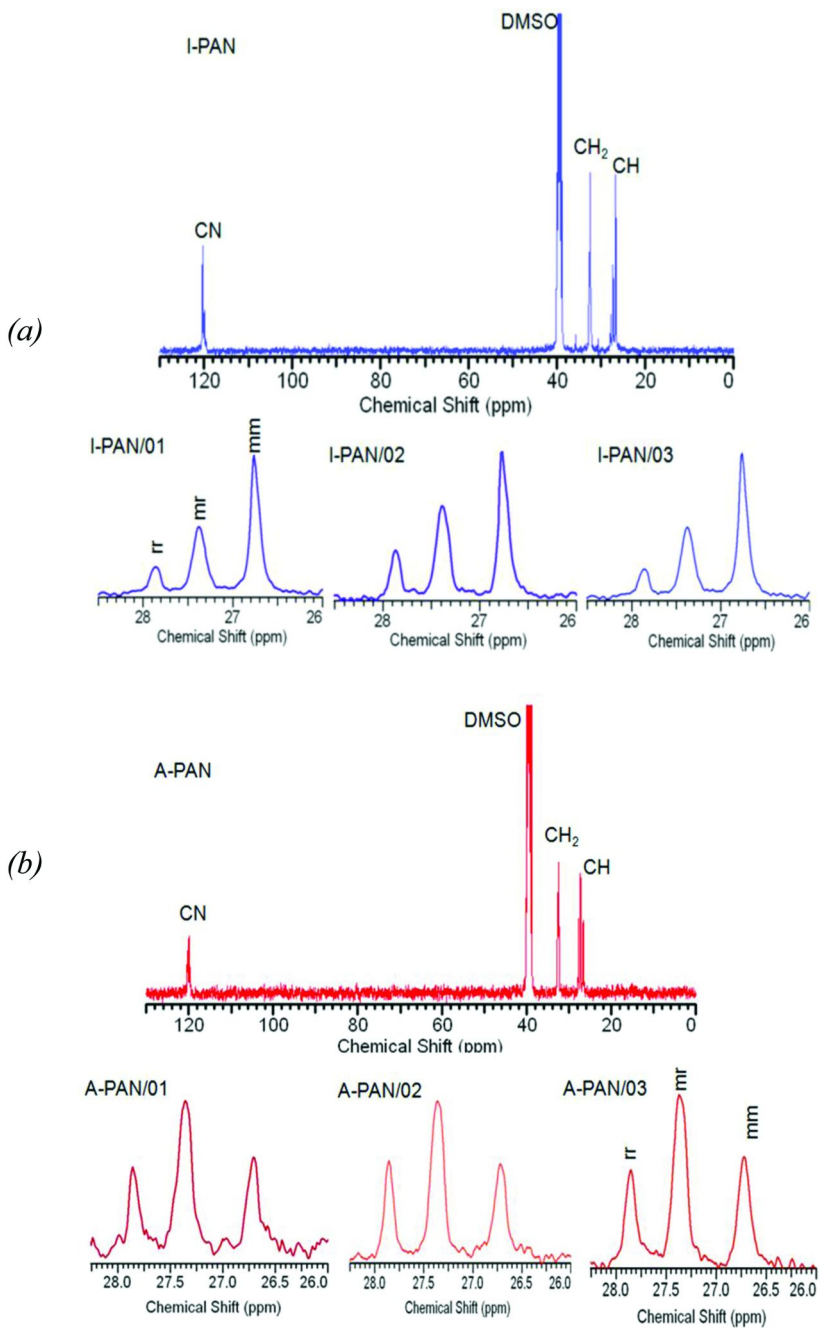


Figure 4. ^{13}C -NMR spectra of (a) I-PAN (above) and (b) A-PAN (below).

Pyrolysis and Thermal Stability

The EGA-MS curves of total ions of the A-PAN (bottom), and I-PAN (top) are shown in Figure 5. The A-PAN (bottom) curve displays two peaks with maxima 280 and 440 °C, respectively. There exists two humps at 140 and 360 °C, thereby clearly forming four distinct regions of thermal degradation. From the results of EGA-MS, the pyrolysis temperatures of A-PAN in Pyrolysis-GC/MS can be set at 150,180,260,280,300,320,380,400,450, and 500 °C. However, the EGA thermogram of the I-PAN clearly shows a peak at 320 °C and a shoulders at 380 and 420 °C. Table III summarizes the results of identification of the peaks corresponding to the specific mass to charge ratios in the mass spectrum. Most gaseous species evolved are identified as ammonia, hydrogen cyanide and alkyl nitrile compounds.

Table III. Identification of pyrolysates from Py-GC-MS

<i>m/z</i> value	<i>Molecular formula</i>	<i>Ionic abundance (%)</i>	
		<i>A-PAN</i>	<i>I-PAN</i>
28	HCN	70	40
41	CH ₃ CN, C ₃ H ₅ , C ₂ H ₃ N	75	50
54	(C ₂ H ₃ CN)H	70	45
80	(C ₂ H ₄ CN)C ₂ H ₃	10	30
107	(C ₂ H ₃ CN) ₂ H	45	25
121	(C ₂ H ₃ CN) ₂ CH ₃	25	20

Figures 6 and 7 show the averaged mass spectra of the evolved gases corresponding to the four different regions i.e., α , β , δ , θ , in the A-PAN and I-PAN. In general, the molecular ion peaks of straight-chain alkyl nitriles are either weak or absent except acetonitrile. The base peak of linear nitriles between C4 and C9 is m/z 41. This peak arises as a result of hydrogen rearrangement in a six membered transition state. The thermal degradation mechanism as in reaction scheme (Scheme 1) accounts for formation of some of the diagnosable ionic fractions in the mass spectrum. The relative ionic abundance of evolved gases generated during thermal degradation are higher (>65%) for A-PAN as compared to that of I-PAN (<50%) suggesting a large extent of weight loss due to the thermal degradation reaction in A-PAN during the process. This demonstrates a distinct degradation behavior exhibited by the I-PAN due to higher isotactic triad content.

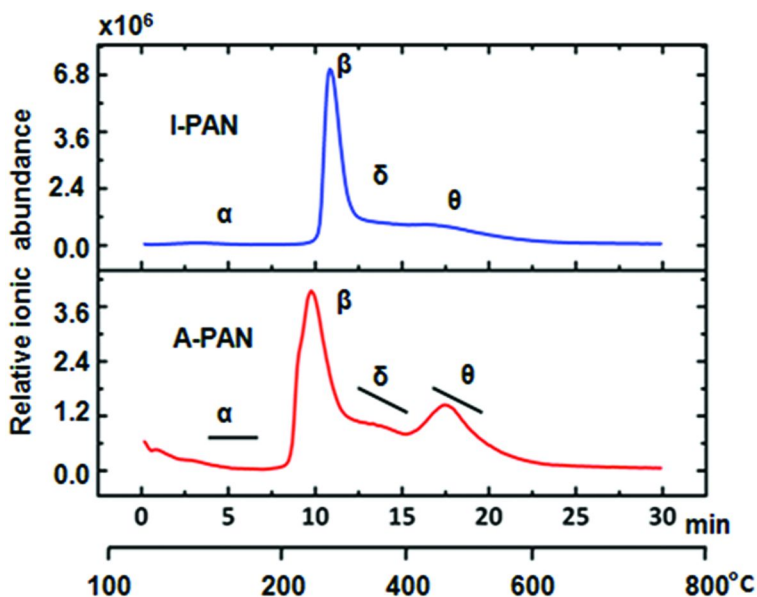
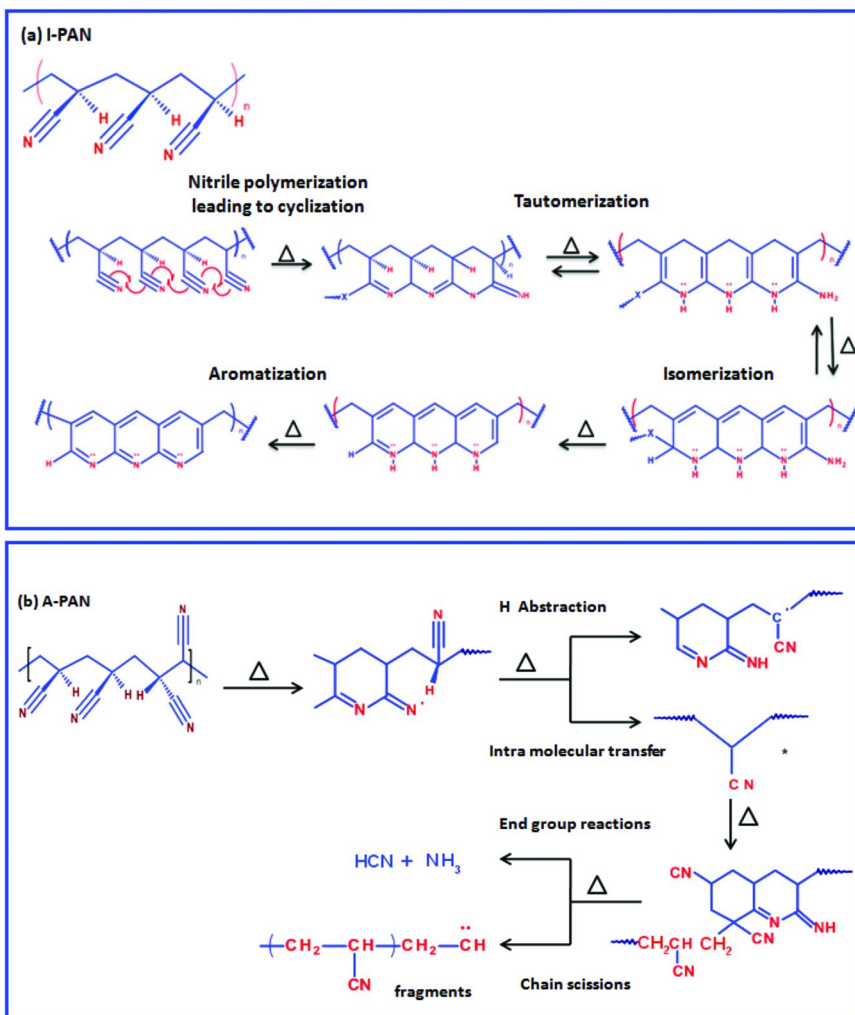


Figure 5. The EGA-MS curves of total ions of the I-PAN and A-PAN.

The total ion current curve (TIC) is a graphical representation of the variation of total ion intensity in terms of ionic abundance as a function of temperature. The TIC spectra of A-PAN and I-PAN obtained using single shot pyrolysis techniques are shown in Figures 8 and 9. The pyrolysates at 320 °C are found to be higher homologs of alkyl nitriles with increased retention time in the pyrogram. The ionic abundance corresponding to the relative intensity of gaseous pyrolysates is generally higher for A-PAN i.e. in the order of 7.4×10^5 as compared to 6.9×10^5 of I-PAN and more number of peaks in TIC of A-PAN suggesting higher and abrupt release of gaseous pyrolysates during thermal degradation.

The thermal degradation behavior of acrylonitrile based polymers with different triad tacticity contents were also studied using TGA-FTIR. In the TGA-FTIR experiments, spectral data of evolved gaseous species as a function of time and temperature are recorded as interferograms and then processed to construct Gram-Schmidt plots (GS Plot) (34). Every point in the GS plot corresponds to the total infrared absorbance of the evolving gaseous components during thermal degradation in the range 400-4000 cm^{-1} . The graphs also represent the intensity of infrared absorption accompanying weight loss due to the thermal degradation reactions in the temperature range 140-640 °C. Thus, the total absorbance intensity of mass loss at each stage is a function of the concentration of evolved gaseous decomposition components and their infrared extinction coefficients i.e., The TGA-FTIR spectra of I-PAN and A-PAN are shown in Figures. 10 and 11. As can be seen, the I-PAN sample exhibited two distinct thermal degradation stages ca. 320 and 450 °C and a small minor degradation at 410 °C. The mass losses corresponding to the first and second stages are ca. 55 and 40%, respectively. In the left hand side of the plot, the total absorbance intensity of evolved gaseous species at 320 and 410 °C are shown.



Scheme 1. The thermal degradation reaction mechanisms in (a) I-PAN and (b) A-PAN.

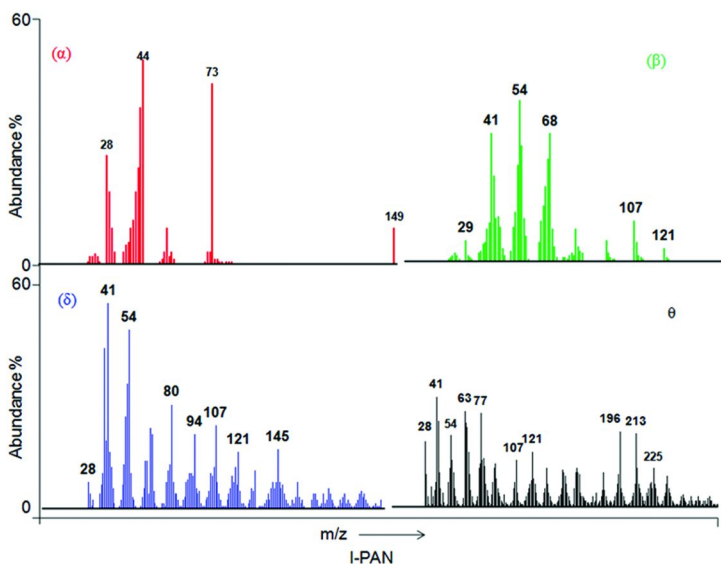


Figure 6. The averaged mass spectra of the evolved gases corresponding to the four different regions, i.e., α , β , δ , θ , in I-PAN.

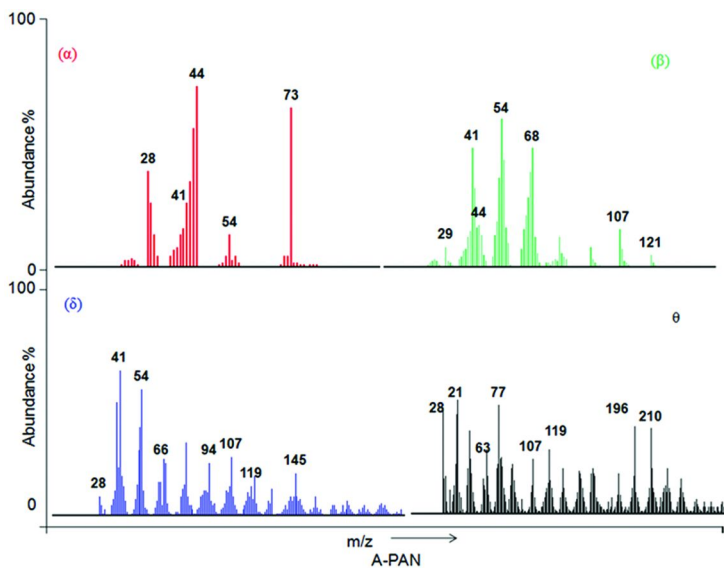


Figure 7. The averaged mass spectra of the evolved gases corresponding to the four different regions, i.e., α , β , δ , θ , in A-PAN.

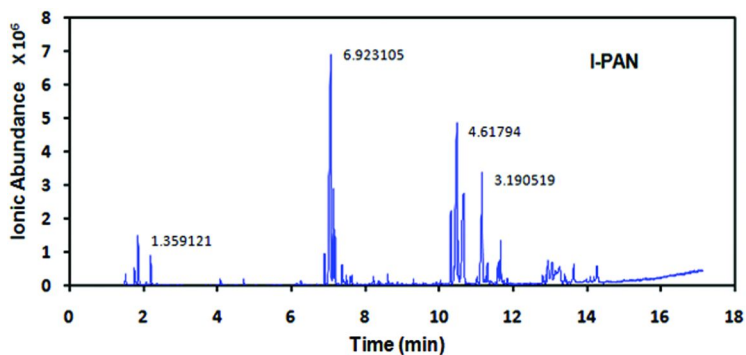


Figure 8. The TIC spectra of I-PAN.

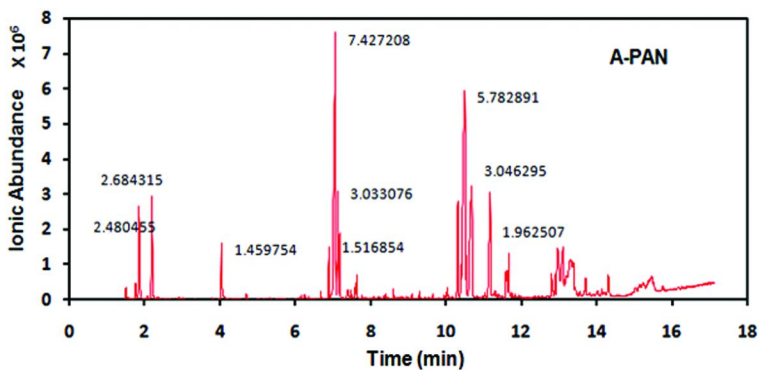


Figure 9. The TIC spectra of A-PAN.

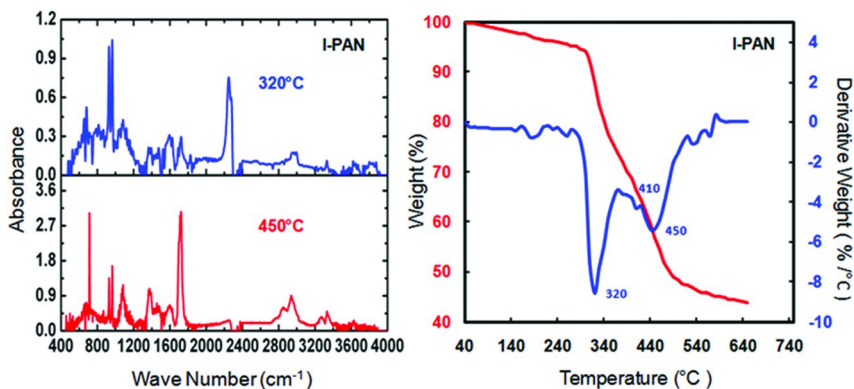


Figure 10. The TGA-FTIR spectra of I-PAN.

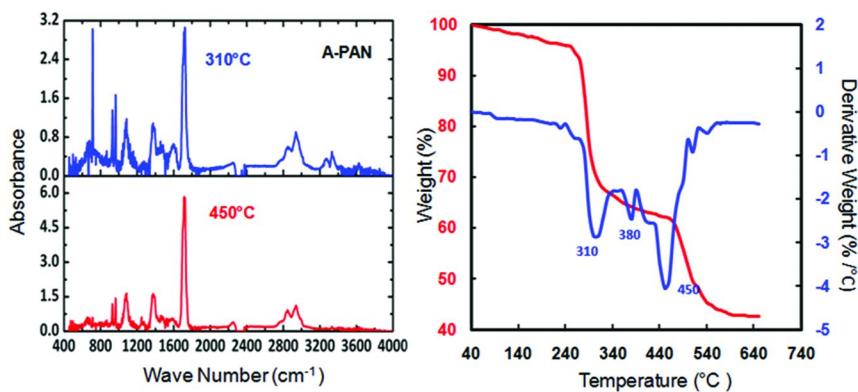
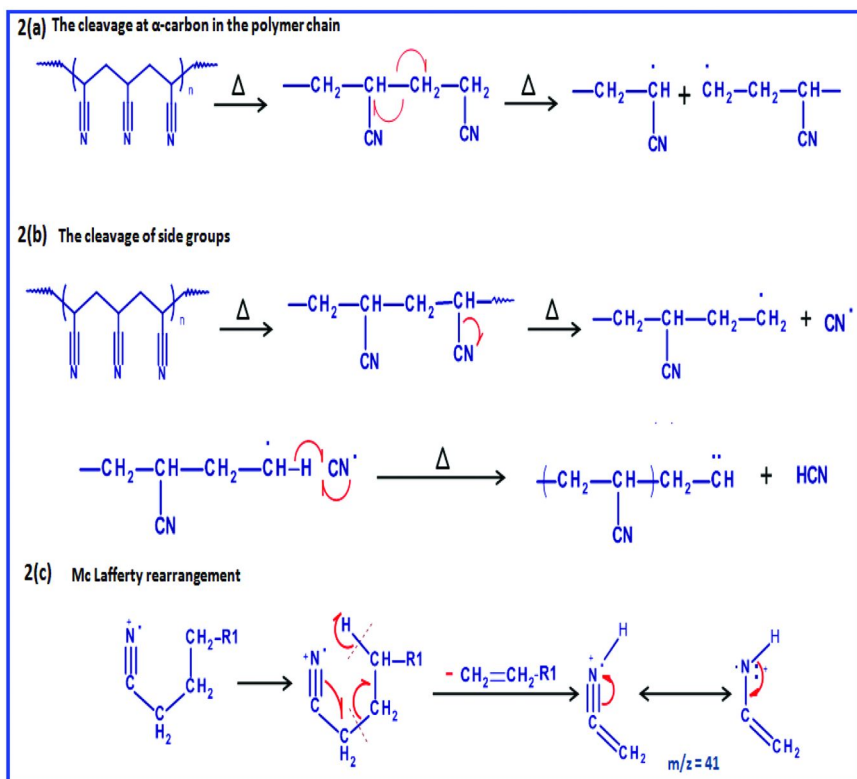


Figure 11. The TGA-FTIR spectra of A-PAN.



Scheme 2. Thermal degradation pathways of PAN polymers.

The absorbance values at 410 and 320 °C are in the range of 1.5 to 3.0 and 0.34 to 1.02, respectively. The higher absorbance values at 410 °C indicate the release of high concentration of ammonia and hydrogen cyanide in the evolved gases. The A-PAN sample showed three distinct thermal degradations at 310, 380 and 450 °C. The mass losses corresponding to the first, second and third stages are

ca. 45, 35 and 55%, respectively indicating the abrupt releases of evolved gases in case of A-PAN. The total absorbance values at 310 and 450 °C are 2.0 to 6.0 and 2.0 to 3.0 suggesting a higher quantity of gas released at 310°C in the case of A-PAN. This differential thermal degradation behavior of A-PAN can certainly be attributed to the higher atactic triad content. The general thermal degradation pathways of acrylonitrile based polymers include random main chain scission and side chain reactions. As a result of random main chain cleavage, homologs of alkyl nitriles are formed. These reactions have been illustrated in Schemes 2a-c.

Conclusions

The thermal degradation behavior and stability of carbon fiber polymer precursors viz., PAN with different microstructures, defined in terms of triad tacticity contents were studied applying hyphenated thermal techniques. These characterization techniques provided a complementary and more accurate methodology to understand the degradation mechanism of carbon fiber precursor polymers. The results based on these thermal degradation data indicate distinct thermal degradation pathways for the micro structurally different poly(acrylonitrile) polymers. The evolved gases during thermal decomposition were identified using TGA-FTIR. The results from Py-GC/MS suggest poly(acrylonitrile) with high isotactic triad content is thermally more stable as compared to that of lower isotacticity. In I-PAN, the nitrile polymerization of pendant cyano functionalities precedes pyrolysis reaction, where as in the case of atactic rich CFPP, an elimination (HCN) → chain fragmentation (β-scission) → nitrile polymerization reaction.

The pyrolysis starts with the evolution of hydrogen cyanide and ammonia initially, followed by the homologs of alkyl nitriles through cleavage at α-carbon and side groups. The PAN with higher isotactic content favors a nitrile polymerization leading to formation of aromatic cyclization which is more stable form of molecular orientation of polymeric carbons thereby accounting for the lesser ionic abundance in the TIC chromatograms. Considering a mass loss greater than 50 % wt. in PAN precursors (ie., a decrease in mass per unit length of PAN precursor is ca. 0.6850 gm⁻¹ to 0. 2 gm⁻¹ in final carbon fiber strand of 3000 filaments) during the thermal stabilization and carbonization processes leading to defects, more thermally stable stereoregular PAN polymers will be certainly beneficial for the fabrication of high tensile grade carbon fibers. The TGA-FTIR results confirmed and complemented the Py-GC/MS data.

Acknowledgments

The author thanks Director, CSIR-National Aerospace Laboratories(CSIR-NAL), and Head, Materials Science Division, CSIR-NAL, Bangalore for their support and permission to publish this work. This work was supported by the Council of Scientific and Industrial Research(CSIR), New Delhi under Supra Institutional Project (SIP-IFCAP-04).

References

1. Fitzer, E.; Foley, A.; Frohs, W.; Hauke, T.; Heine, M.; Jager, H.; Sitter, S. *Ullmann's Fibers*; Wiley VCH: Weinheim, 2008; pp 362–365.
2. Maeda, Y. *The Recent Trends of Carbon Fiber*; CMC Publications: Tokyo, 2007; pp 141–169.
3. Morgan, P. *Carbon Fiber and Their Composites*; CRC Press: Boca Raton, FL, 2005; pp 953–1041.
4. Donnet, J. B.; Wang, T. K.; Rebouillat, S.; Peng, J. C. M. *Carbon Fibers*; Marcel Dekker: New York, 1984; pp 201–215.
5. Eiichi, Y. Carbon fiber from micro to nano. *Tanso* **2011**, *248*, 112–121.
6. Kawakami, D. Carbon fiber. *Sen'i Gakkaishi* **2010**, *66*, 184–191.
7. Folger, T.; Stephen, M. Crazy far. *Natl. Geogr.* **2013**, *1*, 68.
8. Frohs, W.; Jaeger, H. C. Carbon fiber & composite material. *Tanso* **2011**, *249*, 174–178.
9. Huang, X. Fabrication and properties of carbon fibers. *Materials* **2009**, *2*, 2369–2403.
10. Hiromi, A.; Toru, K. Polyacrylonitrile based carbon fiber. *Tanso* **2007**, *227*, 115–121.
11. Hiramatsu, T. *Tanso sen'i no hon*; Nikkan Publishers: Tokyo, 2012; pp 23.
12. Masafumi, I.; Isao, N.; Makoto, E. U.S. Patent 0126442A1, 2012.
13. Shimizu, K. Recent progress in carbon fibers. *Kobunshi* **1993**, *42*, 480–482.
14. Rahman, M. S. A.; Ismail, A. F.; Mustafa, A. A review of heat treatment of carbon fiber. *Polym. Degrad. Stab.* **2007**, *92*, 1421–1432.
15. Whitney, W.; Kimmel, R. M. Griffith equation and tensile strength of carbon fibers. *Nat. Phys. Sci.* **1972**, *237*, 93–94.
16. Griffith, A. A. The phenomena of rupture and flow in solids. *Philos. Trans. R. Soc. London* **1921**, *221*, 163–198.
17. Fitzer, E. Pan-based carbon fibers—Present state and trend of the technology from the viewpoint of possibilities and limits to influence and to control the fiber properties by the process parameters. *Carbon* **1989**, *27*, 621–645.
18. Anqi, J.; Shanyi, G.; Hongyao, X. Effect of comonomer structure on the stabilization and spinnability of polyacrylonitrile copolymers. *Carbon* **2013**, *54*, 323–335.
19. Catta Preta, I. F.; Sakata, S. K.; Garcia, G.; Zimmermann, J. P.; Galembeck, F.; Giovedi, C. Thermal behavior of polyacrylonitrile polymers synthesized under different conditions and comonomer compositions. *J. Therm. Anal. Calorim.* **2007**, *87*, 657–659.
20. Bajaj, P.; Sreekumar, T. V.; Sen, K. Thermal behaviour of acrylonitrile copolymers having vinyl acids. *Polymer* **2001**, *42*, 1707–1718.
21. Ouyang, Q.; Cheng, L.; Wang, H. J.; Li, K. X. DSC study of stabilization reactions in poly(acrylonitrile-co-itaconic acid) with peak-resolving method. *J. Therm. Anal. Calorim.* **2008**, *94*, 85–88.
22. Sreekumar, T. V.; Lal, C.; Srivastava, A.; Kumar, S. Oxidative stabilization of polyacrylonitrile in the presence of functionalized carbon nanotubes. *Carbon* **2007**, *45*, 1105–1136.

23. Zhang, W. X.; Liu, J.; Wu, G. Evolution of structure and properties of PAN precursors during their conversion to carbon fibers. *Carbon* **2003**, *41*, 2805–2812.
24. Burkanudeen, A.; Santhana Krishnan, G.; Murali, N. Thermal behavior of carbon fiber precursor polymers with different stereoregularities. *J. Therm. Anal. Calorim.* **2013**, *112*, 1261–1268.
25. Friedlander, H. N.; Peebles, L. H., Jr.; Brandrup, J.; Kirby, J. R. On the chromophore of polyacrylonitrile—Mechanism of color formation in polyacrylonitrile. *Macromolecules* **1968**, *1*, 79–86.
26. Grassie, N.; McGuchan, R. Pyrolysis of polyacrylonitrile and related polymers—IX: Copolymers of acrylonitrile with vinyl chloride, vinylidene chloride and α -chloroacrylonitrile. *E. Polym. J.* **1973**, *9*, 507–512.
27. Santhana Krishnan, G.; Burkanudeen, A.; Murali, N.; Phadnis, H. Studies on molecular weight distribution of carbon fiber polymer precursors synthesized using mixed solvents. *Chin. J. Polym. Sci.* **2012**, *30*, 664–673.
28. Santhana Krishnan, G.; Burkanudeen, A.; Murali, N.; Phadnis, H. Facile synthesis of stereoregular carbon fiber precursor polymers by template assisted solid phase polymerization. *Express Polym. Lett.* **2012**, *6*, 729–738.
29. Tomoko, I. Japanese Patent 2011042893, 2011.
30. Shibukawa, T.; Masao, S.; Akiyoshi, U. Light scattering study of polyacrylonitrile. *J. Polym. Sci., Part A-1: Polym. Chem.* **1968**, *6*, 147–159.
31. Chuichi, W. Development of analytical Py-GC System of polymeric materials. *Kobunshi* **1994**, *43*, 110–111.
32. Minagawa, M.; Onuma, H.; Ogita, T. Pyrolysis gas chromatographic analysis of polyacrylonitrile. *J. Appl. Polym. Sci.* **2001**, *79*, 473–478.
33. Hatada, K.; Kitayama, T. *NMR Spectroscopy of Polymers*; Springer: Heidelberg, 2004; pp 83–86
34. Christian, V.; Seisler, H. W. Thermal Degradation of poly(ϵ -caprolactone), poly(L-lactic acid) and their blends with poly(3-hydroxy-butyrate) studied by TGA/FT-IR spectroscopy. *Macromol Symp.* **2008**, *265*, 183–194.

Chapter 9

Solution Spinning of PAN-Based Polymers for Carbon Fiber Precursors

E. Ashley Morris* and Matthew C. Weisenberger

Center for Applied Energy Research, University of Kentucky,
2540 Research Park Drive, Lexington, Kentucky 40511, United States

*E-mail: ashley.morris@uky.edu

Solution spinning of PAN-based polymers for carbon fiber precursors begins with a brief history, followed by methods of spinning, of which solution spinning is the focus. Following a discussion of the various solution spinning methods for PAN precursors, applicable polymer and solvent systems are discussed before proceeding into a discussion of dope preparation and rheological characterization. A discussion of the spinning process covers filtration, die swell, coagulation, washing, spin finish application, stretching, drying, collapsing and finally heat setting of the precursors. Following the spinning process, the resulting fiber properties and structure are described. Void and pore structure, fiber cross-section, fiber mechanical properties, and fiber morphology and their effect on the resulting fiber properties are discussed. Throughout, emphasis is placed on understanding the fiber formation mechanisms, particularly with regard to fiber coagulation, and its effect on the structure and properties of PAN precursor fibers.

History

The Union Carbide Corporation (UCC) produced the first industrial-scale structural carbon fibers from the pyrolysis of rayon fiber in the late 1950's and early 1960s (1). Rayon was one of the first synthetic fibers, developed around the turn of the 20th century, and was primarily derived from natural polymers extracted from wood pulp (2). The process used to solubilize and then spin rayon

at that time became known as the viscose process, which is not a particularly simple or clean process. Nonetheless, rayon coincidentally had an important characteristic for a carbon fiber precursor; the tendency to pyrolyze prior to melting. But rayon lacked good carbon yield (often less than 30%) and had to be plastically drawn at graphitizing temperatures to impart it with a desirable tensile modulus. Other work at UCC, including that of Roger Bacon on graphite whiskers, proved that graphite-like filaments could achieve incredibly high tensile modulus and strength (3).

In the 1940s, DuPont sought to solution-spin fiber from polyacrylonitrile (PAN), which was known to be difficult to dissolve and pyrolyze prior to melting. Houtz, at DuPont, carefully studied solvents for PAN, which subsequently made possible the spinning of PAN fiber (4, 5). Introduced in 1950, it was commercialized and sold as Orlon® fiber (6). Coincidentally, there were interesting ties between DuPont's Orlon, and their rayon production. Remarkably, in 1950, Houtz reports in reference to Orlon fiber (4):

Under more drastic heating treatments, its physical properties hold up remarkably well, but color changes do occur, going progressively to yellow, brown, and black as heating is continued. ...The black yarn is remarkably stable to further heating, even in a Bunsen burner flame.

In the same paper, offering an explanation for the observed color change, Houtz describes a "...condensed pyridine type of ring formation...", and provides possible structures strikingly similar to those known today for stabilized PAN. But DuPont had primary interest in PAN as a textile fiber, and had good success with PAN staple fiber. Later in the decade, Courtaulds began making its own acrylic fiber in the UK.

In 1959, after reading about UCC's early rayon-based carbon fibers, Akio Shindo, at the Japanese Governmental Industrial Research Institute (GIRO) in Osaka, began work developing a process to utilize PAN filaments as precursors for carbon fiber. His work (7, 8), which involved a low temperature thermal oxidative stabilization intermediate step, quickly showed improvements in carbon yield (50 to 60%), compared to the rayon precursor, and resulted in intellectual property, which would be licensed by Japanese companies eager to commercialize (9). Of the licensees, Toray Industries, a Japanese synthetic fiber manufacturer, was to become the most successful, and today is the largest manufacturer of carbon fiber in the world. Toray's success has been attributed to their textile roots in fiber processing. But the PAN-based carbon fiber can't be wholly attributed to work in Japan. By the early 1960s, stakeholders in the aerospace industry had gained interest in the development of lightweight, stiff, and tough carbon fiber composite structures. In 1966, independent work by the Watt, Phillips and Johnson group at the Royal Aircraft Establishment (RAE) in Farnborough, UK improved Shindo's process, conserving molecular alignment in the fiber by applying tension during thermal conversion (10). Their process made PAN-based carbon fibers with much improved tensile properties, and heralded the first structural PAN-based carbon fiber. Also in England, Courtaulds was experimenting with an itaconic acid dye adhesion monomeric additive, which proved more useful in the production

of their special acrylic fiber (SAF) PAN precursor for carbon fiber (11). Rolls Royce was involved early-on with work on PAN-based carbon fiber – polymer prepreg material for composites (12). With this advance, and with cross-licensing manufacturing agreements with UCC (9), Toray steadily grew their PAN-based carbon fiber production and improved quality.

Over the years, a number of manufacturers have entered and exited, or have been bought-up, in the PAN-based carbon fiber business. A number of other precursor fiber materials have been investigated, but after over 50 years, PAN remains the precursor of choice for making high performance, structural carbon fiber. It has enabled the production of today's intermediate modulus (IM) fibers, which are a cutting-edge component of high stiffness, high toughness composite structures. It is likely that PAN-based carbon fiber will remain for the foreseeable future.

Methods of Solution Spinning

Central to manufacturing PAN-based carbon fiber is the spinning of PAN precursor fiber from a solution, or dope, of PAN dissolved in solvent. Solution spinning of acrylic fibers is divided into two major processes: dry spinning and wet spinning (13). Wet spinning is divided further into minor processes: wet-jet spinning, air gap spinning, and gel spinning. A discussion of these solution spinning processes follows.

Dry Spinning

In dry spinning, the heated polymer solution is pumped through a spinnerette into a tower with a constant flow of heated inert gas. This inert gas is heated above the boiling point of the dope solvent, causing the majority of the solvent within the nascent filaments to evaporate, leading to solidification of the filaments. These filaments emerge from the tower and are subjected to various post treatments, similar to wet spun fibers (13, 14).

Wet Spinning

In wet spinning, a polymer solution is pumped through a spinnerette and enters a coagulation bath. The coagulation bath is typically a solution of solvent (often the spinning solvent) and non solvent (typically water). Upon contact with the coagulation bath, a dual diffusion process begins in which solvent diffuses out, and non-solvent diffuses into the nascent filaments. This double-diffusion process leads to a phase change from a viscous solution to a solid polymer filament composed of fibrils and small pores. In industrial scale operations, the ratio of non-solvent to solvent in the coagulation bath must be continuously monitored to maintain a constant concentration. Following initial coagulation, the formed filaments emerge from the bath and are subjected to washing, stretching and other post treatments.

Wet-Jet Spinning

The typical wet spinning operation employs a wet-jet spinning method. Here, the polymer solution is pumped through a spinnerette, which is submerged in the coagulation bath. Therefore, the polymer solution immediately begins to solidify upon exiting the spinnerette. The downstream processes of washing, stretching, drying, process oil application and winding then continue as normal.

Air Gap Spinning

Another variation of wet spinning is air gap, or dry-jet, spinning. During air gap spinning, the polymer jets exit the spinnerette and pass through a small air gap (typically 2-10 mm) prior to contacting the coagulation bath, as seen in Figure 1. The length of the air gap for stable spinning is affected by the viscoelastic properties of the polymer solution, and therefore differs from process to process. While some prefer an air gap between 5 and 10 mm (15), others prefer a smaller air gap of 3 mm (16).

Of utmost importance for air-gap spinning is that the polymer solution be capable of withstanding the large extensional forces encountered in the air gap. If the gap is too high, rupture of the polymer jets will occur due to surface tension-induced breakage, and spinning will fail (17). Alternatively, if the gap is too low, there is danger of the coagulating solution “wicking” to the surface of the spinnerette and again causing spinning failure. The ability of the polymer solution to successfully air-gap spin is often referred to as “spinnability”. Spinnability depends on many variables, including the rheological properties of the dope, spinning temperature, jet stretch, spinnerette capillary length, diameter and shape, evaporation, mass flow rate, and coagulation medium and conditions, to name a few (18, 19).

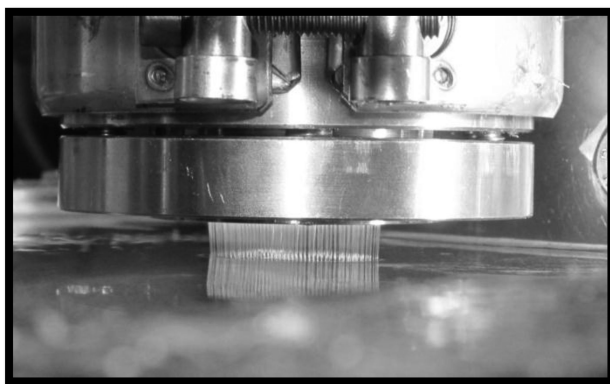


Figure 1. Multi-filament air-gap (5 mm) spinning of PAN polymer solution into a DMAc/H₂O coagulation bath at the University of Kentucky Center for Applied Energy Research.

While the conditions under which successful air-gap spinning may occur are very precise compared to wet-jet spinning, air-gap spinning has several advantages. These include the ability to achieve very high draw in the air gap. The polymer jets are quite extensible in the air gap, as they have not yet encountered the non-solvent. For example, Zeng, et al. found that the ability to stretch the fiber within the coagulation bath, or the jet stretch, increased three fold when moving from a wet-jet spinning process to an air-gap spinning process with an air gap of 5 mm (15). When the jet stretch is increased, so too is the total linear spinning speed, resulting in a much faster fiber spinning process (20). In addition, the high draw in the air gap leads to greater molecular alignment within the polymer jets prior to coagulation, after which the molecules have less mobility. Higher molecular alignment leads to higher modulus fiber. Also, when passing through the air gap, a small amount of evaporation occurs from the polymer jet surface, causing a thin, dense skin to form (15). This skin largely influences the initial rate of coagulation upon entering the coagulation bath (15, 21, 22) and gives dry-jet spun fiber a very smooth surface with high luster, helping to improve the tensile properties of the resulting fibers.

Gel Spinning

Gel spinning has been linked to several different processes in the past few years. Generally, it refers to a thermally induced phase change from a fluid polymer solution to a three-dimensional gel network. The phase change occurs at a temperature lower than the solution's gel point temperature (23). The gel point is often defined as the intersection, or cross-over, of an increasing storage shear modulus with a decreasing loss shear modulus, with respect to decreasing temperature. As the temperature is lowered, the polymer solution behaves more like an elastic solid. This type of gelation is reversible, as the gel structure can be erased by increasing the dope temperature (24). In order to aid gel formation at low temperatures, the spinning solution is often very viscous at room temperature. This increased viscosity has been achieved by increasing the polymer molecular weight (25, 26) or adding a small amount of non-solvent to the spinning solution prior to spinning (23, 27, 28). Due to the increased viscosity of the solution, the majority of gel spinning requires heating the dope to a spinnable viscosity, before quenching it in a cold coagulation bath to form a gel. For example, Smith, et al. pumped a highly viscous polyethylene polymer solution at high temperature (130°C) through a spinnerette and into cold water to form a gel fiber (26).

Gel spinning is advantageous for spinning with high molecular weight polymers, where spinning solutions with low polymer concentration have very high viscosities. While such solutions are more challenging to coagulate, they are capable of achieving very high draw ratios and therefore may produce high tensile performance fiber. In the case of high molecular weight PAN, methanol can be used, instead of water, as a non-solvent. Several researchers have allowed the gelled fibers to soak in methanol for several days for full solvent extraction (28–30). The resulting gel spun fibers have a better packed structure compared to

those gel fibers coagulated using a traditional solvent/non-solvent bath (27), but at the expense of large residence times.

Gel spinning is also advantageous to dry-jet or wet-jet solution spinning because the gel-network mitigates relaxation of the polymer molecules that would otherwise occur during spinning (31). This helps maintain axial molecular alignment within the fiber, which directly affects the fiber modulus. In addition, the gel state is a more stable network compared to a polymer solution, and circular cross-section of the fiber has been found easier to maintain. One disadvantage to the gel spinning method, however, is that the high viscosity of the spinning solution makes extrusion and filtering difficult and negatively impacts spinnability (27). In addition, if high molecular weight polymers are used, low solids content of the spinning solution can lead to voids and pores inside the spun fibers. Such voids negatively affect the fiber mechanical properties despite a high total stretch (23, 27). Finally, the long residence times in the extraction bath, as mentioned previously, can hinder production capabilities.

Polymers and Solvents

The choice of the solvent/polymer/non-solvent system plays a vital role in the development of the resulting precursor fiber.

Polymers

Polyacrylonitrile (PAN) polymer $[(\text{CH}_2\text{CHCN})_n]$ is the dominant polymer precursor for the production of high performance carbon fibers, accounting for over 90% of the world production of carbon fiber (32). The molecular structure of PAN, in Figure 2, contains highly polar nitrile groups, which result in strong intermolecular interactions. Due to these strong interactions and linear structure, PAN is able to pyrolyze quickly without disrupting the basic structure or preferred orientation of the molecular chains (33), and the high melting point enables it to pyrolyze before melting (33, 34), making it suitable for a carbon fiber precursor. Also, vital to the production of high performance carbon fibers is a polymer with a high carbon yield, and PAN typically yields 50-55% carbon when pyrolyzed to 1000°C (33).

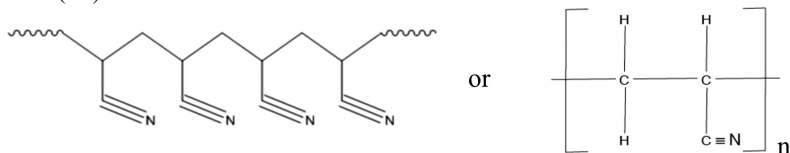


Figure 2. Molecular Structure of Polyacrylonitrile.

Acrylic polymer consisting of 100% PAN, known as homopolymer, is rarely used for manufacturing high performance carbon fibers, as it is difficult to fully dissolve, tends to form gels, and is therefore difficult to spin. In order to avoid gelation of the polymer solutions, small quantities (~ 5%) of comonomers are added to slow the gelation rate and increase solubility. Incorporation of

a comonomer can improve the carbon fiber mechanical properties due to the increased molecular orientation, stemming from increased spinnability, in precursor fibers and the resultant carbon fibers. Neutral comonomers, which are not intended to participate in a chemical reaction, increase the solubility of the polymer in the spinning solvents, modify the fiber morphology and improve diffusion rates (33). Examples of neutral comonomers include methyl acrylate (MA) and vinyl acetate (VA). As an example of a comonomer influencing fiber morphology, Bajaj suggested that MA may hinder inward non-solvent diffusion and slow coagulation, therefore resulting in kidney bean shaped fibers (16).

In addition to affecting fiber morphology, some comonomers facilitate the cyclization reaction in the stabilization step, such as those with acidic groups (acrylic acid or itaconic acid) (34). The presence of the acidic comonomer, in small quantities, catalyzes the cyclization event, mitigating the flux of exothermic heat release. These observations are key for correctly selecting the comonomer based on the desired fiber properties. For example, Bajaj, et al. found that heat treated fibers produced using a methyl acrylate comonomer had better tenacity and elongation than those similarly produced using methyl methacrylate or itaconic acid comonomer (16). A table detailing the effects of various comonomers on fiber properties can be found in the work of Rajalingam (35). Again, the effects of the comonomer(s), and comonomer concentration, on the resulting fiber properties cannot be overlooked.

Molecular Weight

Polymer molecular weight significantly affects the viscosity of the spinning dope and thus the solids content, or concentration of polymer in solvent, comprising the dope. Viscosity and spinnability are extremely sensitive to molecular weight changes (14) and increases in solids content. As the molecular weight increases, the concentration of polymer needed to reach a spinnable viscosity decreases. At high viscosities, or high polymer concentrations, pressures during spinning may exceed their upper safety limits. At the lower end, if polymer concentration is too low, significant structure changes will be seen in the resulting fiber (21). Low polymer concentrations are also more costly, due to higher solvent recovery requirements. Therefore, choosing an appropriate molecular weight polymer to balance production rates and maintain the spinning process is vital.

A typical PAN for production of good precursor fiber will have a molecular weight on the order of 100,000 M_w (36). This results in a polymer concentration ranging from 15-25 wt.% in solvent to achieve a spinnable solution viscosity, depending on the method of spinning used and the desired fiber properties. A typical polymer concentration of approximately 25 wt.% gives a dope viscosity in the 500 Poise (50 Pa-s) range (14), as an example of a possible spinnable viscosity. In addition to spinnability, the production of high performance fibers depends highly on the drawability of the polymer, which is affected by several factors, including chain entanglement density, polymer molecular weight, and drawing technique. Several authors have proposed that ultra-high molecular weight (UHMW) polymers offer a path to high performance PAN-based carbon fibers due to their ability to be highly ordered through drawing (37) (up to 80

times (29)). Further, high draw ratios lead to small diameter fibers, which have been shown to increase the tensile properties of the resulting fiber (38). Indeed, PAN fiber strength has been shown to increase with molecular weight (39).

However, spinning with UHMW PAN has several drawbacks, including issues with spinnability, due to high solution viscosities. UHMW PAN has also been shown to produce undesirable non-circular fibers. These fibers decreased in circularity as molecular weight increased (40). It is likely that the corresponding decrease in polymer content and increase in viscosity with increasing molecular weight produced an unfavorable change in the diffusion coefficients and coagulation process. The change in coagulation also caused a change in the surface morphology of the precursor fibers. Deep surface striations on the fibers have been observed accompanying increases in PAN molecular weight (39, 40). Therefore, selection of polymer molecular weight should be balanced to take advantage of high drawability without negative morphology or processing effects.

Solvents

The solvent chosen to produce the spinning dope can be either a highly polar organic solvent (4) (to solvate the highly polar nitrile group of the PAN) or an inorganic aqueous salt solution. Solvents used to produce spinning dopes are typically aprotic polar molecules with large dipole moments and low molecular weights. The major commercial solvent types for wet spinning include dimethylformamide (DMF), dimethylacetamide (DMAc), dimethylsulfoxide (DMSO), aqueous solutions of sodium thiocyanate, zinc chloride, and nitric acid (14, 41, 42). For dry spinning, the process relies on solvents with high vapor pressures in order to facilitate evaporation in the spinning tower, such as DMF. Each solvent type and strength generates differing fiber structures due to the complex interplay between solvent, polymer composition, and non-solvent (13).

Dope Preparation

In order to prepare the spinning solution, or dope, no single solvent and polymer formula can be given, as each system relies on numerous processing variables. Such variables include the available processing equipment and desired fiber properties. However, once thorough investigation and experimentation of the solvent/polymer system has been undertaken and the appropriate polymer and solvent has been chosen, dissolution of the polymer within the solvent is the central step to prepare the spinning dope. As the standard organic solvents for spinning (DMSO, DMAc, DMF, etc.) and PAN are hydrophilic, it is important to prevent excess exposure to air from which moisture may be absorbed. Absorbed moisture can produce negative effects in the spinning solution and resulting fibers. To produce the dope, the desired polymer concentration is mixed with the solvent. If, at room temperature, part of the polymer appears to dissolve, while the other part remains suspended, this can be indicative of a bimodal distribution, or high polydispersity within the polymer. A bimodal distribution, or excessive

polydispersity, is undesirable and often leads to spinning problems. Assuming good polydispersity, once the polymer has been sufficiently suspended in the solvent, the suspension is then heated while mixing until the polymer is fully dissolved and a homogeneous solution is formed. Following dissolution, the dope is de-gassed under vacuum for the removal of air bubbles and dissolved gases. The de-gassed, homogeneously dissolved dope is then introduced to the spinning system for rigorous filtration and spinning.

Rheological Characterization

The spinning process relies on drawing a polymer solution into a filament. Therefore, it is advantageous to have a thorough understanding of the rheological properties of the polymer solution in order to ensure dope quality and enhance spinning stability. The viscosity of polymer solutions is known to increase with polymer concentration, average molecular weight, and decreasing temperature. Typical wet spinning technologies rely on polymers in the 100,000 to 120,000 Dalton range, with solution viscosities in the range of 500 Poise (13). During the spinning process, the polymer solution encounters numerous forces, including high extension rates (43), all of which affect the resulting solution jet at the exit of the spinnerette capillary. Replication of the experimental spinning process on an analytical instrument, therefore, is not an easy task. Years of research have gone into quantifying the “spinnability” of these polymer solutions. A basic form of spinnability analysis is to determine the steady shear viscosity using a parallel plate rheometer. For a given polymer solution, the steady shear viscosity can be an excellent starting point for determining the viscosity of the solution at low shear rates. However, for analysis of the solution viscosity near actual spinning shear rates, which can be on the order of 10,000 1/s, it is necessary to use a capillary rheometer. Accurate measurement of extensional viscosity of polymer fluids incurs very unique challenges, and can be extremely specialized. Using the steady shear viscosity results, a solution may be deemed a power law fluid if the relationship between shear stress (σ_t) and shear rate ($\dot{\gamma}$) using the following equation remains true, where K is the consistency coefficient and n is the non-Newtonian viscous index.

$$\sigma_t = K\dot{\gamma}^n$$

For power law fluids, when the value of n is less than 1, the solution is shear thinning. The non-Newtonian index continues to decrease with increasing shear rate. This is typical of weakly elastic constant viscosity liquids (44), such as PAN solutions (45), and therefore adds to the complexity in modeling the experimental spinning process. Shear thinning has been attributed to the alignment of the molecular chains and the breakdown of the entangled polymer network (45, 46).

In addition to steady shear viscosity analysis, oscillatory rheology is useful for determining the elastic and viscous characters of the spinning solution. The storage shear modulus, G' , can be used to describe the character of the elastic structure, while the loss shear modulus G'' can be used to describe the viscous character of

the solution. As G'' increases, the solution becomes more viscous in character. At temperatures below the gel point, the elastic character of the solution, G' , is dominant, resulting in a gel. Gelation of polymer solutions forms from strong polymer-polymer interactions. This applies to entangled polymer solutions. Non-entangled solutions do not display this behavior. The gelation of PAN solutions depends on the thermal history of the solution, its composition, and experimental conditions. Therefore, the gelation point is not the same for all PAN solutions (47). It is important to understand the gel point for the given spinning solution, as gelation influences the viscoelasticity of the solution (48).

Gelation is also important when working with UHMW PAN, which tends to gel at lower polymer concentrations. Rheological characterization of UHMW polymer solutions is similar in practice to typical molecular weight polymers, however the results are vastly different. Xinyuan, et al. found that a UHMW PAN/DMSO solution behaved very differently due to chain entanglements (49). Similar chain entanglements have resulted in increased shear viscosities (50). Typically, as readily observed for UHMW PAN, solution viscosity significantly increases with polymer concentration, average molecular weight, and decreasing temperature (40). Therefore, when analyzing a polymer solution for spinnability, it is important to know the qualities of the polymer that may affect its viscoelastic properties, and as a result, its spinnability.

Spinning

The spinning process begins with rigorous filtration of the previously prepared spinning solution, or dope. The solution is then pressurized through the spinnerette and introduced to the coagulation bath, either through a wet-jet, or dry-jet (air gap) method. An illustration of the dry-jet (air gap) solution spinning process is shown in Figure 3. Spinning proceeds through washing and stretching baths, with spin finishes added to aid these processes. Finally, the precursor fiber experiences a drying, collapsing, and heat setting process prior to final collection on a traversing takeup roller. Each of these processes is detailed in the following sections.

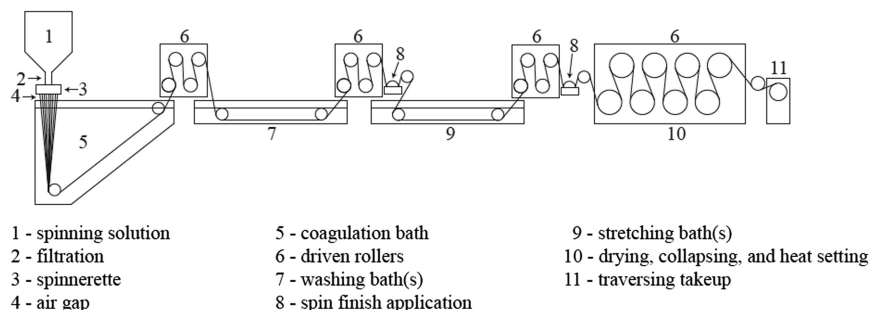


Figure 3. An illustration of the dry-jet (air gap) solution spinning process for precursor PAN fiber.

Filtration

During the dope preparation and spinning process, there are numerous sources of potential contamination. These contaminants (dust, dirt, gels, etc.) lead to imperfections in the resulting fibers. Therefore, cleanliness and filtration are vital to the production of high strength fibers (41). Preferably, fibers are spun in a clean room to minimize possible sources of contamination. However, results have indicated only small differences (15%) in fiber tensile strength of the precursor when spun under clean room conditions, compared to typical spinning practices (41). The resulting carbon fibers see the largest benefit from clean room conditions, as precursor fibers spun under clean room conditions had 35x fewer particles on the fiber surface. These precursor surface particulates lead to imperfections in the final carbon fiber. Indeed, the decrease in the number of contaminants on the precursor surface led to much higher carbon fiber strengths (+84% at 1400°C and +82% at 2500°C) (41). This suggests that cleaner precursors should enable production of carbon fibers with increased breaking strains (51) due to fewer defects. A general rule of thumb is to filter the spinning solution to 10% of the spinnerette capillary diameter.

Die Swell

Polyacrylonitrile (PAN) dopes are viscoelastic fluids, and therefore display a die swell effect upon extrusion exit from the spinnerette capillary (16). The elastic memory of the dope, stress caused by the shear forces in the capillary, and interaction with the coagulation bath contribute to the die swell effect (52, 53). This die swell has a large influence on the formation of the as-spun fibers. Bao-Hua Ji found that a smaller die swell ratio leads to enhanced spin orientation, reduced skin-core differences, and a more compact and homogeneous microstructure, thus increasing the breaking tenacity of the as-spun fibers (54). Die swell can be mitigated by increasing the dope temperature (16) or increasing the jet stretch ratio. Bao-Hua Ji, et al. calculated the die swell (D), as follows (52), where n is the number of filaments, M is the dried weight of the as-spun fibers, ρ is the density of the polymer solution (g/cm^3), C is the mass fraction of polymer to solvent in the spinning solution (%) and L is the length of the filament:

$$D = \sqrt{\frac{4M}{n\pi\rho CL}}$$

Utilizing the calculated die swell, the die swell ratio, B , was then calculated (52), where D is the diameter of the as-spun fibers (cm) and D_0 is the diameter of the capillary (cm):

$$B = \frac{D}{D_0}$$

Correct calculation of die swell is necessary for calculating the jet stretch, and as a result, the overall stretch the fiber receives during processing. During wet-jet spinning, the jet stretch is almost always less than 1, due to a large die

swell effect (13, 52, 55, 56). This jet stretch, including die swell effect, is known as the apparent jet stretch. In order to accurately calculate the stretch the fiber experiences, it is necessary to remove the die swell effect, resulting in the true jet stretch. Ouyang, et al. determined the true jet stretch by determining the velocity of the jet at the point of greatest swell, (V_s), obtained from the following relation (53):

$$V_s = V_0 \left(\frac{D_0}{D_s} \right)^2$$

Here, V_0 is the extrusion velocity of the spinning solution through the spinnerette capillary, D_0 is the diameter of the spinnerette hole and D_s is the diameter of the nascent filament at maximum swell. The true jet stretch, the driven velocity of the fiber out of the coagulation bath divided by V_s , can then be used to calculate the overall stretch during spinning.

Coagulation

Coagulation refers to the complex transformation from dope to fiber. Within a very short time of exposure of the emerging nascent filaments to the coagulation bath, the fundamental mechanisms of heat transfer, mass transfer, and solution thermodynamics play a role forming the fiber. The rate of heat transfer is dependent on both the temperatures of the polymer solution and the coagulation bath, which therefore impact the rate of diffusion and phase separation. Phase separation, in conjunction with relative diffusion rates, is the major factor in the determination of the final fiber structure. For example, when the flux of solvent out of the forming fiber is less than the inward flux of nonsolvent, the filament swells and a circular cross section forms (57). However, if coagulation occurs too rapidly, a skin is formed on the fiber. The fiber then collapses as trapped solvent in the fiber core subsequently diffuses out, while the skin retains its circumference. This results in non-round, often bean-shaped cross section. In addition, if coagulation occurs too quickly, the resulting fiber will have a loosely packed microstructure, with increased porosity (58). Due to the delicate balance of coagulation conditions required to produce high quality fibers, precise control of coagulation bath composition and temperature, and dope composition and temperature, is critical.

Diffusion

As one of the fundamental processes governing the formation of wet-spun acrylic fiber, diffusion is a complex process driven by concentration differences along and within the fiber. The relative rates of solvent to non-solvent diffusion have a major effect on phase separation and govern the rate of phase separation. The diffusion process stems from concentration gradients, and is affected by temperature, and fiber diameter (or diffusion distance). In particular, the

composition of the non-solvent in the bath can have a marked effect on the diffusion process.

The fiber jet stretch in the coagulation bath is highly affected by the diffusion rate. If the diffusion rate is slowed, allowing for more extensible filaments, smaller filament diameters and smaller standard deviations of the diameters are produced (53). In addition, the overall volumetric pump rate influences the shear rate along the capillary walls of the spinnerette. High shear can increase the degree of die swell at the exit of the capillary and thus plays a role in diffusion. Both the concentrations of polymer in the dope and the relative concentrations of the solvent/non-solvent pair in the coagulation bath impact the diffusion rates during coagulation. Increased polymer concentrations in the spinning solution increase the resistance of the boundary layer within the filament, which limits diffusion of both solvent and non-solvent. Also, the relative diffusion rate of solvent out of the fiber, compared to non-solvent into the fiber, increases. Several investigators, such as Jian and Terada, studied the diffusion relationships in DMF, DMSO, and aqueous NaSCN solvents with the non-solvent water (59, 60). In addition, if coagulation occurs quickly and a skin is formed, diffusion is mediated by the skin, and the structure below the skin is formed as a consequence of the relative rates of diffusion across the skin (61). Understanding and controlling diffusion, impacts the resulting fiber morphology, and as a result, the mechanical properties.

Coagulation Bath Concentration

In order to coagulate the polymer jets, the coagulation bath must contain some ratio of solvent and non-solvent. The solvent in the coagulation bath could theoretically vary from 0% to 100%. At 0%, the coagulation bath contains only non-solvent and very rapid coagulation occurs, resulting in poor fiber properties and large voids. However, if the bath contains 100% solvent, no coagulation occurs. As the solvent to non-solvent ratio increases, the diffusion outflux of solvent from the fiber and the diffusion influx of non-solvent into the fiber slows. On the contrary, higher non-solvent concentration favors the influx of non-solvent and bulging of fiber diameter (16). Therefore, the concentration of solvent to non-solvent must be carefully controlled in order to control the coagulation process. A very rapid change in fiber cross-sectional shape can be found to occur over a very small change in coagulation bath composition. This is indicative of the pronounced effect that the composition of the coagulation bath can have on fibers.

Coagulation Bath Temperature

In addition to bath concentration, temperature is another key variable in controlling the diffusion of solvent and non-solvent. For most applications, the coagulation bath is normally within a temperature range of 0° to 50°C. As in most diffusion processes, an increase in temperature increases the diffusion rate. For example, Bajaj, et al. found that at higher temperatures (40°C), coagulation

occurred with an increased influx of water compared to the outflow of solvent (16). However, an increased diffusion rate is not preferable, as coagulation will occur too quickly, resulting in a thick skin, incomplete coagulation, and a loose core structure. Slow coagulation is preferred for production of filaments with a dense, uniform, and circular cross section. Zeng, et al. found that a round cross section fiber can be produced through two avenues: 1) increasing the coagulation rate by using high bath temperature, or using pure water as the coagulation bath, or 2) decreasing the coagulation rate and producing a thin outer structure that uniformly coagulates with the interior of the fiber. As mentioned previously, method (1) results in incomplete coagulation and a loose core structure, detrimental to fiber mechanical properties. However, achieving (2) requires a delicate balance between dope conditions and coagulation bath conditions. This mild formation condition produces excellent structure and is the preferred method for producing round fiber (55, 62).

In addition to producing a circular fiber cross section, slow coagulation aids incremental stretching, resulting in a more perfectly oriented fiber structure, less skin formation and smaller and fewer voids (58, 62). However, it is pivotal to ensure complete coagulation before drastic stretching, or fiber breakage will occur (63). The bath temperature has a complex relationship with the resulting fiber properties and morphology. Low temperatures favor the outflux of solvent from the filament over non-solvent influx. Therefore low temperature coagulation baths can lead to bean-shaped filaments. However low temperature coagulation tends to reduce void content. Here, in addition, careful attention must be given to the coagulation bath composition. A balance between composition and temperature must be achieved.

Washing

While fiber shape and initial structure is set in the coagulation bath, it is important to wash the fiber following the coagulation bath in order to remove residual solvent from within the fiber. Washing may be completed utilizing varying bath arrangements, with varying concentrations of solvent and non-solvent, or with pure wash water. The process must be tailored to the individual spinning process to ensure ideal removal of solvent from the fiber. Residual solvent leads to a swelling effect during drying operations and creates voids within the fiber, compromising mechanical properties (58). In order to remove residual solvent, the fiber is washed by countercurrent flow of non-solvent, typically water. Washing can be conducted preceding, or concurrent with stretching (13). Solvent recovery and waste-water treatment from coagulation and washing is also an important part of the industrial solution spinning process.

The wash segments/baths nearest the coagulation bath contain the highest solvent concentration and the lowest wash temperatures (13). A slow washing procedure has been supported by the work of Wang, et al., who found that slow coagulation/washing, with coagulation/washing occurring gently through three baths (increasing in temperature from 20°C to 60°C and decreasing in solvent concentration from 70% to 20%) produced filaments with dense structure compared to those with only coagulation occurring directly at 60°C (22, 58).

Therefore, slow washing is the preferred method for removal of residual solvent to produce dense precursor filaments with fewer voids.

Spin Finish Application

Following the washing procedure, a chemical treatment is applied to the fiber. The chemical, process oil, or “finish”, is normally an aqueous solution or emulsion and has both lubricants and antistatic components that facilitate fiber processing in the subsequent collapse and drying steps (64). In addition to providing lubrication and antistatic components, desired spin finish properties include: a balanced degree of cohesion, as too much lubricity can lead to fiber slippage during processing; oxidation resistance, for stability during long periods of storage; and the ability to be emulsified, for uniform application to the fiber surface (64). The spin finish for PAN precursor can also play a large role in aiding subsequent thermal conversion.

The antistatic component of the finish is necessary due to the hydrophobic nature of the fibers, which leads to retention of electrostatic charges. This results in static prone fibers, making further processing very difficult. Application of a lubrication component is also important. During fiber drawing, acrylic fibers have a tendency to adhere to neighboring fiber strands, resulting in uneven stretching, non-uniform precursor, or tearing of the precursor surface. In addition, this adhesion can result in fiber fusion during thermal treatment, which reduces the quality of the resulting carbon fiber. It is therefore preferable to apply the finish containing a lubrication component before and after the drawing step, primary and secondary respectively, prior to takeup (65).

There exist a multitude of spin finish types and compositions, which provide the desired properties. Examples of lubricants typically used in spin finish for PAN fiber include silicones, synthetic esters, and others. Common antistatic agents include alkyl compounds and phosphate esters (64). Silicones remain one of the most common spin finishes, and include polydimethylsiloxane, silicone oil, and ethoxysiloxane (66). An amino-modified silicone emulsion is a typical spin finish, often used to improve the heat resistance of the fiber (65). Jin, et al. found that a functional polysiloxane bearing epoxy or amino groups was able to depress the heat released during thermooxidative stabilization of the precursor fiber, likely due to slowing of the diffusion of oxygen into the PAN fiber, slowing dehydrogenation and oxidative reactions. This is vital to preventing fiber fusion during thermal treatment, which is caused by large exothermic reactions (67).

In addition to the finish composition, the amount on the fiber surface can be equally as important for producing high performance fibers (65). Indeed, depending on the end use, the finish quantity may be from 0.1 to 0.7% by weight (13), or up to 0.3 to 5% by weight. However, an amount less than 0.1 wt.% may not prevent fiber adhesion, resulting in decreased fiber tenacity, as mentioned previously (65). Controlling the method of spin finish application is necessary for controlling the resulting spin finish quantity on the fiber. One popular type of application involves a kiss roller, or a roller partially submerged in the spin finish. As the roller rotates, the fiber is passed over the non-submerged portion of the roller to pick up the finish. However, this method has shown non-uniform results

(64). Another method is to simply submerge the fiber through a bath of known spin finish concentration, for a known time, under known tension. One proposed alternative is to foam the spin finish, applying it to the fiber by pushing it through a slot, by which the fiber passes.

There are several methods that may be used to check the uniformity and amount of spin finish applied. For example, one method for the determination of the amount of spin finish applied to a fiber is by extracting the solids of the finish from the fiber using carbon tetrachloride, and measuring the amount of solids within the carbon tetrachloride using standard analytical techniques, such as gravimetric or infrared absorption techniques (68).

Stretching

Once the fiber has been properly washed for removal of residual solvent, the fiber is then stretched to increase molecular alignment and reduce fiber diameter. The stretching process is vital for ordering the fiber structure and enhancing the fiber properties. To enable stretching, the fiber is heated above the glass transition temperature, and stretched 3 to 12 times between godets, often using hot water and/or steam as the heating medium (13). Stretching in hot water not only orients the fibrils in the direction of the fiber axis but also stretches the individual fibrils (69). Steam stretching allows for even greater drawing. In addition, both the amorphous and crystalline regions are oriented in the direction of the fiber axis, and pores are elongated with water trapped in the voids. Under low stretching conditions, and above the glass transition temperature, the fiber is able to completely recover from the stretch and therefore the pores do not stay collapsed. However, during high stretch, above the glass transition temperature (60°C) (70), molecular chains slip, resulting in desirable pore collapse (71). Indeed, the overall stretch the fiber experiences has been directly correlated to the fiber strength. Bajaj found that similarly stretched fibers showed similar tenacities (16). However, it is important to know the upper limits to stretching for the given process, as overstretching results in fiber breakage (72). As a result, stretching reduces the number of pores within the fiber through pore collapse, increasing molecular alignment, and reduces fiber diameter, all of which are necessary to produce high strength fibers.

Drying and Collapsing

Following the final spin finish application and stretching, a drying step is completed for removal of remaining external and internal water from the washing and stretching steps. The fiber tow is passed over heated plates or rollers, at or above the glass transition temperature. During drying, the fiber is held at fixed length to prevent fiber shrinkage, as the molecular chains would prefer to relax to their helical formation. While most shrinkage is mitigated, a certain amount of shrinkage does occur due to slippage of the fiber over godet rollers (73).

During the drying step, water is driven from the internal fibrillar network, and the remaining pore structure collapses further. The collapse is dependent on time, temperature, and mobility of the chain segments. In order for collapse to occur, the

drying temperature must be near the glass transition temperature of the polymer (74), at about 75°C (71, 73). This is consistent with the findings of Paul, who found that while drying fiber at 50°C in a forced air oven gave complete drying, no collapse of the fiber structure had yet occurred (63).

During collapse, fibrils do not change in structure, but come closer in contact with neighboring fibrils (71, 73, 74). This decreases fiber diameter and may lead to bonding between fibrils (74). This bonding event determines the stability of the fiber to reswelling upon exposure to hot, wet conditions. If bonding does not occur, and the void structure reopens, the fiber loses strength and luster changes are observed (13). Due to pore collapse, the fiber porosity decreases (75) and the density of the fibers increases immediately and smoothly until collapse is complete (69). Drying and collapsing of fiber is vital to the production of low porosity fibers. If the collapse is not complete, the fiber will be brittle and luster differences between collapsed and uncollapsed regions will be evident.

Heat Setting

Drying and collapsing of fiber is not completely sufficient to relieve all of the internal stresses caused by drawing. Although previously tensioned heating about the T_g collapsed the fiber voids, the fiber's final state is achieved during tensionless, or low-tension, heat setting. During heat setting, bonds between the polymer chains, previously under tension during the collapse stage, are given some mobility and therefore revert to a lower-energy, more-relaxed state. During heat setting, flaws within the fiber and between the crystalline and amorphous regions are able to heal, increasing the fiber strength, but at the expense of the fiber modulus. This loss in modulus is due to the fiber shrinkage incurred, which alleviates additional shrinkage that will occur during the initial stages of higher temperature thermal treatment (76). A patent by Nikkiso Co., Ltd. noted that a 5-15% shrinkage improves the subsequent stabilizing treatment (77). Heating setting is typically completed using steam, which can be fed through a perforated conveyer steamer. Steam is often used because water is necessary during relaxation for fiber plasticization. Without water, the high temperatures during relaxation will cause fiber discoloration (14).

Fiber Properties and Structure

The properties of the resulting precursor fiber are heavily influenced by the fiber structure. The ideal fiber structure is dense and homogeneous, with little to no voids. However, due to the complicated dual diffusion process the fiber undergoes during coagulation, typical wet spun fibers do not have an ideal structure. Wet spun fibers generally have multiple radial layers, forming a skin-core structure (78). The sheath core radial macrocrystalline structure is predetermined at the time of precursor coagulation (79). The outermost white dense thin layer is the skin followed by the cortex, the endomethecium, and finally the core region. From the skin to the core, the thickness of each layer is about 0.2-0.3 μm , 2-3 μm , 2-3 μm ,

and 6-7 μm , respectively. The skin is composed of stacked layers has a sheet-like structure (78).

The structure of the sheets is dense and homogeneous. In the drawing process in the coagulation bath, the solid skin endures most of the tensile force, causing high crystallization and good orientation of molecular chains. The core, with some amorphous areas and voids, is loose and somewhat disordered. The low tensile force on the endomethecium and the core causes low crystallization and low orientation of crystallites (78). In addition to a skin-core structure, wet spun fibers tend to have capillaries, or porous structures, arranged radially in the filament cross sections. The radially oriented structure extends indefinitely down the length of the fiber. In addition to micropores and voids, surface flaws are also present. These voids and flaws in the original precursor structure can have a major impact on the final structure and properties of the carbon fiber (79, 80), and should be minimized.

Void and Pore Structure

In order to minimize the formation of voids within the fiber, it is necessary to understand their formation mechanisms. Most often, fiber voids form due to: 1) phase separation during coagulation and washing (81); 2) penetration of the coagulation bath into the fiber through surface faults, often caused by minor imperfections in the spinnerette holes (69); 3) existing gases dissolved in the fiber spinning dope (82) or other impurities. Thorne found that such voids are differentiated by their geometrical shape and size. The more cylindrical voids are symptomatic of dissolved gases within the spinning dope (82). These circular voids are evident in the optical microscopy image of a precursor fiber in Figure 4, shown as darkened circles within the fiber. This indicates that the spinning dope was not adequately de-aerated prior to spinning, or that the fiber spinning system is introducing air into the system at some point during processing.

In addition to voids due to dissolved gases, Figure 4 has a high occurrence of tear-drop shaped voids, whose origin exists at the fiber surface. The formation of such voids can be attributed to flaws in the spinnerette capillary (69), which create weak points along the fiber axis. These weak points are then susceptible to penetration by the coagulation solution, leading to formation of such voids. Alternatively, the voids may be attributed to harsh removal of residual solvent during washing. If washing occurs too quickly, the residual solvent is pulled from the fiber, allowing open pores to form on the surface of the fiber (83). This again highlights the importance of a slow washing procedure. Overall, the numerous voids in Figure 4 indicate that the precursor would not possess high mechanical properties, and as a result, would likely produce poor performance carbon fiber.

Like void shape, void size is determined by the rate of diffusion and phase separation the fiber encounters during coagulation and washing. Hong found that void size increases as the rates of diffusion and phase separation increase. As the size of the voids decreases, the number of voids increases (13). The increase in bath temperature accelerates the coagulation of the polymer and a corresponding increase in the closed porosity of the fibers (16, 61, 84). Research has found that even a small change in the coagulation bath temperature, from 2°C to 5-10°C resulted in a 19% increase in the porosity of the resulting fiber, confirming that

the level of porosity in the fiber is very sensitive to coagulation bath temperature (75).

In addition to changes in the coagulation bath temperature, other variables that have been found to impact fiber porosity include the solids content of the spinning dope. For example, Knudsen found that increasing the polymer content in the spinning solution decreased pore size (85). This was attributed to the increased viscosity of the spinning solution, which slowed diffusion and resulted in fewer void formations (70). Aside from increasing the polymer content of the spinning solution, increasing the jet stretch and draw ratio led to reduced porosity (70). In order to minimize the porosity of precursor fibers, which hinders mechanical properties, it is necessary to optimize the coagulation, washing, stretching, and drying processes.

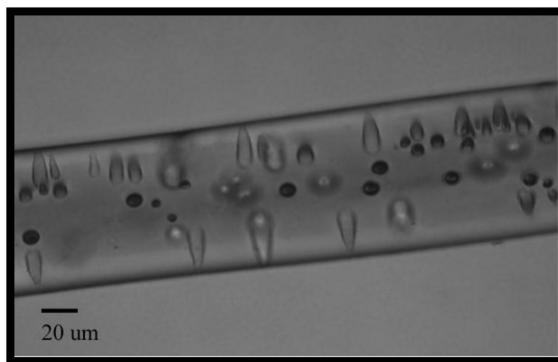


Figure 4. Voids within precursor PAN fiber.

Fiber Cross Section

Fiber cross section is one of the most important structural characteristics of fiber, as any deviation from circularity affects the luster and mechanical properties of the fiber (57). Fiber cross section is altered by changing the coagulation conditions for a given polymer/solvent/non-solvent (86, 87). Changing the coagulation conditions may involve spinning with higher coagulation bath temperatures, higher polymer contents in the spinning dope, higher solvent content in the coagulation bath (88, 89), or lower molecular weight polymer (57), all of which have been found to aid the production of round precursor fibers. A round fiber can be produced by two methods: 1) increasing the coagulation rate and building a thick outer layer that remains round as diffusion proceeds or 2) decreasing the coagulation rate and producing a thin outer layer that uniformly shrinks as diffusion continues (13). The first method, however, has been found to result in fiber with incomplete coagulation, and therefore a loose inner structure with large voids (22). The second method, of using a slow coagulation rate, is the preferred method for creating circular, dense, homogeneous fibers, but requires a balance of processing parameters.

The fibers produced below, in Figure 5, demonstrate the large difference a small change in coagulation rate, due to coagulation bath temperature, can make. Figure 5(a) represents fibers spun into a coagulation bath at 60°C. The fibers have a very round cross section and appear very homogeneous. On the contrary, a drop in coagulation bath temperature to 40°C produced fibers, in Figure 5(b) which are bean-shaped, when spun under similar conditions. This is similar to the results found by Peng (90). Again, it is important to monitor the fiber cross section in order to determine the appropriate coagulation conditions for the given fiber spinning process, in order to produce round fiber which possess the best mechanical properties.

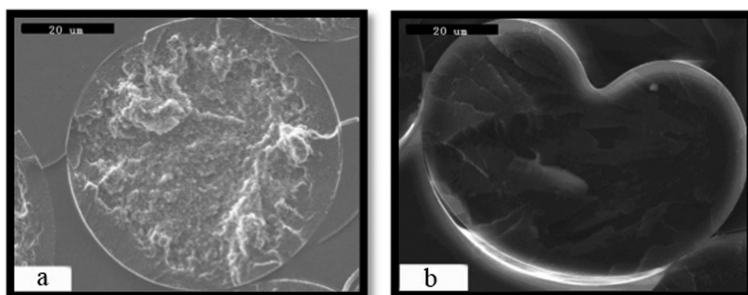


Figure 5. Effect of coagulation bath temperature on the shape of the precursor fibers, from Wang (89). (a) 60°C, (b) 40°C. (Reprinted with permission from Journal of Applied Polymer Science, Vol. 104, 3723-3729, (2007), John Wiley and Sons Publishers.)

Mechanical Properties

Fiber diameter plays a large role in the determination of fiber tenacity. Several authors have confirmed that decreasing fiber diameter leads to increasing fiber tenacity (30, 38). This is consistent with the Griffith theory, which states that at its extreme, a single polymer chain (filament of minimum diameter) would represent the strongest, highest-modulus filamentous form because such a filament could not exist with any defects present (91), and would contain no fraction of misoriented chains. This is supported by the work of Johnson, et al., who found that fiber fracture may be initiated by surface flaws or internal flaws within the fiber. Fibers were found to fail primarily from surface flaws (92).

Decreases in fiber diameter can often be attributed to an increase in the draw ratio of the fibers (58), or a reduction in solids content within the spinning dope (38). Decreasing coagulation bath temperature has also been tied to increased breaking tenacity, increased modulus and decreased breaking elongation (85). It is sensible that breaking tenacity would increase with lower coagulation temperatures, as fewer voids are formed at low temperatures. While tensile properties of commercial precursor filaments are not widely available, previous work, based on commercial examples, report typical precursor fibers to be

between 6 μm and 14 μm in diameter, with a tensile strength between 450 MPa and 700 MPa (38).

While fiber tensile strength depends on fiber diameter, fiber modulus is related directly to the degree of molecular alignment and voids within the fiber. Therefore, fiber stretch is vital to the production of high modulus fiber (70). Stretching does not greatly increase crystallinity, but enhances the axial orientation of the PAN fibrils (93). If the fiber is highly oriented, a higher modulus is expected (85).

Fiber Morphology

The morphology of the resulting precursor fibers is dependent upon a number of variables. The surfaces of the fibers depend highly on the type of spinning method used, the rate of coagulation, and the cleanliness of the process. Typically, the surfaces of wet-jet spun fibers consist of deep ridges (87), which reduce fiber luster. This is due to immediate coagulation of the polymer jets as they leave the spinnerette capillaries. On the contrary, air-gap spun fibers allow the polymer jets to relax prior to coagulation, and in addition, tend to develop a very thin skin within the air gap due to solvent evaporation. This skin results in a much smoother fiber surface following coagulation. However, air-gap spun fibers will have some very small ridges on the fiber surface, but these are consistent with the diffusion process during solution spinning.

Conclusions

Solution spinning of PAN-based polymers for carbon fiber precursors is reviewed starting with a brief history and proceeding through the fundamental processes involved. An example of multifilament, continuous PAN precursor tow, as spun at the University of Kentucky Center for Applied Energy Research, is seen in Figure 6. Lastly, precursor fiber structure and properties are discussed. Throughout, it is emphasized that the fiber spinning process, and particularly the conditions of coagulation, plays a significant role the structure and properties of the PAN precursor fibers.



Figure 6. An example of multi-filament, continuous PAN precursor tow, dry-jet spun at the University of Kentucky Center for Applied Energy Research.

References

1. Ford, C. E.; Mitchell, C. V. U.S. Patent 3,107,152 A, 1960.
2. Dupont Heritage Timeline – 1924, Dupont. http://www2.dupont.com/Phoenix_Heritage/en_US/1924_a_detail.html (accessed February 2014).
3. Bacon, R. *J. Appl. Phys.* **1960**, *31*, 283–290.
4. Houtz, R. C. *Text. Res. J.* **1950**, *20*, 786–801.
5. Nunn, R.; Fox, B. L.; Barnett, N. Making Carbon Fibre Past, Present, and Future. In *Carbon Fibre Future Directions*; Carbon Nexus: Geelong, Australia, 2013.
6. Dupont Heritage Timeline – 1941, Dupont. http://www2.dupont.com/Phoenix_Heritage/en_US/1941_detail.html (accessed February 2014).
7. Shindo, A. *Studies on Graphite Fiber*; Report No. 317; Government Industrial Research Institute: Osaka, 1961.
8. Shindo, A. *J. Ceram. Soc. Jpn.* **2000**, *108*, 35–40.
9. A Patent That Changed an Industry. World Intellectual Property Organization. <http://www.wipo.int/ipadvantage/en/details.jsp?id=2909>.
10. Watt, W.; Phillips, L. N.; Johnson, W. *The Engineer* **1966**.
11. Fitzer, E. *Carbon* **1989**, *27*, 621–645.
12. *FLIGHT International*; September 9, 1971.
13. Masson, J. C., *Acrylic Fiber Technology and Applications*; Marcel Dekker, Inc.: New York, 1995.
14. *Handbook of Fiber Chemistry*, 3rd ed.; CRC Press: Boca Raton, FL, 2007.
15. Zeng, X.; Chen, J.; Zhao, J.; Wu, C.; Pan, D.; Pan, N. *J. Appl. Polym. Sci.* **2009**, *114*, 3621–3625.
16. Bajaj, P.; Sreekumar, T. V.; Sen, K. *J. Appl. Polym. Sci.* **2002**, *86*, 773–787.

17. Tan, L.; Chen, H.; Pan, D.; Pan, N. *J. Appl. Polym. Sci.* **2008**, *110*, 1997–2000.
18. Rahman, M. A.; Ismail, A. F.; Mustafa, A. *Mater. Sci. Eng., A* **2007**, *448*, 275–280.
19. Han, C. D. *Rheol. Acta* **1970**, *9*, 355–365.
20. Serkov, A. T.; Danilin, V. A.; Kotomina, I. N. *Fibre Chem.* **1975**, *7*, 40–47.
21. Baojun, Q.; Ding, P.; Zhenqiou, W. *Adv. Polym. Technol.* **1986**, *6*, 509–529.
22. Wang, C. G.; Dong, X. G.; Wang, Q. F. *J. Polym. Res.* **2009**, *16*, 719–724.
23. Tan, L.; Liu, S.; Song, K.; Chen, H.; Pan, D. *Polym. Eng. Sci.* **2010**, *50*, 1290–1294.
24. Paul, D. R. *J. Appl. Polym. Sci.* **1967**, *11*, 439–455.
25. Pennings, A. J.; van der Hooft, R. J.; Postema, A. R.; Hoogsteen, W.; ten Brinke, G. *Polym. Bull. (Berlin)* **1986**, *16*, 167–174.
26. Smith, P.; Lemstra, P. J. *J. Mater. Sci.* **1980**, *15*, 505–514.
27. Liu, S.; Tan, L.; Pan, D.; Chen, T. *Polym. Int.* **2010**, *60*, 453–457.
28. Zhang, X.; Liu, T.; Sreekumar, T. V.; Kumar, S.; Hu, X.; Smith, K. *Polymer* **2004**, *45*, 8801–8807.
29. Sawai, D.; Yamane, A.; Takahashi, H.; Kanamoto, T.; Ito, M.; Porter, R. S. *J. Polym. Sci., Part B: Polym. Phys.* **1998**, *36*, 629–640.
30. Sawai, D.; Fujii, Y.; Kanamoto, T. *Polymer* **2006**, *47*, 4445–4453.
31. Wyatt, T. P.; Chien, A. T.; Kumar, S.; Yao, D. *Polym. Eng. Sci.* **2014**.
32. How Is Carbon Fiber Made? Zoltek. <http://www.zoltek.com/carbonfiber/how-is-it-made/> (accessed May 2014).
33. Bahl, O. P.; Shen, Z.; Lavin, J. G.; Ross, R. A. *Manufacture of Carbon Fibers*; Marcel Dekker, Inc.: New York, 1998.
34. Huang, X. *Materials* **2009**, *2*, 2369–2403.
35. Rajalingam, P.; Radhakrishnan, G. *J. Macromol. Sci., Part B: Polym. Rev.* **1991**, *31*, 301–310.
36. Morgan, P. *Carbon Fibers and Their Composites*; Taylor & Francis Group: Boca Raton, LA, 2005.
37. Abhiraman, A. S. *Precursor Structure-Fiber Property Relationships in Polyacrylonitrile-Based Carbon Fibers*; Georgia Institute of Technology: Atlanta, GA, 2008.
38. Morris, E. A.; Weisenberger, M. C.; Bradley, S. B.; Abdallah, M. G.; Mecham, S. J.; Pisipati, P.; McGrath, J. E. *Pending publication in Polymer* **2014**.
39. Lin, X.; Wang, C.; Yu, M.; Lin, Z. *Adv. Mat. Res.* **2013**, *781–784*, 2609–2613.
40. Tsai, J. S.; Lin, C. H. *J. Appl. Polym. Sci.* **1991**, *42*, 3045–3050.
41. Moreton, R.; Watt, W. *Carbon* **1974**, *12*, 543–554.
42. Leon y Leon, C. A. U.S. Patent 2013/0330551 A1, 2013.
43. Papanastasiou, T. C.; Macosko, C. W.; Scriven, L. E.; Chen, Z. *AIChE J.* **1987**, *33*, 834–842.
44. Sridhar, T.; Gupta, R. K. *J. Non-Newtonian Fluid Mech.* **1988**, *27*, 349–362.
45. Yang, J.; Mao, L.; Xu, L. *Adv. Mat. Res.* **2006**, *11–12*, 403–406.
46. Du, W.; Chen, H.; Xu, H.; Pan, D.; Pan, N. *J. Polym. Sci., Part B: Polym. Phys.* **2009**, *47*, 1437–1442.

47. Bercea, M.; Morariu, S.; Brunchi, C. E. *Int. J. Thermophys.* **2009**, *30*, 1411–1422.
48. Tan, L.; Wan, A.; Pan, D. *Polym. Int.* **2011**, *60*, 1047–1052.
49. Xinyuan, S.; Xinyuan, Z.; Yongjian, L. *J. Donghua Univ.* **2001**, *18*, 7–10.
50. Jiang, H.; Yin, Q.; Zhou, M.; Pan, D. *Adv. Mat. Res.* **2012**, *430–432*, 687–691.
51. Bennett, S. C.; Johnson, D. J. *J. Mater. Sci.* **1983**, *18*, 3337–3347.
52. Ji, B. H.; Wang, C. G.; Wang, Y. X. *J. Appl. Polym. Sci.* **2007**, *103*, 3348–3352.
53. Ouyang, Q.; Chen, Y. S.; Zhang, N.; Mo, G. M.; Li, D. O.; Yan, Q. *J. Macromol. Sci., Part B: Phys.* **2011**, *50*, 2417–2427.
54. Ji, B. H. *Adv. Mat. Res.* **2011**, *295–297*, 1532–1535.
55. Zeng, X.; Hu, J.; Zhao, J.; Zhang, Y.; Pan, D. *J. Appl. Polym. Sci.* **2007**, *106*, 2267–2273.
56. Perepelkin, K. E.; Pugach, B. M. *Fibre Chem.* **1974**, *6*, 69–72.
57. Tsai, J. S.; Su, W. C. *J. Mater. Sci. Lett.* **1991**, *10*, 1253–1256.
58. Wang, Y. X.; Wang, C. G.; Bai, Y. J.; Bo, Z. *J. Appl. Polym. Sci.* **2007**, *104*, 1026–1037.
59. Qin, J.; Liu, Z.; Pan, D.; Li, F. *Text. Res. J.* **1995**, *65*, 570–582.
60. Terada, K. *Sen'i Gakkaishi* **1973**, *29*.
61. Law, S. J.; Mukhopadhyay, S. K. *J. Appl. Polym. Sci.* **1996**, *62*, 32–47.
62. Sobhanipour, P.; Cheraghi, R.; Volinsky, A. A. *Thermochim. Acta* **2011**, *518*, 101–106.
63. Paul, D. R. *J. Appl. Polym. Sci.* **1969**, *13*, 817–826.
64. Postman, W. *Text. Res. J.* **1980**, *50*, 444–453.
65. Nakayama, T.; Hashimoto, Y.; Nakagawa, M. U.S. Patent 20120021125 A1, 2012.
66. Gupta, A. K.; Paliwal, D. K.; Bajaj, P. *J. Macromol. Sci., Part B: Polym. Rev.* **1991**, *C31*, 1–89.
67. Jin, D.; Huang, Y.; Liu, X.; Yu, Y. *J. Mater. Sci.* **2004**, *39*, 3365–3368.
68. Philip P. Burks, J.; Quinton E. Cooke, J. U.S. Patent 3,859,122 A, 1975.
69. Craig, J. P.; Knudsen, J. P.; Holland, V. F. *Text. Res. J.* **1962**, *32*, 435–448.
70. Arbab, S.; Noorpanah, P.; Mohammadi, N.; Zeinolebadi, A. *Polym. Bull. (Berlin)* **2011**, *66*, 1267–1280.
71. Junjie, H.; Chunxiang, L.; Pucha, Z.; Denghua, L. *Thermochim. Acta* **2013**, *569*, 42–47.
72. Rahman, M. A.; Ismail, A. F.; Mustafa, A.; Ng, B. C.; Hasbullah, H.; Rahaman, M. S. A.; Abdullah, M. S. In *Development in Polymer-Based Carbon Fibre Research in Malaysia*; pp 169–179
73. Bell, J. P.; Dumbleton, J. H. *Text. Res. J.* **1971**, *41*, 196–203.
74. Dumbleton, J. H.; Bell, J. P. *J. Appl. Polym. Sci.* **1970**, *14*, 2402–2406.
75. Zlatoustova, L. A.; Smirnova, V. N.; Medvedev, V. A.; Serkov, A. T. *Fibre Chem.* **2002**, *34*, 200–202.
76. Baojun, Q. *Chin. J. Polym. Sci.* **1987**, *5*, 269–284.
77. Ohsaki, T.; Imai, K.; Miyahara, N. U.S. Patent 4,925,604, 1990.
78. Ge, H.; Liu, H.; Chen, J.; Wang, C. *J. Appl. Polym. Sci.* **2007**.
79. Barnett, F. R.; Norr, M. K. *Composites* **1976**, *7*, 93–99.

80. Chen, J. C.; Harrison, I. R. *Carbon* **2002**, *40*, 25–45.
81. Grobe, V.; Heyer, H. *Faserforsch. Textiltech.* **1968**, *19*, 313–318.
82. Thorne, D. J. *J. Appl. Polym. Sci.* **1970**, *14*, 103–113.
83. Hong, W. D.; Jie, H. J.; Qing, X. X.; Guang, M.; Yu, G.; Xiang, L. C.; Hua, W. *Z. Chin. Phys. C* **2011**, *35*, 870–874.
84. Dart, S. L. *Text. Res. J.* **1960**, *30*, 372–380.
85. Knudsen, J. *Text. Res. J.* **1963**, *33*, 13–20.
86. Han, C. D.; Park, J. Y. *J. Appl. Polym. Sci.* **1973**, *17*, 187–200.
87. Iovleva, M. M.; Banduryan, S. I.; Zlatoustova, L. A.; Radishevskii, V. M.; Serkov, A. T.; Budnitskii, G. A. *Fibre Chem.* **1999**, *31*, 140–142.
88. Ji, B. *Adv. Mat. Res.* **2011**, 287-290, 1832–1836.
89. Wang, Y. X.; Wang, C. G.; Yu, M. J. *J. Appl. Polym. Sci.* **2006**, *104*, 3723–3729.
90. Peng, G. Q.; Wen, Y. F.; Yang, Y. G.; Liu, L. *Int. J. Polym. Anal. Charact.* **2008**, *13*, 369–375.
91. Griffith, A. A. *Philos. Trans. R. Soc. London, A* **1921**, *221*, 163–198.
92. Johnson, J. W.; Thorne, D. J. *Carbon* **1969**, *7*, 659–661.
93. Edie, D. D. *Carbon* **1997**, *36*, 345–362.

Chapter 10

Designing the Structure of Carbon Fibers for Optimal Mechanical Properties

Soydan Ozcan,* Frederic Vautard, and Amit K. Naskar

Materials Science and Technology Division, Oak Ridge National Laboratory,
Oak Ridge, Tennessee 37830, United States

*E-mail: ozcans@ornl.gov, soydanozcan@gmail.com

The formulation of carbon structures from various polymer precursors is reviewed along with the resultant fiber properties. The final structures and end properties of the carbon fiber can differ significantly depending on both the precursor chemistry and the associated processing. Polyacrylonitrile (PAN) and mesophase pitch are the predominant precursors. PAN-based carbon fibers consist of nanocrystalline graphitic domains typically 1.5–5 nm in size surrounded by amorphous carbon. With PAN based carbon fibers, the skin–core structure plays a significant role in their mechanical properties and a more homogenous carbon fiber microstructure offers the possibility of a new set of tensile strength and elastic moduli. Pitch-based carbon fibers are 10–50 nm crystallites with the graphitic (002) planes mostly aligned parallel to the fiber axis. Here we show that microstructural defects distribution (0.1–200 nm) measured by small angle X-ray scattering are directly related to the tensile strength of carbon fibers. Ultimately a comprehensive understanding of carbon fiber structure, defects and processing science offers the opportunity to design carbon fiber microstructures with improved properties and from alternative precursor at reduced cost.

Introduction

Carbon fibers are widely used advanced materials with exceptional specific strength and elastic modulus (1–4). In the manufacturing of high performance carbon fiber composites, outstanding mechanical properties are needed for their application in aerospace and aeronautics, transportation, sport and recreation, compressed gas storage, and civil engineering. The properties of a carbon fiber composite depend on the properties of its constituents (fibers and matrix) and also depend on the properties of the interface/interphase (5–9). Depending on the nature of the matrix, carbon fiber composites can be used for a wide range of applications. For example, carbon fiber/ceramic matrix and carbon fiber/carbon matrix composites are able to withstand the mechanical loading associated with elevated temperatures in extreme environments (10–12). Consequently, they have attracted interest in the fields related to high temperature energy materials. These markets demand constant improvements in performance. In comparison, polymer matrix composites demand exceptional mechanical properties at relatively low temperature; with easier processing and favorable cost-to-performance ratio.

Historically, carbon fibers have been produced at the industrial scale from three main polymer precursors: rayon, pitch, and polyacrylonitrile (PAN). While the carbon fiber market is presently dominated by PAN precursors (95%), pitch-based precursors are used for specific carbon fiber applications. The typical manufacturing of carbon fibers consists of manufacturing a thermoplastic fiber (spinning of the precursor) followed by an oxidative stabilization step, carbonization, and eventually graphitization. The nature of the precursor and the process conditions have a very strong influence on the properties of the final graphite-like microstructure (degree of crystallinity, size and orientation of the crystallites). As a result, the mechanical, thermal, and electronic properties of the fibers depend on the type of precursor and its associated processing. Each step of the manufacturing process is described in the following section to facilitate an understanding of our results on the properties and microstructures of different carbon fibers.

Spinning of the Precursor Fiber

PAN-based fibers are processed industrially by use of the solution spinning. Although the modified melt-spinning process was discovered in the 1970s (13–15), it has not been scaled up for industrial applications. PAN polymer is highly polar due to the nitrile pendant groups in its molecular structure (Figure 1a) and has a glass transition temperature of ~100 °C. PAN thermally alters its chemical structure before reaching its melting point and is suitable for spinning from its solution in polar solvents. Typical solvents are dimethylsulfoxide (DMSO), dimethylformamide (DMF), ethylene carbonate, dimethylacetamide (DMAc), aqueous sodium thiocyanate, and aqueous zinc chloride (16). The PAN-based solution is pushed through a spinneret into a coagulation bath to form threads. The newly formed polymer fiber goes through several stages of washing and stretching. Lubricants, antistatic agents, and emulsifiers are applied to the spun fiber to improve the handling of fiber tow (typically thousands of individual

Oxidative Stabilization

Mesophase-pitch and PAN precursor fibers typically undergo oxidative stabilization from controlled heating in air for 1.5 to 2 hours (22). The oxidative/stabilization temperature is typically increased stepwise during the process owing to the exothermic nature of the associated reactions (e.g., cyclization, dehydrogenation, aromatization, oxidation, and crosslinking) that can raise the fiber temperature to between 180 °C and 300 °C (23, 24). The thermal treatment converts the thermoplastic PAN precursor into an infusible/cyclic ladder structure by cyclization of the nitrile groups (Figure 2) and crosslinking of the chain molecules (25, 26). The stabilization prevents melting or fusion of the fiber during the subsequent carbonization step. Stabilization, also helps to optimize the carbon yield (27), and is the most important step in the carbon fiber manufacturing process. Precise control of the stabilization reactions is very critical, since over-oxidized precursor usually produces brittle carbon fibers with poor mechanical properties while under-oxidized precursor retains the thermoplastic phase and allows the filaments to fuse during carbonization.

PAN precursor can be stabilized in air or in an inert atmosphere such as nitrogen. However, it has been demonstrated that a polymer backbone containing oxygen-containing groups in the ladder structure provides greater stability during carbonization (28, 29). Fitzer et al. (28) found that oxygen acts as an initiator for the cyclization of the nitrile groups. Particularly, C=O groups (ketones) are generated in the carbon backbone because of the presence of oxygen (30) and those groups promote the initiation of the cyclization process through a nucleophilic reaction. Oxygen also leads to some dehydrogenation and generates other oxygen-containing groups such as hydroxyl and carboxylic acids. These reactions are at the origin of the generation of carbon monoxide, carbon dioxide, and water during the oxidative stabilization process (28). A typical chemical structure of oxidized PAN precursor and its associated ^{13}C Nuclear Magnetic Resonance spectrum is shown in Figure 3.

Various structures and mechanisms have been proposed for the oxidative stabilization of PAN precursor, including structures with epoxide-bridge-type bonding (31) or bearing hydroxyl and carbonyl groups (32). During the stabilization, stretching the PAN polymer precursor is important because it prevents the polymer chains from relaxing and losing their orientation.

The range of temperature for the oxidative stabilization of a mesophase-pitch precursor is between 250 °C and 400 °C. The increase of temperature during the process has to be incremental as well. The stabilization mechanism includes dehydrogenation and crosslinking of the pitch precursor along with release of CO, CO₂, and H₂O. It is believed that more stable oxygen-containing functional groups are generated along with some carbonyl and phenolic hydroxyl groups as well (33, 34). A general mechanism is depicted in Figure 4.

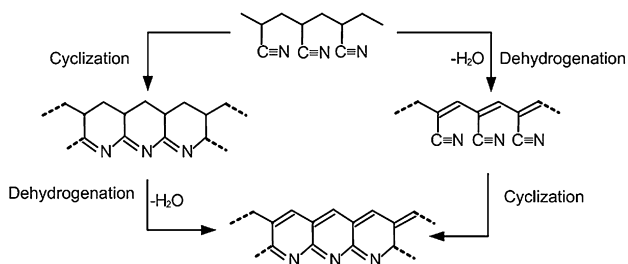


Figure 2. Cyclization and dehydration mechanisms generating the ladder structure during the oxidative stabilization process of PAN precursor. (Reproduced with permission from ref (24). Copyright 1989 Elsevier.)

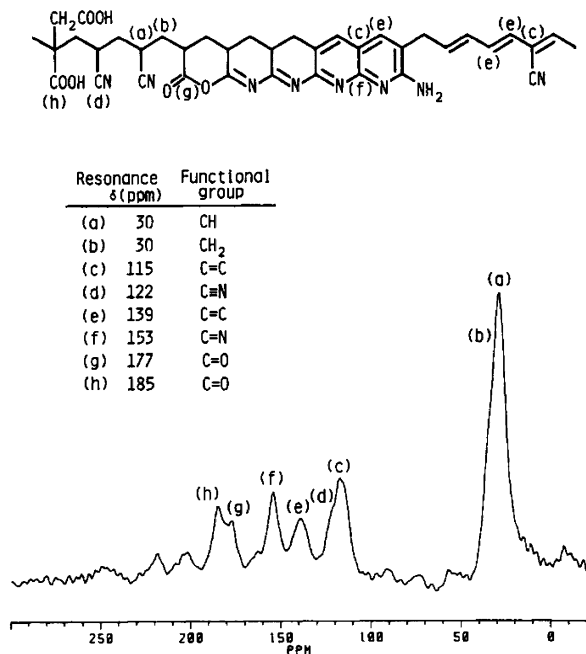


Figure 3. Ladder structure obtained by stabilizing PAN in the presence of oxygen shown with typical ¹³C Nuclear Magnetic Resonance spectrum. (Reproduced with permission from ref (26). Copyright 1990 American Chemical Society.)

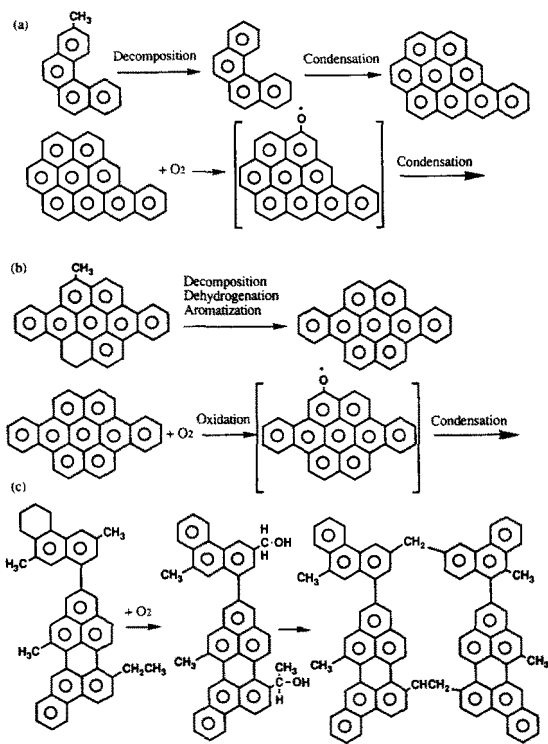


Figure 4. Possible reaction mechanisms of the oxidative stabilization of pitch precursor. (Reproduced with permission from ref (34). Copyright 1993 Elsevier.)

Carbonization

The purpose of the carbonization step is simply to eliminate all elements but carbon from the stabilized precursor and to generate a graphite-like carbon microstructure (Figure 5). The carbonization protocol varies depending on the chemistry of the precursor. The carbonization of PAN precursors occurs under tension at temperatures ranging from 600 °C to 1600 °C. The heteroatoms and some carbon and hydrogen elements are released in the form of methane, hydrogen, nitrogen, hydrogen cyanide, water, carbon monoxide, carbon dioxide, ammonia, and various other gases (35). To avoid a thermal shock, a pre-carbonization step can be applied at temperatures ranging from 300 °C to 700 °C. Controlling the temperature is as essential during the carbonization step as during the stabilization step. A too rapid carbonization rate will introduce defects in the carbon fiber, while a too slow carbonization rate will cause the loss of too much nitrogen at the early stages of the carbonization, which can generate pores and quickly decrease the flexibility of the molecular structure. High purity nitrogen is used during carbonization to prevent oxidation of the fiber at high temperature and to dilute the toxic gas that is produced. The diameter of the fiber is significantly reduced. During the process, the fiber is stretched to prevent excessive shrinkage as well as some loss in the preferred

orientation of the growing graphitic crystallites. Figure 5 shows the formation of a graphite-like microstructure from the ladder structure of PAN obtained after oxidative stabilization.

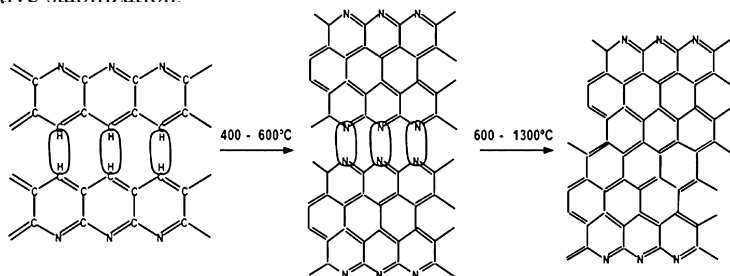


Figure 5. Possible reactions occurring during the carbonization of stabilized polymer PAN precursor. (Reproduced with permission from ref (36). Copyright 2002 Elsevier.)

A high temperature heat treatment called graphitization can follow the carbonization step. The graphitization process requires temperatures up to 3000 °C and an argon atmosphere, because nitrogen could react with carbon to generate carbon nitride (37). During this step, the turbostratic carbon structure becomes more ordered, which increases the size of the crystallites in the fiber axis direction and reduces the interlayer spacing as well as the void content. The resulting fibers are composed of 99% carbon, with a more-ordered carbon microstructure. The fibers have a slightly higher modulus but at the expense of the ultimate tensile strength.

When it comes to mesophase-pitch precursor, high modulus carbon fibers can be produced relatively easily. During carbonization, the heteroatoms are eliminated and the crystallites made of aromatic hydrocarbon are enlarged. With the increasing heat treatment temperature, both the tensile strength and modulus continually increase and the graphitic structure forms (38). This occurs because the mesophase pitch is made of repeating aromatic hydrocarbon layers, with low heteroatom content and low levels of impurities (38). However, the final properties of the fiber strongly depend on the thermal history, which requires optimization (maximum temperature and soak time) based on mesophase content and structure of the pitch precursor (39). Despite the possibility of gaining very high tensile modulus, the major disadvantage of pitch-based carbon fibers is their brittle nature and their low ultimate tensile strength as compared to PAN-based carbon fibers.

Experimental Procedures

Five references of PAN-based carbon fibers manufactured by Hexcel (AS4, IM10, and UHMS) and Toray (T700 and T1000) and two references of pitch-based carbon fibers manufactured by Amoco Performance Products, Inc. (Thornel P120) and Cytec (K1100) were used as-received for this study. The average mechanical properties (tensile properties) of these fibers, as reported by the manufacturers, are given in Table 1.

Wide-Angle X-ray Diffraction (WAXD) was used to measure the crystalline parameters that characterize the microstructure of the fibers. These parameters include (a) the d-spacing between the graphitic layers; (b) the so-called “stack height” of the graphitic layers, reported as L_c ; (c) the crystal size in the direction parallel to the graphene planes, reported as L_a ; and (d) the orientation of the graphitic layers relative to the fiber axis, reported as the misorientation angle ϕ . All measurements were made on a fully automated Panalytical Materials Research Diffractometer using $\text{CuK}\alpha$ radiation ($\lambda = 1.5418 \text{ \AA}$) in transmission geometry. The sample consisted of a parallel array of fibers. The breadth of the (002) reflection was measured on the equator (perpendicular to the fibers), while the breadth of the (100) reflection was measured in the meridian direction (parallel to the fibers).

For Small-Angle X-ray Scattering (SAXS) measurements, samples were made from randomly oriented chopped and crushed fibers. The pore-size parameters of a high modulus fiber are not affected when it is ground into a powder. The SAXS measurements were performed by use of a three pinhole system. Copper $\text{K}\alpha$ radiation was provided by a double focusing mirror, and the patterns were recorded using a two-dimensional wire detector. Two sample-to-detector distances (1.5 m and 0.5 m) allowed the measurements to be performed over a scattering vector range ($q = 4 \sin\theta/\lambda$) of 0.01 to 0.45 \AA^{-1} . The two-dimensional patterns were corrected for flat field errors and scattering from the sample holder. In the case of the powder patterns, the two-dimensional data were integrated azimuthally to obtain a one-dimensional plot of intensity versus the scattering vector, q , and the intensity was converted to absolute units (cm^{-1}) by use of previously calibrated standards made of polyethylene and/or glassy carbon. The data were analyzed with Irena software.

Transmission Electron Microscopy (TEM) studies were conducted on a Hitachi HF3300 TEM/STEM operating at 200 kV. Transverse cross-sections of carbon fibers were prepared for TEM analysis using a focused ion beam (FIB) with a Hitachi NB5000 FIB-SEM instrument. Standard in situ lift-out techniques were used for preparing transverse cross sections of the fibers. EPON G2 epoxy resin was used to attach the carbon fibers to the TEM omniprobe grids. A protective layer of electron-beam-deposited tungsten was centered on the fiber axis. Sections were milled with a 40 keV ion beam to a thickness of about 100–200 nm. The specimens were further thinned with a 5 keV ion beam, which was followed by multiple polishing with a 2 keV ion beam.

Results and Discussion

The relationship between microstructure and ultimate tensile strength was investigated for both PAN- and pitch-based carbon fibers. Two moderate strength PAN-based carbon fibers (AS4 and T700), two high strength PAN-based carbon fibers (T1000 and IM10), and a high modulus (UHMS) PAN-based fibers were chosen. In addition, two high modulus pitch-based carbon fibers (P120 and K1100) were also included. Each set of carbon fibers was chosen because of its unique microstructure and possible levels of internal defects. The average tensile

mechanical properties and the diameter and density of those fibers, as supplied by the manufacturers, are shown in Figure 6 and Table 1.

Typically, PAN-based carbon fibers have a higher strength and a lower modulus compared to mesophase-pitch-based fibers. As discussed hereafter, this is directly related to their microstructures. The value of the modulus is mainly determined by the degree of order in the carbon structure of the crystallites and the orientation of the crystallites towards the axis of the fiber. Mesophase-pitch-based fibers have a much more crystalline and oriented graphitic structure compared to PAN-based fibers (Table 2). The theoretical modulus of graphene (1060 GPa) is almost achieved by mesophase-pitch fibers (~95% of the theoretical value), because of the highly oriented and highly crystalline microstructure. A comparison of both types of precursors clearly reveals that the tensile strength and the strain at break decrease as the modulus increases (Table 1). The highest strength carbon fiber now commercially available approaches 7000 MPa; however, that corresponds to only ~7% of the theoretical tensile strength of graphene (100 GPa) (40).

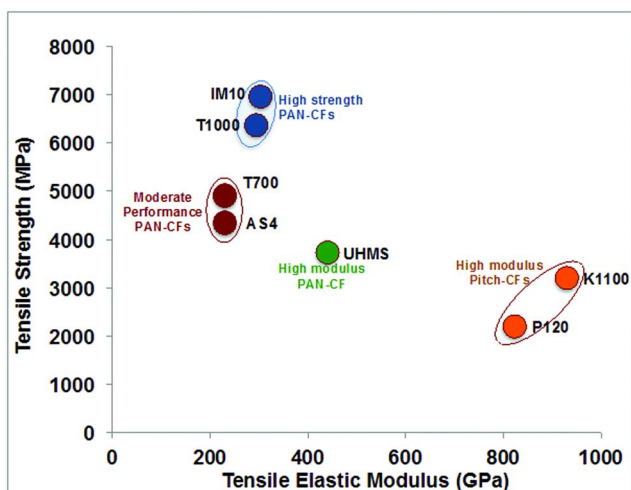


Figure 6. Tensile strength and modulus of the different carbon fibers used in this study. (see color insert)

As shown in Table 1, PAN-based carbon fibers T1000 and IM10, which have the highest values for strain at break, also have the smallest diameters of PAN-based carbon fibers (5.0 μm and 4.2 μm respectively), with similar density values. This is particularly true when comparing the other PAN-based fibers such as AS4. This observation is not valid for the two pitch-based fibers, so other parameters are responsible for the difference in tensile strength. Mittal et al.^{6a} also noticed that the tensile strength of PAN-based carbon fibers increased as the diameter decreased. Reducing the diameter of the fiber statistically decreases the chances of a rupture-producing structural defect in the tested sample. The principle in operation is the same as the one explaining the sensitivity of tensile strength to

gauge length (Weibull theory). Typically, PAN-based fibers are smaller in diameter than pitch-based fibers.

When comparing the crystalline parameters (Table 2), it is clear that pitch-based fibers show a more graphitic carbon structure, as the interlayer distance d_{002} is significantly lower, the average size of the crystallites is much larger, and their misorientation angle is much lower than those of PAN-based fibers. This is in agreement with higher density and a much higher modulus observed in pitch-derived carbon fibers. When comparing both pitch-based fibers, it appears that a higher value of misalignment (i.e., less degree of orientation) leads to lower values of modulus and strength. A comparison of the crystalline parameters of the PAN-based fibers AS4, T700, T1000, and IM10 provides trends about their influence on the mechanical properties. The larger the crystallites (especially in the fiber axis direction), when associated with a lower misalignment, the higher are the strength and modulus.

Table 1. Density, diameter, and strain at break of the different fibers used in this study

<i>Sample</i>	<i>Density (g/cm³)</i>	<i>Filament diameter (μcm)</i>	<i>Tensile strength (MPa)</i>	<i>Tensile modulus (GPa)</i>	<i>Strain at break (%)</i>
AS4	1.79	6.1	4330	231	1.8
T700	1.80	7.0	4900	230	2.1
T1000	1.80	5.0	6370	294	2.2
IM10	1.79	4.2	6964	310	2.0
UHMS	1.88	5.0	3730	440	1.1
P120	2.16	10.0	2400	830	0.3
K1100	2.20	12.0	3200	930	0.2

Nevertheless, the fiber UHMS is the exception of the group, as even larger crystallites with better alignment in the fiber axis led to a higher modulus, which is expected, but with lower strength and strain at break. A more detailed study of its structure at the molecular level was conducted to explain this discrepancy.

Nowadays, robust quality control is in place for the industrial production of carbon fibers. Contamination of the precursor, during its synthesis, fiber spinning to its stabilization, and carbonization, is avoided by applying rigorous process control. The carbonization step is optimized to minimize the rate of gas release. Such a controlled carbonization helps to systematically eliminate the formation of macroscopic voids in state-of-the-art carbon fiber production lines. Obviously, nano- to microscale defects in the carbon structure determine the mechanical performance of the fibers. In this study, our focus was on quantification of the nanoscale voids characterized by SAXS. Moreover, the load transfer throughout the carbon structure can especially be affected by the presence of basal extra-plane dislocations and dislocation loops. Therefore, each specimen

was analyzed by TEM. The TEM observations were combined with WAXD and SAXS measurements.

Figure 7 shows the pore size distribution obtained by SAXS analysis for pitch-based fibers P120 and K1100, as well as a TEM image of the cross section of K1100 fibers. Details of the methodology for pore size analysis of the fibers are discussed elsewhere (41–45). The majority of the pores in P120 fibers have a diameter less than 30 Å, which is not observed in K1100 fibers. Both references show a significant amount of large pores averaging 50 Å and 80–90 Å in diameter, and even a few pores with diameters of 400 Å and 600 Å. Even though the mesophase-pitch-based fibers have a much higher degree of order, with larger crystallites that are better aligned in the fiber axis, as shown in the TEM picture in Figure 7b, the existence of larger pores is likely responsible for a much lower tensile strength. Figure 7a suggests that both pitch-based fibers have very large pores, but the total amount of porosity is lower in K1100 fibers. It was also observed that the average misorientation angle of the crystallites is lower in the K1100 fibers. This explains the higher tensile strength of the K1100 fibers.

Table 2. Crystalline parameters of the carbon structure of the different fibers determined by wide-angle X-ray diffraction measurement

<i>Sample</i>	d_{002} (Å)	L_c (Å)	L_a (Å)	<i>Misorientation angle, φ (degree)</i>
AS4	3.51	16.2	45.3	19.2
T700	3.49	18.1	62.1	16.8
T1000	3.49	17.7	49.1	17.1
IM10	3.49	20.0	64.0	15.3
UHMS	3.43	48.2	157.3	9.9
P120	3.38	114.9	466.0	6.6
K1100	3.37	229.6	377.5	4.9

Figure 8 displays the pore size distributions obtained by SAXS analysis for the three types of PAN-based fibers (moderate strength, high strength, and high modulus). The fiber having the largest pores is the high modulus UHMS fiber. Its structure has larger and better aligned crystallites, with a lower interplanar distance than the other two fibers. The carbon layers constituting its structure are crumpled and parallel to the fiber, with pores elongated parallel to the fiber axis, as shown by the TEM image in Figure 8. A similar type of structure was observed by Guigon et al. and Ozcan et al. as well (46, 47). UHMS fibers have pore diameters larger than 20 Å, with the total amount of porosity less than that for AS4 fibers. Again, the comparison of porosity in the PAN-based fibers suggests that the strength value is determined by the diameter of the largest pores existing in the carbon structure.

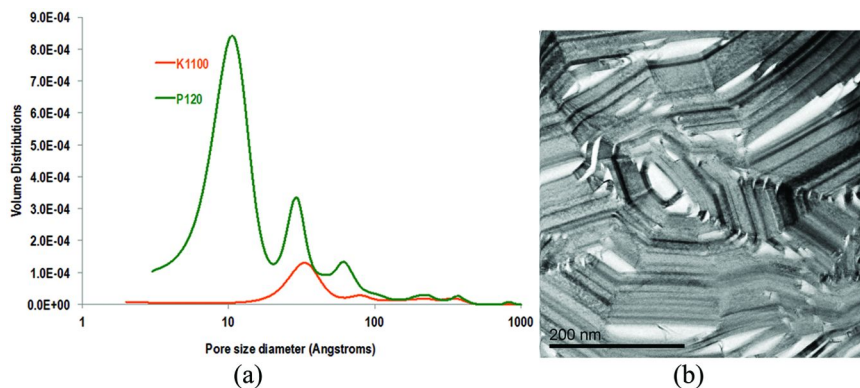


Figure 7. (a) Pore size distributions existing in P120 and K1100 carbon fibers. (b) TEM image corresponding of the cross section of K1100 carbon fibers. (see color insert)

The pore size distributions in the moderate and high strength fibers are compared in Figure 9. The distributions are very similar. The largest pores have a diameter of 30–50 Å, which correlates with values obtained by Thünemann and Ruland with PAN-based fibers (48). One noticeable result is that, on the basis of largest pores, IM10 fibers show a slightly lower pore diameter than that of the other fibers. This is in agreement with the lower value of misorientation angle and the larger size of crystallites existing in IM10 fibers. This also leads to the conclusion that reducing the size of pores in the 30–50 Å range makes a sharp difference in terms of tensile strength. The TEM micrograph corresponding to IM10 fibers (Figure 9) clearly shows a turbostratic structure, much less organized in comparison with the pitch-based fibers and the high modulus PAN-based fibers, but with no visible pores.

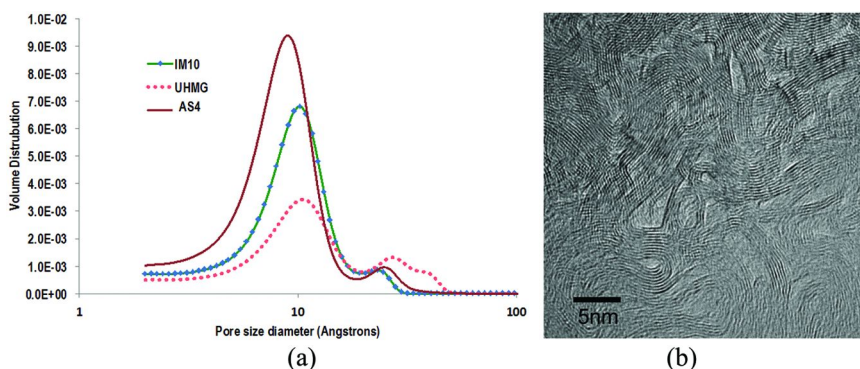


Figure 8. (a) Comparison of pore size distributions existing in moderate strength, high strength, and high modulus PAN-based carbon fibers. (b) TEM image of the cross section of a high modulus PAN-based carbon fiber (UHMS). (see color insert)

Comparing the nano- and microstructures of the different fibers in terms of crystalline parameters and pore size distributions highlights the relationship between the tensile mechanical properties and those structures. A carbon structure made of highly graphitic, large and well-oriented crystallites (like the ones existing in mesophase-pitch-based fibers) usually leads to a lower volume of porosity, but the pores are much larger than the less-organized structures existing in PAN-based fibers. Similar data was also reported by Takaku and Shioya (49). The presence of those large pores is directly responsible for the lower tensile strength of mesophase-pitch-based fibers, in comparison with PAN-based fibers.

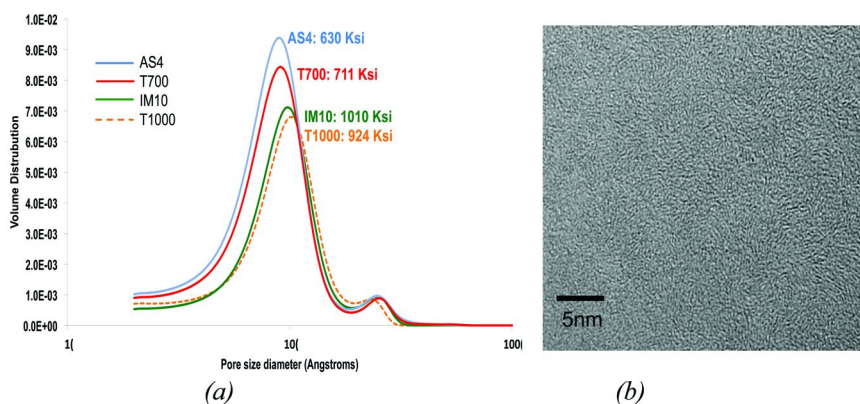


Figure 9. (a) Comparison of pore size distributions existing in moderate strength (AS4 and T700) and high strength (IM10 and T1000) PAN-based carbon fibers. (b) TEM image of the cross section of high strength PAN-based carbon fibers (IM10). (see color insert)

Nevertheless, the highly graphitic and well-aligned structure existing in mesophase-pitch-based fibers is the origin of the high values in tensile modulus. For PAN-based fibers, it appears that improved order in the carbon structure, increased crystallite size, and enhanced orientation lead to higher values for both modulus and strength, as long as it does not produce too much graphite stacking and porosity created by folded graphite sheets. An improvement in the level of order existing in a turbostratic structure can potentially decrease the size of the pores, but there is a threshold that should not be passed. A more graphitic structure beyond that threshold leads to the generation of larger pores that affect tensile strength. Those conclusions are supported by the SAXS characterization and molecular dynamics simulation of Zhu et al. (50) The report showed that, under tensile load, the volume of microvoids pre-existing in a carbon fiber increases and the stress generated locally in the structure reaches its ultimate strength, provoking fiber rupture. Bennett et al. (51) claimed that misorientation of the crystallites around the pores leads to the failure. Similar experimental work led to identical conclusions in the case of aramid fibers (52); that is, the greater

the number of microvoids and the larger they are, the weaker is the aramid fiber. The observation is in agreement with the Weibull theory, as the probability of finding large defects determines the probability of failure under load (weakest link approach).

In this study, the characterization of the crystalline parameters and of the pore size distribution was done through analysis in volume. The possibility of heterogeneity of pore distribution or of crystallinity in the fiber's carbon structure, as is possible in a skin-core type structure, was not investigated. Of course this can influence the value of ultimate tensile strength as well (53), and this will be investigated in future work.

All in all, to achieve very high values of ultimate tensile strength, several conditions must be met. A PAN-based precursor should be used, and the generation of a turbostratic carbon structure is a necessity. As little porosity as possible should be present, and, most important, the size of the largest pores should be minimized. Last, a skin-core structure should be avoided, and the diameter of the fiber should be as small as possible.

Conclusions

The carbon structures and pore size distributions of different PAN-based and pitch-based carbon fibers were characterized and compared. Highlighted were the influence of the degree of order in the carbon structure, the influence of size and orientation of crystallites, and the influence of largest pore size on ultimate tensile strength and tensile modulus. The tensile modulus is essentially dictated by the degree of order in the carbon structure and the size and orientation of the crystallites. The ultimate tensile strength is mainly dictated by the diameter of the largest pores in that structure and the diameter of the fiber.

Acknowledgments

The authors would like to acknowledge generous support from Late Prof. Joseph E. Spruiell, Department of Materials Science and Engineering, University of Tennessee at Knoxville, in X-ray characterization and analysis of the data. This research was sponsored by DARPA's Advanced Structural Fibers Program. The authors would like to thank the SHaRE user facility operated for the U.S. Department of Energy Office of Science by Oak Ridge National Laboratory. Jane Howe and Dorothy W. Coffey are sincerely acknowledged for their help regarding electron microscopy characterization. Hexcel and Thornel are gratefully thanked for providing some of the carbon fibers used in this study.

This book chapter has been authored by UT-Battelle, LLC, under Contract No. DE-AC05-00OR22725 with the US Department of Energy. The US government retains and the publisher, by accepting the article for publication, acknowledges that the US government retains a nonexclusive, paid-up, irrevocable, worldwide license to publish or reproduce the published form of this manuscript, or allow others to do so, for US government purposes.

References

1. Chung, D. D., *Carbon Fiber Composites*; Butterworth-Heinemann: Newton, MA, 1994.
2. Liu, Y.; Kumar, S. Recent progress in fabrication, structure, and properties of carbon fibers. *Polym. Rev.* **2012**, *52* (3–4), 234–258.
3. Papkov, D.; Goponenko, A.; Compton, O. C.; An, Z.; Moravsky, A.; Li, X. Z.; Nguyen, S. T.; Dzenis, Y. A. Improved graphitic structure of continuous carbon nanofibers via graphene oxide templating. *Adv. Funct. Mater.* **2013**, *23*, 5763–5770.
4. Vautard, F.; Ozcan, S.; Poland, L.; Nardin, M.; Meyer, H. Influence of thermal history on the mechanical properties of carbon fiber-acrylate composites cured by electron beam and thermal processes. *Composites, Part A* **2012**, *45*, 162–172.
5. Schultz, J.; Nardin, M. Some physico-chemical aspects of the fibre-matrix interphase in composite materials. *J. Adhes.* **1994**, *45* (1–4), 59–71.
6. Vautard, F.; Ozcan, S.; Meyer, H. Properties of thermo-chemically surface treated carbon fibers and of their epoxy and vinyl ester composites. *Composites, Part A* **2012**, *43* (7), 1120–1133.
7. Vautard, F.; Grappe, H. A.; Ozcan, S. Stability of carbon fiber surface chemistry under temperature and its influence on interfacial adhesion with polymer matrices. *Appl. Surf. Sci.* **2013**, *268*, 61–72.
8. Tezcan, J.; Ozcan, S.; Gurung, B.; Filip, P. Measurement and analytical validation of interfacial bond strength of PAN-fiber-reinforced carbon matrix composites. *J. Mater. Sci.* **2008**, *43* (5), 1612–1618.
9. Vautard, F.; Ozcan, S.; Paulauskas, F.; Spruiell, J.; Meyer, H.; Lance, M. J. Influence of the carbon fiber surface microstructure on the surface chemistry generated by a thermo-chemical surface treatment. *Appl. Surf. Sci.* **2012**, *261*, 473–480.
10. Lamouroux, F.; Bertrand, S.; Pailler, R.; Naslain, R.; Cataldi, M. Oxidation-resistant carbon-fiber-reinforced ceramic-matrix composites. *Compos. Sci. Technol.* **1999**, *59* (7), 1073–1085.
11. Ozcan, S.; Krkoska, M.; Filip, P. Frictional Performance and Local Properties of C/C Composites. In *Developments in Advanced Ceramics and Composites: Ceramic Engineering and Science Proceedings*; American Ceramic Society: Danvers, MA, 2005; Volume 26, pp 127–138.
12. Ozcan, S.; Filip, P. Wear Of carbon fiber reinforced carbon matrix composites: Study of abrasive, oxidative wear and influence of humidity. *Carbon* **2013**, *62*, 240–247.
13. Porosoff, H. Melt-Spinning Acrylonitrile Polymer Fibers. U.S. Patent 4,238,442, 1979.
14. Pfeiffer, R. E.; Peacher, S. E. Process for Melt-Spinning Acrylonitrile Polymer Fiber. U.S. Patent 4,220,617, 1980.
15. Blickenstaff, R. A. Improved Acrylonitrile Polymer Spinning Process. U.S. Patent 4,94,948, 1978.
16. Masson, J. *Acrylic Fiber Technology and Applications*; Marcel Dekker: New York, 1995.

17. Mittal, J.; Bahl, O.; Mathur, R. Single step carbonization and graphitization of highly stabilized PAN fibers. *Carbon* **1997**, *35* (8), 1196–1197.
18. Yusof, N.; Ismail, A. Post spinning and pyrolysis processes of polyacrylonitrile (PAN)-based carbon fiber and activated carbon fiber: A review. *J. Anal. Appl. Pyrolysis* **2012**, *93*, 1–13.
19. Chen, J.; Harrison, I. Modification of polyacrylonitrile (PAN) carbon fiber precursor via post-spinning plasticization and stretching in dimethyl formamide (DMF). *Carbon* **2002**, *40* (1), 25–45.
20. Edie, D.; Dunham, M. Melt spinning pitch-based carbon fibers. *Carbon* **1989**, *27* (5), 647–655.
21. Joo, S. H.; Pak, C.-h. Mesoporous Carbon, Manufacturing Method Thereof, and Fuel Cell Using the Mesoporous Carbon. U.S. Patent 7776779 B2, 2010.
22. Hou, Y.; Sun, T.; Wang, H.; Wu, D. Effect of heating rate on the chemical reaction during stabilization of polyacrylonitrile fibers. *Text. Res. J.* **2008**, *78* (9), 806–811.
23. Paiva, M.; Kotasthane, P.; Edie, D.; Ogale, A. UV stabilization route for melt-processible PAN-based carbon fibers. *Carbon* **2003**, *41* (7), 1399–1409.
24. Fitzer, E. Pan-based carbon fibers—Present state and trend of the technology from the viewpoint of possibilities and limits to influence and to control the fiber properties by the process parameters. *Carbon* **1989**, *27* (5), 621–645.
25. Ko, T. H. Influence of continuous stabilization on the physical properties and microstructure of PAN-based carbon fibers. *J. Appl. Polym. Sci.* **1991**, *42* (7), 1949–1957.
26. Usami, T.; Itoh, T.; Ohtani, H.; Tsuge, S. Structural study of polyacrylonitrile fibers during oxidative thermal degradation by pyrolysis-gas chromatography, solid-state carbon-13 NMR, and Fourier-transform infrared spectroscopy. *Macromolecules* **1990**, *23* (9), 2460–2465.
27. Bashir, Z. A critical review of the stabilisation of polyacrylonitrile. *Carbon* **1991**, *29* (8), 1081–1090.
28. Fitzer, E.; Müller, D. The influence of oxygen on the chemical reactions during stabilization of PAN as carbon fiber precursor. *Carbon* **1975**, *13* (1), 63–69.
29. Rahaman, M.; Ismail, A. F.; Mustafa, A. A review of heat treatment on polyacrylonitrile fiber. *Polym. Degrad. Stab.* **2007**, *92* (8), 1421–1432.
30. Watt, W. Nitrogen evolution during the pyrolysis of polyacrylonitrile. *Nature* **1972**, *236* (62), 10–11.
31. Standage, A.; Matkowsky, R. Thermal oxidation of polyacrylonitrile. *Eur. Polym. J.* **1971**, *7* (7), 775–783.
32. Donnet, J.-B. *Carbon Fibers*; CRC Press: Boca Raton, FL, 1998.
33. Palmer, K. R.; Marx, D.; Wright, M. A. *Carbon and Carbonaceous Composite Materials: Structure–Property Relationships*; World Scientific Publishing: Singapore, 1996.
34. Zeng, S. M.; Maeda, T.; Tokumitsu, K.; Mondori, J.; Mochida, I. Preparation of isotropic pitch precursors for general purpose carbon fibers (GPCF) by air blowing. II. Air blowing of coal tar, hydrogenated coal tar, and petroleum pitches. *Carbon* **1993**, *31* (3), 413–419.

35. Jain, M. K.; Abhiraman, A. Conversion of acrylonitrile-based precursor fibres to carbon fibres. *J. Mater. Sci.* **1987**, *22* (1), 278–300.
36. Zhu, D.; Xu, C.; Nakura, N.; Matsuo, M. Study of carbon films from PAN/VGCF composites by gelation/crystallization from solution. *Carbon* **2002**, *40* (3), 363–373.
37. Liu, F.; Wang, H.; Xue, L.; Fan, L.; Zhu, Z. Effect of microstructure on the mechanical properties of PAN-based carbon fibers during high-temperature graphitization. *J. Mater. Sci.* **2008**, *43* (12), 4316–4322.
38. Matsumoto, T. Mesophase pitch and its carbon fibers. *Pure Appl. Chem* **1985**, *57* (11), 1553–1562.
39. Jones, S.; Fain, C.; Edie, D. Structural development in mesophase pitch based carbon fibers produced from naphthalene. *Carbon* **1997**, *35* (10), 1533–1543.
40. Chand, S. Review carbon fibers for composites. *J. Mater. Sci.* **2000**, *35* (6), 1303–1313.
41. Johnson, D.; Tyson, C. Low-angle X-ray diffraction and physical properties of carbon fibres. *J. Phys. D: Appl. Phys.* **1970**, *3* (4), 526.
42. Beaucage, G. Approximations leading to a unified exponential/power-law approach to small-angle scattering. *J. Appl. Crystallogr.* **1995**, *28* (6), 717–728.
43. Beaucage, G. Small-angle scattering from polymeric mass fractals of arbitrary mass-fractal dimension. *J. Appl. Crystallogr.* **1996**, *29* (2), 134–146.
44. Beaucage, G.; Rane, S.; Sukumaran, S.; Satkowski, M.; Schechtman, L.; Doi, Y. Persistence length of isotactic poly (hydroxy butyrate). *Macromolecules* **1997**, *30* (14), 4158–4162.
45. Debye, P.; Bueche, A. Scattering by an inhomogeneous solid. *J. Appl. Phys.* **1949**, *20* (6), 518–525.
46. Guigon, M.; Oberlin, A.; Desarmot, G. Microtexture and structure of some high tensile strength, PAN-base carbon fibres. *Fibre Sci. Technol.* **1984**, *20* (1), 55–72.
47. Ozcan, S.; Tezcan, J.; Filip, P. Microstructure and elastic properties of individual components of C/C composites. *Carbon* **2009**, *47* (15), 3403–3414.
48. Thünemann, A. F.; Ruland, W. Microvoids in polyacrylonitrile fibers: a small-angle X-ray scattering study. *Macromolecules* **2000**, *33* (5), 1848–1852.
49. Shioya, M.; Takaku, A. Characterization of microvoids in carbon fibers by absolute small-angle x-ray measurements on a fiber bundle. *J. Appl. Phys.* **1985**, *58* (11), 4074–4082.
50. Zhu, C.; Liu, X.; Yu, X.; Zhao, N.; Liu, J.; Xu, J. A small-angle X-ray scattering study and molecular dynamics simulation of microvoid evolution during the tensile deformation of carbon fibers. *Carbon* **2012**, *50* (1), 235–243.
51. Bennett, S.; Johnson, D.; Johnson, W. Strength-structure relationships in PAN-based carbon fibres. *J. Mater. Sci.* **1983**, *18* (11), 3337–3347.
52. Zhu, C.; Liu, X.; Guo, J.; Zhao, N.; Li, C.; Wang, J.; Liu, J.; Xu, J. Relationship between performance and microvoids of aramid fibers revealed

- by two-dimensional small-angle X-ray scattering. *J. Appl. Crystallogr.* **2013**, *46* (4), 1178–1186.
53. Loidl, D.; Paris, O.; Rennhofer, H.; Müller, M.; Peterlik, H. Skin-core structure and bimodal Weibull distribution of the strength of carbon fibers. *Carbon* **2007**, *45* (14), 2801–2805.

Subject Index

A

- Acetylated softwood kraft lignin, carbon fibers, 137
- Ace-SKL carbon fiber
 - cross section shape analysis, 146
 - properties, 149*t*
 - tensile strength and modulus, 148*f*
- experimental
 - fiber characterization, 141
 - fiber spinning, 140
 - materials, 139
 - thermal treatment, 141
- result of SKL before and after wash, elemental analysis, 140*t*
- results and discussion
 - capillary rheometer test, 145*f*
 - characterization of Ace-SKL carbon fibers crystallinity, 149
 - controlled acetylation of Ace-SKL, 143
 - different spinning condition, Ace-SKL carbon fiber, 147*t*
 - dry spinning of Ace-SKL, 145
 - DSC of Ace-SKL with different reaction composition, 145*f*
 - FT-IR spectra of acetylated lignin (Ace-SKL), 144*f*
 - melt spinning of Ace-SKL with high acetylation content, 142
 - Raman spectra of Ace-SKL carbon fibers carbonized, 150*f*
 - softening point of Ace-SKL with different reaction composition, 144*f*
 - tension effect during carbonization, 148
 - thermal treatment of Ace-SKL fibers and characterization, 146
 - wide-angle x-ray diffraction of Ace-SKL carbon fibers, 151*f*
 - tensile properties of carbon fibers, 140*t*

B

- Block copolymer-templated nanoporous carbon films, 35
- large area alignment of ordered domains, 50
- cold zone annealing, 52

- elastomer shear through solvent vapor annealing, 55
- GISAXS profiles for FDU-15 film, zone annealing, 54*f*
- pluronic-resol mixture, 53
- surface of PEO-b-PEA-b-PS:resol polymer films, 55*f*
- zone annealing apparatus and temperature gradient profile, 53*f*
- zone casting, 51
- outlook and opportunities, 56
- soft templated carbon films, solvent-assisted processing, 44
- mass flow controllers, 46*f*
- residual low volatility solvent, 48
- solvent vapor annealing, 45
- surface of mesoporous carbon films, 47*f*
- surface of mesoporous polymer films, 49*f*
- thin film effects, 37
- influence of interfaces on structure, 38
- layers of thick mesoporous carbon, 42*f*
- mesoporous carbon film, 41*f*
- mesoporous cross-linked phenolic resin, 39*f*
- PEO and PPO, 40
- Pluronic F127, 41
- Pluronic P123, 40
- structure formation and maintenance through carbonization, 43
- wetting conditions, 39*f*

C

- Carbon membranes with thiol-substituted HPBs, 2D, 10
- freestanding CNMs, 12*f*
- nanomembrane formation by electron irradiation and pyrolysis, 11*f*
- nitrogen doped HPB **5** and **6**, chemical structure, 13*f*
- pyrolysed carbon membranes, 13*f*
- synthesis of nitrogen doped HPB **5**, 14*f*
- 3',4',5',6'-tetraphenyl-[1,1':2',1''-terphenyl]-4,4''-dithiol, molecular structure, 12*f*
- Carbon nanomembranes (CNMs), 10
- Carbonaceous pitch oligomers, 85

97% pure trimer cut of M-50 pitch, cross-polarized light photomicrograph, 132*f*
coal-derived materials, 88
continuous fractionation of petroleum pitches, 93*f*
continuous SCE fractionation, 94
extraction of petroleum pitch, 92*f*
industrial-grade petroleum pitch, MALDI mass spectrum, 89*f*
isolating petroleum pitch oligomers via supercritical extraction, 90
isolation of intermediate oligomers, 96*f*
mesophase formation, 131
mesophase spheres, 87*f*
molecular weight distribution (MWD), 88
oligomers of petroleum pitch, FT-IR spectroscopy, 127
pitch-rich liquid phase, 95
SCE extraction, mesophases of increasing orientation, 130*f*
semi-continuous fractionation of petroleum pitches, 94*f*
semi-continuous SCE fractionation, 97
solvent-rich liquid phase, 95
supercritical toluene offers, 91*f*
temperature gradient effects, 95
transmission FT-IR analysis, 128*f*
trimer fraction of M-50 pitch, liquid crystallinity, 129
CNMs. *See* Carbon nanomembranes (CNMs)

D

1D and 2D carbon structures
self-assembly of polyaromatic precursors, 1
low-molecular weight amphiphiles and high-molecular weight analogues, 3*f*
molecular structure, 3*f*
Designing structure of carbon fibers, optimal mechanical properties, 215
carbonization, 220
crystalline parameters of carbon structure, 225*t*
cyclization and dehydration mechanisms, 219*f*
different carbon fibers, tensile strength and modulus, 223*f*
different fibers, density, diameter, and strain, 224*t*

experimental procedures, 221
oxidative stabilization, 218
polyacrylonitrile and aromatic pitch, chemical structure, 217*f*
pore size distributions, 226*f*
comparison, 227*f*
precursor fiber, spinning, 216
results and discussion, 222
Dimer constituents of petroleum pitches, identification, 112
experimental
GPC fractions via prep-scale GPC from SCE dimer cuts 1-2, 114
pre-fractionation and concentration of M-50 petroleum pitch, 99
UV-Vis, MALDI, and MALDI-PSD analysis of GPC dimer fractions, 115
results and discussion
dimer molecular weights and degree of alkyl substitution, MALDI and PSD, 115
dimers form primarily via 5-membered ring linkages, 120*f*
linkages connecting monomer units in dimers, 118
MALDI-PSD fragmentation analysis, 116*f*
molecular structure of dimers, MALDI and PSD, 117
precursor monomer units and resultant major oligomers, 119*t*

F

Fibers of HPB/HBC with PEG chains, ID Aida's HBC derivative and HBC-PEG derivative, 8*f*
bundles of fibers of molecule, 8*f*
HBC-PEG compound, synthesis, 9*f*
HBC-PEG derivatives, self-assembly, 8
HPB and HBC, molecular structure, 4*f*
schematic representation of solutions, 6*f*
structural parameters for the self-assembled structures, 7*t*

H

HPB-PEG derivative
molecular structure, 5*f*
self-assembly, 4
synthesis, 6*f*

I

- I-PAN and A-PAN
 - C-NMR spectra, 178*f*
 - different molecular weight averages, 176*t*
 - EGA-MS curves of total ions, 180*f*
 - thermal degradation reaction
 - mechanisms, 181*s*
 - triad tacticity contents, 177*t*

L

- Lignin, pore textural characteristics, 75

M

- Monomeric constituents of petroleum pitches, identification, 98
 - experimental
 - GPC fractions via prep-scale GPC
 - from SCE monomer cuts 1-3, 100
 - individual monomer species
 - identification by HPLC + UV-Vis/PDA, 101
 - MALDI and PSD, 102
 - pre-fractionation and concentration of petroleum pitch, 99
 - results and discussion
 - alkylpyrenes, 104*f*
 - benzo[e]pyrene, benzo[a]pyrene, and benzo[ghi]perylene, 106*f*
 - determination of degree of alkyl substitution, 106
 - determination of PAH backbones for M-50 pitch monomers, 102
 - GPC fractions 7 and 6, 105*f*
 - HPLC chromatogram of SCE monomer cut 1, 103*f*
 - individual species, MALDI-PSD fragmentation analysis, 108*f*
 - M-50 pitch, estimating species compositions, 109
 - MALDI-PSD, 107
 - monomeric portion of M-50 pitch, major species, 111*t*
 - PAH backbones, 110*f*
 - PSD fragmentation analysis, 109*f*
 - signal distribution, 107

P

- PAN. *See* Poly(acrylonitrile) (PAN)
- PAN-based polymers, solution spinning
 - coagulation, 200
 - coagulation bath concentration, 201
 - coagulation bath temperature, 201
 - diffusion, 200
 - die swell, 199
 - drying and collapsing, 204
 - fiber properties and structure, 205
 - fiber cross section, 207
 - fiber morphology, 209
 - mechanical properties, 208
 - void and pore structure, 206
 - filtration, 199
 - heat setting, 205
 - history, 189
 - methods
 - air gap spinning, 192
 - dry spinning, 191
 - gel spinning, 193
 - wet spinning, 191
 - wet-jet spinning, 192
 - molecular weight, 195
 - dope preparation, 196
 - rheological characterization, 197
 - solvents, 196
 - polymers, 194
 - polymers and solvents, 194
 - spin finish application, 203
 - spinning, 198
 - stretching, 204
 - washing, 202
- PEO. *See* Poly(ethylene oxide) (PEO)
- PILs. *See* Polymerized ionic liquids (PILs)
- Poly(acrylonitrile) (PAN), 170
- Poly(ethylene oxide) (PEO), 66
- Poly(ionic liquid)-derived
 - functional-shaped carbon nanomaterials, 17
 - carbon materials with variable chemical compositions
 - heteroatoms-doped carbon, 26
 - metal NPs, 27
 - carbon nanomaterials derived from PILs, potential applications
 - adsorbent, 30
 - catalysis, 31
 - fire-retardant material, 28
 - carbon nanomaterials with variable morphologies and structures
 - carbon nanoparticles, 23
 - formation of HCSs, 21*f*
 - hollow carbon spheres (HCSs), 20
 - layer-by-layer (LbL) technique, 22

- monolith, 25
 - nanofiber and film, 24
 - nanotube, 24
 - introduction, 18
 - PILs as carbon precursors, carbon yield and nitrogen content, 19*t*
 - summary and outlook, 32
 - Polymerized ionic liquids (PILs), 17
 - Polypropylene oxide (PPO), 66
 - PPO. *See* Polypropylene oxide (PPO)
 - Pyrolysis and thermal stability of carbon fiber polymer precursors, 169
 - average molecular weight determinations
 - ¹³C nuclear magnetic resonance spectroscopy (13C NMR), 174
 - membrane osmometry, 173
 - size exclusion chromatography (SEC), 173
 - solution capillary viscometry, 172
 - averaged mass spectra of evolved gases
 - A-PAN, 182*f*
 - I-PAN, 182*f*
 - identification of pyrolysates from Py-GC-MS, 179*t*
 - isotactic poly(acrylonitrile) (I-PAN) and atactic poly(acrylonitrile) (A-PAN), synthesis, 172
 - molecular characteristics and microstructural elucidation, 175
 - molecular characterizations, 172
 - PAN fiber density and oxidized PAN fibers, 171*f*
 - synthesis of poly(acrylonitrile) with different microstructures, 172
 - TGA-FTIR spectra
 - A-PAN, 184*f*
 - I-PAN, 183*f*
 - thermal characterizations
 - pyrolysis-gas chromatography-mass spectrometry, 174
 - TGA-fourier transform infrared spectrometry, 175
 - thermal degradation pathways of PAN polymers, 184*s*
 - TIC spectra
 - A-PAN, 183*f*
 - I-PAN, 183*f*
- S**
- Soft-templated mesoporous carbons, 61
 - activation, 70
 - activation temperatures, 78
 - atom transfer radical polymerization (ATRP), 66
 - chemical activation, 71
 - controlling mesoporosity, 67
 - degree of burn-off with BET SSA and pore volume, 72*f*
 - hysteresis loop, types, 75*f*
 - KOH activation, 73
 - limitation of hard-templating, 62
 - mesoporous carbon synthesis, 65*f*
 - N₂ adsorption-desorption plots of lignin and pore size distribution of LMC samples, 77*f*
 - phenolic resin hydrogen bonded with PS-block-P4VP, 69*f*
 - physical or CO₂ activation protocol, 71
 - pore textural properties, 76*t*
 - precursors, 68
 - principles of soft templating, 64
 - silicate frameworks, 78
 - strategy of synthesizing from lignin, 70*f*
 - structural characteristics, 74
 - templates, 66
 - Solvent fractionation of lignin, 156, 157*s*
 - chemical compositions, 154
 - chemical properties, 163
 - common chemical bonds, 155*f*
 - effect of solvent fractionation on molecular weights, 158
 - fractionation of organosolv (alccl) lignin, 162*t*, 163*t*
 - hydroxyl group contents (mmol/g) of lignin, 164*t*
 - isolation, 154
 - kraft lignin with and without LiBr, 159*f*
 - lignin fractions from *Eucalyptus pellita*, 157*t*
 - MeOH fractionated lignin, T_g and thermal degradation properties, 165*t*
 - MeOH fractionation of hardwood Alcell lignin, 161
 - molecular weight distributions for lignin fractions, 162*f*
 - molecular weight of lignin via MeOH fractionation, 160*t*
 - molecular weight of lignin with addition of LiBr, 160*t*
 - M_w, M_n, and PDI of lignin fractions from *Eucalyptus Pellita*, 162*t*
 - organosolv lignin, 161
 - structural units, 155*f*
 - thermal properties, 164
 - yields of lignin fractions after sequential solvent fractionation, 158*t*

T

- Templated nanoporous carbons, 36
- Trimer and tetramer constituents of petroleum pitches, identification, 121
 - experimental
 - GPC fractions via prep-scale GPC from SCE dimer cut 3, 123
 - MALDI, MALDI-PSD, and UV-Vis analysis of GPC trimer and tetramer fractions, 123
 - pre-fractionation and concentration of M-50 petroleum pitch, 113
 - results and discussion
 - MALDI-PSD fragmentation analysis, 125^f
 - molecular weight, degree of alkyl substitution, and molecular structure, 123
 - tetramer portion of M-50 pitch, MALDI spectrum, 126^f
 - trimer portion of M-50 pitch, MALDI spectrum, 124^f

U

- Ultra-small HCSs, 22

W

- Wetting conditions, block copolymer-templated nanoporous carbon films, 39^f

Z

- Zone casting, block copolymer-templated nanoporous carbon films, 51